
Continuum modeling, analysis and simulation of the self-assembly of thin crystalline films

vorgelegt von
Diplom-Mathematiker
Maciej Dominik Korzec
geboren in Łódź (Polen)

Von der Fakultät II - Mathematik und Naturwissenschaften
der Technischen Universität Berlin
zur Erlangung des akademischen Grades
Doktor der Naturwissenschaften
Dr. rer. nat.

genehmigte Dissertation

Promotionsausschuss:

Vorsitzender: Prof. Dr. Martin Skutella
Gutachter: Prof. Dr. Volker Mehrmann
Gutachter: PD Dr. Barbara Wagner
Gutachter: PD Dr. Andreas Münch
weiterer Gutachter: Prof. Dr. Piotr Rybka

Tag der wissenschaftlichen Aussprache: 11.10.2010

Berlin 2010
D 83

Abstract

Derivation of realistic continuum models for epitaxial growth of thin solid films on crystalline substrates yields Cahn-Hilliard type equations of fourth or sixth order. To describe and understand solutions and solution spaces to these semi- or quasilinear partial differential equations (PDEs), the development of elaborated theory is necessary. Existence of solutions has to be shown in untypical high order Sobolev spaces, the numerics has to be capable to deal with high order derivatives for the time-dependent problems and with high order phase spaces for the stationary case and methods of matched asymptotics require matching at many orders. In this work new theory is presented for reduced models of high order.

For a sixth order PDE that describes the faceting of a growing surface in 2D [89] it is shown that weak solutions exist. While for a related convective Cahn-Hilliard equation proving the existence of absorbing balls directly brings along existence of solutions [24], estimates for the sixth order model are more difficult to obtain since the anisotropic surface energy leads to undesired terms. The problem is solved by application of fractional operators to derive lower order bounds from a transformed equation, which are then used to obtain higher order bounds from the original equation. Next, new types of stationary solutions are found by an extension of a method of matched asymptotics where exponentially small terms are retained. By using this generalization of the ansatz by Lange [62], the hump spacing is related to the Lambert W function and analytical expressions are found for the far-field parameter in the limit of small driving force strength. These solutions live in a five dimensional phase space and a continuation technique allows to track them on branches in a parameter plane. The asymptotic solutions can be used as initial input for the numerical method.

A new model for the self-assembly of quantum dots has been derived. It extends a work by Tekalign and Spencer [102] by an anisotropic surface energy and an atomic flux such that realistic simulations of a Stranski-Krastanov growth can be carried out. A linear stability analysis to the fourth order quasilinear PDE shows the destabilizing effect of the anisotropy, which can also be observed in simulations based on a pseudospectral method. While in the work for the isotropic case single bell-shaped dots were calculated, here huge arrays — hundreds of faceted nanoislands — are simulated, so that the evolution of the structures can be compared to experiments. Higher flux rates yield bigger island densities and smaller dots are absorbed in favor of the bigger ones, resulting in an Ostwald ripening process.

Keywords:

Self-assembly of quantum dots, continuum modeling, small slope reduction, pseudospectral method, anisotropic surface energy, exponential matched asymptotics, existence of solutions, Ostwald ripening, linear stability analysis

Contents

Introduction	1
0.1 A quantum of self-assembled solids	1
0.2 Production processes and applications of quantum dots	5
0.3 Growth types and crystal properties	8
0.4 Ge/Si(001) quantum dots	11
0.5 Content, results and structure of this work	13
1 Surface diffusion based continuum modeling	17
1.1 Atomic flux	19
1.2 Types of surface energies	20
1.2.1 Functional derivatives of surface energy formulas	23
1.2.2 Anisotropic surface energy of regular surfaces	26
1.3 The strain energy density for Ge/Si like systems	28
1.3.1 The base state	31
2 The HCCH equation: Derivation and existence of solutions	34
2.1 The faceting of a growing surface	35
2.1.1 The HCCH equation	36
2.2 Related phase separation systems	40
2.3 Preliminaries: Concepts from functional analysis	42
2.3.1 Operators, fractions, eigenvalues and eigenfunctions	43
2.3.2 Spaces involving time, dual spaces, inequalities and other useful results	46
2.4 Existence of solutions to the HCCH equation	53
3 Stationary solutions and kink dynamics to the HCCH equation	60
3.1 Stationary solutions to the HCCH equation	61
3.1.1 A phase space method	64
3.1.2 Exponential matched asymptotics	67
3.1.3 Comparison between numerical data and analytical results	78

3.2	Coarsening dynamics for the HCCH equation	79
4	The QDM equation: Derivation, analysis and simulation results	86
4.1	Derivation of the QDM equation	87
4.2	Linear stability analysis	94
4.3	Periodic stationary solutions	97
4.4	Evolution on big domains	101
4.4.1	Coarsening of two-dimensional arrays	102
4.4.2	Three-dimensional self-assembly	104
4.5	Effect of deposition	108
5	Numerical methods for evolution equations on periodic domains	114
5.1	Finite difference methods (FDMs)	116
5.2	Pseudospectral methods (PSMs)	124
5.2.1	Spectral differentiation and accuracy	124
5.2.2	PSMs for 3D problems	131
6	Summary and discussion	137
A	Mathematical basics: Surface modeling	149
B	Mathematical basics: Dynamical systems	152
C	Elasticity	155

For a true writer each book should be a new beginning where he tries again for something that is beyond attainment. He should always try for something that has never been done or that others have tried and failed. Then sometimes, with great luck, he will succeed.

Ernest Hemingway (1899 - 1961)

0.1 A quantum of self-assembled solids

Maybe true scientists have a similar motivation as true writers, since it is the researchers' job to try for something that is beyond attainment. Sometimes, with great luck, they succeed and their results change the world. Who would have believed in a wireless world thirty years ago when programming meant printing holes into paper? Who believed in flying 200 years ago? These ideas were out of range for everyone except for a few visionaries.

By now a majority is aware of the existence of the nano-world, of nano-particles, nano-coatings and nano-scales. However, most people might still miss spots where 'nano' plays a role. Quietly and unintrusively nano-technology settles in everyday life. The founders of the nano- or mesoscopic world generate changes on an invisible scale. When people drink out of a plastic bottle, they do not think about chambers, plasmas, and resulting coatings on the inside of their drinking vessel.

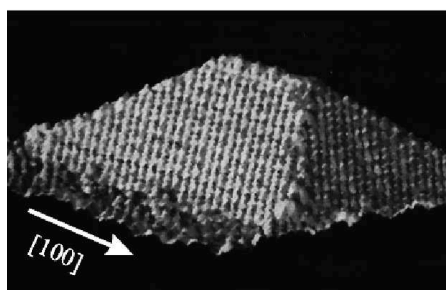


Figure 1: STM picture of a Si_{1-x}Ge_x/Si(001) quantum dot. All facets are {105} oriented. Picture reprinted with permission from Teichert [101].

During the last decades incorporation of nano-structures in various fields of engineering has become very popular and successful. They are used to develop lasers with short wave lengths, processors for computers, mobile phones or car accessories. Nano-coatings are employed for the creation of water-resistant or scratch-proof materials or treatment of medical equipment. Many other applications are possible and the understanding of the world on micro-scales is necessary to improve production processes. In this work mathematical aspects connected to epitaxial growth of solids on the nano/mesoscale are in focus. Anisotropy of the surface energy is important on such small scales. It is added to surface diffusion models that describe the self-assembly of thin

crystalline films. The resulting partial differential equations (PDEs) are of high order and new theory is developed to analyze them on several aspects, such as equilibrium states, linear stability or general existence of solutions. The results are supported by simulations that are carried out with help of pseudospectral methods.

One of the small structures that has raised great attention in recent years and which plays a big role in this work is the so-called *quantum dot*, or also *nanodot*, *nanoisland* or *artificial atom*. Quantum dots (QDs) are very small crystals whose typical sizes range between 1 and 100 nm. This scale constrains the motion of electrons in the conduction band and holes in the valence band in all directions, labeling such a nanoisland a zero-dimensional structure. In Figure 1 one such pyramidal crystal — germanium and silicon grown on silicon with a particular crystal grid orientation, $\text{Si}_{1-x}\text{Ge}_x/\text{Si}(001)$ — is made visible by scanning tunneling microscopy (STM). Anisotropy leads to preferred facets created during growth, so that characteristic slopes appear that are typically small. In the picture the vertical scale is exaggerated.

A nanodot can be excited and the band gap energy is directly related to its size. The wave length of the emitted light is controllable once control over the growth is achieved. This property makes artificial atoms very useful for optoelectronic devices such as LEDs or for lasers. The creation of solar power systems with higher conversion efficiencies — solar cells of third generation [20] — is a promising idea for the application of the nano crystals. Because of the current growth of the photovoltaic industry, an effective implementation could revolutionize the nano crystal market. Although so far QDs do not play a major role on the market, neither as LEDs, nor as photovoltaic systems or lasers, their influence will grow significantly in the next few years. Predictions are made which state that the demand for the tiny crystals will explode during the next five years, when displays and lasers based on QDs will be produced for the market [88]. Furthermore quantum computing based on QDs is under research, though independently of the type of implementation it has remained a visionary goal for several decades [66].

The sizes and shapes of quantum dots are relevant for their optoelectronic properties. Complicated etching techniques give proper control over the shapes, but they are expensive, which makes alternative self-assembly properties popular. Understanding and properly influencing this kind of growth would improve the quality of the produced devices. Self-assembly is known from everyday life, so many other physical systems where patterning can be observed have already been analyzed. In particular the field of fluids is popular in this respect (e.g. [45, 54, 72]). Generally self-organization appears in many situations at many sites, be it on glaciers, on stalagmites or as shown in Figure 2 on sand, water or mud, in the sky and on crystalline surfaces. Patterning can be observed on large scales (cloud formation), intermediate scales (boiling water) or on very small scales — so small that they cannot be made visible with optical microscopes. When atoms are deposited onto a substrate in a suitable manner, formation of patterns can be observed. An understanding of the mechanisms of this assembly is necessary to control the distribution and the sizes of the nano-structures. Since surface diffusion is responsible for the ordering of the surface

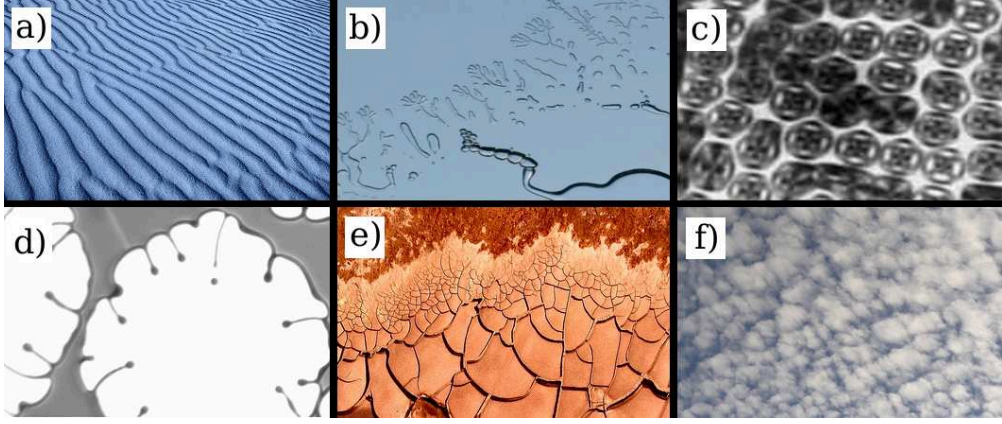


Figure 2: (a) Sand in the desert*; (b) Water between glass plates* ; (c) A Si,Ge film on a Si(001) substrate (reprint Courtesy of International Business Machines Corporation, copyright 2009 ©International Business Machines Corporation); (d) A polymer film dewets a hydrophobic substrate (image courtesy of Chiara Neto, The University of Sydney; for dewetting polymer films see e.g. her work with Jacobs [72]); (e) Drying mud*; (f) Cloud formation*; (a), (b), (e) and (f) depict examples for macroscopic patterns, while (c) and (d) show self-assembly on small scales.

* Pictures courtesy of the flickr members *Mr. Mark*, *Daveybot*, *pictoscribe*, *tracitodd*.

atoms, its analysis is fundamental.

The central focus in this thesis lies in elaborate continuum modeling based on surface diffusion, model reduction, analysis and simulation of self-assembled patterning of thin-film crystalline nano-structures. Here not only QD growth will be considered, but also thin crystalline surfaces that undergo faceting during growth. Mathematically a big task lies in the analysis of the properties of a smooth real function, $h : \Omega \times I_T \rightarrow \mathbb{R}$, $(x, y, t) \mapsto h(x, y, t)$, that describes the evolution of a self-assembled surface — similar to the thin film depicted in Figure 2 (c). Here $\Omega \subset \mathbb{R}^2$ is a fixed domain with Lipschitz boundary or an infinite domain. Typically it will be chosen $\Omega = [0, L]^2$ and periodicity will be assumed at the boundaries. $I_T = [0, T]$ is a time interval so that overall $(x, y) \in \Omega$ and $t \in I_T$. One could consider a function with more dependencies $h^* : \Omega \times I_T \times P \rightarrow \mathbb{R}$, $(x, y, t, p_1, \dots, p_k) \mapsto h^*(x, y, t, p_1, \dots, p_k)$, where $(p_1, \dots, p_k) \in P$ is a vector of parameters — material properties such as elasticity constants or growth conditions like temperature or deposition rate. However, these quantities are usually combined in a few variables. The mathematical concept of nondimensionalization is applied to work with dimensionless units and this makes the first notation preferable. During accomplishment of parameter studies the dependencies are then explicitly discussed. Mathematically challenge lies in the high order of the semi- or quasilinear PDEs that define the functions h as their solutions. New theory in different fields of mathematics has to be established to deal with the high derivatives and the nonlinearities.

There are different approaches for modeling and simulation of epitaxial growth, differing in their scale, their level of detail and their mathematical foundation [106]. On the microscopic

level the models describe atom interactions and are quite accurate (molecular dynamics methods, Monte-Carlo simulations [49]), but the computational costs for investigating long-time behavior of big arrays of QDs are excessive. Only early stages of the self-assembly and relatively small arrays can be studied. Mean-field models as in the work by Ross et al. for QD self-assembly [86] can yield a coarse description of the island distribution, but they do not account for the shapes of the dots and the layout of the arrays, which are essential information needed for the anticipated improvement of the electro-optical properties. Continuum models describe the evolution of islands, including positions and shapes on the analyzed time domain. Anisotropic surface energy is used to describe growing crystalline surfaces that have preferred orientations. For modeling of QD growth an additional stress description is needed. Opposite to homoepitaxy, which is a one solid system, in heteroepitaxy film and substrate have different lattice spacings. The film grows coherently on top of the substrate, so that a coherency strain induces stresses inside both solids that compete with the surface energy. Typically linear elasticity theory in form of the Navier-Cauchy equations is applied. These can be solved numerically in terms of a three-dimensional finite element code as done by Zhang et al. [117, 118]. Without optimized FEM codes and high-speed machines this approach again results in run time problems for large-scale simulations which motivates the idea to derive simplified expressions that do not rely on FEM computations.

Two equations are derived and analyzed in this work. One describes the faceting of a growing surface and the other the evolution of Ge/Si or $\text{Si}_x\text{Ge}_{1-x}$ /Si QDs. For both the modeling ansatz originates from Mullins' surface diffusion formula [69]. A chemical potential has to be defined to model the forces driving the surface diffusion. Over the last two decades the resulting PDE models based on this approach gained complexity by including more and more of the important effects that influence the growth. A few of the recently appeared publications on continuum theory for self-arranging surfaces can be found in the following list of references [16, 26, 27, 42, 89, 97, 102, 103, 116]. It is far from complete and a more detailed discussion will be accomplished throughout the work, in particular in Chapter 1. Continuum models often can be reduced to simpler PDEs that contain less terms and nonlinearities, making simulations easier, faster and more stable. Therefore small quotients of different characteristic length scales can be employed to identify small terms in suitable expansions that can be neglected. This has been done previously in the field of fluid dynamics where the full Navier-Stokes equations can be reduced to lubrication models (see for example Atherton and Homsy [5] or for a more recent paper the work by Münch et al. [70], where models for different slip-regimes are derived). Here the reduction approaches are applied to obtain equations describing the growth of thin solid crystalline films — an idea that is pursued since about a quarter century. The coarsening of faceted growing crystals and quantum dot arrays reminds of coarsening in liquids [39, 45] and also of solid phase separating systems like binary alloys [79, 83, 109]. A new model for the QD self-assembly will be introduced, it is probably the most realistic model for such an Ostwald ripening system. A different, yet existing

model for the faceting of a growing surface will be analyzed on many aspects. A detailed listing of the results will be given in Section 0.5, where also the general structure of the thesis is explained. Readers familiar with crystals, epitaxy and in particular with the topic of self-assembled QDs might want to jump forward and continue with this section, others can get an overview over these important aspects and an understanding for why self-assembled nanostructures can be very valuable. Observations during the deposition process in the Ge/Si system, which is qualitatively very similar to $\text{Si}_x\text{Ge}_{1-x}/\text{Si}$, are outlined step-by-step. These will be useful when they will be compared with the simulation results achieved in this work. The most important aspects of QDs are outlined on the following pages, however, a complete discussion is not offered. For further details the reader is referred to a book by Freund and Suresh [34].

0.2 Production processes and applications of quantum dots

The sizes and shapes of QDs depend on many aspects of fabrication, in particular on the materials and temperature used in the growth chamber. Spontaneous arrangement of nano-structures can be observed during a process that is called epitaxial growth. It is carried out at high temperatures, typically $> 500^\circ\text{C}$, so that surface diffusion plays a major role. A crystalline material is precipitated with a low flux rate onto a substrate. As mentioned before, if the same material is used for film and substrate, one talks about homoepitaxial growth, while heteroepitaxy is the case for two different materials — it is the common method for QD self-assembly. For certain film and substrate combinations an initially monotonously growing planar film develops an instability after some time. A mismatch (or analogously misfit) between the lattices of film and substrate leads to stresses that are released once a critical height is exceeded. This instability, where surface energy is of order of the bulk stresses, is called Asaro-Tiller-Grinfeld (ATG) instability [22]. Small humps, often called *pre-pyramids*, form and evolve to pyramids that coarsen throughout the process (these islands have square bases and $\{105\}$ facets; Miller indices are explained in Section 0.3). Smaller islands vanish in favor of the bigger ones which develop more pronounced facets. Such ripening phenomena are well analyzed in related fields, for example in alloy mixtures or other phase boundaries of solids (for a modeling paper see Thornton et al. [104]) and they also appear in liquid droplet dynamics (see for example [38, 45, 54]). Researchers hope to predict the layout of the arrays of QDs that form after sufficiently long evolution. Since some applications need dense arrays, while others need equally sized artificial atoms and/or equally distributed dots, the nano-industry would benefit from the knowledge of how the island distribution is influenced. Simulations with different parameters could make costly experiments redundant and could save a lot of work and resources.

Results from early experimental works left many open questions for several years, because some of them seemed to contradict others. The major reason for the rather obscure findings was the impossibility to carry out in situ observations of the self-assembly of QDs. Only since Ross

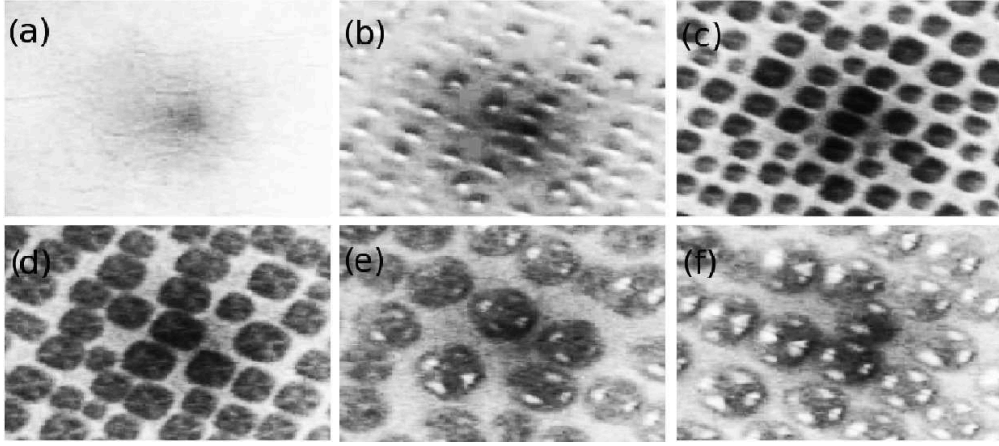


Figure 3: Quantum dots grown by researchers from IBM. As in the Ge/Si(001) system one sees that $\text{Si}_{1-x}\text{Ge}_x$ dots grown on Si(001) coarsen (here at 690°C and a flux rate of 5 monolayer (ML) per minute), that smaller humps vanish and that bigger artificial atoms develop a pyramidal shape that eventually becomes a multi-faceted dome-structure. Reprint Courtesy of International Business Machines Corporation, copyright 2009 ©International Business Machines Corporation.

and her co-workers managed to implement a transmission electron microscopy (TEM) apparatus that works in a chamber during growth, the understanding of the evolution of QDs has lead to a consistent view [85]. Results of the important work are shown in Figure 3. The IBM pictures visualize how a silicon substrate is covered with germanium and silicon atoms and how the resulting film evolves. In (a) a flat state is visible. Atoms are deposited continuously onto the surface and the film grows for some time in vertical direction as flat surface. In (b) the Asaro-Tiller-Grinfeld (ATG) instability sets in and leads to formation of rather rounded structures, the pre-pyramids. These pass into pyramidally formed nanodots as seen in (c) and (d). Here one can also observe that smaller islands are absorbed by a thin layer which connects the dots, so that the overall number of islands decreases. The bigger dots grow and when they exceed a base length of about 50nm, the pyramids change their shape again and domes — multi-faceted islands — appear as in (e) and (f). Clearly the average size of the nano-structures grows with time since the atoms from vanishing islands are redistributed to neighboring QDs while further deposition takes place.

In Figure 4 one particular coarsening event is depicted. A smaller dot surrounded by three bigger pyramids is 'eaten'. The 'fat' dots survive and continue to grow. Throughout the whole evolution this Ostwald ripening process¹, which is also called *survival of the fittest*, is visible. More details on Ge/Si(001) heteroepitaxy is given in Section 0.4.

Although Ge/Si is a common and well studied material combination for fabrication of QDs

¹Originally the term Ostwald ripening refers to the Gibbs-Thomson effect driven coarsening that appears in a system with fixed volume. However, recently it is also used for other, similar phenomena, like the ripening of QDs.

(and it is in focus at most points in this work concerning QDs), different other ways of self-assembly are possible. Apart from different materials for film and substrate, such as indium arsenide or indium gallium arsenide on gallium arsenide (InAs/GaAs, InGaAs/GaAs), cadmium on selenium (Cd/Se) and others, the growth can be realized by diverse processes. A distinction is drawn between chemical vapor deposition (CVD) and physical vapor deposition (PVD), which both may be subdivided into many methods. One of the most common processes in this field is a PVD method, so-called molecular beam epitaxy (MBE). Pure elements are heated in effusion cells until they evaporate. The atoms then move in a beam, which means that they do not interact with each other until they reach the wafer. The other, the CVD technique, is based upon reactions in a gas which lead to deposition of atomic layers. The CVD process is divided into many different types, for example plasma enhanced CVD, atomic pressure CVD, atomic layer CVD or ultra high vacuum CVD, among others. There exist also other PVD or liquid epitaxy methods, however, giving a complete overview is outside the scope of this document.

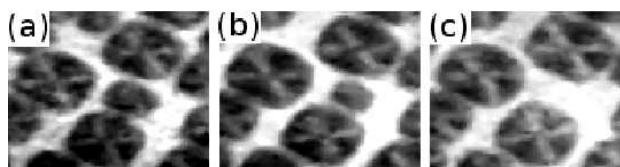


Figure 4: Collapse of a quantum dot during $\text{Si}_{1-x}\text{Ge}_x/\text{Si}(001)$ heteroepitaxy: While the three neighboring pyramids on top, bottom and on the left continue to grow, the middle dot shrinks until it is absorbed by the thin layer. Reprint Courtesy of International Business Machines Corporation, copyright 2009 ©International Business Machines Corporation.

Optoelectronic devices based on QDs use the discrete energy structure of the nano-islands. Electrons in the QDs can be excited so that they release a photon by falling back from the conduction band to the valence band. For photovoltaic devices it is the other way round as incoming photons free electrons which then create a current.

One of the most important applications of self-assembled nanostructures so far is for blue lasers. Because of the semiconductor devices developed by Nakamura in the 1990s, which incorporate self-assembled QDs or quantum wires (nano-structures that are confined in two dimensions only, forming longitudinal ridges) high-frequency lasers were born — see his book with Fasol and Pearton [71]. The nano-crystals enabled the development of lasers with blue light, giving the blue-ray technology its name. Also another big storage disc technology, the HD-DVD, uses self-assembled nano-structures. The shorter wave length of 405 nanometer of blue light (in comparison to 650 nanometer for red lasers) enables to focus the beam on smaller bumps, so that it is possible to reduce the track pitch significantly. The smaller track width and smaller pits form a high information density that allows the single-layer blue ray discs to store 27 GB, while the standard DVD can store only about 5GB. At the time of writing this thesis the blue-ray technology just became standard for high definition films.

Another upcoming application is for photovoltaics. It is common to classify solar cells into three generations. Each subsequent technology is supposed to give benefits in price per area of the cells and in conversion efficiency and quantum dots are supposed to give the newest generation a boost. The first generation still covers most of the market. For these established systems silicon crystal pillars are created by Czochralski growth. These are cut into slices that serve as photovoltaic panels. In comparison to thin-film multicrystalline layers, which define the second generation and cover nearly ten percent of the market, the first generation substrates are thick and much of the material is lost when the big bulk crystals are cut. Although this makes them expensive, they still enjoy great popularity since bulk material cells have had a higher conversion efficiency up to now. Since only a few years ago, third generation photovoltaics are under consideration. Additional layers that improve the conversion properties are incorporated. They can comprise various materials, for example they can be made of polymer cells, or of most relevance for this work, of QDs. The fundamental ability of QDs that wakes hopes for improving solar cells lies in the multiple exciton generation (MEG) effect. One incoming photon is able to exciting several excitons in a single QD. For solar cells stacked QDs are needed for implementations.

Quantum computers are a vision whose realization would revolutionize the world. Spins of electrons would take the place of the usual on and off positions of traditional computers. Therefore a string of so-called qubits needs to become controllable, so that all on-off combinations can be computed at once, which would immensely decrease run-times. To achieve this goal, accessible qubits have to be created. Loss and DiVincenzo [66] describe how one of these tiny crystals could represent one qubit and also other results keep the vision of the supercomputers alive. For example conjunctions between two dots via lithography have been achieved, it is possible to monitor the numbers of electrons in the islands and the spin states have been detected (see Jeong et al. [50]). Once the quantum states of QDs can be controlled, strings of nano-islands will have to be created. These would have a similar role as registers in personal computers. Regular arrays of QDs with the same shapes and same quantum properties are essential for a successful realization.

The applications show that it is important to grow QDs that are in a sense regular, be it in size and/or in the patterning. To obtain control over the evolution, the mechanisms behind the self-ordering have to be understood. Properties of crystals have to be discussed.

0.3 Growth types and crystal properties

In this section some useful concepts from crystallography are introduced. To derive realistic models that describe growth of crystalline structures these basics have to be known. First, growth types typically observed in PVD and CVD methods for heteroepitaxial growth are outlined, second, basic properties of crystal structures are explained and third, Miller indices that are used

for the description of crystal orientations are defined.

Growth types:

Atom deposition methods such as PVD or CVD lead to different growth types that are classified into three groups in case of heteroepitaxy. They are named Frank-van der Merwe, Volmer-Weber and Stranski-Krastanov growth and they are sketched in Figure 5. In the first case a film grows layer by layer. An even surface remains planar and gains in thickness. During a Volmer-Weber growth process the surface directly develops islands and parts of the substrate are uncovered. Here terminology from liquid films is used. In similar situations these are called dewetted, and this expression is used for solid films, too. A prominent example for a material combination that exhibits this behavior is Si/Ge. Here the substrate and film materials are interchanged in comparison to the system considered in this thesis. Silicon has a higher surface energy than germanium, so that the substrate mainly remains uncovered to minimize the overall surface energy. For the third, the Stranski-Krastanov growth mode, the Ge/Si and $\text{Ge}_x\text{Si}_{1-x}/\text{Si}$ systems are archetypes. For such heteroepitaxial QD combinations first a flat film increases its thickness (pseudomorphic growth phase), then it becomes unstable and forms islands after a critical height is exceeded. Once these are big enough, they are called QDs. A thin film covers the substrate, it is wetted, and connects the nanoislands. These can be different in size and shape and typically increase their average size during further deposition. The QD model that will be derived and discussed in this thesis describes a Stranski-Krastanov growth process. For the second model under consideration in this thesis none of the above schemes fits to describe the behavior of the surface. However, there exist more growth types. In homoepitaxial, one-material systems a surface does not wet the substrate. Also here slope-selection can be observed so that faceted island-like structures, e.g. pyramids that have direct contact to their neighbors, form, grow and coarsen.

Bravais lattices:

The materials under consideration in this work are crystals, hence by definition they are characterized by repeating patterns — so-called Bravais lattices. Figure 6 depicts basis cubes for crystals with cubic symmetry. Additionally to the nodes at the corner of simple cubes additional knots can be found in the center of the facets for face centered cubic (fcc) crystals or in the middle of the cube in body centered cubic (bcc) lattices. Illustrious examples of materials with diamond cubic symmetry (following an fcc lattice with additional atoms inside the cube) are the semiconductor materials silicon and germanium. Although many other and in particular more complex symmetries can be found in crystals, only cubic symmetry will be considered throughout this work.

The repeating structure of crystals leads to anisotropy in the surface energy γ , which is an energy per unit area ($[\gamma] = J/m^2$). A two-dimensional model crystal with 'cubic symmetry' as sketched in Figure 7 explains the different properties of such a material in different directions.

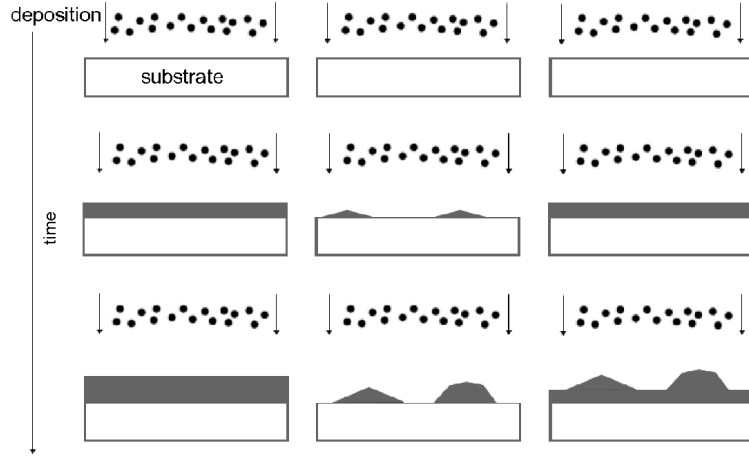


Figure 5: Schematic description of possible island growth in heteroepitaxy. From left to right: Frank-van der Merwe, Volmer-Weber and Stranski-Krastanov growth.

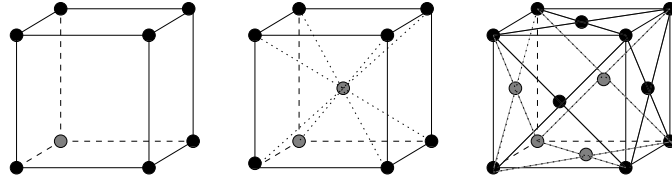


Figure 6: Bravais lattices for crystals with cubic symmetry. From left to right: simple, body-centered and face-centered. The main axes have the same length and form an angle of 90 degrees to each other.

Depending on the orientation of a formed surface, the number of atoms lying in the range of nearest neighbor interactions, which is sketched in the figure by single circles, differs and leads to variations in the bond strengths and hence the surface energy. In the general 3D case it depends on the outward unit normal $n = (n_1, n_2, n_3)$, $\gamma = \gamma(n_1, n_2, n_3)$. In Section 1.2.2 anisotropy of the surface energy will be discussed in detail. It is fundamentally different than for most liquids, such as water or oil, which have an isotropic surface energy. Fluids typically have a round form in equilibrium since such shapes minimize the surface, and simultaneously yield the minimum of the surface energy. Anisotropy adds a certain amount of complexity, since it has to reflect the rich structure of crystals.

Miller indices:

When anisotropy of crystals is considered triplet indices such as (klm) , $\{klm\}$, $\langle klm \rangle$ or $[klm]$ are used. These are *Miller indices* and for materials with cubic symmetry they have the following meaning: (klm) is the surface which is orthogonal to the direction $(k, l, m)^T$ in Euclidean space

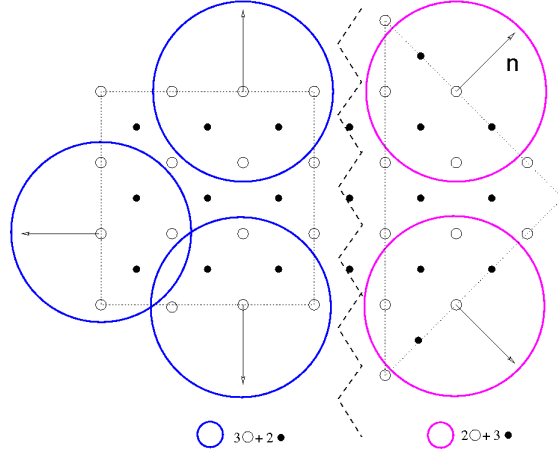


Figure 7: Anisotropy of crystalline materials. Here a two-dimensional model crystal with 'cubic symmetry in 2D' is sketched and nearest neighbor interactions are indicated by the bigger circles. On the left (01) orientations give a different amount of black/white dots in such a circle than on the right, where the crystal is (11) oriented. Here Miller indices in 2D, explained below in 3D, were used.

(these are directions in Cartesian coordinates). Mathematically this gives the set

$$(klm) = \{(a, b, c)^T \in \mathbb{R}^3 : ak + bl + cm = 0\} \quad .$$

$\{klm\}$ are all planes that are equivalent to the (klm) plane under cubic symmetry — that is equivalence under 90 degree rotations. One example is (the six planes of a Bravais cube are in one class; \bar{k} denotes $-k$ in crystallography)

$$\{001\} = \{(100), (001), (010), (00\bar{1}), (0\bar{1}0), (\bar{1}00)\} \quad .$$

$[klm]$ represents the direction $(k, l, m)^T$ and $\langle klm \rangle$ is the set of all symmetrically equivalent directions and the example for the equivalent planes can be translated to the directions analogously.

0.4 Ge/Si(001) quantum dots

As mentioned, two germanium and silicon based epitaxial systems are very common, the $\text{Si}_{1-x}\text{Ge}_x/\text{Si}$ and the Ge/Si combinations, where the substrate is typically (001) oriented. These materials have a cubic diamond symmetry, which follows a face-centered cubic bravais lattice, and share similar lattice constants. Qualitatively the resulting surfaces during heteroepitaxial growth for both systems are nearly the same, so in many cases they are studied in parallel (see e.g. Drucker [23]). In Figures 3 and 4 pictures from the $\text{Si}_{0.7}\text{Ge}_{0.3}/\text{Si}(001)$ system show how the evolution takes place — as Stranski-Krastanov growth type with an instability that appears as small humps, which evolve to faceted islands and coarsen while further atoms are deposited onto the surface.

In the following the data for a pure germanium film will be used. However, mixtures as above could be considered analogously, see for example [102]. In this section details of the two stages of the evolution are presented. The following numbers and facts are based on the information given in Drucker's review [23] and the references therein. The described heteroepitaxial system will be compared to numerical results at later stages of this thesis.

Phase one: Pseudomorphic growth

Germanium is deposited on top of a silicon wafer. Both materials are in the same symmetry class, but the inherited grid spacing of germanium is slightly bigger than that of silicon. The film atoms adjust their grid spacing to the substrate's lattice. A flat, but due to compression stressed, film grows until it reaches a critical thickness $h_c = h_c(T, F)$. It is about three monolayers (ML) high, but this value changes with temperature of the chamber T and the constant deposition rate F , which lies in the range of a few monolayers per minute. IBM states $1 - 5 \text{ ML/min}$ in their Ge/Si experiments and using the value from Burbaev et al. [10], one monolayer is 0.14 nm thick, so that the deposition rate can be written as $0.00233 \text{ nm/s} - 0.01165 \text{ nm/s}$.

Phase two: Island evolution

After the first stage, ripples begin to evolve into island structures. After some time they show anisotropic behavior and coarsening takes place throughout the whole phase. The following description is valid for temperatures in the range of 500 to 600°C : Square-based pyramids form out of the rounded nano-islands. These have $\{105\}$ facets and a contact angle of 11 degrees. Smaller mounds coalesce, while bigger pyramids continue to grow. Further deposition of germanium atoms leads to a complex transition to octagonal based domes with diameters above 50 nm and higher contact angle of 25 degrees, resulting in a bimodal distribution of islands [86]. Stable facets of the domes are $\{113\}$, $\{102\}$ and $\{15323\}$. Dislocations are introduced, interdiffusion between substrate and film takes place and the interface between the two solids changes from curvature-free to cone-like. For higher temperatures elongated islands with the same facets are more common. Then also the effect of intermixing of germanium and silicon is more important, because in this case the interface kinetics is not much slower than the shape change kinetics. This is a point that is not addressed in continuum models so far and a flat interface will be considered.

When dislocations appear, the quality of the artificial atoms deteriorates and continued growth can halt desirable quantum effects to appear. To obtain small, qualitatively good dots with a discrete energy spectrum, the process has to be stopped early enough.

A short list summarizes the most important facts that will be needed during the modeling and for parameter definitions.

- Growth mode: Stranski-Krastanov
- Temperature: $500 - 600^\circ \text{C}$
- Deposition rate: $\approx 0.002 - 0.02 \text{ nm/s}$

- Materials and symmetry: Ge, Si(001), cubic
- Interface between film and substrate: Flat (assumption reasonable under small slope assumption)
- Facets of the pyramids: $\{105\}$
- Critical height: $\approx 3ML \approx 0.42nm$
- Time range (from onset of the instability, through formation of ripple structures, coarsening, faceting, growth until diameters of about 50nm are reached): $\approx 0.5 - 3$ minutes (dependent on the chosen flux rate)

Note that these are observations for a special heteroepitaxial system. They will be useful in Chapter 4, where a QD model for its self-assembly will be derived, analyzed and compared to experiments. However, the other parts of this work are devoted to an already existing model for homoepitaxial growth. Rather than modeling aspects, in this case the mathematical analysis is in the foreground. The overall content is outlined in detail in the following section.

0.5 Content, results and structure of this work

In this first paragraph the content is shortly summarized, thereafter details on the results are outlined. The main body of this document begins with general continuum modeling for surface diffusion based evolution of crystalline films. A surface diffusion equation is derived that leaves many degrees of freedom for further modeling by allowing for a general chemical potential. The model goes back to the fundamental work by Mullins [69]. Throughout the work two different energies are introduced that result in two models. The first has already been known, it is a sixth order semilinear PDE that describes the faceting of a growing surface. The second is a new fourth order quasilinear evolution equation for the self-assembly of quantum dots. Although it does not have the sixth order term, it can be seen as an extension of the first model, since it also incorporates anisotropy of the surface energy and an atomic flux. Both models under consideration are Cahn-Hilliard type equations and their high order requires elaborated theory for their analysis. To work with simplified PDEs, the equations are nondimensionalized. Asymptotic expansions that make use of typical small slopes are applied to derive reduced models by neglecting small terms in the expanded expressions of the full equations. These are analyzed on stationary solutions, which requires to work in high order phase spaces, matching to many orders or also new matching procedures. The numerics for the dynamical behavior has to be capable to treat high order derivatives. This task is solved here via spectral differentiation. For the first equation the existence of weak solutions and higher regularity has been proved. The last regular chapter is devoted to the set-up of efficient pseudospectral methods in Matlab. These allow to

simulate domain-wall interactions or huge arrays of QDs, so that their evolution can be compared to experiments.

The content and results in detail: In Chapter 1 the modeling of a surface diffusion driven process is carried out. After the general derivation of an evolution equation for crystalline surfaces and a discussion about atomic fluxes, different kinds of surface energies are introduced. Various formulas have been proposed in literature to improve existing models and this chapter gives a small review of the important publications. Different terms influencing the chemical potential are a result of the functional derivative of the free energy. Furthermore in heteroepitaxy a second major influence has to be considered, the strain energy density. Different lattice constants in film and substrate lead to stresses that are modeled here in terms of linear elasticity theory. After its introduction the solution for a simple configuration, the base state, is derived. However, an approximate solution for the full elastic subproblem, which is considered for modeling of the self-assembly of QDs in a later chapter, is taken from Tekalign and Spencer [102]. A detailed re-calculation of the results is given within Appendix C.

In the following Chapters 2 and 3 a model for the faceting of a growing surface is analyzed. For systems where two characteristic scales are given, one small and one large, often their ratio is used as small parameter. By expanding in terms of this quantity, PDEs can be simplified to equations that are easier to solve. This is done here to obtain a semilinear evolution equation of sixth order. The model has already been derived by Savina and her co-workers [41, 89] and some references therein. Here the calculations are repeated in a compact way. In the same framework a related and new model for quantum dot self-assembly will be derived later on. In a certain sense it extends the first model. In Section 2.2 some notes on phase-separating systems of Cahn-Hilliard type are stated, because the derived equation for the description of faceting of a growing surface is a close relative of these models. In fact, formally it is a convective Cahn-Hilliard equation (see e.g. [24, 40, 44, 115]) of higher order and throughout the work it will be addressed as the HCCH equation. Existence of weak solutions is proved in $L^2(0, T; \dot{H}_{per}^3(\Omega)) \cap C^0([0, T], \dot{L}^2(\Omega))$. Therefore an introduction to the most important aspects of functional analysis and operator theory is given before the actual proof based on a Galerkin approach is carried out. A compact operator, the inverse of the bi-Laplacian working on a suitable Sobolev space, is applied onto the PDE and a similar structure as for a convective reaction-diffusion equation is obtained. It can be used to derive bounds in lower order spaces. By further testing the HCCH equation and using the previously obtained results, suitable estimates give — by passing to the limit of the Galerkin approximation — existence in the higher order Sobolev space. In Chapter 3 equilibrium solutions and long-time behavior are discussed. New types of stationary solutions are derived with help of a boundary value problem formulation in a five dimensional phase space. With the numerical method solutions are characterized on branches in a parameter plane. Characteristic quantities such as far-field value and hump-spacing are compared with analytically calculated values. To derive actual formulas for these quantities the method of matched asymptotics is used with the

additional feature that exponentially small terms have to be retained, extending the method by Lange [62] to higher-order singularly perturbed nonlinear boundary value problems. Solutions in three neighboring regions are expanded, solved to four successive orders and they are matched to determine unknown constants. As result analytical features of spatially non-monotone solutions are derived in the limit of vanishing driving force strength. The width of the characteristic humps of the solution is related to the Lambert W function and analytical expressions for the behavior in the far-field are derived. Finally the coarsening mechanisms for the HCCH equation are analyzed with help of a numerical study. Kinks, kink-pairs and kink-triplets show behavior that governs the overall evolution. It turns out that stationary patterns with a still quite rich structure exist and that also traveling waves are possible. Typical frequencies of the solutions grow like the logarithm of the deposition parameter. A pseudospectral method introduced in Chapter 5 is used to obtain these results.

In Chapter 4 a reduction similar as in Chapter 2 is applied to a quantum dot model. It yields a fourth order, quasilinear PDE that incorporates a nonlocal term through the elastic problem. To guarantee that all desired effects are still apparent in the reduced equations, the coefficients appearing in the problem are scaled with care. The resulting PDE is called the quantum dot model (QDM) equation. It is a new thin-film approximation that includes the effects of stresses, anisotropic surface energy, wetting interactions and deposition at once. The reduction is carried out in a consistent way, similarly as by Tekalign and Spencer [102, 103] or by Korzec and Evans [56]. A numerical method based on spectral differentiation, which is presented in detail in Chapter 5, allows to simulate the self-assembly of QDs. Before stationary shapes are studied on the influence of the anisotropy, a linear stability is carried out. It indicates that higher values of the anisotropy strength lead to more oscillatory surfaces and that the critical thickness in this Stranski-Krastanov system decreases. The stationary solutions obtained in two and in three dimensions can be recovered during simulations of the surface evolution on large domains in different scales. One observes hundreds of islands that are separated by a thin layer of the film's material. The QDs are pyramidal in shape as demanded by the anisotropy formula, but it is also shown that other anisotropies are admissible. The coarsening analysis shows that the number density of nano-islands decays over time like a power law. In particular stronger anisotropy parameters initiate the coarsening phase earlier, which on the other hand is slower than for the isotropic case. Finally an atomic flux is added and the numerical solutions reveal a behavior as it can be expected from the results from the case without deposition. In fact only now the Stranski-Krastanov growth mode anticipated can now be simulated and as in experiments higher flux rates result in more, but smaller dots, when comparing the surfaces after deposition of the same amount of material. The island density remains for longer times on a higher level, since smaller dots that tend to get absorbed in the case without deposition survive due to the additional adatoms attaching to the dots. The coarsening rates still can be described approximately by a power law. There have been many models describing the QD self-assembly under discussion. For

Ge/Si like systems the presented theory yields probably the most convincing results. Not only has the theory by Tekalign and Spencer [102, 103] been extended by a surface energy anisotropy and an atomic flux, also the simulations are particularly strong. While in the isotropic case only single dots have been considered that tend to become unrealistically steep, here hundreds of faceted dots can be simulated.

The last regular Chapter 5 introduces the numerics used for the simulations presented throughout the thesis. It begins with an explanation of simple differentiation matrices for finite difference methods (FDMs) and it is shown how few lines of Matlab code can suffice to simulate even not so simple PDEs. Then pseudospectral methods (PSMs) are motivated in terms of trigonometric interpolation, which is connected to the previously introduced theory since finite differences can be interpreted as derivatives of local interpolants. It is explained how the Fourier transform based methods can be used for the simulation of three-dimensional QD growth. Comparisons between finite difference approximations and spectral derivatives are presented, showing the superiority of the latter for a certain class of well-behaving problems. Although the method is not new — trigonometric interpolation based methods used for simulations of PDEs exist since the 1970s — the presentation should motivate any reader to use PSMs, if the underlying problem allows for an application. The thesis finishes with conclusions and discussions for the future in Chapter 6.

Chapter 1

Surface diffusion based continuum modeling

After 1980, you never heard reference to space again. Surface, the most convincing evidence of the descent into materialism, became the focus of design. Space disappeared.

Arthur Erickson (1924 - 2009)

Surface treatments of any kind became popular in the last century, be it for Teflon pans, cars, glasses or clothes. The thicknesses of such coatings decreased with increased knowledge. Its success accelerated once fundamental understanding of the processes on the nano and mesoscale existed and methods for efficient coating were available. Nowadays scratch proof, water resistant, as membrane functioning or other surfaces with special properties due to coating can be found all over the place. As described in the introduction, many of such thin-film applications can be realized by epitaxy. In this chapter a theoretical description for the surface evolution is given. Continuum modeling based on a surface diffusion formula derived by Mullins more than half a century ago, 1957, is presented [69]. It results in an evolution equation, which has to be further specified by the definition of a reasonable chemical potential that states how the surface diffusion is driven. It will be shown that it can be used to adequately model the faceting of a growing surface or heteroepitaxial systems such as Ge/Si. Generally the atomic flux has to be taken into account and also anisotropy has to be noticed since the underlying materials have crystalline structures. For QD growth it is necessary to incorporate additional bulk stresses, which result from the lattice mismatch of two different crystalline materials. Figure 1.1 sketches the set-up for surface diffusion. Atoms impinge on a solid film. These are then driven by several physical effects along the surface, which results in an evolution of the film.

The Nernst-Einstein relation gives the average normal velocity of surface atoms. It is proportional to the flux on the surface J , which is just the surface gradient acting on a diffusion

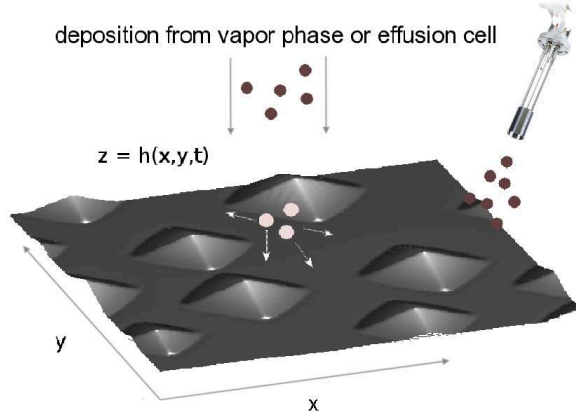


Figure 1.1: Schematic surface diffusion in a heteroepitaxial system.

potential

$$J = -\mathcal{D} \nabla_s \mu \quad . \quad (1.1)$$

Here ∇_s is the surface gradient, μ is the chemical potential and \mathcal{D} is a quantity dependent on material properties that is assumed to be constant throughout this document. It is defined as

$$\mathcal{D} = \frac{\Omega^2 D_s \sigma}{kT} \quad , \quad (1.2)$$

where k is the Boltzmann constant, T is the absolute temperature in the chamber, Ω the atomic volume, σ the surface density of adatoms and D_s a surface diffusion constant. In Section 4.5 typical values for quantities used in Ge/Si heteroepitaxy are collected and used for simulations that are comparable to experiments.

To obtain the speed of the surface in normal direction v , the negative surface divergence of the

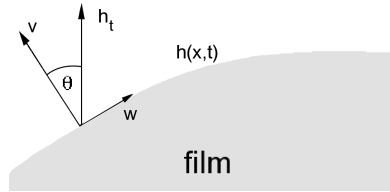


Figure 1.2: Configuration for the orthogonal projection.

surface flux has to be taken,

$$v = -\nabla_s \cdot J = \mathcal{D} \nabla_s^2 \mu \quad . \quad (1.3)$$

As depicted in Figure 1.2 a projection yields the vertical growth velocity h_t . One has

$$\cos(\theta) = v/h_t = e_3 \cdot n = 1/\sqrt{1 + |\nabla h|^2} \quad , \quad (1.4)$$

where n is the outward unit normal that will be used frequently throughout this work,

$$n = \begin{pmatrix} -h_x \\ -h_y \\ 1 \end{pmatrix} / \sqrt{1 + |\nabla h|^2} \quad . \quad (1.5)$$

Here $|\cdot|$ denotes the Euclidean norm for n -vectors (in this case $n = 2$) as in the whole document. By using (1.3) and (1.4) the general evolution equation based on surface diffusion in absence of deposition becomes

$$h_t = \mathcal{D} \sqrt{1 + |\nabla h|^2} \nabla_s^2 \mu \quad . \quad (1.6)$$

To describe the surface energy, one of the major influences for the chemical potential, several models have been proposed (e.g. isotropic [95], or various anisotropic versions [19, 27, 89]). The terms that result from taking the functional derivative of the surface free energy will be calculated after a discussion of an atomic flux from the gas phase, which is necessary for a realistic description of an epitaxy process. After these two parts the elastic problem will be introduced in Section 1.2. In heteroepitaxial systems, such as those for QD growth, the strain energy density forms a part of the chemical potential. Since film and substrate are crystalline materials, they have characteristic grid spacings a^f and a^s in film and substrate, respectively. Typically these values differ in the second decimal place, e.g. for silicon and germanium it is about 4 percent with a bigger spacing for germanium. During early stages of deposition atoms from the film material adjust their spacing to the substrate's grid. A compression induces stresses that result in a nonzero strain energy density \mathcal{E}_{sed} . Eventually the coherency stress release is reflected in the evolution by formation of nano-islands.

1.1 Atomic flux

Already in one of the first works on continuum modeling of QD self-assembly, deposition has been taken into account [42, 95, 98]. A perfect beam of atoms was assumed to impinge onto the surface. No perturbation of the deposited material was allowed. Generally, let f^a be the material flux, then the average normal velocity (1.3) is changed by adding the simple term $-f^a \cdot n$. The evolution equation becomes

$$h_t = \sqrt{1 + |\nabla h|^2} (-f_a \cdot n + \mathcal{D} \nabla_s^2 \mu) \quad . \quad (1.7)$$

Under the assumption that all atoms have a vertical deposition direction, $f^a = (0, 0, -F)$, the evolution equation simplifies to

$$h_t = F + \sqrt{1 + |\nabla h|^2} \mathcal{D} \nabla_s^2 \mu \quad . \quad (1.8)$$

It shows that this kind of deposition results in a vertical shift in the solution $h \rightarrow h + Ft$, if the chemical potential does not depend on h .

Savina et al. [89] used a slightly different approach. Their flux points into the normal direction of the surface $f^a = -Fn$, then (1.7) becomes

$$h_t = \sqrt{1 + |\nabla h|^2}(F + \mathcal{D}\nabla_s^2\mu) \quad . \quad (1.9)$$

The authors argued that such a differently oriented flux is suitable for the description of a CVD like process, where reactions in the gas lead to arbitrarily oriented atom trajectories in the chamber. Their model will be analyzed in this work, though for the QD growth model it is proposed to use a perturbed deposition flux — Gaussian noise perturbs a perfect beam, which is assumed to impinge vertically onto a flat surface. More precisely, white noise is added to simulate the natural fluctuations that are generic in such deposition methods. $f^a = (f_1, f_2, f_3)$ has to reflect this random disturbance. In an MBE like process, the atoms are deposited in a beam and they are oriented downwards, $f_3 < 0$ (i.e. no evaporation is considered in the presented models). The deviation from the vertical flux is randomly distributed and variations in x and y directions have the same probability. The flux at one space point at different time points is not correlated and finally the strength of the flux f^a is just the flux rate F . Out of these properties one can deduce the flux

$$f^a = -\frac{w}{|w|}F \quad \text{with} \quad w = (r(0, \sigma_1), r(0, \sigma_1), r(1, \sigma_2)) \quad , \quad (1.10)$$

where r is a function generating Gaussian random numbers with expectations 0, 0 and 1 and standard deviations σ_1 and σ_2 . In each time step these numbers have to be recomputed, hence an implicit time dependency is assumed for these values. For simplicity it will be written here and in later sections $r_1 = r(0, \sigma_1)$, $r_2 = r(0, \sigma_1)$ and $r_3 = r(1, \sigma_2)$ — each expression represents a random generator function call in a numerical implementation. Overall adding the flux yields a perturbed version of (1.8), namely

$$h_t = \frac{F}{|w|}(-r_1 h_x - r_2 h_y + r_3) + \sqrt{1 + |\nabla h|^2} \mathcal{D}\nabla_s^2\mu \quad . \quad (1.11)$$

1.2 Types of surface energies

A considerable amount of equations for the description of QD growth or other surface diffusion based processes such as homoepitaxy has been derived throughout the years starting from evolution equation (1.7). Different formulas for the surface energy, typically denoted by γ , influence the chemical potential in various ways. In this section it is explained how the dependencies appear in the energy. In the first models, such as those by Spencer and his co-workers, neither intermolecular interactions between film and substrate nor anisotropy have been considered [95, 97, 98]. Furthermore neither the experimentally observed wetting layer connecting the nanostructures nor faceting of the dots is incorporated in these early works. Golovin et al. extended the fundamental theory by including wetting effects [42]. Other groups such as Pang and Huang

[77, 78] or Tekalign and Spencer [102, 103] were also able to incorporate this extension. While the former group used the Cerruti solution for a semi-infinite solid as approximation of the full elastic problem, the authors from the latter references considered linear elasticity in film and in substrate. They incorporated expansions of the displacements based on characteristic scales in both materials and solved the Navier-Cauchy equations for lower orders to derive a simple, reduced, non-local term. Savina and her colleagues created a model for CVD like growth in absence of elastic stresses [89]. The group used a formula for strong anisotropic surface energy, with a penalizing term for the edges which is necessary in case of corners in the equilibrium shapes. The model was further extended by Golovin et al. [43]. Wetting interactions are added to the anisotropic surface energy, this can be achieved by letting γ depend not only on the slopes, but also on the surface height h in a suitable manner. However, both works are not related to growth based on the ATG instability since no elastic subproblem is considered. For the heteroepitaxial case, a cusped anisotropic surface energy has been used by Eisenberg and Kandel [25, 26, 27]. Although 2D simulations were carried out and showed promising results, the drawback remains that methods based on derivatives cannot handle such discontinuities offhand. No 3D simulations have been carried out. Others, such as Chiu and Huang [18, 19], do consider wetting and anisotropy in a smooth framework. However, these authors do not apply a long wave approximation to their problem. The anisotropy and wetting layer formulas differ from the equations used in this work and the elasticity problem allows only for material constants of the substrate.

Successively several classes of surface energies will be discussed now and more related literature will be cited during the discussion. The impact of the different formulas for γ onto the chemical potential term \mathcal{E}_{surf} is given with the functional derivative of the surface free energy

$$\mathcal{E}_{surf} = \frac{\delta}{\delta h} \int \gamma dS \quad . \quad (1.12)$$

Here the integral is a surface integral and dS is an infinitesimal surface element. To actually evaluate (1.12), formula (A.4) from appendix A will be applied repeatedly. Note that the term surface energy is somewhat ambiguous in this work and also in most other references. Dependent on the situation it stands for the surface energy density γ (in other references also *surface tension* as for liquids) or the surface free energy $\int \gamma dS$. It will be clear from the context which one is meant.

Five different surface energy types are considered in this chapter. They are denoted by $SE_k, k \in \{I, II, III, IV, V\}$. After an introduction of these five formulas with an explanation of their differences, constituent terms of \mathcal{E}_{surf} resulting from the derivative (1.12) are calculated in Section 1.2.1. These are the actual equations needed for the set-up of useful PDEs.

In the first continuum models for heteroepitaxy the surface energy was assumed to be isotropic, hence it was just a constant. Many groups worked with surface diffusion models which included stresses and this simple surface energy. To mention a few references: [95, 96, 97, 98, 114, 118, 119].

$$\mathbf{SE}_I: \quad \gamma = \text{const} \quad .$$

Simulations of the self-assembly of QDs based on this formulation contradict the experiments in that no thin layers connecting the nano-structures are observed. Therefore the formula has to be extended such that it varies with surface height (for example by incorporation of a boundary layer formula used by Spencer [93]). This dependency suits as a smooth transition between the different surface energies of the film and the substrate. In fact, if the two materials have different surface energies, there is a gap between these two values. Smoothing out this discontinuity by adding this mathematical dependency on h , which artificially introduces an interfacial energy, has become quite popular. In fact the blurring may be not only favorable because of smoothness and implementation issues, but it may be also more realistic than a simple jump. A certain amount of atoms interdiffuses at the interface and in a way the intermixing is approximated by defining a smooth transition. The resulting effect is reminiscent of wetting potentials in fluid dynamics (such as van der Waals interactions). If the surface energy of the film is lower, regions covered by a flat thin film are created to minimize the overall energy of the system. This happens in most Stranski-Krastanov systems, so these kind of models receive a huge amount of attention, see e.g. [3, 12, 42, 77, 102, 103],

$$\text{SE}_{II}: \quad \gamma = \gamma(h) \quad .$$

One major characteristic of a crystal is its anisotropy that comes in generically with its regular structure (see e.g. Section 0.3). It leads to preferred orientations during growth, these correspond to lower energy states. SE_{II} can be extended by adding an orientation dependency that can be expressed by using the surface gradient as argument of the surface energy (find more explanations in Section 1.2.2). This gives a third surface energy formula class,

$$\text{SE}_{III}: \quad \gamma = \gamma(h, h_x, h_y) \quad .$$

This kind of surface energy is used in Section 4.1 to derive an elaborated model that includes a thin layer between QDs that develop preferred facets. It has been also used by several groups that have not applied a thin-film reduction, and worked with full equations instead, see e.g. [16, 17, 18, 19, 117]. Equivalent formulations to the gradient dependence of the surface energy can be found by using the outward unit normal as argument, $\gamma = \gamma(n)$, or two angles (in polar coordinates) $\gamma = \gamma(\theta_1, \theta_2)$. However, these are rather common in works on equilibrium shapes than for modeling the evolution of thin films and here the first notation is used.

One can further extend the surface energy by adding an edge regularization term. When anisotropy is strong, corners appear in the equilibrium shapes, which can lead to an unphysical backward diffusion when the formula is used for evolution equations. The nonsmooth corners in the Wulff plots in case of a nonconvex surface energy (see e.g. in the work by Li et al. [65]) lead to the idea of penalizing high curvature regions by adding a scaled κ^2 term to the surface energy, where κ is the mean curvature. The regularization approach has been addressed several works in crystal growth theory, e.g. in [11, 89, 94]. In evolution equations this results in a sixth order term, which may imply higher demands on numerical schemes. For incorporation of the

Wilmore regularization higher order gradients have to be considered in the surface energy,

$$\mathbf{SE}_{IV}: \quad \gamma = \gamma(h, h_x, h_y, h_{xx}, h_{xy}, h_{yy}) \quad .$$

This formula will be used in a slightly alternative, a simpler, form without dependency on the surface height h in Section 2.1 for the derivation of the model by Savina et al. describing the faceting of a growing surface [89]. To accentuate the importance of this case in this thesis, it is treated separately, although it is just a special case of \mathbf{SE}_{IV} .

$$\mathbf{SE}_V: \quad \gamma = \gamma(h_x, h_y, h_{xx}, h_{xy}, h_{yy}) \quad .$$

Other approaches have been proposed. The most common for the anisotropic surface energy is to let γ depend on an angle of orientation θ . However, since this quantity is related to the surface slopes, it is somewhat equivalent. Bonzel and Preuss [8] or Eisenberg and Kandel [25, 26] pursued this approach by giving preferred facets a cusped minimum. It has to be regularized again to make standard simulations possible and apparently the approach has not been tracked further to achieve 3D simulations for QD array studies. Wetting stress has been added in the work by Levine et al. [64], however, here it will not be mentioned further, since it turned out that it has not influence to leading order in a long wave approximation — the approach that is tracked in this thesis.

The chemical potential part that stems from the surface energy (1.12) is now calculated for the five energy types $\mathbf{SE}_k, k \in \{I, II, III, IV, V\}$. Therefore here and throughout the document some abbreviations will be used,

$$N = \sqrt{1 + h_x^2 + h_y^2} \quad , \quad (1.13)$$

$$\partial_w = \frac{\partial}{\partial w} \quad , \quad \nabla \nabla h = (\partial_{h_x}, \partial_{h_y})^T \quad \text{and} \quad \nabla_{\Delta h} = \partial_{h_{xx}} + \partial_{h_{yy}} \quad , \quad (1.14)$$

so that

$$\nabla \cdot \nabla \nabla h = \partial_x \partial_{h_x} + \partial_y \partial_{h_y}$$

$$\text{and} \quad \nabla^2 \nabla_{\Delta h} = \partial_{xx} \partial_{h_{xx}} + \partial_{xx} \partial_{h_{yy}} + \partial_{yy} \partial_{h_{xx}} + \partial_{yy} \partial_{h_{yy}} \quad .$$

1.2.1 Functional derivatives of surface energy formulas

In this section the functional derivative of the surface free energy, defined as the surface integral over one of the formulas $\mathbf{SE}_k, k \in \{I, II, III, IV, V\}$, is consecutively calculated. The surface height is assumed to be sufficiently smooth, so that all terms used in the propositions are well-defined.

Proposition 1 (\mathbf{SE}_I) *Assume γ is constant. Then*

$$\mathcal{E}_{surf} = -\gamma \kappa \quad .$$

Proof

$$\begin{aligned}
\mathcal{E}_{surf} &= \frac{\delta}{\delta h} \int \gamma dS \\
&= \gamma \frac{\delta}{\delta h} \int N dx dy \\
&= \gamma [\partial_h - \nabla \cdot \nabla_{\nabla h}] N \\
&= -\gamma \left(\partial_x \left(\frac{h_x}{N} \right) + \partial_y \left(\frac{h_y}{N} \right) \right) \\
&= -\gamma \frac{h_{xx}(1 + h_y^2) + h_{yy}(1 + h_x^2) - 2h_x h_y h_{xy}}{N^3} .
\end{aligned}$$

□

Here the mean curvature κ is defined as in the appendix A, formula (A.2). Its sign is chosen such that it is bigger zero for a standard parabola that is bounded below. In other notes you may find it with a different sign which comes from a switch of perspectives between convexity and concavity. Also an additional scaling with $1/2$ can be found in other papers. These small variations may appear puzzling, since a sign switch in evolution equations generally implies quite the opposite effect — such as blow up of the solutions.

The above derived term is hereditary in that it shows up in the following types of surface energies which all extend SE_I . Formally the abbreviation

$$\mathcal{E}_\kappa = -\gamma\kappa \quad (1.15)$$

will be used from now on — deliberately concealing the dependencies of γ .

Proposition 2 (SE_{II}) *By adding dependency on the surface height, $\gamma = \gamma(h)$, the surface energy terms become*

$$\mathcal{E}_{surf} = \gamma'(h)n_3 + \mathcal{E}_\kappa . \quad (1.16)$$

Proof

$$\begin{aligned}
\mathcal{E}_{surf} &= N\gamma'(h) - \nabla \cdot \gamma(h)\nabla_{\nabla h} N \\
&= N\gamma'(h) - \left(\partial_x \left(\gamma(h) \frac{h_x}{N} \right) + \partial_y \left(\gamma(h) \frac{h_y}{N} \right) \right) \\
&= \gamma'(h) \left(N - \frac{h_x^2 + h_y^2}{N} \right) - \gamma(h) \left(\partial_x \left(\frac{h_x}{N} \right) + \partial_y \left(\frac{h_y}{N} \right) \right) \\
&= \frac{\gamma'(h)}{N} - \gamma(h)\kappa .
\end{aligned}$$

□

It was used that $1/N$ is just the third component of the outward unit normal n_3 . The additional term is abbreviated as

$$\mathcal{E}_{wet} = n_3 \partial_h \gamma . \quad (1.17)$$

Now the more general surface energy SE_{III} is considered. The result is fundamental for the derivation of the QDM equation in Section 4.1 — a QD self-assembly model that captures many properties of the Ge/Si system.

Proposition 3 (SE_{III}) *The chemical potential terms for a surface energy varying with the film thickness and the surface slopes, $\gamma = \gamma(h, h_x, h_y)$, are*

$$\mathcal{E}_{surf} = \mathcal{E}_{wet} + \mathcal{E}_\kappa + \mathcal{E}_{anis}$$

with

$$\begin{aligned} \mathcal{E}_{anis} = & -2 \left(\frac{h_x h_{xx} + h_y h_{xy}}{N} \partial_{h_x} \gamma + \frac{h_y h_{yy} + h_x h_{xy}}{N} \partial_{h_y} \gamma \right) - N \partial_x \partial_{h_x} \gamma - N \partial_y \partial_{h_y} \gamma. \end{aligned} \quad (1.18)$$

Proof

$$\begin{aligned} \mathcal{E}_{surf} &= \frac{\delta}{\delta h} \int \gamma(h, h_x, h_y) N dx dy \\ &= N \partial_h \gamma - \nabla \cdot \nabla_{\nabla h} (\gamma N) \\ &= N \partial_h \gamma - \nabla \cdot \gamma \nabla_{\nabla h} (N) - \nabla \cdot N \nabla_{\nabla h} (\gamma) \\ &= N \partial_h \gamma - \partial_x \left(\gamma \frac{h_x}{N} \right) - \partial_y \left(\gamma \frac{h_y}{N} \right) - \partial_x (N \partial_{h_x} \gamma) - \partial_y (N \partial_{h_y} \gamma) \\ &= N \partial_h \gamma - \frac{h_x^2 + h_y^2}{N} \partial_h \gamma - \frac{h_x h_{xx} + h_y h_{xy}}{N} \partial_{h_x} \gamma - \frac{h_y h_{yy} + h_x h_{xy}}{N} \partial_{h_y} \gamma \\ &\quad - \gamma \left(\partial_x \left(\frac{h_x}{N} \right) + \partial_y \left(\frac{h_y}{N} \right) \right) - \partial_x (N \partial_{h_x} \gamma) - \partial_y (N \partial_{h_y} \gamma) \\ &= (\partial_h \gamma) n_3 - \gamma(h, h_x, h_y) \kappa + \mathcal{E}_{anis} \quad . \end{aligned}$$

□

Now the most complex case is considered, SE_{IV} , the anisotropic surface energy formula that is allowed to vary with the film thickness and depends on higher order gradients. It yields the following terms.

Proposition 4 (SE_{IV}) *The variational derivative of the surface free energy based on SE_{IV} leads to the four term expression*

$$\mathcal{E}_{surf} = \mathcal{E}_\kappa + \mathcal{E}_{wet} + \mathcal{E}_{anis} + \mathcal{E}_{hot} \quad ,$$

with

$$\mathcal{E}_{hot} = [\partial_{xx} \partial_{h_{xx}} + \partial_{xx} \partial_{h_{yy}} + \partial_{yy} \partial_{h_{xx}} + \partial_{yy} \partial_{h_{yy}}] (\gamma N) \quad .$$

Proof The first three terms are obtained in the same way as before, they are formally not influenced by the higher order gradient dependency. The additional term is simply the third term from the functional derivative (see formula (A.4) in the appendix)

$$\mathcal{E}_{hot} = \nabla^2 \nabla_{\Delta h} (\gamma N) \quad . \quad (1.19)$$

□

This formula is used for the derivation of a higher order Cahn-Hilliard (HCCH) equation in Section 2.1. There the special case SE_V is needed for which (1.19) can be used accordingly. Only the wetting term \mathcal{E}_{wet} can be neglected since in this case $\partial_h \gamma = 0$. An additional proposition for SE_V is redundant.

Summary of the surface energy formulas

In general, for one of the surface energies $SE_k, k \in \{I, II, III, IV, V\}$, the chemical potential influence \mathcal{E}_{surf} depends on γ ,

$$\mathcal{E}_{surf}(\gamma) = \mathcal{E}_\kappa(\gamma) + \mathcal{E}_{wet}(\gamma) + \mathcal{E}_{anis}(\gamma) + \mathcal{E}_{hot}(\gamma) \quad . \quad (1.20)$$

Table 1.1 summarizes which entries appear for the different surface energy formulas. It should help to understand related articles on evolution of surfaces based on surface diffusion.

\mathcal{E}_{surf}	$\mathcal{E}_\kappa(\gamma)$	$\mathcal{E}_{wet}(\gamma)$	$\mathcal{E}_{anis}(\gamma)$	$\mathcal{E}_{hot}(\gamma)$
$SE_I: \gamma = \gamma_c$	•	○	○	○
$SE_{II}: \gamma = \gamma(h)$	•	•	○	○
$SE_{III}: \gamma = \gamma(h, h_x, h_y)$	•	•	•	○
$SE_{IV}: \gamma = \gamma(h, h_x, h_y, h_{xx}, h_{xy}, h_{yy})$	•	•	•	•
$SE_V: \gamma = \gamma(h_x, h_y, h_{xx}, h_{xy}, h_{yy})$	•	○	•	•

Table 1.1: SE_{I-V} : The left column shows the dependencies of the surface energy. The bullets • indicate that the term appears in the chemical potential. The circles ○ show in which cases the terms do not appear.

1.2.2 Anisotropic surface energy of regular surfaces

The slopes of the evolving surface, h_x and h_y , serve as arguments for the surface energy types SE_{III} , SE_{IV} and SE_V . This dependency is used to model anisotropy of the surface energy, which, as already discussed in Section 0.3, depends on the orientation of the surface. The outward unit normal $n = (n_1, n_2, n_3)$ is used naturally as argument for γ . Furthermore for a mathematical description of crystals with cubic symmetry the regular structure implies

$$\gamma_1(n_1, n_2, n_3) = \gamma_1(\pi(n_1, n_2, n_3)) = \gamma_1(\delta_1 n_1, \delta_2 n_2, \delta_3 n_3), \delta_i \in \{\pm 1\} \quad , \quad (1.21)$$

for any permutation π of the three components. In Figure 6 the bravais lattices for cubic crystals have already been introduced and in Figure 7 (Section 0.3) the properties in (1.21) are visually supported for a 2D model crystal. For regular surfaces the surface energy can be written as

$\gamma_2(h_x, h_y) = \gamma_1(n(h_x, h_y))$. When it is treated as function dependent on the surface slopes h_x and h_y , then the symmetry (1.21) transforms to

$$\gamma_2(h_x, h_y) = \gamma_2(h_y, h_x) = \gamma_2(\delta_1 h_x, \delta_2 h_y), \delta_i \in \{\pm 1\} \quad . \quad (1.22)$$

In fact, the symmetries (1.21) and (1.22) are equivalent for regular surfaces as it will be shown now. This may be of interest, because in some publications the γ_1 version is used, while in others it is γ_2 .

Proposition 5 *Let $h : \Omega \rightarrow \mathbb{R}, (x, y) \mapsto h(x, y)$ be the smooth parameterization of a connected surface \mathcal{M} over a bounded domain $\Omega \subset \mathbb{R}^2$. Furthermore, let $n : \mathbb{R}^2 \rightarrow \mathcal{S}^2, (a, b) \mapsto (-a, -b, 1)/\sqrt{1+a^2+b^2}$ be the outward unit normal function which maps onto the unit sphere \mathcal{S}^2 . Then by defining $\gamma_2 : \mathbb{R}^2 \rightarrow \mathbb{R}, \gamma_2 := \gamma_1 \circ n$ the symmetries (1.21) and (1.22) are equivalent.*

Proof Since the surface is smooth, the third component of n is always bigger than or equal to zero, $n_3(a, b) \geq 0, \forall (a, b) \in \Omega$, and hence $\delta_3 = +1$ in (1.21). Furthermore the 3-permutation $\pi = (\pi(1), \pi(2), \pi(3))$ is only permitted if $\pi_{\pi(3)} \geq 0$. Let $\delta_1, \delta_2 \in \{\pm 1\}$ be arbitrary. " \Rightarrow " Let (1.21) hold and $\pi(n) = (n_2, n_1, n_3)$, then

$$\begin{aligned} \gamma_2(h_x, h_y) &= \gamma_1 \circ n(h_x, h_y) = \gamma_1(n_1, n_2, n_3) \\ &= \begin{cases} \gamma_1(\delta_1 n_1, \delta_2 n_2, n_3) = \gamma_1 \circ n(\delta_1 h_x, \delta_2 h_y) = \gamma_2(\delta_1 h_x, \delta_2 h_y) \\ \gamma_1(\pi(n_1, n_2, n_3)) = \gamma_1(n_{\pi(1)}, n_{\pi(2)}, n_{\pi(3)}) = \gamma_1(n_2, n_1, n_3) = \gamma_2(h_y, h_x) \end{cases} \end{aligned}$$

" \Leftarrow " Let (1.22) hold, then as before $\gamma_1(n_1, n_2, n_3) = \gamma_2(h_x, h_y) = \gamma_2(\delta_1 h_x, \delta_2 h_y) = \gamma_1(\delta_1 n_1, \delta_2 n_2, n_3)$. There is nothing to show for the interchange of the first two normal components since one can directly calculate $\gamma_1(n_1, n_2, n_3) = \gamma_2(h_y, h_x) = \gamma_1(n_2, n_1, n_3)$.

Let n_3 permute with one of the other components (consider $\pi(n) = (n_3, n_2, n_1)$, the other case can be treated analogously). Since $n_1 > 0$, there exist $(a, b) \in \mathbb{R}^2$ such that $(n_3, n_2, n_1) = (-a, -b, 1)/\sqrt{1+a^2+b^2}$. Since $(n_1, n_2, n_3) = (-h_x, -h_y, 1)/N$, one obtains the identity

$$(1, -h_y, -h_x)/\sqrt{1+h_x^2+h_y^2} = (-a, -b, 1)/\sqrt{1+a^2+b^2} \quad , \quad (1.23)$$

which gives $b = -h_y/h_x$ and $a = 1/h_x$. Hence

$$\gamma_1(\pi(n_1, n_2, n_3)) = \gamma_1(n_3, n_2, n_1) = \gamma_2(a, b) = \gamma_1(n_1, n_2, n_3)$$

because of (1.23). □

In the following the anisotropic surface energy will be expressed as

$$\gamma(h_x, h_y) = \sum_{k=0}^{\infty} \sum_{j=0}^k g_{kj} h_x^j h_y^{k-j} \quad , \quad (1.24)$$

where for practical use the first sum is truncated to be finite. Because of Proposition 5, often a surface energy $\gamma(n)$ has an analogous description via gradient dependency $\gamma(h_x, h_y)$ and when the slopes are small, an expansion as in (1.24) is realistic. In this work the formula will be used for two long wave reduced models describing epitaxial growth. In general the anisotropy coefficients g_{kj} have to be determined by experiments. However, it will be shown that they can be chosen properly, when preferred orientations are known in advance.

The anisotropy is important for any sort of crystalline material. For the heteroepitaxial system that is considered for QD growth, also an elastic subproblem has to be taken into account. In the next section it is shown how linear elasticity can be used for a two material set-up.

1.3 The strain energy density for Ge/Si like systems

It is known that in certain heteroepitaxial processes the surface energy has the same order of magnitude as the bulk energy that results from a misfit between two crystalline materials. The chemical potential of such an Asaro-Tiller-Grinfeld (ATG) instability driven evolution (see e.g. [4] or [22]) can be divided into a sum of these two energies

$$\mu = \mathcal{E}_{surf} + \mathcal{E}_{sed} \quad ,$$

where \mathcal{E}_{surf} has already been introduced in (1.12), where the strain energy density \mathcal{E}_{sed} results from mechanical deformations. The governing equations for the latter are discussed in this section. Two different books may be worth a reading to acquire knowledge in the field of elasticity. A discussion on an engineering level is given by Sadd [87], while a more theoretical, mathematical approach is presented in the classic book by Landau and Lifshitz [61]. The following theory has been used analogously by Tekalign and Spencer [102, 103] to derive a reduced term that will be used in a model for heteroepitaxial growth in Chapter 4.

For homogeneous, isotropic media Hooke's law is used to relate stress and strain. Once the deformations are known, these quantities can be calculated and the strain energy density can be evaluated at the surface, giving the energy from mechanical deformations. It can be written as the sum

$$\mathcal{E}_{sed} = \frac{1}{2} \sigma_{ij} \epsilon_{ij} |_{z=h} \quad , \quad (1.25)$$

where $(\sigma_{ij})_{i,j \in \{1,2,3\}}$ and $(\epsilon_{ij})_{i,j \in \{1,2,3\}}$ are the stress and the strain tensor, respectively. As usually in elasticity Einstein's summation convention is used and repeated indices are summed up. However, this agreement will be applied in this work only in this section and in the elasticity appendix C. In all other parts equations are treated with a straightforward notation. To avoid confusion it should be noted at this point that while the strain tensor will always be written with indices, the lattice mismatch, which is introduced now, will stand on its own as index-free variable ϵ .

In heteroepitaxy with materials such as silicon and germanium the lattice spacings, a^f for the film and a^s for the substrate, differ by some percent. When the deposited atoms arrange to match the substrate's lattice instead of building up their natural grid, the displacements are small, but present (see also Figure 1.4 for a visual aid). The mismatch (or synonymously: the misfit)

$$\epsilon = \frac{a^f - a^s}{a^f} \quad (1.26)$$

is the relative difference of the lattice spacings. For the Ge/Si(001) system it is approximately 4 percent and for other systems such as $\text{Ge}_x\text{Si}_{1-x}/\text{Si}(001)$ it is even smaller. This motivates to relate the stress and the strain by linear elasticity (Hooke's law)

$$\sigma_{ij} = C_{ijkl} \sigma_{kl} \quad . \quad (1.27)$$

The rank four tensor $C = (C_{ijkl})_{ijkl}$ is called the stiffness tensor. In most cases many of the 81 entries are redundant and more pleasant relations between stress and strain can be recorded. For isotropic materials equation (1.27) becomes

$$\sigma_{ij} = \frac{E}{1+\nu} \epsilon_{ij} + \frac{E\nu}{(1+\nu)(1-2\nu)} \epsilon_{kk} \delta_{ij} \quad i, j \in \{1, 2, 3\}, \quad (1.28)$$

with Poisson's ratio ν and the elastic modulus E . Slightly different formulas are cited elsewhere, because it is possible to express E and ν in terms of two other elasticity constants, the shear modulus or Lamé's first parameter. Conversion between these quantities is simple and it is given within Table C.1 in Appendix C.

Pang and Huang used anisotropic coefficients in a recent work on Stranski-Krastanov growth [78] and the approach presented here might also be expanded to this case. However, only the material constants of one solid can be considered following their ansatz — here elasticity in film and in substrate are considered. In any case the anisotropy of the elasticity problem is not sufficient to model faceting of the growing surface as shown with help of a phase field model by Seol et al. [91]. In a way this is confirmed by Pang and Huang, since the surface shapes in their work indeed do not show faceting. In the QD growth model that will be described here, faceting will be a result of the anisotropy that is incorporated in the surface energy.

In linear elasticity the partial derivatives of the displacements u_i define the strain tensor. It is the symmetric part of their gradient tensor

$$(\epsilon_{ij})_{i,j \in \{1,2,3\}} = \frac{1}{2} (\nabla u + \nabla u^T) \quad . \quad (1.29)$$

It is assumed that the mechanical steady state is obtained instantly while the thermodynamical evolution happens on a much longer time scale. This yields the mechanical equilibrium condition

$$\nabla \cdot \sigma = 0 \quad . \quad (1.30)$$

Plugging in the definition of the strains (1.29) and the stress-strain-relation (1.28) into the equilibrium condition (1.30), results in the well-known Navier-Cauchy equations of isotropic linear

elasticity theory

$$(1 - 2\nu)\Delta u + \nabla(\nabla \cdot u) = 0 \quad . \quad (1.31)$$

Boundary conditions have to be defined to obtain well-defined solutions to the above PDE. Once the displacements are available one can calculate the strain tensor, then the stress tensor and finally the strain energy density using (1.25).

In Figure 1.3 the set-up for the self-assembly of QDs is sketched. A time-dependent thin film with height $h(x, y, t) > 0$ sits on top of a relatively thick substrate that is treated for simplicity as a whole half-space bounded by the film on top. The interface between the materials is assumed to be at $z = 0$, conditions at this interface and on the boundaries are necessary.

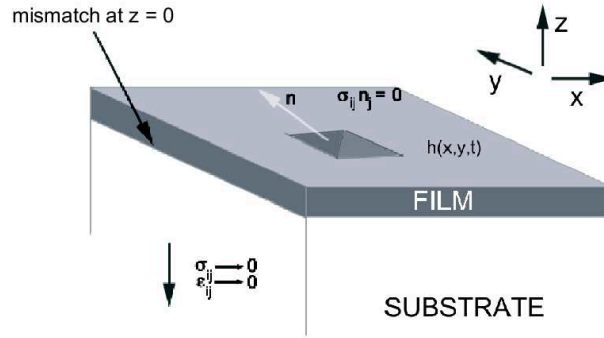


Figure 1.3: Sketch of the epitaxy setting: A film of thickness h grows on a substrate occupying an infinite half-space.

On top of the film the pressure is assumed to be negligible, so that there the boundary condition is

$$\sigma \cdot n = 0 \quad \text{at} \quad z = h \quad . \quad (1.32)$$

The small distortions near the interface do not have a big impact on the displacements deep inside the bulk material, hence there the stresses vanish by incorporating the condition

$$u_i^s \rightarrow 0 \quad \text{for} \quad z \rightarrow -\infty \quad . \quad (1.33)$$

At the interface between the two crystalline materials it is assumed that the displacements of the film are equal to those of the substrate with an additional correction in x and y directions arising from lattice mismatch

$$u_i^f = u_i^s + \epsilon[x, y, 0]^T \quad \text{at} \quad z = 0 \quad , \quad (1.34)$$

with the lattice constants misfit parameter (1.26). Throughout the document the superscript f indicates a quantity that belongs to the film while the index s is related to the substrate. Variables without superscripts are supposed to be understood from the context. Often this is

expected to be the case and no indices are used. In other cases superscripts are reserved as usually for taking powers.

At the film-substrate interface, continuity of the normal component of the stress tensor is assumed. The interface is treated as planar, hence curvature free. Since the slopes of the interface are one order of magnitude smaller than the small parameter, at least in the early time domain of the Ge/Si(001) system, this assumption is reasonable in view of application of the small slope approximation. Then the outward unit normal vector is just the third Cartesian basis vector, which gives the continuity condition

$$(\sigma_{i3}^f)|_{z=0} = (\sigma_{i3}^s)|_{z=0} \quad . \quad (1.35)$$

A typical additional curvature dependent term vanishes under the given assumptions.

The complete elasticity problem is now fully described by the equations (1.28)-(1.35) and for simple problems it can even be solved analytically. Often it is useful to define a reference state where the solution to the problem can be obtained easily. Here, for the heteroepitaxial problem, the base state is a flat film adjusting its lattice spacing to the undeformed substrate. The strain energy density

$$\mathcal{E}_{sed}^{base} = \frac{E}{1-\nu} \epsilon^2 \quad (1.36)$$

of this configuration is derived in the following Section 1.3.1. In Section 4.1, during the derivation of a realistic QD model, it will serve as scaling parameter for the strain energy density, since it defines a characteristic measure for the elastic problem.

1.3.1 The base state

Figure 1.4 shows the set-up of the base state. The strain energy density for this configuration will be calculated in terms of linear elasticity using the theory from the last section. When atoms

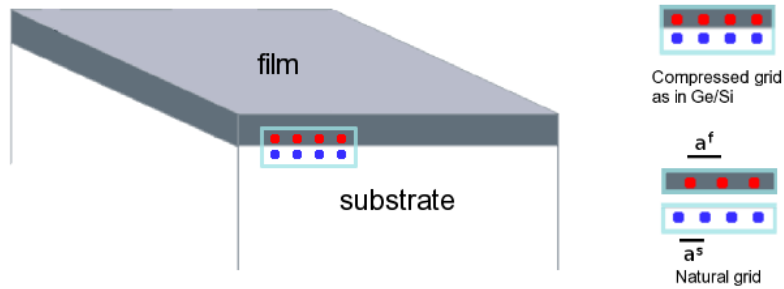


Figure 1.4: Base state of the elasticity problem and a sketch of the grid compression typical for many Stranski-Krastanov systems.

from a growing film carry over the lattice spacing from the substrate material instead of building up their natural grid, certain knowledge about the stress state is available. The displacements

of the film in the x and y directions are $u_1^f = \epsilon x$ and $u_2^f = \epsilon y$. For the vertical direction z is not specified, hence it is $u_3^f = \varphi(x, y, z)$ with some function φ . Using (1.29), one derives the strain tensor for the film

$$(\epsilon_{ij}^f)_{ij} = \begin{pmatrix} \epsilon & 0 & \frac{1}{2}\partial_x\varphi \\ 0 & \epsilon & \frac{1}{2}\partial_y\varphi \\ \frac{1}{2}\partial_x\varphi & \frac{1}{2}\partial_y\varphi & \partial_z\varphi \end{pmatrix} .$$

Assuming that the film undergoes a compression to fit its generic lattice to a^s in lateral directions, this results in an equal biaxial force in x and y directions and in the diagonal stress tensor

$$(\sigma_{ij}^f)_{ij} = \begin{pmatrix} \sigma_0 & 0 & 0 \\ 0 & \sigma_0 & 0 \\ 0 & 0 & 0 \end{pmatrix} .$$

Here σ_0 is a quantity that is specified later on. Since the off-diagonal entries are proportional to the same entries of the strain tensor, the lateral derivatives of φ vanish, $\partial_x\varphi = 0$ and $\partial_y\varphi = 0$, which gives $\varphi = \phi_1(y, z) + \text{const}$ and $\varphi = \phi_2(x, z) + \text{const}$, so that overall

$$\varphi = \phi(z) + \text{const} ,$$

with some function $\phi(z) = \phi_1(y, z) = \phi_2(x, z)$. Using (1.28) yields

$$\partial_z\varphi = \partial_z\phi = -\frac{2\nu^f}{E^f}\sigma_0 .$$

Integrating once and considering that in the base state the substrate is unchanged, $u^s = 0$, and that $u_3^s = u_3^f$ at $z = 0$, the third component of the film-displacement can be defined as

$$u_3^f = -\frac{2\nu^f}{E^f}\sigma_0 z .$$

The overall strain tensor now simplifies to

$$(\epsilon_{ij})_{ij} = \begin{pmatrix} \epsilon & 0 & 0 \\ 0 & \epsilon & 0 \\ 0 & 0 & -\frac{2\nu^f}{E^f}\sigma_0 \end{pmatrix} .$$

The stress-strain relation (1.28) gives

$$\sigma_{11} = \sigma_0 = \frac{E^f}{1 + \nu^f}\epsilon + \frac{E^f\nu^f}{(1 + \nu^f)(1 - 2\nu^f)}(2\epsilon - \frac{2\nu^f}{E^f}\sigma_0)$$

and hence

$$\sigma_0 = \frac{E^f}{1 - \nu^f}\epsilon .$$

The results for the base state at one go are

$$u^f = \begin{pmatrix} \epsilon x \\ \epsilon y \\ -\frac{2\nu}{1-\nu}\epsilon z \end{pmatrix}, (\sigma_{ij}^f)_{ij} = \begin{pmatrix} \frac{E^f}{1-\nu^f}\epsilon & 0 & 0 \\ 0 & \frac{E^f}{1-\nu^f}\epsilon & 0 \\ 0 & 0 & 0 \end{pmatrix}, (\epsilon_{ij}^f)_{ij} = \begin{pmatrix} \epsilon & 0 & 0 \\ 0 & \epsilon & 0 \\ 0 & 0 & -\frac{2\nu^f}{1-\nu^f}\epsilon \end{pmatrix} \quad (1.37)$$

and the strain energy density (1.36) can be read off directly. These expressions will be used in Section 4.1, where a heteroepitaxial model incorporates stresses in the bulk and the film which drive the instability.

Chapter 2

The HCCH equation: Derivation and existence of solutions

An ounce of action is worth a ton of theory.

Friedrich Engels (1820 - 1895)

This and the following chapter present the analysis of a sixth order semilinear PDE describing the faceting of a growing surface in two dimensions. It will be derived in Section 2.1 and it will be called the higher order convective Cahn-Hilliard (HCCH) equation. While in the subsequent Chapter 3 long-time behavior and stationary solutions will be discussed, here a more fundamental aspect, the existence of solutions, is considered. The general topic is of major interest since many decades. The at the present time most illustrious PDE for such a problem is the Navier-Stokes equation. Since the 19th century researchers try to find out if regular solutions exist and meanwhile it became a Millennium problem (the official description of the problem can be found at <http://www.claymath.org>). For the PDE considered here, it is also sought to make substantial progress toward a mathematical theory that reveals important properties of the equation. However, the problem here is much simpler than for the Millennium problem. For the incompressible Navier-Stokes equation the one- and two-dimensional cases were solved, and the task remains to show or disprove existence of regular solutions in three dimensions, which, of course, is a more complex and ongoing task.

Before discussing the existence of solutions, the equation is derived in the limit of small slopes. Therefore important terms of suitable expansions are identified and those which do not have a major influence are ignored. In the framework of this approach, the thin-film assumption has to hold true: *The vertical scale H_0 is much smaller than the horizontal scale L .* The quotient of these two quantities, $\alpha = H_0/L \ll 1$, is the small parameter used for asymptotic expansions. In many applied mathematical problems such small quantities are used to expand functions and

determine important terms. Very often this is done in the field of matched asymptotics, where two or more regions of the solutions are scaled differently and yield simpler problems. If these can be solved, they leave constants that have to be determined by matching with neighboring regions. However, in this chapter no matching procedures will be needed. This topic will be of interest in Chapter 3. Here asymptotic expansions are solely used to determine simpler evolution equations, though the formal framework is similar. The final equation originates from the work by Savina et al. [89]. It describes the faceting of a growing anisotropic surface under surface diffusion and a normal flux. The derivation in the reference is somewhat longsome and requires the study of preceding works by Golovin et al. and McFadden et al. [41, 67]. Here, based on the theory from Chapter 1, a slightly alternative derivation is shown in a way that can be used analogously for the second major PDE considered in this work, a new model for the coarsening of QDs, in Chapter 4. The problem of faceted, growing surfaces experiences continued interest. Apart from the set-up of various PDEs, for a convective Cahn-Hilliard equation a so-called coarsening dynamical systems (CDS) has been introduced for the case with one lateral variable. There each facet is an unknown in an ODE describing the evolution [109]. Only recently this idea has been extended to two lateral dimensions for the case of sharp facets during growth of materials such as CuO_2 . Watson and Norris derived a piecewise-affine dynamical surface (PADS) to describe the evolution of the strongly anisotropic surface [73, 108]. Such approaches may slightly deteriorate the accuracy of the model, in exchange numerical simulations can be carried out orders of magnitude faster than by solving corresponding PDEs.

2.1 The faceting of a growing surface

A higher order convective Cahn-Hilliard (HCCH) equation is derived in this section [57, 89]. Formally it is similarly structured as the convective Cahn-Hilliard (CCH) equation. However, higher derivatives in the parabolic terms make it a PDE of very high, of sixth order. Evolution equation (1.9) that incorporates a normal flux from the gas phase is used with a chemical potential that depends on a strongly anisotropic surface energy. Additionally an edge regularization term that smoothes out corners in case of strong anisotropy is considered. Altogether this yields a model for the faceting of a growing surface. A small slope approximation is then used to derive a simplified PDE.

The surface free energy in this model is an integral over the anisotropic surface energy density γ and it defines the chemical potential as usually as its functional derivative (see Chapter 1, formula (1.12)). Ω is a half-space that is bounded above by a smooth surface. Expanding the surface energy in terms of the outward unit normal components $n_i, i = 1, 2, 3$, and using the anisotropy for crystals with cubic symmetry, one can derive the surface energy

$$\gamma_a = \gamma_0 + \gamma_4(n_1^4 + n_2^4 + n_3^4) + \gamma_6(n_1^6 + n_2^6 + n_3^6) \quad , \quad (2.1)$$

where γ_0, γ_4 and γ_6 are anisotropy coefficients that have to be determined by experiments. For

details of the derivation of (2.1) one can study the work by McFadden et al. [67], where it is shown how to use invariance under rotations of 90 degrees and reflections to obtain this expansion in terms of the outward unit normal components. Additionally to the polynomial γ_a , which leads to an unphysical backward diffusion term in the evolution equation if the anisotropy coefficients are big, Savina et al. [89] introduced an edge regularization term that is also known as Wilmore regularization

$$\gamma_e = \frac{1}{2}\nu\kappa^2 \quad , \quad (2.2)$$

with an edge regularization factor $\nu > 0$ and the mean curvature κ (see Appendix A, equation (A.2)). Then the overall surface energy is

$$\gamma = \gamma_a + \gamma_e = \gamma_0 + \gamma_4(n_1^4 + n_2^4 + n_3^4) + \gamma_6(n_1^6 + n_2^6 + n_3^6) + \frac{1}{2}\nu\kappa^2 \quad . \quad (2.3)$$

The κ term punishes high curvature and by its incorporation kinks are smoothed out. As already mentioned the Wilmore term has raised attention in the last years, for example in a recent work by Spencer [94], where equilibrium crystal shapes are determined. In conjunction with faceted surfaces it has been derived by Golovin et al. [40]. It bases on a quite common step model where instead of smooth slopes crystals steps are considered [106].

2.1.1 The HCCH equation

In Chapter 1 it has been shown how to incorporate an anisotropic surface energy into a surface diffusion evolution equation. Here the results for the fifth formula SE_V are needed, since γ defined as in (2.3) depends on slopes and second derivatives of the surface h . The terms for SE_V , which are marked in Table 1.1, will be derived. Proposition 5 with formula (1.24) shows that the surface energy γ can be written in terms of the slopes instead of the normals under the assumption that the surface can be parametrized regularly. It yields

$$\gamma = \gamma(h_x, h_y, h_{xx}, h_{xy}, h_{yy}) = \gamma_0 \bar{\gamma} = \gamma_0 (1 + \mathcal{W}(h_x, h_y) + \frac{1}{2}\tilde{\nu}\kappa^2) \quad , \quad (2.4)$$

where $\bar{\gamma}$ is the dimensionless surface energy that contains the nonlinear slope-dependent correction \mathcal{W} . Since the slopes for this model are assumed to be small, instead of a function with arbitrary nonlinearities, the polynomial

$$\mathcal{W}(h_x, h_y) = \sum_{k=1}^N \sum_{j=0}^k g_{kj} h_x^j h_y^{k-j} \quad (2.5)$$

is used. The anisotropy coefficients g_{kj} are dimensionless while the edge regularization coefficient $\tilde{\nu} = \nu/\gamma_0$ still has a unit, $[\tilde{\nu}] = m^2$.

The surface energy (2.4) is used with the evolution equation (1.9). Table 1.1 from Section 1.2.1 yields

$$\begin{aligned} \mu &= \frac{\delta}{\delta h} \int \gamma_0 (1 + \mathcal{W}(h_x, h_y) + \frac{1}{2}\tilde{\nu}\kappa^2) dS \quad , \\ &= \mathcal{E}_\kappa + \mathcal{E}_{anis} + \mathcal{E}_{hot} \quad , \end{aligned}$$

with

$$\begin{aligned}\mathcal{E}_\kappa &= -\gamma\kappa \quad , \\ \mathcal{E}_{anis} &= -2\left(\frac{h_x h_{xx} + h_y h_{xy}}{N} \partial_{h_x} \gamma + \frac{h_y h_{yy} + h_x h_{xy}}{N} \partial_{h_y} \gamma\right) - N \partial_x \partial_{h_x} \gamma - N \partial_y \partial_{h_y} \gamma \quad , \\ \mathcal{E}_{hot} &= [\partial_{xx} \partial_{h_{xx}} + \partial_{xx} \partial_{h_{yy}} + \partial_{yy} \partial_{h_{xx}} + \partial_{yy} \partial_{h_{yy}}](\gamma N) \quad .\end{aligned}$$

Here the abbreviation (1.13) and the derivatives (1.14) from before are used. Now the still quite general evolution equation writes

$$h_t = \sqrt{1 + |\nabla h|^2} (F + \mathcal{D} \nabla_s^2 [\mathcal{E}_\kappa + \mathcal{E}_{anis} + \mathcal{E}_{hot}]) \quad .$$

The chemical potential terms contain many nonlinearities that can be simplified under the assumption that the slopes of the surface remain small. Therefore characteristic lengths are introduced and the PDE is nondimensionalized. Let H_0 be a small characteristic thickness scale and let L be a bigger scale for the substrate directions x and y , then the parameter $\alpha = H_0/L \ll 1$ can be used for asymptotic expansions [95, 102]. The characteristic space scales which are used to work with dimensionless quantities are H_0 and L , so that

$$h = H_0 H, \quad x = LX, \quad y = LY \quad . \quad (2.6)$$

They induce the characteristic time scale

$$t = \tau T \quad \text{with} \quad \tau = \frac{L^4}{\mathcal{D} \gamma_0} \quad .$$

It is derived by nondimensionalization of the evolution equation. Therefore the chemical potential is written as

$$\mu = \frac{\gamma_0}{L} \bar{\mu}, \quad \bar{\mu} = \bar{\mathcal{E}}_\kappa + \bar{\mathcal{E}}_{anis} + \bar{\mathcal{E}}_{hot}$$

and similarly the surface Laplacian and the mean curvature are

$$\nabla_s^2 = \frac{1}{L^2} \bar{\nabla}_s^2, \quad \kappa = \frac{1}{L} \bar{\kappa} \quad .$$

The evolution equation then writes (derivative operators such as the nabla operator are from now on in the new scales, $\nabla = (\partial_X, \partial_Y)^T$)

$$H_T = \sqrt{1 + \alpha^2 |\nabla H|^2} (\bar{F} + \frac{1}{\alpha} \bar{\nabla}_s^2 [\bar{\mathcal{E}}_\kappa + \bar{\mathcal{E}}_{anis} + \bar{\mathcal{E}}_{hot}]) \quad . \quad (2.7)$$

Here the dimensionless deposition rate is $\bar{F} = FL^4/(H_0 \mathcal{D} \gamma_0)$ and with $\tilde{\nu} = L^2 \bar{\nu}$ the chemical potential terms write

$$\begin{aligned}\bar{\mathcal{E}}_\kappa &= -\bar{\gamma} \bar{\kappa} \quad , \\ \bar{\mathcal{E}}_{anis} &= -2\alpha \frac{(H_X H_{XX} + H_X H_{XY}) \partial_{H_X} \mathcal{W} + (H_Y H_{YY} + H_Y H_{XY}) \partial_{H_Y} \mathcal{W}}{(1 + \alpha^2 (H_X^2 + H_Y^2))^{1/2}} \\ &\quad - \frac{1}{\alpha} (1 + \alpha^2 (H_X^2 + H_Y^2))^{1/2} (\partial_X \partial_{H_X} \mathcal{W} + \partial_Y \partial_{H_Y} \mathcal{W}) \quad , \\ \bar{\mathcal{E}}_{hot} &= \frac{1}{\alpha} \nabla^2 [\partial_{H_{XX}} + \partial_{H_{YY}}] (\frac{1}{2} \bar{\nu} \bar{\kappa}^2 (1 + \alpha^2 (H_X^2 + H_Y^2))^{1/2}) \quad .\end{aligned}$$

All terms in the evolution equation are now expanded in powers of α to obtain a leading order evolution equation that captures all involved effects. Since it turns out that the nonconstant chemical potential terms are of order α , the time scale is already chosen such that the small parameter will not appear at these terms. Expanding the surface Laplacian gives

$$\bar{\nabla}_s^2 = \nabla^2 + \mathcal{O}(\alpha^2) \quad . \quad (2.8)$$

To capture the anisotropy in a reduced formula, all corresponding surface energy terms have to be incorporated in the evolution equation. Therefore these terms have to be of the same order, which is only the case when

$$g_{kj} = G_{kj}\alpha^{-k+2}, \quad G_{kj} = \mathcal{O}(1) \quad . \quad (2.9)$$

In this way

$$\bar{\gamma} = \gamma/\gamma_0 = 1 + \alpha^2 W(H_X, H_Y) + \frac{\alpha^2}{2} \bar{\nu} (\nabla^2 H)^2 + \mathcal{O}(\alpha^3) \quad ,$$

with the anisotropy influence

$$W(H_X, H_Y) = \sum_{k=1}^N \sum_{j=0}^k G_{kj} H_X^j H_Y^{k-j} \quad . \quad (2.10)$$

Expanding the nondimensionalized chemical potential

$$\bar{\mu} = \bar{\mu}^{(0)} + \alpha \bar{\mu}^{(1)} + \mathcal{O}(\alpha^2) \quad ,$$

the square root in equation (2.7) and the surface Laplacian with respect to the small parameter α and considering the evolution equation in a frame that moves with the growth rate ($H \rightarrow H + \bar{F}T$) leads to an evolution equation to order α

$$H_T = \frac{\bar{F}}{2} |\nabla H|^2 + \nabla^2 (\bar{\mu}^{(0)} / \alpha + \bar{\mu}^{(1)}) \quad , \quad (2.11)$$

with $\bar{F} = FL^4/(H_0 \mathcal{D} \gamma_0)$. It will be shown that $\nabla \mu^{(0)}$ is zero, so that it can be neglected in the formula above. Expansions of the chemical potential yield terms of leading order α ,

$$\begin{aligned} \bar{\mathcal{E}}_\kappa &= -\alpha \nabla^2 H + \mathcal{O}(\alpha^3) \quad , \\ \bar{\mathcal{E}}_{anis} &= -\alpha \nabla \cdot \nabla_{\nabla H} W(H_X, H_Y) + \mathcal{O}(\alpha^3) \quad , \\ \bar{\mathcal{E}}_{hot} &= \frac{1}{\alpha} \nabla^2 (\partial_{H_{XX}} + \partial_{H_{YY}}) \left[\frac{1}{2} \bar{\nu} \alpha^2 (\nabla^2 H)^2 \right] + \mathcal{O}(\alpha^3) \\ &= \alpha \bar{\nu} \nabla^4 H + \mathcal{O}(\alpha^3) \quad , \end{aligned}$$

so that the overall evolution equation becomes

$$H_T = \frac{\bar{F}}{2} |\nabla H|^2 + \nabla^2 [-\nabla^2 H - \nabla \cdot \nabla_{\nabla H} W(H_X, H_Y) + \bar{\nu} \nabla^4 H] \quad ,$$

with the still very general anisotropy influence

$$\begin{aligned} \nabla \cdot \nabla_{\nabla H} W(H_X, H_Y) = & \sum_{k=2}^N \sum_{j=0}^k G_{kj} \left(j(j-1) H_X^{j-2} H_Y^{k-j} H_{XX} \right. \\ & \left. + (k-j)(k-j-1) H_X^j H_Y^{k-j-2} H_{YY} + 2j(k-j) H_X^{j-1} H_Y^{k-j-1} H_{XY} \right). \end{aligned}$$

Setting all $G_{kl} = 0$ except of $G_{20} = G_{22} = G_1 < -1/2$ and G_{40}, G_{42}, G_{40} bigger than zero (these are conditions that have been obtained during the modeling of a surface energy by Savina et al. [89] and the references therein), gives

$$\begin{aligned} H_T = & \frac{\tilde{F}}{2} |\nabla H|^2 + \nabla^2 \left[(-2G_1 - 1) \nabla^2 H - 2G_{42} (H_X^2 H_{YY} + H_Y^2 H_{XX} + 4H_X H_Y H_{XY}) \right. \\ & \left. - 12G_{44} H_X^2 H_{XX} - 12G_{40} H_Y^2 H_{YY} + \bar{\nu} \nabla^4 H \right] \end{aligned} \quad (2.12)$$

or equivalently with $g = -2G_1 - 1 > 0$ a time-scale change $T \rightarrow Tg$ and $\delta = \tilde{F}/g$

$$\begin{aligned} H_T = & \frac{\delta}{2} |\nabla H|^2 + \nabla^2 \left(\nabla^2 H - 2 \frac{G_{42}}{g} (H_X^2 H_{YY} + H_Y^2 H_{XX} + 4H_X H_Y H_{XY}) \right. \\ & \left. - 12 \frac{G_{44}}{g} H_X^2 H_{XX} - 12 \frac{G_{40}}{g} H_Y^2 H_{YY} + \frac{\bar{\nu}}{g} \nabla^4 H \right). \end{aligned}$$

Rescaling the X and Y variables once again ($X \rightarrow (\bar{\nu}/g)^{1/2} X$), then

$$\begin{aligned} \left(\frac{\nu}{g}\right)^2 H_T = & \frac{\delta}{2} |\nabla H|^2 + \nabla^2 \left(\frac{\nu}{g} \left(-2 \frac{G_{42}}{g} (H_X^2 H_{YY} + H_Y^2 H_{XX} + 4H_X H_Y H_{XY}) \right. \right. \\ & \left. \left. - 12 \frac{G_{44}}{g} H_X^2 H_{XX} - 12 \frac{G_{40}}{g} H_Y^2 H_{YY} \right) \right) + \nabla^4 H + \nabla^6 H. \end{aligned}$$

Defining $b = 2\nu/g^2 G_{42}$, setting the anisotropy coefficients to $G_{44} = G_{40} = g/4$ and a last time scale change $T \rightarrow T(\nu/g)^2$ gives the final semilinear PDE describing the faceting of a growing anisotropic surface,

$$\begin{aligned} H_T = & \frac{\delta}{2} |\nabla H|^2 + \nabla^4 H + \nabla^6 H \\ & - \nabla^2 \left[b (H_X^2 H_{YY} + H_Y^2 H_{XX} + 4H_X H_Y H_{XY}) + 3H_X^2 H_{XX} + 3H_Y^2 H_{YY} \right]. \end{aligned} \quad (2.13)$$

By reducing the equation to one lateral dimension and differentiating the whole expressions one obtains

$$H_{XT} = \frac{\delta}{2} (H_X^2)_X + (H_{XXX} + H_{XXXX} - (3H_X^2 H_{XX})_X)_{XX}.$$

Setting $u = H_X$ and using the small letters x, t for the lateral direction X and time T again this gives a sixth order equation, in the form derived by Savina et al. [89].

$$u_t - \frac{\delta}{2} (u^2)_x = (u_{xx} + u - u^3)_{xxxx} \quad (2.14)$$

It is called higher order Cahn-Hilliard (HCCH) equation from now on and it is the equation that will be studied extensively in the following sections. The reduced models are suitable to describe

faceting of a growing surface in one and two lateral dimensions, respectively. In Chapter 3 new types of stationary solutions to this equation are derived and in Section 3.2 the results from time-dependent simulations are shown. Before proving existence for this PDE, some notes on related phase separating systems are made and mathematical basics are introduced.

2.2 Related phase separation systems

The spatial derivative term on the left in the HCCH equation (2.14) is called convective term since it reminds of the convection term appearing in fluid dynamics, i.e. in the Navier-Stokes equation. However, here the temperature is fixed and no real convection takes place. The terms on the right hand side can be interpreted as a higher order regularization term replacing the Laplacian in the viscous case of Burger's equation. Anyhow it seems more useful to compare (2.14) to equations of Cahn type. There are many related PDEs in this class of models. Now a few of them are introduced, each in a form that resembles most the HCCH equation. For all of these evolution equations more complicated versions based on more elaborated potentials exist.

The Allen-Cahn (AC) equation [2]

$$u_t = u_{xx} + u - u^3 \quad (2.15)$$

contains already part of the structure that appears in the HCCH equation. However, this PDE does not preserve mass, since the nonlinearity is not differentiated, the order is different and furthermore a convection term is missing. It is also known as one of the reaction-diffusion equations, or as Chafee-Infante equation. It has a structure that is fundamental for the analysis of the HCCH equation as the leading order solutions in a matched asymptotics ansatz will show. It is already well understood, for example the existence of solutions is proved in standard PDE books such as the monograph by Robinson [82]. A version of the AC equation with convective term can be written as

$$u_t - \frac{\delta}{2}(u^2)_x = u_{xx} + u - u^3 \quad (2.16)$$

This convection-reaction-diffusion equation is labeled convective Allen-Cahn (CAC) equation and it has been also analyzed quite deeply. For example long time behavior of its solutions has been studied by Chen et al. [14] and existence, uniqueness and regularity results have been established already earlier (see e.g. Ladyzenskaja et al. [60]). The needed estimates to establish the existence are easy to obtain. For Cahn-Hilliard (CH) equations this is already somewhat more complicated. These mass conserving versions of the above models arouse more interest recently. One CH equation without mechanical deformations (e.g. considered in [74]) can be written as

$$u_t = (u^3 - u - u_{xx})_{xx} \quad (2.17)$$

Formally this is the HCCH equation (2.14) without the deposition term, a different sign on the right hand side and two derivatives less around the brackets. Elliott and Songmu [28] have

proved the existence of solutions. A potential function is essential to proceed in the way these authors did. For the HCCH equation without the deposition term, $\delta = 0$, one could use the same Lyapunov function to obtain similar results. However, since $\delta > 0$, the potential character is destroyed and this ansatz cannot be used anymore. Here it is more promising to have a look on the theory for the CCH equation, which adds a convective term that stems from some external force to the CH equation

$$u_t - \frac{\delta}{2}(u^2)_x = (u^3 - u - u_{xx})_{xx} \quad . \quad (2.18)$$

Eden and Kalantarov have shown that an attractor for the CCH equation exists [24]. Along the way the theory yields the existence of weak solutions. It is not that easy for the HCCH equation, because the nonlinearity from the surface energy anisotropy is a term that is more difficult to treat than for the CCH equation. By testing (2.18) with u , the u^3 nonlinearity gives a negative (hence 'good' term) term on the right hand side and this is not the case for the HCCH equation. The convective version of the CH equation has been analyzed in various other works (see e.g. [29, 40, 109, 115]) and many properties of the solutions are yet known.

The structure of the CCH equation is even more reminiscent of the HCCH equation and it will be shown what a sign switch and two more derivatives on the right hand side change. In the next chapter stationary solutions are found and it is shown that a corresponding parameter diagram reveals close similarities to the CCH system. Also the coarsening behavior reminds of the CCH equation. Stationary and traveling wave patterns are analyzed for small values of δ . By increasing this parameter more oscillations in the solutions can be observed and in the limit $\delta \rightarrow \infty$ rough surfaces develop. This is in analogy to the CCH equation, see also [44]. A transition from a regime with stationary and traveling wave solutions to chaotic behavior is observed.

Recently it became popular to include mechanical deformations to improve models for phase separation phenomena. The resulting PDE is called Larché-Cahn equation [63]. Much work on this topic has been carried out by Garcke and his co-workers, see e.g. [37]. Extending chemical potentials by certain terms to model effects so far neglected reminds of the surface diffusion equation for crystal growth (1.7). In Chapter 4 an equation will be derived as extension of a previous work by Tekalign and Spencer [102]. The chemical potential is extended by anisotropy terms. It can also be viewed as an extension of the previous model for the faceting of a growing surface by adding the strain energy density and a wetting term to the chemical potential.

So far nothing has been said about boundary conditions in this chapter. Relating to this work it seems most meaningful to treat the equations on a domain $[0, L]$ with periodic boundary conditions, hence

$$\partial_x^k u(x + L) = \partial_x^k u(x), \quad k = 0, 1, \dots \quad . \quad (2.19)$$

These fit generically to pseudospectral methods based on Fourier transforms and describe infinite panels of the order parameter u . They allow to work with periodic Sobolev spaces which can be convenient, since one can just apply partial integration and neglect boundary terms without much thought. Note that when working in other spaces it is common to define the boundary

conditions in a way that unwanted boundary terms from partial integration vanish (such as $u = 0$ on $\partial\Omega$). However, the standard Sobolev spaces with restrictions for the boundary conditions and the periodic versions share a lot of equivalent properties.

Many numerical works have been accomplished for simulating equations of Cahn type, extensions to more complicated free energies, to vector-valued problems and/or to steep transitions between the phases have been of interest and the set-up of finite element codes and their analysis has been carried out (see for example one recent work by Kornhuber and Krause [55], who present an effective multigrid method for application on a vector-valued Allen-Cahn equation with the rather complicated logarithmic potential, and many of the references therein). Generally more papers could be discussed that are concerned with stationary solutions [75, 110, 111] or the interactions between domain walls [9, 29, 51, 109]. However, there lacks a complete review on equations of Cahn type and their properties. Still there are many publications that can be considered. The available methods from these references should help to analyze the higher order model. Most important for the next sections are certainly the works by Elliott and Songmu [28] and by Eden and Kalantarov [24]. A Galerkin ansatz as in the former work with the art of estimating from the proof of absorbing balls in the latter work were combined here. Though, the PDE considered here is of higher order than in the mentioned references. Equations of such a high order are untypical and only few theory is available at all. There exist a few thin-film equations and blow up of solutions to these equations has been analyzed [30]. However, the analysis is focused on singular events of degenerate models. Sixth order semilinear equations with nonlinearities up to fourth order are completely untypical and display new challenges in the existence theory. Before presenting the existence results, aspects of functional analysis are introduced that are essential for the following discussions.

2.3 Preliminaries: Concepts from functional analysis

There exists much standard literature that can be proposed as introduction to theory of PDEs. Related to existence proofs of evolution equations and infinite-dimensional dynamical systems the books by Evans [31] and Robinson [82] are good choices. Some concepts, such as weak derivatives, partial integration, standard Sobolev spaces, completeness are premised as basic knowledge that is necessary to understand the following theory. Since certain properties of operators will be very important for the existence proofs, these are discussed in some more detail. Furthermore fundamental inequalities are introduced together with additional basic theorems. To motivate the definitions following on the next pages, it should be kept in mind that the equation under discussion is related to the negative Laplacian $-\nabla^2$, the bi-Laplacian ∇^4 and the negative tri-Laplacian $-\nabla^6$, which are all symmetric, linear, unbounded, positive operators that each have an inverse if they act on suitable spaces. These inverse linear mappings are in some sense the opposite of the differentiation operators. They are compact, linear operators and in certain

situations their fractions can be very useful. The terminology will be introduced now.

2.3.1 Operators, fractions, eigenvalues and eigenfunctions

Let H, W be Banach spaces over \mathbb{R} with norms $\|\cdot\|_H$ and $\|\cdot\|_W$. A linear operator $L : H \rightarrow W$ is *bounded* if its images are bounded by their preimages in corresponding norms,

$$\exists C > 0 \forall x \in H \|Lx\|_W \leq C\|x\|_H \quad .$$

Through this property an operator norm for all bounded operators $\mathcal{L}(H, W)$ can be defined as

$$\|L\|_{\mathcal{L}} = \sup_{x \in H, x \neq 0} \frac{\|Lx\|_W}{\|x\|_H}$$

and the tuple $(\mathcal{L}(H, W), \|\cdot\|_{\mathcal{L}})$ becomes a Banach space itself. An operator is *unbounded* if it is not bounded. L is called *compact* if the images of bounded sets are precompact (the closure is compact). Precisely one has

$$\overline{L(B)} \quad \text{is compact for all } B \subset H \text{ bounded.}$$

Remark Compact operators are bounded. □

Note that always if instead of a proof the proof box □ appears, the proof is given in Robinson's book [82].

For a Hilbert space H , a scalar product $(\cdot, \cdot)_H$ is defined together with an associated norm $\|u\|_H = (u, u)_H^{1/2}$. Then for a suitable subspace $W \subset H$ the linear operator $L \in \mathcal{L}(W, H)$ is called *symmetric* if

$$(Lu, v)_H = (u, Lv)_H \quad \forall u, v \in W \quad .$$

The eigenvalues and eigenfunction of linear operators will be useful for certain expansions and estimates. The Hilbert-Schmidt theorem for the compact case will be directly applied later on in the existence proofs. Therefore let H be an infinite-dimensional Hilbert space, $A : H \rightarrow H$ be the unbounded, symmetric, linear operator and let $M = A^{-1} : H \rightarrow H$ be its inverse, a compact, symmetric, linear operator.

Lemma 6 (Hilbert-Schmidt Theorem) *The eigenvalues $\bar{\lambda}_j$ of M defined by the characteristic equation*

$$M\varphi_j = \bar{\lambda}_j\varphi_j, \quad j = 1, 2, \dots$$

are real and they can be ordered such that

$$|\bar{\lambda}_{j+1}| \leq |\bar{\lambda}_j|, \quad j = 1, 2, \dots$$

and

$$\lim_{j \rightarrow \infty} \bar{\lambda}_j = 0 \quad .$$

The set of eigenfunctions $\{\varphi_j\}_j$ forms an orthonormal basis for H . The application of the operator to a function can be expressed in terms of the eigenvalues as

$$Mu = \sum_{j=1}^{\infty} \bar{\lambda}_j (u, \varphi_j)_H \varphi_j \quad . \quad (2.20)$$

□

For the unbounded operator A one obtains a similar result. It bases on the fact that the eigenfunctions can be chosen as for the compact operator M , while the corresponding eigenvalues are $\lambda_j = 1/\bar{\lambda}_j$. This results from the transformation of the characteristic equation

$$M\varphi_j = \bar{\lambda}_j \varphi_j \quad \Leftrightarrow \quad \varphi_j = \bar{\lambda}_j M^{-1} \varphi_j \quad \Leftrightarrow \quad \lambda_j \varphi_j = A\varphi_j \quad .$$

Note that with the ordering from above one has

$$|\lambda_{j+1}| \geq |\lambda_j|, \quad j = 1, 2, \dots \quad (2.21)$$

and

$$\lim_{j \rightarrow \infty} |\lambda_j| = \infty \quad . \quad (2.22)$$

Multiplication of equation (2.20) by A two times gives

$$Au = \sum_{j=1}^{\infty} \frac{1}{\lambda_j} (u, \varphi_j)_H A^2 \varphi_j = \sum_{j=1}^{\infty} (u, \varphi_j)_H A \varphi_j = \sum_{j=1}^{\infty} \lambda_j (u, \varphi_j)_H \varphi_j \quad . \quad (2.23)$$

The results can be summarized in the following lemma.

Lemma 7 *Let A be a symmetric, linear, unbounded operator with the compact, linear inverse M , than A has an infinite set of eigenvalues $\{\lambda_j\}_j$ that correspond to the set of eigenfunctions $\{\varphi_j\}_j$. They can be ordered as in (2.21), so that they tend to infinity with $j \rightarrow \infty$. The eigenfunctions can be chosen as orthonormal basis of H and A applied to a function u has an expansion as in (2.23).* □

Remark If A is positive, that is $(A\varphi, \varphi) \geq 0$ for all $\varphi \in H$, then all eigenvalues are positive. □

Assume that A and M are operators that are defined as for the last two lemmata. If they are positive, then the expansions in terms of the eigenfunctions allow to define *fractional powers of operators* applied to a function. Let $\alpha > 0$, then for the operator A its fraction is defined via

$$A^\alpha u = \sum_j \lambda_j^\alpha c_j \varphi_j \quad ,$$

where now shortly $c_j = (u, \varphi_j)_H$. For the inverse operator $M = A^{-1}$ one defines analogously

$$M^\alpha u = \sum_j \bar{\lambda}_j^\alpha c_j \varphi_j \quad .$$

These expressions will be used later on for calculations like the following (for $u = \sum_k c_k \varphi_k$ and $w = \sum_k d_k \varphi_k$)

$$\begin{aligned}
(Mu, w)_{L^2} &= \left(\sum_k \bar{\lambda}_k c_k \varphi_k, \sum_j d_j \varphi_j \right)_{L^2} \\
&= \sum_{k,j} \bar{\lambda}_k c_k d_j \int \varphi_k \varphi_j dx \\
&= \sum_k \bar{\lambda}_k^{1/2} c_k \bar{\lambda}_k^{1/2} d_k \\
&= \sum_{k,j} \bar{\lambda}_k^{1/2} c_k \bar{\lambda}_j^{1/2} d_j \int \varphi_k \varphi_j dx \\
&= (M^{1/2}u, M^{1/2}w)_{L^2} \quad .
\end{aligned} \tag{2.24}$$

This partition of the operator will be useful for certain estimates. Using the Hölder inequality for the scalar product in (2.24) one can further estimate the resulting L^2 norms of each argument by using

$$\begin{aligned}
\|M^{1/2}u\|^2 &= \left(\sum_k \bar{\lambda}_k^{1/2} c_k \varphi_k, \sum_j \bar{\lambda}_j^{1/2} c_j \varphi_j \right)_{L^2} \\
&= \sum_{k,j} \bar{\lambda}_k c_k c_j \int \varphi_k \varphi_j dx \\
&= \sum_k \bar{\lambda}_k c_k^2 \\
&\leq \bar{\lambda}_1 \sum_k c_k^2 \\
&= \bar{\lambda}_1 \|u\|^2 \quad .
\end{aligned} \tag{2.25}$$

In particular this result shows that $M^{1/2}$ is a bounded operator. It should be noted that the above estimate particularly holds for $M = A^{-1}$ with $A \in \{-\nabla^2, \nabla^4, -\nabla^6\}$ working on suitable normalized periodic Sobolev spaces. Then for each operator the eigenvalue $\bar{\lambda}_1$ is differently defined.

Let \dot{H}_{per}^k be the Sobolev space H^k that is restricted to periodic functions on $\Omega = [0, L]$ which have zero mean. $A_1 = -\partial_{xx} : \dot{H}_{per}^1 \rightarrow \dot{L}^2$, $A_2 = \partial_{xxxx} : \dot{H}_{per}^2 \rightarrow \dot{L}^2$, $A_3 = -\partial_{xxxxx} : \dot{H}_{per}^3 \rightarrow \dot{L}^2$ with inverse operators $M_k = A_k^{-1}$, $k = 1, 2, 3$. The mappings M_k are bounded from \dot{L}^2 to one of the higher order Sobolev spaces. However, bounded subsets in \dot{H}_{per}^k are compact in \dot{L}^2 , so that the inverse mappings are in fact compact operators from \dot{L}^2 into the same space. More detailed information on the spaces will be given in the next section.

Consider the characteristic equations

$$A_j \varphi_k = \lambda_{jk} \varphi_k, j = 1, 2, 3, k = 0, 1, 2, \dots$$

With $\varphi_k = e^{i \frac{2\pi k}{L} x}$ one has

$$A_j e^{i \frac{2\pi k}{L} x} = \lambda_{jk} e^{i \frac{2\pi k}{L} x}, j = 1, 2, 3$$

and the smallest nonzero eigenvalue is given for $k = 1$. For the three operators one obtains the eigenvalues by a simple calculation

$$\begin{aligned} \left(\frac{2\pi k}{L}\right)^2 e^{i\frac{2\pi k}{L}x} &= \lambda_{1k} e^{i\frac{2\pi k}{L}x} \Rightarrow \lambda_{1k} = \left(\frac{2\pi k}{L}\right)^2, \\ \left(\frac{2\pi k}{L}\right)^4 e^{i\frac{2\pi k}{L}x} &= \lambda_{2k} e^{i\frac{2\pi k}{L}x} \Rightarrow \lambda_{2k} = \left(\frac{2\pi k}{L}\right)^4, \\ \left(\frac{2\pi k}{L}\right)^6 e^{i\frac{2\pi k}{L}x} &= \lambda_{3k} e^{i\frac{2\pi k}{L}x} \Rightarrow \lambda_{3k} = \left(\frac{2\pi k}{L}\right)^6. \end{aligned}$$

It is interesting to see that all three operators have the same eigenfunctions and that the eigenvalues of the bi- and tri-Laplacian are just powers of the eigenvalues of A_1 , $\lambda_{jk} = \lambda_{1k}^{2j}$, $j = 2, 3$. As another result one obtains the inequality

$$\|u\|_{L^2(\Omega)} \leq \left(\frac{L}{2\pi}\right)^{2j} \|A_j u\|_{L^2(\Omega)},$$

since

$$\|A_j u\|_{L^2(\Omega)}^2 = \left\| \sum_k c_k A_j \varphi_k \right\|_{L^2(\Omega)}^2 = \left\| \sum_k \lambda_{jk} c_k \varphi_k \right\|_{L^2(\Omega)}^2 \geq \lambda_{j1}^2 \left\| \sum_k c_k \varphi_k \right\|_{L^2(\Omega)}^2 = \lambda_{11}^{4j} \|u\|_{L^2(\Omega)}^2.$$

Analogously the estimates (2.25) can be written more precisely as

$$\|M_j u\|_{L^2(\Omega)}^2 \leq \left(\frac{L}{2\pi}\right)^{2j} \|u\|_{L^2(\Omega)}^2, j = 1, 2, 3.$$

The set $\{\varphi_k\}_k$ forms an orthonormal basis of \dot{L}^2 . Furthermore, due to the periodicity and smoothness, which allows for partial integration with zero boundary terms, one has

$$\begin{aligned} ((\varphi_k)_x, (\varphi_l)_x)_{L^2} &= (A_1 \varphi_k, \varphi_l)_{L^2} = \lambda_{1k} \delta_{kl}, \\ ((\varphi_k)_{xx}, (\varphi_l)_{xx})_{L^2} &= (A_2 \varphi_k, \varphi_l)_{L^2} = \lambda_{2k} \delta_{kl}, \\ ((\varphi_k)_{xxx}, (\varphi_l)_{xxx})_{L^2} &= (A_3 \varphi_k, \varphi_l)_{L^2} = \lambda_{3k} \delta_{kl}, \end{aligned}$$

hence the basis functions $\{\varphi_k\}_k$ are orthogonal in $\dot{H}_{per}^j(\Omega)$, $j = 1, 2, 3$ (and analogously for higher orders) and form a basis for these spaces on bounded domains.

Now the here already used spaces are introduced more clearly and useful aspects of functional analysis are discussed.

2.3.2 Spaces involving time, dual spaces, inequalities and other useful results

Dual spaces and compact embeddings

The *dual space* of a Banach space H is the set of all linear functionals acting on H and it is denoted by $H^* = \mathcal{L}(H, \mathbb{R})$. A functional $f \in H^*$ maps from H to \mathbb{R} . Its norm is defined as before for linear operators

$$\|f\|_{H^*} = \sup_{x \in H, x \neq 0} \frac{|fx|}{\|x\|_H}.$$

A paradigm for Banach spaces and their dual are the p integrable functions L^p , here $p \in (1, \infty)$. The corresponding dual space is $(L^p)^* \simeq L^q$ (where \simeq denotes an isometry, so that the spaces can be identified with each other). The indices are conjugate, that means $1/p + 1/q = 1$. In particular for $p = q = 2$ the dual of the Hilbert space L^2 can be identified with the underlying space itself. The well-known representation theorem by Riesz generalizes this result.

Lemma 8 (Riesz representation theorem) *Let H be a Hilbert space with dual H^* . Then H^* can be canonically identified with H in the following sense: For any $u^* \in H^*$ there exists a unique element $u \in H$ such that*

$$u^*(v) = (u, v)_H \quad \forall v \in H$$

and

$$\|u^*\|_{H^*} = \|u\|_H \quad .$$

□

A sequence $(x_n)_n \subset H$ in a Hilbert space H *converges weakly* to $x \in H$ if it converges in the scalar product with any test function that is bounded in H ,

$$\exists x \in H \forall y \in H \text{ bounded} \quad (x_n, y)_H \xrightarrow{n \rightarrow \infty} (x, y)_H$$

and therefore the notation

$$x_n \rightharpoonup x$$

is used.

It will be necessary to relate certain spaces to each other. To establish weak convergence out of boundedness in appropriate spaces a lemma will be applied that works for three Banach spaces X, Y, Z , where X is compactly embedded in Y and Y is continuously embedded in Z . Before formulating the actual statement, the terminology has to be clarified.

A Banach space X is *continuously embedded* in a Banach space Y (therefore the notation $X \hookrightarrow Y$ will be used) if $X \subset Y$ and the following continuity condition is fulfilled

$$\exists C \in \mathbb{R} \forall a \in X \|a\|_Y \leq C \|a\|_X \quad .$$

To define compact embeddings, the concept of precompact sequences has to be introduced first. Let H be a Hilbert space. A sequence $(u_k)_k \subset H$ is *precompact* if there exists an element $u \in H$ and a converging subsequence:

$$\exists \text{subsequence } (v_l)_{l \in \mathbb{N}} \subset (u_k)_k : v_l \xrightarrow{l \rightarrow \infty} u \quad \text{in } H \quad .$$

Compact embedding are special continuous embeddings. A Banach space X is *compactly embedded* in a Banach space Y if

- X is continuously embedded in Y , $X \hookrightarrow Y$,
- $(u_n)_{n \in \mathbb{N}} \subset X$ bounded \Rightarrow the sequence is precompact in Y .

For this relation it will be written $X \hookleftrightarrow Y$.

Periodic spaces

The Sobolev spaces $W^{m,p}$ (or $H^m = W^{m,2}$), the spaces of p -integrable functions, which have weak derivatives to order m that are also integrable in L^p , are standard constructs that are taught in any functional analysis course, so they will not be introduced in detail. However, here the Hilbert spaces H^m will be considered with additional constraints. Let $\Omega = [0, L]^n \subset \mathbb{R}^n$ be the domain of interest. Then the space of infinitely differentiable, periodic functions $C_{per}^\infty(\Omega)$ is just $C^\infty(\Omega)$ with the restriction that the functions $f \in C_{per}^\infty(\Omega)$ have the property $f(x + Le_j) = f(x)$, $j = 1, \dots, n$. The completion of this space with respect to the H^k norm yields the periodic Sobolev spaces $H_{per}^k(\Omega)$.

For any $u \in C_{per}^\infty(\Omega)$ the Fourier series

$$u(x) = \sum_{k \in \mathbb{Z}^n} a_k e^{2\pi i k x / L}, \quad \bar{a}_k = a_{-k}, \quad x \in \Omega \quad (2.26)$$

is uniformly convergent and any $v \in H_{per}^m(\Omega)$ can be approximated by such functions in the corresponding Sobolev norm. The bar on the coefficients denotes the complex conjugate value. The derivatives are easy to obtain by differentiating the exponential, giving the following result.

Lemma 9 *The norm*

$$\|u\|_{H_f^m(\Omega)} = \left(\sum_{k \in \mathbb{Z}^n} (1 + |k|^{2m}) |a_k|^2 \right)^{1/2}$$

and the standard norm

$$\|u\|_{H_{per}^m(\Omega)} = \|u\|_{H^m(\Omega)}$$

are equivalent. □

The definition states that $\|u\|_{H_f^m(\Omega)} < \infty$ for $\sum_{k \in \mathbb{Z}^n} (1 + |k|^{2m}) |a_k|^2 < \infty$. This holds if

$$\Psi_m(u) = \sum_{k \in \mathbb{Z}^n} |k|^{2m} |a_k|^2 < \infty, \quad ,$$

so that overall one can define the periodic Sobolev spaces as

$$H_{per}^m(\Omega) = \{u = \sum_{k \in \mathbb{Z}^n} a_k e^{2\pi i k x / L} : \bar{a}_k = a_{-k}, \sum_{k \in \mathbb{Z}^n} |k|^{2m} |a_k|^2 < \infty\}.$$

However, Ψ_m is not a norm since the positive definiteness property is not given — it is a semi-norm. It can become a norm for a slightly adjusted space.

Lemma 10 *The expression*

$$\|u\|_{\dot{H}_{per}^m(\Omega)} = \sqrt{\Psi(u)}$$

is a norm for the subspace

$$\dot{H}_{per}^m(\Omega) = \{u \in H_{per}^m(\Omega) : \int_{\Omega} u \, dV = 0\}$$

and then it is equivalent to the H^m norm. \square

The \dot{H}_{per}^m inner product is $(u, v)_{\dot{H}_{per}^m} = (D^m u, D^m v)_{L^2} = \sum_{k \in \mathbb{Z}^m} |k|^{2m} a_k b_k$, when u as in (2.26) and

$$v(x) = \sum_{k \in \mathbb{Z}^n} b_k e^{2\pi i k x / L}, \quad \bar{b}_k = b_{-k}, \quad x \in \Omega \quad .$$

Banach-valued vector spaces

Solutions of time-dependent PDEs can be viewed as trajectories in infinite dimensional phase spaces

$$u : [0, T] \rightarrow X, \quad u = u(t) \quad ,$$

where X is a Banach space, typically L^p or H^k . This approach motivates to define Banach space valued function spaces

$$L^p(0, T; X)$$

that are Banach spaces themselves. These contain the functions whose X -norm is p -integrable,

$$\|u\|_{L^p(0, T; X)} = \left(\int_0^T \|u\|_X^p dt \right)^{1/p} < \infty \quad .$$

For $X = L^p(\Omega)$ the spaces simplify to

$$L^p(0, T; L^p(\Omega)) = L^p([0, T] \times \Omega) \quad .$$

Another common notation is $C^0([0, T], X)$, which can be used when the functions change continuously with time. In particular it is used when applying the next result.

Lemma 11 *Let H and \tilde{H} be Hilbert spaces with $H \hookrightarrow \tilde{H} \hookrightarrow H^*$ and let*

$$u \in L^2(0, T; H), \quad u_t \in L^2(0, T; H^*) \quad ,$$

then

$$u \in C^0([0, T], \tilde{H}) \quad .$$

\square

The next lemma shows that bounded sequences have convergent subsequences in certain cases (similarly as in finite-dimensional spaces given with the theorem by Bolzano-Weierstrass).

Lemma 12 (*Reflexive weak compactness*) *Let $(u_n)_{n \in \mathbb{N}}$ be a bounded sequence in the reflexive Banach space X . Then there exists a subsequence that converges weakly in X .* \square

Here reflexive means that H is isometrically isomorph to H^{**} , the dual of the dual space. For Hilbert spaces this is always the case. Also the Lebesgue spaces $L^p, p \in (1, \infty)$ are reflexive, with dual space L^q , where q is conjugate to p , so that $1/p + 1/q = 1$. Although L^1 has the dual L^∞ , these spaces are not reflexive. The properties hold analogously for the restricted spaces $\dot{L}^p(\Omega) = \{f \in L^p(\Omega) : \int f dV = 0\}$. It is useful to mention that the dual space of a time dependent space is $L^p(0, T; X)^* = L^q(0, T; X^*)$ and that reflexivity is carried over generically from X .

This result shows that once boundedness of a sequence in a Hilbert space or in one of the L^p spaces is proved, the extraction of a weakly convergent subsequence is possible. However, often strong convergence is needed. The next two lemmata are very useful to extract subsequences of weakly convergent sequences that converge strongly. Together with the preceding result they are a foundation for most existence proofs based on Galerkin approximations in periodic spaces.

Lemma 13 *For $\Omega \subset \mathbb{R}^n$ with a bounded C^1 domain, and in particular on intervals $\Omega = [a, b] \subset \mathbb{R}$, for $k \in \mathbb{N}$ the following embeddings are valid*

$$\begin{aligned} \dot{H}_{per}^{k+1}(\Omega) &\hookrightarrow \dot{H}_{per}^k(\Omega) \quad , \\ \dot{H}_{per}^k(\Omega) &\hookrightarrow \dot{L}^2(\Omega) \quad , \\ \dot{L}^2(\Omega) &\hookrightarrow H^{-k}(\Omega) \quad . \end{aligned}$$

\square

On intervals $\Omega = [0, L]$ one even has the compact embedding $\dot{H}_{per}^{k+1}(\Omega) \hookrightarrow \dot{H}_{per}^k(\Omega)$.

The properties of these Sobolev spaces will be used in the following lemma (Aubin-Lions theorem).

Lemma 14 *Let X, Y, Z be Banach spaces with $X \hookrightarrow Y \hookrightarrow Z$ and let X, Y be reflexive. One has for all $p \in (0, \infty)$ and conjugate index q that the embedding of*

$$L^p(0, T; X) \cap L^q(0, T; Z)$$

into

$$L^p(0, T; Y)$$

is compact.

\square

Inequalities and other results

Certain inequalities are used over and over again in existence theory. The most important ones are repeated here, beginning with a Poincaré inequality that holds for periodic spaces.

Lemma 15 For $u \in \dot{H}_{per}^1(\Omega)$ one has

$$\|u\|_{L^2(\Omega)} \leq C \|Du\|_{L^2(\Omega)}, \quad C = L/(2\pi) \quad . \quad (2.27)$$

□

For simple intervals, a function in H^k is already smooth to order $k - 1$. This result is part of the Poincaré embedding theorems.

Lemma 16 Let Ω be an interval in \mathbb{R} and suppose that $u \in H^k(\Omega)$. Then if $k \geq j + 1$ then $u \in C^j(\bar{\Omega})$ and there exists a constant C such that

$$\|u\|_{C^j(\bar{\Omega})} \leq C \|u\|_{H^k(\Omega)}$$

□

To establish useful estimates usually a lot of technical calculations have to be carried out. Several inequalities are applied again and again to derive the desired results. The most common ones are *Young's*, *Hölder's*, *Cauchy's* and *Minkowski's* inequalities.

Let $p > 1$ and $q > 1$ be a conjugate pair ($1/p + 1/q = 1$), then *Young's inequality* can be written as

$$ab \leq \frac{a^p}{p} + \frac{a^q}{q}, \quad \forall a, b \in \mathbb{R}_{\geq 0} \quad .$$

It can be used to prove *Hölder's inequality*

$$\|fg\|_{L^1} \leq \|f\|_{L^p} \|g\|_{L^q}, \quad \forall f \in L^p, g \in L^q \quad .$$

The special case which will be used here frequently is the *Cauchy inequality*, that is Hölder with $p = q = 2$, giving

$$\|fg\|_{L^1} \leq \|f\| \|g\|, \quad \forall f, g \in L^2 \quad .$$

In the following $\|\cdot\|$ denotes the 2-norm $\|\cdot\|_{L^2(\Omega)}$.

Combining the Cauchy inequality with Young's inequality and by introducing an artificial epsilon, another useful inequality becomes

$$\|fg\|_{L^1} \leq \frac{\epsilon}{2} \|a\|^2 + \frac{1}{2\epsilon} \|b\|^2 \quad . \quad (2.28)$$

Analogously Young's inequality and the Hölder inequality can be used to derive the Minkowski inequality (this is the generalized triangle inequality). Since it will not be applied in this work, it is not stated here.

A very useful differential inequality is the *Gronwall inequality*.

Lemma 17 If an inequality of the form

$$\frac{d}{dt_+} f(t) \leq g(t)f(t) + h(t)$$

is given (d/dt_+ is the right-hand derivative), then

$$f(t) \leq f(0)e^{G(t)} + \int_0^t e^{G(t)-G(s)} h(s) ds, \quad t \in [0, T] \quad ,$$

with

$$G(t) = \int_0^t g(r) dr \quad .$$

□

The special case with constant coefficients

$$\frac{d}{dt_+} f(t) \leq g f(t) + h \quad . \quad (2.29)$$

yields

$$f(t) \leq (f(0) + \frac{h}{g})e^{gt} - \frac{h}{g} \quad .$$

Now many useful tools from functional analysis are at hand, however, some more basic theory is necessary. The section is finished off with additional standard results from analysis. The first is an existence result for ODEs:

Lemma 18 *For continuous right hand side $f : \mathbb{R}^n \rightarrow \mathbb{R}^n, x \mapsto f(x)$ the ODE*

$$\dot{x} = f(x), \quad x(0) = u_0$$

has at least one solution on $[0, T]$ for some $T > 0$.

□

The next statement is often applied in existence proofs when nonlinearities come into play. It is a weak version of the dominated convergence theorem:

Lemma 19 *Let $\Omega \subset \mathbb{R}^n$ open, bounded and let $(f_n)_n \subset L^p(\Omega)$ with $\|f_n\|_{L^p(\Omega)} \leq C$ be a sequence of functions that are pointwise converging a.e. to a function $f \in L^p(\Omega)$. Then it also converges weakly, $f_n \rightharpoonup f$ in $L^p(\Omega)$.*

□

To show the pointwise convergence used in the above lemma, the next result is useful.

Lemma 20 *For a sequence $(u_n)_n \subset L^2(\Omega)$ that converges in L^2 , $u_n \rightarrow u \in L^2(\Omega)$, there exists a subsequence that converges to u a.e.*

□

Now the most important theoretical results from functional analysis have been introduced. They are applied to prove existence of solutions to the HCCH equation.

2.4 Existence of solutions to the HCCH equation

Consider the HCCH equation in the form

$$\begin{aligned} u_t - \delta g(u)_x &= (u_{xx} - f(u))_{xxx} = 0, \quad x \in \mathbb{R}, \delta > 0 \\ u(x, 0) &= u_0(x), \quad x \in \mathbb{R}, \end{aligned} \quad (2.30)$$

with periodic boundary conditions on an interval $\Omega = [0, L]$ for $t \in [0, T]$ and where the nonlinearities are simple polynomials in u ,

$$g(u) = \frac{1}{2}u^2, \quad f(u) = u^3 - u.$$

Theorem 21 (Weak solutions to the HCCH equation) *Equation (2.30) on a periodic interval with initial condition $u_0 \in L^2(\Omega)$ has a weak solution for sufficiently small values of δ : For any $T > 0$ there exists a function*

$$u \in L^2(0, T; \dot{H}_{per}^3(\Omega)) \cap L^4(0, T; \dot{L}^4(\Omega)) \cap C^0([0, T], \dot{L}^2(\Omega))$$

that fulfills

$$\begin{aligned} \int_{\Omega_T} u_t \varphi \, dxdt + \delta \int_{\Omega_T} g(u) \varphi_x \, dxdt + \int_{\Omega_T} u_{xxx} \varphi_{xxx} \, dxdt - \int_{\Omega_T} f'(u) u_x \varphi_{xxx} \, dxdt &= 0, \\ \text{for all } \varphi \in L^4(0, T; \dot{H}_{per}^3(\Omega)) \end{aligned} \quad (2.31)$$

Proof Consider the Galerkin approximation

$$u^N = \sum_{k=1}^N c_k \varphi_k, \quad (2.32)$$

where u^N is expanded in terms of the eigenfunctions of the negative Laplacian with periodic boundary conditions $\{\varphi_j\}_j$. These functions form an orthonormal basis for \dot{L}^2 and also serve as orthogonal basis of \dot{H}_{per}^k , $k = 1, 2, 3, \dots$. The superscript N in the approximation exclusively stands for the finite-dimensionality of the function and not a power as superscripts usually stand for. Then the following weak form is defined for u^N

$$\begin{aligned} \int_{\Omega} u_t^N \varphi \, dx + \delta \int_{\Omega} \Pi^N[g(u^N)] \varphi_x \, dx + \int_{\Omega} u_{xxx}^N \varphi_{xxx} \, dx - \int_{\Omega} \Pi^N[f'(u^N) u_x^N] \varphi_{xxx} \, dx &= 0, \\ \text{for all } \varphi \in \dot{H}_{per}^3(\Omega). \end{aligned} \quad (2.33)$$

Here the projection Π^N is defined via

$$\Pi^N \left(\sum_{k=1}^{\infty} b_k \varphi_k \right) = \sum_{k=1}^N b_k \varphi_k, \quad (2.34)$$

mapping \dot{L}^2 functions to the finite dimensional space. It has the property

$$(\Pi^N v, w)_{L^2} = (v, \Pi^N w)_{L^2} \quad \forall v, w \in \dot{L}^2.$$

This attribute together with the orthogonality of the basis functions allows to deduce simplified equations from the weak form that have to hold

$$\int_{\Omega} u_t^N \varphi_j dx + \delta \int_{\Omega} g(u^N)(\varphi_j)_x dx + \int_{\Omega} u_{xxx}^N (\varphi_j)_{xxx} dx - \int_{\Omega} f'(u^N) u_x^N (\varphi_j)_{xxx} dx = 0, \\ j = 1, \dots, N.$$

Because of the orthogonality of the chosen basis the first integral just gives the time derivatives of the coefficients. Hence the ODE

$$\dot{c}_j = -\tilde{\lambda}_j c_j + \delta(g(u^N)_x, \varphi_j)_{L^2} - (f'(u^N) u_x^N, (\varphi_j)_{xxx})_{L^2}, \quad j = 1, \dots, N \quad (2.35)$$

is derived, where the $\tilde{\lambda}_j$ are the positive eigenvalues of the negative tri-Laplacian. Since g, f and the basis function are in C^∞ , the right hand side is a continuous function, dependent on the other coefficients c_k . Hence by Lemma 18 a solution exists locally in time and it can be extended globally if the solutions do not blow up. To prove global existence an auxiliary equation will be used. The HCCH equation (2.30) can be written as

$$u_t - \delta u u_x + A(f(u) - u_{xx}) = 0, \quad (2.36)$$

where A is the bi-Laplacian, which is a linear, symmetric, unbounded, positive operator acting on \dot{H}_{per}^4 . Let M be its inverse operator, $M = A^{-1}$, and let the corresponding eigenvalues be denoted by $\lambda_1, \bar{\lambda}_1$ for A and M , respectively, when they are ordered as in the Hilbert-Schmidt Theorem 6.

Applying the compact, linear operator M to (2.36) yields

$$M u_t - \delta M(u u_x) + f(u) - u_{xx} = 0. \quad (2.37)$$

The corresponding weak form for the Galerkin approximation writes

$$\int_{\Omega} M^{1/2}[u_t^N] M^{1/2}[\varphi] dx - \delta \int_{\Omega} M^{1/2}[\Pi^N(g(u^N)_x)] M^{1/2}[\varphi] dx \\ + \int_{\Omega} u_x^N \varphi_x dx + \int_{\Omega} f(u^N) \Pi^N(\varphi) dx = 0, \quad \varphi \in \dot{H}_{per}^1(\Omega). \quad (2.38)$$

It was used that $M^{1/2}(\Pi^N(v)) = \Pi^N(M^{1/2}v)$, which one can see when inserting the definition of the fractional operator and of the projection (2.34).

Testing with u^N yields

$$\frac{1}{2} \frac{d}{dt} \|M^{1/2} u^N\|^2 + \|u_x^N\|^2 + \int_{\Omega} (u^N)^4 dx \\ = \int_{\Omega} (u^N)^2 dx + \delta \int_{\Omega} M^{1/2}[\Pi^N(g(u^N)_x)] M^{1/2}[u^N] dx. \quad (2.39)$$

As before and as in the following $\|\cdot\|$ denotes the L^2 norm over the space domain Ω . Several estimates will have to be carried out and the appearing constants will be denoted by C . These

quantities may differ from line to line, even from estimate to estimate. If they are supposed to be fixed numbers, they will be written with some subscript, C_k for some k . The constants may depend on the domain Ω and the time T .

The terms on the right are estimated as follows

$$\begin{aligned}
\int_{\Omega} (u^N)^2 dx &\leq \frac{1}{4} \|(u^N)^2\|_{L^2}^2 + C = \frac{1}{4} \|u\|_{L^4}^4 + C \quad , \\
\delta \int_{\Omega} M^{1/2} [\Pi^N(g(u^N)_x)] M^{1/2} u^N dx &\leq \delta \|M^{1/2} [\Pi^N(g(u^N)_x)]\| \|M^{1/2} u^N\| \\
&\leq \epsilon_1 \frac{\delta \sqrt{\bar{\lambda}_1}}{8} \|u^N\|_{L^4}^4 + \frac{\delta \bar{\lambda}_1}{2\epsilon_1} \|u^N\|^2 \\
&\leq \frac{\delta(\sqrt{\bar{\lambda}_1}\epsilon_1^2 + 2\bar{\lambda}_1\epsilon_2)}{8\epsilon_1} \|u^N\|_{L^4}^4 + C \quad . \quad (2.40)
\end{aligned}$$

Here ϵ_1 and ϵ_2 are arbitrary constants and the quantity C depends on their inverse values. Furthermore it was used that for any v^N that can be expanded as in (2.32) it is

$$\begin{aligned}
\|M^{1/2} v_x^N\|^2 &= \int \sum_{k,l=1}^N \bar{\lambda}_k^{1/2} \bar{\lambda}_l^{1/2} c_k c_l (\varphi_k)_x (\varphi_l)_x dx \\
&= \sum_{k,l=1}^N \bar{\lambda}_k^{1/2} \bar{\lambda}_l^{1/2} c_k c_l \int (-\varphi_k)_{xx} \varphi_l dx \\
&= \sum_{k=1}^N \bar{\lambda}_k \lambda_k^{1/2} c_k^2 \\
&\leq \sqrt{\bar{\lambda}_1} \|v^N\|^2 \quad .
\end{aligned}$$

This holds, because the eigenvalues of the negative Laplacian are just the roots of the eigenvalues of the bi-Laplacian λ_j on the periodic spaces under consideration. Since $\Pi^N(g(u^N)_x)$ is of the form (2.32) one obtains $\|M^{1/2} [\Pi^N(g(u^N)_x)]\|^2 \leq \sqrt{\bar{\lambda}_1} \|\Pi^N(g(u^N))\|^2 \leq \sqrt{\bar{\lambda}_1} \|g(u^N)\|^2$. Now choosing $\epsilon_1 = (1 + \sqrt{2})/(2\delta\sqrt{\bar{\lambda}_1})$ (for the case without deposition, $\delta = 0$ the estimate is not needed, hence it can be assumed $\delta > 0$ here) and $\epsilon_2 = 1/(8\delta^2(\bar{\lambda}_1)^{3/2})$ guarantees that the coefficient in front of the L^4 term in (2.40) is equal to 1/4. Then after integration of (2.39) with respect to time the overall estimate becomes

$$\frac{1}{2} \|M^{1/2} u^N(T)\|^2 + \int_0^T \|u_x^N\|^2 dt + \frac{1}{2} \int_0^T \|u^N\|_{L^4}^4 dt \leq C + \frac{1}{2} \|M^{1/2} u^N(0)\|^2 \leq C \quad ,$$

so that the following bounds can be deduced

$$\begin{aligned}
M^{1/2} u^N &\text{ is uniformly bounded in } L^\infty(0, T; \dot{L}^2(\Omega)) \quad , \\
u^N &\text{ is uniformly bounded in } L^2(0, T; \dot{H}_{per}^1(\Omega)) \quad , \\
u^N &\text{ is uniformly bounded in } L^4(0, T; \dot{L}^4(\Omega)) \quad , \\
g(u^N) &\text{ is uniformly bounded in } L^2(0, T; \dot{L}^2(\Omega)) \quad .
\end{aligned}$$

The last bound follows directly from the L^4 result. The second bound implies by the Sobolev embedding theorem for one-dimensional domains a bound in $L^2(0, T; C^0(\Omega))$. A uniform in time bound will be needed in the following. It can be derived by testing (2.37) with u_t^N . It yields (with the double well $W(u) = \frac{1}{4}u^4 - \frac{1}{2}u^2$)

$$\begin{aligned} \|M^{1/2}u_t^N\|^2 + \frac{1}{2}\frac{d}{dt}\|u_x^N\|^2 + \frac{1}{2}\frac{d}{dt}\int_{\Omega} W(u^N)dx &= \delta \int_{\Omega} M^{1/2}[\Pi^N g(u^N)_x]M^{1/2}[u_t^N]dx \\ &\leq \frac{\delta^2}{2}\|M^{1/2}[\Pi^N g(u)_x]\|^2 + \frac{1}{2}\|M^{1/2}u_t^N\|^2 \\ &\leq \frac{\delta^2\sqrt{\lambda_1}}{8}\|u\|_{L^4(\Omega)}^4 + \frac{1}{2}\|M^{1/2}u_t^N\|^2 \quad . \end{aligned}$$

Subtracting the last term, multiplication by 2, integration in time and using the L^4 bound and the H^1 bound of the initial condition yields

$$\int_0^T \|M^{1/2}u_t^N\|^2 dt + \|u_x^N(T)\|^2 + \int_{\Omega} W(u^N(T))dx \leq \|u_x^N(0)\|^2 + \frac{\delta^2\sqrt{\lambda_1}}{4}\|u\|_{L^4(\Omega_T)}^4 \leq C \quad .$$

This gives the uniform bound

$$u^N \text{ is uniformly bounded in } L^\infty(0, T; \dot{H}_{per}^1(\Omega)) \quad ,$$

which in particular implies by the Sobolev embedding theorem that u^N is continuous for all times. Due to differentiability one can further deduce

$$\|f'(u^N)\|_\infty \leq C, \quad \|f''(u^N)\|_\infty \leq C, \dots \forall t \in [0, T] \quad .$$

The original weak equation (2.33) gives with the test function u^N

$$\frac{1}{2}\frac{d}{dt}\|u^N\|^2 + \|u_{xxx}^N\|^2 - \int_{\Omega} f'(u^N)u_x^N u_{xxx}^N dx = 0 \quad . \quad (2.41)$$

Here periodicity was used with

$$\int_{\Omega} u^N u_x^N u^N dx = \frac{1}{3} \int_{\Omega} ((u^N)^3)_x dx = 0 \quad ,$$

which is a property commonly used for the Navier-Stokes or the Korteweg-de-Vries equation. By using the time uniform bound $|f'(u^N)| \leq C_1$ one can further conclude

$$\begin{aligned} \frac{1}{2}\frac{d}{dt}\|u^N\|^2 + \|u_{xxx}^N\|^2 &\leq \left| \int_{\Omega} f'(u^N)u_x^N u_{xxx}^N dx \right| \\ &\leq C_1 \int_{\Omega} |u_x^N u_{xxx}^N| dx \\ &\leq C_1 \left(\frac{1}{2\epsilon} \|u_x^N\|^2 + \frac{\epsilon}{2} \|u_{xxx}^N\|^2 \right) \quad . \end{aligned}$$

Choosing $\epsilon = 1/C_1$ yields

$$\frac{d}{dt}\|u^N\|^2 + \|u_{xxx}^N\|^2 \leq C \|u_x^N\|^2 \quad .$$

Integration in time yields

$$\|u^N(T)\|^2 + \int_0^T \|u_{xxx}^N\|^2 dt \leq C \quad ,$$

so that additional results are established

$$\begin{aligned} u^N & \text{ is uniformly bounded in } L^\infty(0, T; \dot{L}^2(\Omega)) \quad , \\ u^N & \text{ is uniformly bounded in } L^2(0, T; \dot{H}_{per}^3(\Omega)) \quad , \end{aligned}$$

and one can additionally conclude that

$$f'(u^N)u_x^N \text{ is uniformly bounded in } L^2(0, T; \dot{L}^2(\Omega)) \quad .$$

The previously derived bounds yield boundedness in the dual space

$$\begin{aligned} \|u_t^N\|_{H^{-3}} &= \sup_{\varphi \in \dot{H}_{per}^3(\Omega), |\varphi|=1} \left| \int u_t^N \varphi dx \right| \\ &\leq \sup_{\varphi \in \dot{H}_{per}^3(\Omega), |\varphi|=1} \int |\delta u^N u_x^N \varphi| + |u_{xxx}^N \varphi_{xxx}| + |u_{xx}^N \varphi_{xx}| + |3(u^N)^2 u_x^N \varphi_{xxx}| dx \\ &\leq C \|u_x^N\| (\|\varphi\| + \|\varphi_{xxx}\|) + \|u_{xxx}^N\| \|\varphi_{xxx}\| + \|u_{xx}^N\| \|\varphi_{xx}\| \leq C \quad , \end{aligned}$$

hence

$$u_t^N \text{ is uniformly bounded in } L^2(0, T; H^{-3}(\Omega)) \quad .$$

This shows the existence of the Galerkin approximation in the weak sense for all times. To show existence of weak solutions, the limit $N \rightarrow \infty$ has to be analyzed. Therefore the reflexive weak compactness theorem gives the following weakly convergent subsequences (as usually not relabeled)

$$\begin{aligned} u^N &\rightharpoonup u \quad \text{in } L^2(0, T; \dot{H}_{per}^3(\Omega)) \\ u_t^N &\rightharpoonup u_t \quad \text{in } L^2(0, T; H^{-3}(\Omega)) \\ f'(u^N)u_x^N &\rightharpoonup \chi_1 \quad \text{in } L^2(0, T; \dot{L}^2(\Omega)) \\ g(u^N) &\rightharpoonup \chi_2 \quad \text{in } L^2(0, T; \dot{L}^2(\Omega)). \end{aligned}$$

The two first weak limits imply by application of the compactness theorem, lemma 14 with

$$\dot{H}_{per}^3(\Omega) \hookrightarrow \dot{L}^2(\Omega) \hookrightarrow H^{-3}(\Omega)$$

that L^2 convergence of a subsequence is established

$$u^N \rightarrow u \quad \text{in } L^2(0, T; \dot{L}^2(\Omega)) \quad .$$

Additionally one obtains by application of lemma 11 that

$$u \in C^0([0, T], \dot{L}^2(\Omega)) \quad .$$

Since Ω is a bounded interval, it further holds $\dot{H}_{per}^3(\Omega) \hookrightarrow \dot{H}_{per}^1(\Omega) \hookrightarrow H^{-3}(\Omega)$ and lemma 14 yields

$$u_x^N \rightarrow u_x \quad \text{in} \quad L^2(0, T; \dot{L}^2(\Omega)) \quad .$$

The convergence in L^2 is important when dealing with the nonlinearities.

It has to be shown that indeed also with the projections $\Pi^N f'(u^N)u_x^N$ and $\Pi^N g(u^N)$ converge weakly. Therefore consider

$$\Xi^N(\varphi) = \varphi - \Pi^N(\varphi) \quad ,$$

which converges strongly to zero in $L^2(\Omega_T)$. Then

$$\int_{\Omega_T} \Pi^N[g(u^N)]\varphi dxdt = \int_{\Omega_T} g(u^N)\varphi dxdt - \int_{\Omega_T} \Xi^N[g(u^N)]\varphi dxdt, \quad \varphi \in L^2(\Omega_T).$$

The first integral tends to zero as derived before. The second also tends to zero, since

$$\int_{\Omega_T} \Xi^N[g(u^N)]\varphi dxdt = \int_{\Omega_T} g(u^N)\Xi^N[\varphi] dxdt$$

and $\Xi^N[\varphi] \rightarrow 0$ in $L^2(\Omega_T)$. For $\Pi^N[f'(u^N)u_x^N]$ one can proceed analogously, just by replacing g with this nonlinearity. Hence it remains to show that the limits are indeed those anticipated.

The L^2 convergence of $u^N, (u^N)^2$ and u_x^N gives with Lemma 20 a subsequence for that (again without relabeling) $u^N \rightarrow u, (u^N)^2 \rightarrow u^2$ and $u_x^N \rightarrow u_x$ a.e. in Ω_T . Then by continuity $g(u^N)$ and $f'(u^N)u_x^N$ converge almost everywhere to $g(u)$ and $f'(u)u_x$. Lemma 19 with the L^2 bounds yields weak limits $g(u^N) \rightharpoonup g(u), f'(u^N)u_x^N \rightharpoonup f'(u)u_x$ that hold in L^2 , so that by uniqueness of weak limits one has $\chi_1 = f'(u)u_x$ and $\chi_2 = g(u)$, respectively.

As last step it has to be shown that indeed $u(0) = u_0$. Here again a standard trick can be applied. Therefore define a test function $\varphi \in C^1([0, T], \dot{H}_{per}^3(\Omega))$ that fulfills $\varphi(T) = 0$. This function is also in $L^2(0, T; \dot{H}_{per}^3(\Omega))$ and partial integration in time of the weak form (2.31) yields

$$\begin{aligned} - \int_{\Omega_T} u \varphi_t dxdt + \left[\int_{\Omega} u \varphi dx \right]_0^T + \delta \int_{\Omega_T} g(u) \varphi_x dxdt \\ + \int_{\Omega_T} u_{xxx} \varphi_{xxx} dxdt - \int_{\Omega_T} f'(u) u_x \varphi_{xxx} dxdt = 0 \quad . \end{aligned} \quad (2.42)$$

Analogously for the Galerkin approximation we have the equation

$$\begin{aligned} - \int_{\Omega_T} u^N \varphi_t dxdt + \left[\int_{\Omega} u^N \varphi dx \right]_0^T + \delta \int_{\Omega_T} \Pi^N(g(u^N)) \varphi_x dxdt \\ + \int_{\Omega_T} u_{xxx}^N \varphi_{xxx} dxdt - \int_{\Omega_T} \Pi^N(f'(u^N)u_x^N) \varphi_{xxx} dxdt = 0 \quad . \end{aligned} \quad (2.43)$$

The weak convergence shows that in the limes the integrals are the same. The bracket terms become $[\int_{\Omega} u^N \varphi dx]_0^T = - \int_{\Omega} u^N(0) \varphi(0) dx$ and $[\int_{\Omega} u \varphi dx]_0^T = \int_{\Omega} u_0 \varphi(0)$. Subtraction of the two weak equations and arbitrariness of $\varphi(0)$ yields $u_0 = u(0)$. \square

Currently the result is extended to higher order Sobolev spaces and also a uniqueness statement is in preparation. The whole theory on existence of solutions to the HCCH equation will appear in a single publication by Korzec and Rybka [58]. For the more general 2+1D model (2.13) a different theory is being developed. A proof of existence of weak unique solutions will also appear soon by Bodzenta et al. [7]. The ansatz is different than in the presented proof since it bases on a fix point argument instead of a Galerkin approximation.

Chapter 3

Stationary solutions and kink dynamics to the HCCH equation

Someone told me that each equation I included in the book would halve the sales.

Stephen Hawking (1942 -)

It has been proved in the last chapter that weak solutions to the HCCH equation (2.14) exist globally in time. Now their actual appearance, their form in equilibrium and their behavior on a large time scale are analyzed with help of methods from dynamical systems, matched asymptotics and numerics. New types of stationary solutions will be derived. Therefore a numerical scheme for approximately solving a corresponding ODE in a boundary value problem framework is presented and an extension of the method of matched asymptotics that retains exponentially small terms during the matching procedure is carried out. A particular equilibrium solution is considered in two inner layers and one outer region. Appropriate scaling, expanding and solving in each region together with a non-standard matching procedure allows to calculate new spatially nonmonotone solutions with hump spacings and far-field parameters, given as analytical expressions in the limit of vanishing deposition flux $\delta = 0$. The results from this part of the chapter originate from the work by Korzec et al. [57]. A vast amount of other examples for the application of the method of matched asymptotics exist. The here presented approach generalizes the work by Lange [62] to higher-order singularly perturbed nonlinear boundary-value problems, where standard application of matched asymptotics is not able to locate the position of interior layers that delimit the oscillations of the non-monotone solutions. The internal layer structure of the solutions to the boundary value problem for the related Cahn-Hilliard and viscous Cahn-Hilliard equations has been resolved by Reyna and Ward [81]. Their approach bases on a previous work by Ward [107], who used a near solvability condition for a corresponding linearized problem in his asymptotic analysis. His work was inspired by publications by O'Malley [76] and Rosenblat et al. [84], who

investigated the problem of spurious solutions to singular perturbation problems of second-order nonlinear boundary-value problems. For the related Kuramoto-Sivashinsky equation, a multiple-scales analysis of the corresponding third-order nonlinear boundary-value problem by Adams et al. [1] shows that the derivation of monotone and oscillating traveling-wave solutions involve exponentially small terms.

After the analysis of equilibrium states ripening of faceted surfaces in 2D for the HCCH equation is investigated. Simulations based on a pseudospectral method show how coarsening takes place. With the numerical method one could reproduce the rates obtained by Savina et al. [89]. However, here the attention is turned to how the coarsening is driven and when or how it stops. Kink interactions are analyzed and stationary or traveling wave solutions are found. With increasing deposition rate oscillations with higher wave numbers can be observed in the solutions. The result is very similar as for the related CCH equation. From coarsening to roughening, an analogous work as by Golovin et al. [44] could be written for the HCCH equation.

3.1 Stationary solutions to the HCCH equation

In general, PDEs involving nonlinearities are hard to solve, so it is common to simplify the equations as much as possible in a way that the reduced systems still contain the useful information. Stationary solutions to PDEs are easier to obtain than those of the underlying equation with dynamics since essentially one dimension less has to be treated in the analysis. The HCCH equation (2.14) is defined for one lateral dimension only, hence by setting $u_t = 0$ it even simplifies to an ODE that can be handled with standard tools of analysis and numerics. Having stationary solutions at hand may be adjuvant for the understanding of the evolution. Especially in case of phase-separating systems, often moving fronts can be observed that resemble stationary shapes that move with low velocity. This behavior can be used to derive sharp interface models. This has been done for example for the CCH equation by Watson et al. [109], or for droplet dynamics by Glasner and Witelski [39].

The simplest case of equation (2.14) is given with $\delta = 0$. Integrating four times and setting the integration factors to zero gives

$$u_{xx} + u - u^3 = 0 \quad . \quad (3.1)$$

This ODE is just the stationary version of the Allen-Cahn equation (2.15) or of the Cahn-Hilliard equation (2.17) (also with zero integration factors). It is known for a long time that the tangentials $u_0 = \tanh(x/\sqrt{2})$ can solve the equation and yield the transition from one state to another. Since u is the slope of the shape in case of the HCCH equation, the stationary profiles for this problem are given as

$$h_0(x) = \pm\sqrt{2} \ln \cosh(x/\sqrt{2}) \quad ,$$

hence simple kinks or antikinks (triangular shapes). These functions will serve as leading order solutions when using asymptotic expansions for the determination of special equilibrium shapes.

It is inevitable to discuss the case with deposition, $\delta > 0$. The parameter is assumed to be small, say $0 < \delta \ll 1$, which is a realistic assumption for epitaxial processes. From the last chapter it is known that in this case solutions exist. Integration of the HCCH equation (2.14) yields

$$\frac{\delta}{2}(u^2 - A) + (u_{xx} + u - u^3)_{xxx} = 0 \quad , \quad (3.2)$$

under the assumption that u tends to a constant value in the far field

$$\lim_{x \pm \infty} u(x) = \mp \sqrt{A} \quad .$$

The constant equilibrium points are $u^\pm = \pm \sqrt{A}$, since the convective term vanishes and also all derivatives are zero. The character of the stationary points can be read off from the characteristic polynomial

$$\mathcal{P}^\pm(\lambda) = \mathcal{P}(u^\pm) = \lambda^5 + (1 \mp 3A)\lambda^3 \pm \delta\sqrt{A} = 0 \quad . \quad (3.3)$$

It can be obtained by either transforming (3.2) to a first order system, linearizing and computing the characteristic polynomial of the Jacobian in the equilibrium points, or by linearizing directly around the equilibrium point with the ansatz $u = \pm \sqrt{A} + \delta e^{\lambda x}$.

The signs of the Eigenvalues yield information about the orbits, positive signs imply exponential growth of the special solution to the linearized problem while negative signs indicate exponential decay in directions of the corresponding eigenvectors. Since the linearization gives qualitatively the same results near the equilibrium points, these information can be used for the computation of stable and unstable manifolds. In Appendix B a short introduction to dynamical systems contains most of the important concepts used here. Detailed information can be found in the books by Guckenheimer and Holmes [46] or Hale and Kocak [47]. In any way saddle points offer a rich behavior worth studying and it will be shown that the equilibrium points u^\pm are such saddles.

Analytic solutions for the roots of fifth order polynomial are not offered by nature as this is the case for its lower order companions. However, they can be approximated by making use of usual asymptotic analysis tools [48, 52]. To expand solutions in powers of the small parameter δ , it is necessary to find out a suitable power $\nu \in \mathbb{Q}_+$ for the expansion series

$$\lambda = \sum_{j=0}^{\infty} \lambda_j \delta^{j\nu} \quad .$$

Independently of the choice of ν , the $\mathcal{O}(1)$ terms ($j = 0$) gives the five roots

$$\lambda_0^{(k)} = 0, \quad k = 1, 2, 3 \quad \text{and} \quad \lambda_0^{(k)} = \pm \sqrt{3A \mp 1}, \quad k = 4, 5 \quad .$$

Insertion of the next order approximation $\lambda = \lambda_0 + \lambda_1 \delta^\nu$ into equation (3.3) gives the following orders that all have to be zero if λ is indeed a root.

$$\begin{aligned} \mathcal{O}(\delta) : & \quad \pm \sqrt{A} & \mathcal{O}(\delta^{3\nu}) : & \quad (10\lambda_0^2 + (1 \mp 3A))\lambda_1^3 \\ \mathcal{O}(\delta^\nu) : & \quad (5\lambda_0^4 + (1 \mp 3A)3\lambda_0^2)\lambda_1 & \mathcal{O}(\delta^{4\nu}) : & \quad 5\lambda_0\lambda_1^4 \\ \mathcal{O}(\delta^{2\nu}) : & \quad (10\lambda_0^3 + (1 \mp 3A)3\lambda_0)\lambda_1^2 & \mathcal{O}(\delta^{5\nu}) : & \quad \lambda_1^5 \quad . \end{aligned}$$

Dependent on the fraction ν the $\delta\sqrt{A}$ term is balanced with one of the other orders. For the standard choice $\nu = 1$ it would be the $\mathcal{O}(\delta^\nu)$ terms and the solution for λ_1 for the nonzero roots of λ_0 would be $\lambda_1^{(k)} = \mp\sqrt{A}/(2(3A \mp 1)^2)$, $k = 4, 5$. Then for the other roots no solutions in leading order could be obtained which indicates a wrong scaling of the exponents. Hence an increase of the denominator $q \in \mathbb{N}$ in the small parameter $\nu = 1/q$ can be pursued. For $\nu = \frac{1}{2}$ the same situation with the $\mathcal{O}(\delta^{2\nu})$ terms balancing the $\mathcal{O}(\delta)$ term would appear. Expanding in the powers of third roots improves the situation, because for $\nu = \frac{1}{3}$ the fourth equation balances the first and

$$(10\lambda_0^2 + (1 \mp 3A))\lambda_1^3 \pm \sqrt{A} = 0 \Leftrightarrow \lambda_1^3 = \frac{\mp\sqrt{A}}{10\lambda_0^2 + (1 \mp 3A)} \quad (3.4)$$

is well defined for all λ_0^k , $k = 1, \dots, 5$ (the equivalence holds as long as $A \neq \pm 1/3$). Thus using lower orders of the expansion

$$\lambda = \sum_{j=0}^{\infty} \lambda_j \delta^{j/3} \quad ,$$

and analyzing further equation (3.4) in terms of the signs of the coefficients gives the leading order signs of the roots. These carry along enough information to see whether the eigenvalues correspond to stable or to unstable directions.

Case 1: $u = u^+ = \sqrt{A}$ and $3A > 1$

The five asymptotics are

$$\lambda^{(1)} = \delta^{\frac{1}{3}} \left(\frac{\sqrt{A}}{(3A-1)} \right)^{\frac{1}{3}} + \mathcal{O}(\delta^{\frac{2}{3}}) \quad (3.5)$$

$$\lambda^{(2,3)} = \delta^{\frac{1}{3}} \left(\frac{\sqrt{A}}{(3A-1)} \right)^{\frac{1}{3}} \left(\frac{-1 \pm i\sqrt{3}}{2} \right) + \mathcal{O}(\delta^{\frac{2}{3}}) \quad (3.6)$$

and

$$\lambda^{(4,5)} = \pm\sqrt{3A-1} + \mathcal{O}(\delta^{\frac{1}{3}}) \quad . \quad (3.7)$$

Hence the first and fourth root have positive real part, while the others have a switched sign.

Case 2: $u = u^- = -\sqrt{A}$ and $3A > 1$: The signs of the real parts of the asymptotics in (3.5) and (3.6) are simply switched due to the different sign in \sqrt{A} and the leading orders of $\lambda^{(k)}$, $k = 4, 5$ are unchanged from (3.7). Hence three real parts are positive and two are negative.

Case 3 ($u = u^+ = \sqrt{A}$ and $3A < 1$) and case 4 ($u = u^- = -\sqrt{A}$ and $3A < 1$) are ignored, since

the leading parts of $\lambda^{(k)}$, $k = 4, 5$ are imaginary in these cases. These solutions oscillate near $x = 0$ and hence do not describe appropriate surface shapes.

Savina et al. [89] use the method of matched asymptotics to obtain the approximate solution as simple stationary state for a small deposition rate δ . The calculations will be repeated in Section 3.1.2 and extended to other steady solutions that were found. Before using a method of matched asymptotics for the analytical determination of particular steady states and some of their properties, brunches of stationary solutions are computed numerically with help of a boundary value formulation.

3.1.1 A phase space method

It is useful to rescale the HCCH equation such that the equilibrium points become ± 1 . Then they do not vary with changed parameter A which makes the implementation of a boundary value problem formulation much easier. By setting $u = \sqrt{A}\tilde{u}$ the problem writes

$$\delta\sqrt{A}(1 - \tilde{u}^2) - 2(\tilde{u}_{xx} + \tilde{u} - A\tilde{u}^3)_{xxx} = 0, \quad \lim_{x \rightarrow \pm\infty} \tilde{u} = \mp 1 \quad . \quad (3.8)$$

Reduction to a first order system $U' = F(U)$ gives a system function $F : \mathbb{R}^5 \rightarrow \mathbb{R}^5$ with

$$\begin{aligned} F_i(U) &= U_{i+1}, \quad i = 1, 2, 3, 4 \quad , \\ F_5(U) &= 6A(U_2)^3 + 18AU_1U_2U_3 + (3A(U_1)^2 - 1)U_4 + \delta\sqrt{A}(1 - (U_1)^2)/2 \quad . \end{aligned}$$

The steady states are $U^\pm = \pm e_1^T$, where e_1 is the first Cartesian basis vector in \mathbb{R}^5 . At these points the characteristic polynomials remain unchanged (3.3). In the following the connections between the two equilibria U^+ and U^- , the *heteroclinic connections*, are sought. The discussion on the roots of the polynomial (3.3) shows for small δ that the dimensions of the unstable manifolds in the upper steady state $W^u(U^+)$ and the stable manifold of the lower equilibrium point $W^s(U^-)$ both equal two. Finding heteroclinic solutions on these manifolds is a codimension two event if no additional properties of the solutions are taken into account. However, it may be reduced, because the HCCH equation is reversible with the linear transformation

$$R : \mathbb{R}^5 \rightarrow \mathbb{R}^5, \quad R(U) = ((-1)^j U_j)_{j=1,\dots,5} \quad (3.9)$$

that fulfills

$$R^2 = Id \quad \text{and} \quad RF(U) = -F(RU) \quad .$$

It represents the reversibility in the phase space and it is an involution (a reflection). Its set of fixed points is the symmetric section of the reversibility. This means odd components vanish, $U_i = 0$ for i odd. A solution that crosses such a point is necessarily symmetric under R , and for each point U on the connection there exists a corresponding transformed point RU somewhere on the branch. Odd solutions cross a point in the symmetric section, hence the distance function

$$d_A(U) = \min_x \sqrt{\sum_{i \text{ odd}} U_i(x)^2} \quad , \quad (3.10)$$

becomes zero at the symmetry point. The codimension of a reversible system reduces by one so that here finding the heteroclinic connections becomes a codimension one problem. However, since there are two parameters A and δ , one may be tempted to expect solution branches in the (A, δ) parameter plane and indeed, as for the CCH equation such branches were found.

The phase space is sketched in Figure 3.1, indicating the linearizations of the intersecting manifolds in the equilibrium points. A boundary value formulation has been used to numerically solve the problem.

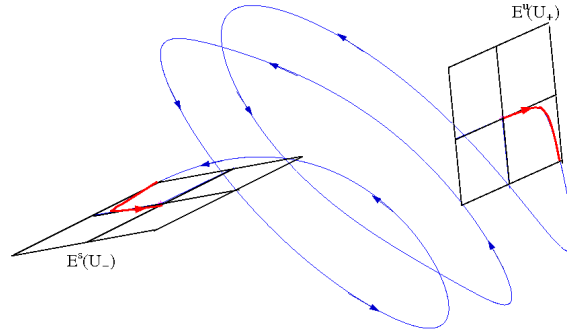


Figure 3.1: For the HCCH one searches for heteroclinic orbits between the equilibrium points in a 5D phase space that is indicated here in 3D. The two-dimensional manifolds $W^u(U^+)$ and $W^s(U^-)$ are suggested by the two planes in the picture.

Boundary value problem formulation

There exist several possibilities to set up equations for finding heteroclinic connections in a boundary value problem framework. Here the translation invariance gives rise to infinitely many solutions. Several suitable phase conditions that pick one solution due to phase shifts are possible [35, 6]. However, in the discussed case a simpler approach can be pursued by halving the domain length and using symmetry of the solutions. Then phase conditions become redundant, because the phase is already fixed.

Equation (3.8) contains two parameters, A , δ , and in addition it has to be truncated to a finite domain length L . Rescaling the domain to $[0, 1]$ yields the ODE

$$\begin{aligned} U'_i &= LU_{i+1}, \quad i = 1, 2, 3, 4 \quad , \\ U'_5 &= L \left(6A(U_2)^3 + 18AU_1U_2U_3 + (3A(U_1)^2 - 1)U_4 + \delta\sqrt{A}\frac{(1 - (U_1)^2)}{2} \right) \quad , \\ A' &= 0 \quad . \end{aligned}$$

In the implementation the problem is solved and the computations are continued after extrapolating to an approximate value the free parameter A for a nearby chosen and fixed δ . This is a system of six equations, one for the parameter and five given by the original ODE, which have to

be supplemented by the same number of boundary conditions. These are given by the necessity that on the left domain end the equilibrium has to be met

$$U_1(0) = 1, \quad U_2(0)^2 + U_3(0)^2 = 0, \quad U_4(0)^2 + U_5(0)^2 = 0$$

while the condition on the right interval end gives due to the reversibility

$$U_1(1) = U_3(1) = U_5(1) = 0 \quad .$$

The boundary value solvers used are based on mono-implicit Runge-Kutta formulae [53, 92]. Final shapes are obtained by reflecting the solution and its derivatives around zero and changing the signs of the first, third and fifth component. Examples of branches of different solutions are shown in Figure 3.2. With the above boundary value formulation it is possible to compute new

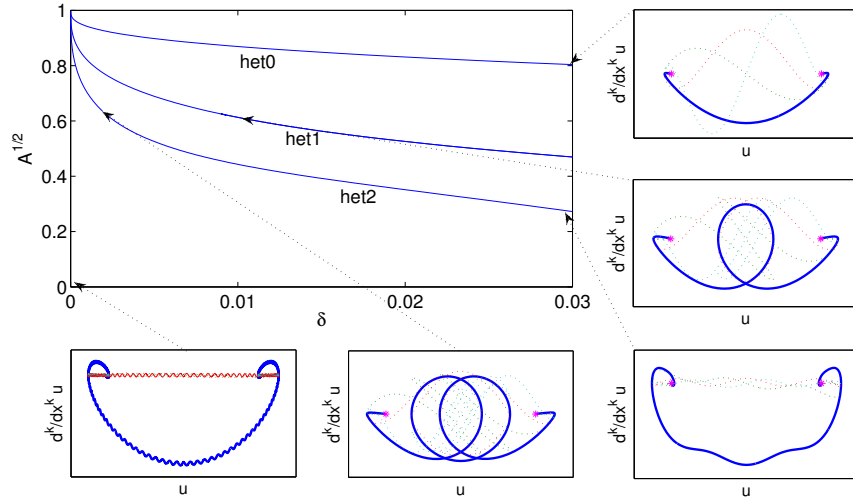


Figure 3.2: (\sqrt{A}, δ) -plane with curves for the first three heteroclinic connection branches for the HCCH equation. Below and to the right five phase space diagrams are shown (tuples $(U_1, U_2), (U_1, U_3), \dots$) for selected solutions pointed out with arrows marking the corresponding parameters. The first pair (U_1, U_2) is plotted as bold solid curve, while the other connections are visualized with dotted lines.

stationary solutions to the HCCH equation. Heteroclinic orbits in a two- or three-dimensional phase space can be visualized easily and connections indeed indicate that solutions were found. For dimension four or higher the situation becomes more complicated. Plotting the solution in a three dimensional phase space can show a connection that not necessarily implies that also the fourth (or higher) derivative is correctly connected to be a solution. However, one can plot the 2D phase spaces $(U_1, U_k), k = 2, 3, 4, 5$ and demand connections between the equilibrium tuples $(\pm\sqrt{A}, 0)$ as a necessary condition for heteroclinic orbits in the higher order space. Several such projections onto 2D are shown in Figure 3.2, where also a very rapidly oscillating heteroclinic curve in the bottom left is plotted which was found by a shooting approach with a minimization

procedure that used the two parameters and an angle as free parameters and the distance function (3.10) as objective function. It indicates that as shown for the CCH equation one can in fact find many more het_k branches than those presented for $k = 0, 1, 2$, all emerging from $(A, \delta) = (1, 0)$, which corresponds to the CH equation.

In Figure 3.3 the change in appearance of solutions on the het_2 branch is shown as δ is increased. The shape varies from a solution with two pronounced humps to a monotone one, similar to the het_0 solution, although associated with different, smaller, values of A . This is crucial if one wants to compute solutions for bigger δ with a boundary value solver. It easily happens that the solver switches between solution branches. However, this can be prevented by starting continuation in a parameter regime where the high-slope parts of the solutions are non-monotone, and continuing with small steps towards bigger values of δ . A characteristic of

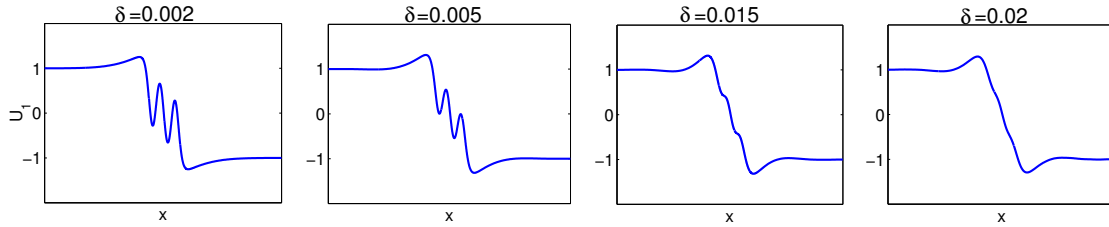


Figure 3.3: Structural change of the scaled het_2 solution as δ is increased.

the HCCH solutions is the overshoot from the equilibrium value before the solutions go down. This height decreases with decreasing value of δ . For the CCH equation the shapes are more similar at these regions to hyperbolic tangent functions.

3.1.2 Exponential matched asymptotics

Consider a one-hump solution as sketched in Figure (3.4), which will be denoted as the het_1 solution from now on. Two internal layers are given in the regions r_l near $\kappa_l < 0$ and r_0 around κ_0 , and an outer layer is marked by R_l . The symmetry point is κ_0 and as in the numerics section before, it is assumed that $\kappa_0 = 0$, then $\kappa_l = -\kappa_r$ and layers right of r_0 may be ignored. Solution in the inner layers will be derived and matched to the outer solution.

For monotone antikink solutions to the HCCH equation it has been demonstrated by Savina et al. [89] that it is necessary to match terms up to order δ in order to obtain the correction A_1 , given the asymptotic expansion of A

$$A = 1 + \sum_{k=1}^{\infty} \delta^{k/3} A_k. \quad (3.12)$$

The motivation for the one third power law expansion in δ stems from the eigenvalue analysis presented in Section 3.1. Here, for the non-monotone antikinks the *inner* and *outer* solutions in

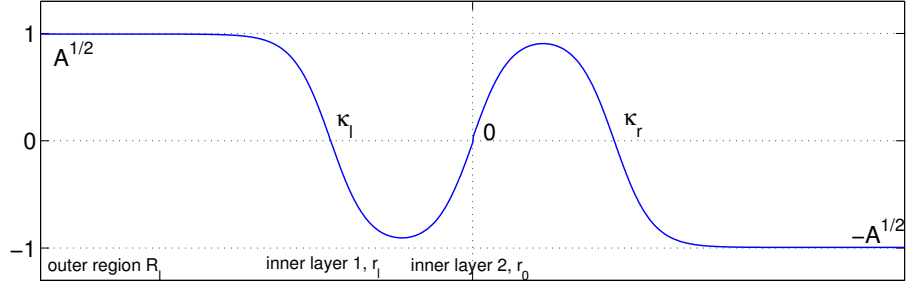


Figure 3.4: Sketch of a symmetric one-hump, or het_1 solution to the HCCH equation showing the general setup with the three regions R_l, r_l, r_0 under consideration for the matching procedure.

r_l and R_l , respectively, have to be matched. Then also an exponential matching of the *inner* layers in r_l and r_0 is necessary. This has to be carried through iteratively up to three orders of magnitude in order to obtain the correction A_1 and the expression for the width of the humps. First, the scalings for the three regions are described, before solving the individual problems and starting with the matching procedure. The outer solution has been derived by Savina et al. [89], the inner solutions have been obtained by Korzec et al. [57].

The inner solutions will be denoted by u_l and u_0 in r_l and r_0 , respectively. These solutions live in the variables x_l and x_0 , while the outer solution U in R_l obtains the variable ξ .

The inner layer r_l

The analysis of the internal layers is performed in the inner scaling and the variable near κ_l is

$$x_l = (x - \bar{\kappa}_l)/\sqrt{2} \quad , \quad (3.13)$$

where κ_l is expanded in terms of the small parameter δ

$$\kappa_l = \bar{\kappa}_l + \sqrt{2} \sum_{k=1}^{\infty} \delta^{k/3} \kappa_{lk} \quad .$$

Then the stationary form of (2.14) is

$$2^{3/2} \delta (u_l^2 - A) + [u_l'' - 2f(u_l)]''' = 0 \quad , \quad (3.14)$$

where the prime ($'$) denotes partial differentiation with respect to the variable of the actual region, here x_l , and f is a double-well derivative,

$$f(u) = u^3 - u \quad .$$

For the boundary conditions again κ_l is placed near the point where u_l crosses zero, i.e.

$$u_l \left(\frac{\kappa_l - \bar{\kappa}_l}{\sqrt{2}} \right) = 0 \quad . \quad (3.15)$$

The condition towards $-\infty$ needs to be matched to the outer solution in the region R_l (see Figure 3.4).

The inner layer r_0

In the region near the symmetry point $\kappa_0 = 0$, the variable $x_0 = x/\sqrt{2}$ is used, giving

$$2^{3/2}\delta(u_0^2 - A) + [u_0'' - 2f(u_0)]''' = 0 \quad . \quad (3.16)$$

The reversibility at zero gives the three conditions

$$u_0(0) = 0, \quad u_0''(0) = 0 \quad \text{and} \quad u_0'''(0) = 0, \quad (3.17)$$

plus additional conditions from the exponential matching to the internal layer at r_l as $x_0 \rightarrow -\infty$.

The outer layer R_l

For the *outer* region where x_l becomes very large, the ansatz

$$\xi = \delta^{1/3} x_l \quad \text{and} \quad U(\xi; \delta) = u_l(x_l; \delta) \quad (3.18)$$

is used to obtain the *outer* problem

$$2^{3/2}(U^2 - A^2) + [\delta^{2/3} U_{\xi\xi} - 2f(U)]_{\xi\xi\xi} = 0 \quad (3.19)$$

with the far field condition

$$\lim_{\xi \rightarrow -\infty} U(\xi) = \sqrt{A}. \quad (3.20)$$

Expansions in the different regions

It is assumed that the solutions to these three problems for U , u_l and u_0 can be represented by asymptotic expansions

$$u_\alpha(x_\alpha) = u_{\alpha 0}(x_\alpha) + \sum_{k=1}^{\infty} \delta^{k/3} u_{\alpha k}(x_\alpha), \quad \text{where} \quad \alpha = 0, l \quad (3.21)$$

valid in r_l and r_0 , respectively, and

$$U(\xi) = U_0(\xi) + \sum_{k=1}^{\infty} \delta^{k/3} U_k(\xi), \quad (3.22)$$

valid in the outer region R_l . In the following the outer problem is solved. It has already been derived by Savina et al. [89]. For most of the calculations the assistance of Maple was very helpful.

Solving the outer problem in R_l

To solve the outer problem, the expansions for U , (3.22), for the powers U^2, U^3

$$\begin{aligned} U^2 &= U_0^2 + \delta^{1/3} 2U_0 U_1 + \delta^{2/3} [2U_0 U_2 + U_1^2] + \delta [2U_0 U_3 + 2U_1 U_2] + \mathcal{O}(\delta^{4/3}), \\ U^3 &= U_0^3 + \delta^{1/3} 3U_0^2 U_1 + \delta^{2/3} [U_0(2U_0 U_2 + U_1^2) + 2U_0 U_1^2 + U_0^2 U_2] \\ &\quad + \delta [2U_0 U_1 U_2 + U_0(2U_0 U_3 + 2U_1 U_2) + U_0^2 U_3 + U_1(2U_0 U_2 + U_1^2)] + \mathcal{O}(\delta^{4/3}), \end{aligned} \quad (3.23)$$

and for the far-field parameter (3.12) are used in equation (3.19) and the condition (3.20). In this way different problems for consecutive orders can be defined. These are solved, leaving integration constants that will have to be determined in a matching procedure with the solutions to the left inner layer.

The leading order problem becomes $\mathcal{O}(1)$:

$$\begin{aligned}\sqrt{2}(U_0^2 - 1) + (U_0 - U_0^3)_{\xi\xi\xi} &= 0 \quad , \\ \lim_{\xi \rightarrow -\infty} U_0(\xi) &= 1 \quad .\end{aligned}$$

It has the trivial solution

$$U_0 = 1 \quad . \quad (3.24)$$

$\mathcal{O}(\delta^{1/3})$: To this order the problem becomes

$$\begin{aligned}\frac{1}{\sqrt{2}}A_1 + (U_1)_{\xi\xi\xi} - \sqrt{2}U_1 &= 0 \quad , \\ \lim_{\xi \rightarrow -\infty} U_1(\xi) &= \frac{A_1}{2} \quad .\end{aligned} \quad (3.25)$$

The general solution consists of a constant, a $e^{2^{1/6}\xi}$ term and terms that are unbounded for $\xi \rightarrow \infty$. Hence the boundary condition leaves only the integration constant c_1 and

$$U_1 = c_1 e^{2^{1/6}\xi} + \frac{A_1}{2} \quad . \quad (3.26)$$

$\mathcal{O}(\delta^{2/3})$:

To this order the equation and far-field condition become

$$\begin{aligned}\frac{1}{\sqrt{2}}A_2 + (U_2)_{\xi\xi\xi} - \sqrt{2}U_2 + \frac{3}{2}(U_1^2)_{\xi\xi\xi} - \frac{1}{\sqrt{2}}U_1^2 &= 0 \quad , \\ \lim_{\xi \rightarrow -\infty} U_2(\xi) &= \frac{A_2}{2} - \frac{A_1^2}{8} \quad .\end{aligned}$$

The solution to the ODE is with $\tilde{\xi} = 2^{1/6}\xi$ and an integration constant c_2 is

$$U_2 = \frac{A_2}{2} - \frac{A_1^2}{8} + e^{\tilde{\xi}}(c_2 + A_1 c_1(1 - \tilde{\xi})) - \frac{23}{24}(c_1 e^{\tilde{\xi}})^2 \quad .$$

The last problem to be solved for the outer solution is

$\mathcal{O}(\delta)$:

$$\begin{aligned}U_{3\xi\xi\xi} - \sqrt{2}U_3 &= -\frac{A_2}{\sqrt{2}} + \frac{1}{4}U_{1\xi\xi\xi\xi} + \sqrt{2}U_1U_2 - \frac{1}{2}(U_1^3 + 6U_1U_2)_{\xi\xi\xi} \quad , \\ \text{with } \lim_{\xi \rightarrow -\infty} U_3(\xi) &= \frac{A_3}{2} - \frac{A_1A_2}{4} + \frac{A_1^3}{16} \quad .\end{aligned} \quad (3.27)$$

One obtains

$$U_3 = \frac{A_3}{2} - \frac{A_1A_2}{4} + \frac{A_1^3}{16} + (c_3 + d_1 + d_2\xi + d_3\xi^2)e^{\tilde{\xi}} + (d_4 + \frac{23}{21}A_1c_1^2\tilde{\xi})(e^{\tilde{\xi}})^2 + \frac{127}{28}c_1^3(e^{\tilde{\xi}})^3, \quad (3.28)$$

with another integration constant c_3 and the abbreviations $d_k, k = 1, 2, 3, 4$ given in the end of Appendix C, (C.26). Finally, the asymptotic representation in terms of x_l can be obtained by using (3.18) and expanding the exponentials. It yields an expression correct to order $\mathcal{O}(\delta)$,

$$U = 1 + (c_1 + \frac{1}{2}A_1)\delta^{1/3} + \left(c_1 2^{1/6}x_l + \check{e}_1\right)\delta^{2/3} + \left(-\frac{23}{7}c_1^2 + c_2\right)2^{1/6}x_l + \frac{1}{2}c_1 2^{1/3}x_l^2 + \check{e}_2\right)\delta + \mathcal{O}(\delta^{4/3}). \quad (3.29)$$

Here again new constants were introduced and \check{e}_1, \check{e}_2 can also be found in the appendix.

The inner regions

The solutions to the other regions are discussed now. The strategy is similar as for the outer region.

Leading order in r_l

To leading order in δ one obtains the problem in r_l

$$(u_{l0}'' - 2f(u_{l0}))''' = 0, \quad (3.30a)$$

$$u_{l0}(0) = 0. \quad (3.30b)$$

Matching to the leading order outer solution (3.24) $U_0 = 1$ gives a typical Cahn-Hilliard solution

$$u_{l0}(x_l) = -\tanh(x_l). \quad (3.31)$$

Its representation towards the internal layer about $x = 0$ is given by

$$u_{l0} = -1 + 2e^{-2x_l} - 2e^{-4x_l} + \mathcal{O}(e^{-6x_l}) \quad (3.32)$$

as $x_l \rightarrow \infty$.

Leading order in r_0

The leading order problem for this region is

$$(u_{00}'' - 2f(u_{00}))''' = 0, \quad (3.33a)$$

$$u_{00}(0) = 0, \quad u_{00}''(0) = 0 \quad \text{and} \quad u_{00}'''(0) = 0, \quad (3.33b)$$

and its solution is

$$u_{00}(x_0) = \tanh(x_0). \quad (3.34)$$

As $x_0 \rightarrow -\infty$ its behavior is given by

$$u_{00} = -1 + 2e^{2x_0} - 2e^{4x_0} + \mathcal{O}(e^{6x_0}). \quad (3.35)$$

$\mathcal{O}(\delta^{1/3})$ in r_l

The expansion of (3.14) and (3.15) to order $\delta^{1/3}$ yields

$$\mathcal{L}(u_{l1}, x_l) = f_{l1}(x_l) \quad , \quad (3.36a)$$

$$u_{l1}(0) = -u'_{l0}(0) \kappa_{l1} = \kappa_{l1} \quad , \quad (3.36b)$$

where \mathcal{L} is defined by

$$\mathcal{L}(v, z) = v'' + 2(1 - 3 \tanh^2(z)) v \quad (3.37)$$

and

$$f_{l1}(x_l) := c_{1l}x_l^2 + c_{2l}x_l + c_{3l} \quad . \quad (3.38)$$

The homogenous solutions are therefore

$$\phi_l(x_l) = -u'_{l0}(x_l) = 1 - \tanh^2(x_l) \quad , \quad (3.39)$$

$$\psi_l(x_l) = \left(\int_0^{x_l} \frac{dz}{\phi_l^2(z)} \right) \phi_l(x_l) \quad . \quad (3.40)$$

The constants c_{1l}, c_{2l}, c_{3l} are obtained by three successive integrations of the ODE for u_{l1} obtained at this order. The inhomogeneous solution is now chosen so that it grows only algebraically as $x_l \rightarrow -\infty$ and vanishes at $x_l = 0$. Particular solutions to (3.36b) are of the form

$$\varphi_{\alpha j}(x_\alpha) = \psi_\alpha(x_\alpha) \int_0^{x_\alpha} \phi_\alpha f_{\alpha j} dz - \phi_\alpha(x_\alpha) \int_0^{x_\alpha} \psi_\alpha f_{\alpha j} dz + \gamma_{\alpha j} \psi_\alpha(x_\alpha) \quad , \quad (3.41)$$

so that φ_{l1} is obtained for $\alpha = l, j = 1$ in (3.41) and

$$\gamma_{l1} = -\frac{\pi^2}{12}c_{1l} + \ln(2)c_{2l} - c_{3l} \quad .$$

Hence the solution is

$$u_{l1}(x_l) = -\kappa_{l1}\phi_l(x_l) + \varphi_{l1}(x_l) \quad . \quad (3.42)$$

As $x_l \rightarrow -\infty$ the limiting behavior of u_{l1} is

$$\begin{aligned} u_{l1}(x_l) = & -\frac{1}{8}(c_{1l} + 2c_{3l}) - \frac{1}{4}c_{2l}x_l - \frac{1}{4}c_{1l}x_l^2 \\ & + \left(\frac{1}{64}(-7c_{1l} - 8c_{3l} + 256\kappa_{l1} + 30c_{2l} + 4c_{2l}\pi^2 - 72c_{1l}\zeta(3)) \right. \\ & \left. + \frac{1}{16}(-6c_{2l} + 15c_{1l} + 24c_{3l})x_l + \frac{1}{8}(6c_{2l} - 3c_{1l})x_l^2 + \frac{1}{2}c_{1l}x_l^3 \right) e^{2x_l} + \mathcal{O}(e^{4x_l}) \quad , \end{aligned} \quad (3.43)$$

where ζ is the Riemann Zeta function, and u_{l1} must match the outer solution that is given by (3.29) and has only constant terms to this order. Hence it can be required $c_{2l} = 0$ and $c_{1l} = 0$. The matched solution is now

$$u_{l1}^{(l)}(x_l) = (1 - \tanh^2(x_l)) \kappa_{l1} - \frac{c_{3l}}{16} \left(-2e^{6x_l} + 4 + 10e^{2x_l} - 12e^{4x_l} - 24x_l e^{2x_l} \right) \frac{e^{-2x_l}}{(e^{2x_l} + 1)^2} \quad , \quad (3.44)$$

where $u_{l1}^{(l)}$ denotes the solution that is obtained by matching to the outer solution U . As it will become clear later, exponential matching to the inner solution u_0 , i.e. as $x_l \rightarrow \infty$, where it is found that

$$u_{l1}^{(l)}(x_l) = \frac{1}{8}c_{3l}e^{2x_l} + \frac{1}{2}c_{3l} + \left(-\frac{7}{4}c_{3l} + 4\kappa_{l1} + \frac{3}{2}c_{3l}x_l\right)e^{-2x_l} + \left(\frac{11}{4}c_{3l} - 8\kappa_{l1} - 3c_{3l}x_l\right)e^{-4x_l} + O(e^{-6x_l}),$$

requires also $c_{3l} = 0$. Hence, denoting by $u_{l1}^{(e)}$ the solution that has been exponentially matched to the inner solution u_0 near $x = 0$, one obtains

$$u_{l1}^{(e)}(x_l) = (1 - \tanh^2(x_l)) \kappa_{l1}. \quad (3.45)$$

$\mathcal{O}(\delta^{1/3})$ in \mathbf{r}_0

To this order the problem in the region near κ_0 is

$$\mathcal{L}(u_{01}, x_0) = f_{01}(x_0), \quad (3.46a)$$

$$u_{01}(0) = 0, \quad u_{01}''(0) = 0 \quad \text{and} \quad u_{01}'''(0) = 0, \quad (3.46b)$$

with

$$f_{01}(x_0) = c_{10}x_0^2 + c_{20}x_0 + c_{30}. \quad (3.47)$$

Its general solution reads

$$u_{01}(x_0) = \varphi_{01}(x_0) + g_1 \psi_0(x_0), \quad (3.48)$$

where the homogeneous solutions are as before and the inhomogeneous solution is given by equation (3.41) with $\alpha = 0, j = 1$ and

$$\gamma_{01} = -\frac{\pi^2}{12}c_{10} + \ln(2)c_{20} - c_{30},$$

so that $\varphi_{01}(0) = 0$ and φ_{01} grows algebraically as $x_0 \rightarrow -\infty$. Furthermore, symmetry requires $\varphi_{01}''(0) = 0$ and $\varphi_{01}'''(0) = 0$, which implies $c_{10} = 0$ and $c_{30} = 0$ leading to

$$\begin{aligned} \varphi_{01}(x_0) = & \frac{c_{20}}{16(1+e^{-2x_0})^2} \left(1 - 4x_0 + 12 \operatorname{dilog}(e^{2x_0} + 1)e^{-2x_0} - e^{-4x_0} + 12x_0^2 e^{-2x_0} \right. \\ & + \pi^2 e^{-2x_0} + 12x_0 e^{-4x_0} - 14x_0 e^{-2x_0} - \ln(1+e^{-2x_0})e^{2x_0} + 8e^{-4x_0} \ln(1+e^{-2x_0}) \\ & \left. - 8 \ln(1+e^{-2x_0}) + e^{-6x_0} \ln(1+e^{-2x_0}) + 2e^{-6x_0}x_0 \right), \end{aligned}$$

where dilog denotes the dilogarithm function. The remaining free parameters of u_{01} that have to be matched are c_{20} and g_1 . As will be demonstrated later, exponential matching to u_l requires an expression for u_{01} as $x_0 \rightarrow -\infty$

$$\begin{aligned} u_{01}(x_0) = & -\frac{g_1}{16}e^{-2x_0} - \frac{1}{4}c_{20}x_0 - \frac{3}{8}g_1 \\ & + \frac{1}{32} \left(2c_{20}\pi^2 + 15c_{20} + 26g_1 + (48g_1 - 12c_{20})x_0 + 24c_{20}x_0^2 \right) e^{2x_0} \\ & + \frac{1}{48} \left(-36g_1 - 89c_{20} - 6c_{20}\pi^2 + (84c_{20} - 144g_1)x_0 - 72c_{20}x_0^2 \right) e^{4x_0} + O(e^{6x_0}) \end{aligned}$$

and then re-expanding u_0 in the variable x_l . This shows that also $c_{20} = 0$, $g_1 = 0$ and $c_{3l} = 0$. Any other choice leads to a system for the parameters having no solution. Hence, only κ_l remains as a free constant in the two regions. The exponentially matched solution is therefore simply

$$u_{01}^{(e)}(x_0) = 0. \quad (3.49)$$

Internal layer in \mathbf{r}_l for $\mathbf{O}(\delta^{2/3})$

The problem to this order near κ_l is

$$\mathcal{L}(u_{l2}, x_l) = f_{l2}(x_l), \quad (3.50)$$

$$u_{l2}(0) = -u'_{l0}(0) \kappa_{l2} - \frac{1}{2} u''_{l0} \kappa_{l1}^2 - u'_{l1}(0) \kappa_{l1} = \kappa_{l2} - u'_{l1}(0) \kappa_{l1}, \quad (3.51)$$

where

$$f_{l2}(x_l) = d_{1l} x_l^2 + d_{2l} x_l + d_{3l} + 6 u_{l0} (u_{l1}^{(e)})^2. \quad (3.52)$$

Note that $u_{l1}^{(l)'}(0) = 0$. Again the inhomogeneous solution is chosen so that it grows only algebraically as $x_l \rightarrow -\infty$ and vanishes at $x_l = 0$ to obtain (3.41) with $\alpha = l, j = 2$ and

$$\gamma_{l2} = -\frac{\pi^2}{12} d_{1l} + \ln(2) d_{2l} - d_{3l} - \kappa_{l1}^2,$$

so that the general solution is represented as

$$u_{l2}(x_l) = -\kappa_{l2} \phi_l(x_l) + \varphi_{l2}(x_l). \quad (3.53)$$

As $x_l \rightarrow -\infty$ it has to be compared

$$\begin{aligned} u_{l2}(x_l) = & -\frac{1}{8}(d_{1l} + 2d_{3l}) - \frac{1}{4}d_{2l}x_l - \frac{1}{4}d_{1l}x_l^2 \\ & + e^{2x_l} \left(\frac{1}{64} [(-7 - 72\zeta(3))d_{1l} - 8d_{3l} + 256(\kappa_{l2} - \kappa_{l1}^2) + (30 + 4\pi^2)d_{2l}] \right. \\ & \left. + \frac{3}{16}(5d_{1l} - 2d_{2l} + 8d_{3l})x_l + \frac{3}{8}(2d_{2l} - d_{1l})x_l^2 + \frac{1}{2}d_{1l}x_l^3 \right) + O(e^{4x_l}) \end{aligned}$$

with the outer solution. Matching the constant and the linear terms in x_l yields

$$\begin{aligned} -\frac{1}{4}d_{3l} &= \frac{1}{2}A_1 - \frac{1}{8}A_1^2 + \frac{1}{3}c_1A_1 + \frac{23}{14}c_1^2 + c_2, \\ -\frac{1}{4}d_{2l} &= 2^{1/6}c_1. \end{aligned}$$

There is no quadratic term in the outer solution (3.29), hence $d_{1l} = 0$. There are further matching conditions but they do not simplify the problem structurally at this point and will be enforced later, so that d_{2l} , d_{3l} and κ_{l2} remain to be determined via exponential matching. As $x_l \rightarrow \infty$, the expansion to this order can be written as

$$\begin{aligned} u_{l2}^{(l)} = & \frac{1}{2}d_{3l} - \frac{1}{4}d_{2l}x_l + \frac{1}{8}d_{3l}e^{2x_l} + \frac{e^{-2x_l}}{32} \left(-56d_{3l} - 15d_{2l} \right. \\ & \left. - 2d_{2l}\pi^2 + 128(\kappa_{l1}^2 + \kappa_{l2}) + (48d_{3l} - 12d_{2l})x_l - 24d_{2l}x_l^2 \right) + O(e^{-4x_l}). \end{aligned} \quad (3.54)$$

Internal layer in \mathbf{r}_0 for $O(\delta^{2/3})$

As for the $O(\delta^{1/3})$ problem, at $O(\delta^{2/3})$ one has

$$\mathcal{L}(u_{02}, x_0) = f_{02}(x_0), \quad (3.55a)$$

$$u_{02}(0) = 0, \quad u_{02}''(0) = 0 \quad \text{and} \quad u_{02}'''(0) = 0, \quad (3.55b)$$

with

$$f_{02}(x_0) = d_{10}x_0^2 + d_{20}x_0 + d_{30}. \quad (3.56)$$

The general solution is

$$u_{02}(x_0) = \varphi_{02}(x_0) + g_2 \psi_0(x_0), \quad (3.57)$$

where the homogeneous component is as before and the inhomogeneous part is obtained by setting $\alpha = 0, j = 2$ and $\gamma_{02} = 0$ in (3.41), so that $\varphi_{02}(0) = 0$ and φ_{02} grows algebraically as $x_0 \rightarrow -\infty$. Symmetry requires $\varphi_{02}''(0) = 0, \varphi_{02}'''(0) = 0$, which implies $d_{10} = 0$ and $d_{30} = 0$. The remaining free parameters to be matched are d_{20} and g_2 . In order to exponentially match to u_l to $O(\delta^{2/3})$ and obtain $u_{l2}^{(e)}$, again $u_{02}(x_0)$ has to be expanded as $x_0 \rightarrow -\infty$, giving

$$\begin{aligned} u_{02}(x_0) = & -\frac{\hat{\mu}}{16}e^{-2x_0} - \frac{1}{4}d_{20}x_0 - \frac{3}{8}\hat{\mu} \\ & + \frac{1}{32}\left((15 + 2\pi^2 + 2\ln(2))d_{20} + 26g_2 + (48\hat{\mu} - 12d_{20})x_0 + 24d_{20}x_0^2\right)e^{2x_0} \\ & + \frac{1}{48}\left(-(89 + 6\pi^2)d_{20} - 36\hat{\mu} + (84d_{20} - 144\hat{\mu})x_0 - 72d_{20}x_0^2\right)e^{4x_0} + O(e^{6x_0}), \end{aligned}$$

where the abbreviation $\hat{\mu} = d_{20} \ln(2) + g_2$ has been used. This has to be re-expressed in terms of x_l .

Internal layer in \mathbf{r}_l for $O(\delta)$

The problem to be solved at order $O(\delta)$ is

$$\begin{aligned} \mathcal{L}(u_{l3}, x_l) &= f_{l3}(x_l), \\ u_{l3}(0) &= -u_{l2}'(0)\kappa_{l1} - u_{l0}''(0)\kappa_{l1}\kappa_{l2} - u_{l0}'(0)\kappa_{l3} \\ &\quad - \frac{1}{6}u_{l0}'''(0)\kappa_{l1}^3 - u_{l1}'(0)\kappa_{l2} - \frac{1}{2}u_{l1}''(0)\kappa_{l2}^2, \end{aligned} \quad (3.58a)$$

with

$$\begin{aligned} f_{l3}(x_l) = & 2\left((u_{l1}^{(e)})^3 + 6u_{l0}u_{l1}^{(e)}u_{l2}^{(e)}\right) \\ & - 2^{3/2}\left[\frac{1}{2}\text{dilog}(e^{2x_l} + 1) + \frac{1}{2}(1 + k_{1l})x_l^2 + (\ln(2) + k_{2l})x_l + k_{3l}\right]. \end{aligned} \quad (3.59)$$

Again the inhomogeneous solution is chosen so that it grows only algebraically as $x_l \rightarrow -\infty$ and vanishes at $x_l = 0$ and so that $\varphi_{l3}(x_l)$ is obtained by using formula (3.41) with $\alpha = l, j = 3$ and $\gamma_{l3} = 0$. The solution is

$$u_{l3}(x_l) = -u_{l3}(0)\phi_l(x_l) + \varphi_{l3}(x_l), \quad (3.60)$$

where k_{1l} , k_{2l} , k_{3l} and κ_{l3} remain to be determined via matching. In order to exclude exponential growth as $x_l \rightarrow -\infty$ the relation

$$k_{2l} = \frac{\sqrt{2}}{48 \ln(2)} \left(\kappa_{l1} (-(12 + 9\pi^2)d_{2l} + 12d_{3l} - 24\kappa_{l2}) + \sqrt{2}(24k_{3l} - 12 \ln(2)^2 + k_{1l}\pi^2) \right)$$

is obtained, so that the expansion derived as $x_l \rightarrow -\infty$ is

$$u_{l3}(x_l) = \frac{1}{4\sqrt{2}}(1 + k_{1l} + 4k_{3l}) + \frac{1}{\sqrt{2}}(\ln(2) + k_{2l})x_l + (k_{1l} + 1)\frac{\sqrt{2}}{4}x_l^2 + O(e^{2x_l}). \quad (3.61)$$

Comparing this with the outer solution to $O(\delta)$, equation (3.29), yields the matching conditions

$$\begin{aligned} \frac{1}{4\sqrt{2}}(1 + k_{1l} + 4k_{3l}) &= \left(-\frac{1}{4}A_1 + \frac{1}{3}c_1\right)A_2 + \left(\frac{7}{12}c_1^2 + \frac{1}{3}c_2\right)A_1 \\ &+ \frac{1}{2}A_3 - \frac{59}{216}c_1A_1^2 - \frac{1}{12}2^{1/3}c_1 + c_3 - \frac{23}{7}c_1c_2 + \frac{1}{16}A_1^3 + \frac{127}{28}c_1^3 \end{aligned} \quad (3.62)$$

for the constant terms,

$$\frac{1}{\sqrt{2}}(\ln(2) + k_{2l}) = (c_2 - \frac{23}{7}c_1^2)2^{1/6} \quad \text{and} \quad (k_{1l} + 1)\frac{\sqrt{2}}{4} = 2^{-2/3}c_1$$

for the linear and the quadratic terms, respectively.

Expanding the solution as $x_l \rightarrow \infty$ one finds

$$\begin{aligned} u_{l3}(x_l) &= \frac{1}{192} \left(\kappa_{l1}d_{2l}(9\pi^2 + 24) - 48\kappa_{l1}d_{3l} + 2\sqrt{2}\pi^2(1 - k_{1l}) - 48\sqrt{2}k_{3l} \right) e^{2x_l} \\ &+ \frac{1}{96} \left(\kappa_{l1}d_{2l}(27\pi^2 + 72) + \sqrt{2}(k_{1l}(12 - 6\pi^2) - 96k_{3l} - 12 + 2\pi^2) \right) \\ &+ \frac{1}{\sqrt{2}}(\ln(2) + k_{2l})x_l + (k_{1l} + 1)\frac{\sqrt{2}}{4}x_l^2 + O(e^{-2x_l}), \end{aligned}$$

and it will be exponentially matched to the solution near $x = 0$.

Internal layer in r_0 for $O(\delta)$

The general solution to the $O(\delta)$ problem

$$\mathcal{L}(u_{03}, x_0) = f_{03}(x_0), \quad (3.63a)$$

$$u_{03}(0) = 0, \quad u_{03}''(0) = 0 \quad \text{and} \quad u_{03}''''(0) = 0, \quad (3.63b)$$

with

$$f_{03}(x_0) = -2^{1/2} [\text{dilog}(e^{2x_0} + 1) - \text{dilog}(2) + 2\mu_2x_0 + (1 + k_{10})x_0^2] \quad (3.64)$$

and the abbreviation $\mu_2 = \ln(2) + k_{20}$ becomes

$$u_{03}(x_0) = \varphi_{03}(x_0) + g_3 \psi_0(x_0), \quad (3.65)$$

where it has been required that $u_{03}(0) = 0$ and $u_{03}''(0) = 0$. If it is further enforced $u_{03}''''(0) = 0$ then $k_{10} = 0$. Again an inhomogeneous solution $\varphi_{03}(x_0)$ is taken which satisfies the above conditions, so that the general solution is obtained with

$$\mu_1 = \sqrt{2}(\ln(2)^2 + 2k_{20} \ln(2)) - g_3 \quad \text{and} \quad \omega = \int_0^1 \frac{1}{z} \ln\left(\frac{z^2 + 1}{2z}\right)^2 - \frac{\ln(2z)^2}{z} dz \approx 0.3094,$$

as

$$\begin{aligned} u_{03} = & \frac{12\mu_1 - \pi^2\sqrt{2}}{192} e^{-2x_0} + \frac{1}{96}(36\mu_1 + \sqrt{2}(12 - \pi^2)) + \frac{\mu_2}{\sqrt{2}}x_0 + \frac{\sqrt{2}}{4}x_0^2 \\ & + \left[\frac{1}{192} \left(156\mu_1 + \sqrt{2}[(19 - 24k_{20})\pi^2 - 15 - 288\omega - 180\mu_2] \right) \right. \\ & \left. + \frac{1}{16} \left(-24\mu_1 + \sqrt{2}(12\mu_2 - 11) \right) x_0 + \frac{\sqrt{2}}{8} (3 - 12\mu_2) x_0^2 - \frac{1}{\sqrt{2}} x_0^3 \right] e^{2x_0} + O(e^{4x_0}). \end{aligned}$$

For exponentially matching to u_l this again has to be re-expressed in x_l and combined with the corresponding expressions for u_{00} , u_{01} and u_{02} .

Exponential matching

The rest of the solution $u_l(x_l)$ has to be matched to the rest of the solution $u_0(x_0)$. This requires matching the exponential terms in addition to the algebraic terms, i.e. matching of the solution describing the internal layer in r_l to the solution in r_0 requires expressing the variable x_0 in terms of x_l (or vice versa). Recalling that $x_0 = x_l + \bar{\kappa}_l/\sqrt{2}$ and that $\bar{\kappa}_l < 0$ one obtains

$$e^{2x_0} = e^{2x_l} e^{\sqrt{2}\bar{\kappa}_l}, \quad (3.66)$$

so that the e^{2x_0} terms in the u_0 expansion will produce scaled e^{2x_l} terms (and analogously for e^{-2x_0} terms). Their corresponding matching partner will be found at a different order in δ in the u_l expansion. It is necessary to determine the relationship between $e^{\sqrt{2}\bar{\kappa}_l}$ and δ and in principle several choices are possible, but only one allows a consistent matching of both expansions. One can observe that the choice $e^{\sqrt{2}\bar{\kappa}_l} = \rho\delta^{1/3}$, where ρ is some constant, quickly leads to a contradiction. However, the next natural choice

$$e^{\sqrt{2}\bar{\kappa}_l} = \rho\delta^{2/3} \quad (3.67)$$

leads to a $O(\delta^{2/3})$ shift of terms, which is clear when inserting the shift e.g. into equation (3.66). Then e^{2x_0} shifts to a term $\delta^{2/3} e^{2x_l}$ or e^{-2x_0} will end up as a term $\delta^{-2/3} e^{-2x_l}$ and other terms change accordingly. As a consequence e.g. a term e^{2x_0} in the leading order part of the u_0 expansion will have to match a e^{2x_l} term in the $O(\delta^{2/3})$ part of the u_l expansion, or a e^{-2x_0} term in the $O(\delta)$ part of the u_0 expansion will have to match a e^{-2x_l} term in the $O(\delta^{1/3})$ part of the u_l expansion. These matching conditions calculate straightforward once the correct shift is chosen. In this way also terms are produced that have no partner term in the transformed

expansion. Their coefficients must then be set to zero. If now the expansions for $u_{01}(x_0)$, $u_{02}(x_0)$ and $u_{03}(x_0)$ are summed and re-expanded using (3.67), one obtains

$$\begin{aligned} u_0(x_l) = & -1 - \frac{1}{16} \left(d_{20} \ln(2) + g_2 \right) e^{-2x_l} \rho + \frac{1}{192} \left(12\mu_1 - \sqrt{2}\pi^2 \right) e^{-2x_l} \rho \delta^{1/3} \\ & + \frac{1}{24} \left(d_{20}(3 \ln(\rho) - 9 \ln(2) - 2 \ln(\delta)) - 9g_2 - 6d_{20}x_l + 48e^{2x_l}/\rho \right) \delta^{2/3} \\ & + \left[\frac{1}{96} \left(36\mu_1 + \sqrt{2}[12 + (16 \ln(\delta) - 24 \ln(\rho))\mu_2 + 6(\ln(\rho) - \frac{2}{3} \ln(\delta))^2 - \pi^2] \right) \right. \\ & \left. + \frac{\sqrt{2}}{12} (2 \ln(\delta) + 6\mu_2 - 3 \ln(\rho)) x_l + \frac{\sqrt{2}}{4} x_l^2 \right] \delta, \end{aligned}$$

which has to match $u_{l1}(x_l)$, $u_{l2}(x_l)$ and $u_{l3}(x_l)$ to each order, respectively. From this further conditions for the parameters in addition to those already found are derived. Solving the complete system of equations then yields the solutions for the width of the hump

$$\Delta = \frac{\sqrt{2}}{6} \ln \left(\frac{\beta}{W(\beta^{1/3})^3} \right), \quad (3.68)$$

with $\beta = 2^{11}/(27\delta^2)$, where W is the Lambert W function (which is defined as solution to $x = W \exp(W)$). The expressions for the remaining matching constants c_1, c_2 , etc. are omitted. The first correction in (3.12) has the coefficient

$$A_1 = -3 \cdot 2^{1/6}. \quad (3.69)$$

3.1.3 Comparison between numerical data and analytical results

In light of the expansion for the far-field parameter (3.12) the $\mathcal{O}(\delta^{1/3})$ terms A_1 for the different heteroclinic connections in a range of very small δ are estimated. In Figure 3.5 the numerically obtained values for A are plotted and a curve for the analytical expression is drawn in the same plot for comparison. The values behave like $A = 1 - 2^{1/6}\delta^{1/3}$ in case of the *het*₀ solutions, so that $A_1 = -2^{1/6}$, which is consistent with the result in Savina et al. [89]. The numerical result for *het*₁ is in line with the analytical value (3.69) and since for *het*₂ the agreement $A_1 \approx -5 \cdot 2^{1/6}$ is observed, for *het*_k the general approximation

$$A_1 \approx -(2k+1) 2^{1/6} \quad (3.70)$$

can be proposed. It is reminiscent of the CCH expression $A_1^{CCH}(k) = -(2k+1)2^{-1/2}$ which has been obtained by Korzec et al. [57]. The HCCH formula (3.70) is used in Figure 3.5 to plot the analytical values.

The distances between the first and second root for the *het*₁ and the *het*₂ solutions are shown in Figure 3.5 on the right. These values are compared to the derived analytical expression (3.68) for the one-hump solutions in the same figure. For small δ the agreement is good. For both *het*₁ and *het*₂ solutions the distance is seen to increase logarithmically as δ decreases.

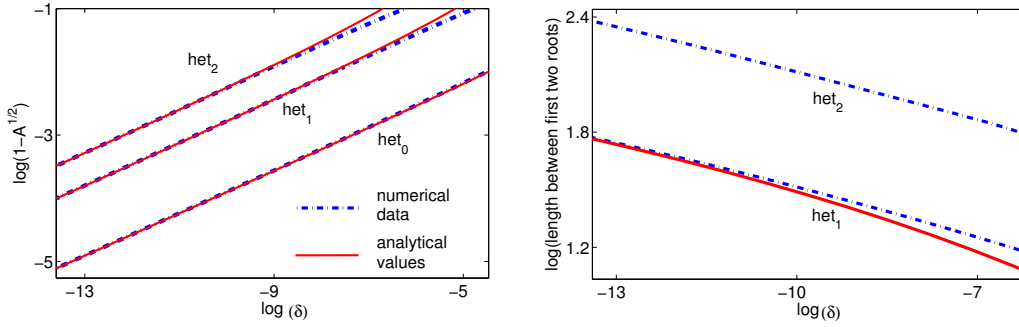


Figure 3.5: Left: Logarithmic (\sqrt{A}, δ) plot for very small δ . Analytical values are given as solid lines, dash-dotted lines are the values computed with the BVP solver. On the right the distances between the first two roots of the het_1, het_2 solutions are visible, numerically and for het_1 via the analytical expression (3.68) (solid line).

3.2 Coarsening dynamics for the HCCH equation

Savina et al. [89] derived coarsening rates for the HCCH equation (2.14). The authors observed that after formation of oscillatory surfaces with wave lengths approximately prescribed by the linear stability analysis, a power-law dictates the coarsening for small values of δ . This fast ripening regime, which is initiated after a transient slow phase, obeys approximately a $t^{1/2}$ law. For increased values of δ (in the paper the range $\delta \in (0, 0.1)$ was discussed) this phase starts earlier and tends to slow down at lower characteristic lengths before coarsening finally stops. Hence one can guess that stationary solutions with higher frequencies are observed for growing values of δ . The mechanisms behind the coarsening are discussed on the following pages and a numerical study confirms a growth in the characteristic wave numbers of the stationary or traveling wave solutions. The used pseudospectral method will be explained in Chapter 5. It extends earlier numerical implementations such as by Rogers et al. [83], who made numerical simulations for a CH equation.

As expected it turns out that adding the first order nonlinearity makes the behavior of solutions to the HCCH equation richer than for the case $\delta = 0$. Additionally to stationary patterns, also multi-hump traveling wave solutions can be observed. With increasing δ the wave number of these structures grows, until a chaotic regime is reached. This reminds of the $\delta \rightarrow \infty$ limit of the CCH equation, known for its chaotic behavior, as already mentioned by Savina et al. [89].

In Figure 3.6 a typical simulation run for the HCCH equation is shown for $\delta = 0.04$ on an 80π long domain for the time points $t = 10^k, k = 2, 4, 5$. A random perturbation of the zero state evolves to regions where the slopes are nearly constant, $u(x, t) = h_x(x, t) \approx \pm 1$. These values are smaller in modulus when δ is increased. The slopes are plotted on the left of this figure and the corresponding shapes $h(x, t)$ are given as triangular kink, antikink patterns on the right. They coarsen, bigger 2D pyramids survive and continue to grow. This behavior is also known from quantum dot systems, as in those which will be introduced in Chapter 4, and indeed an

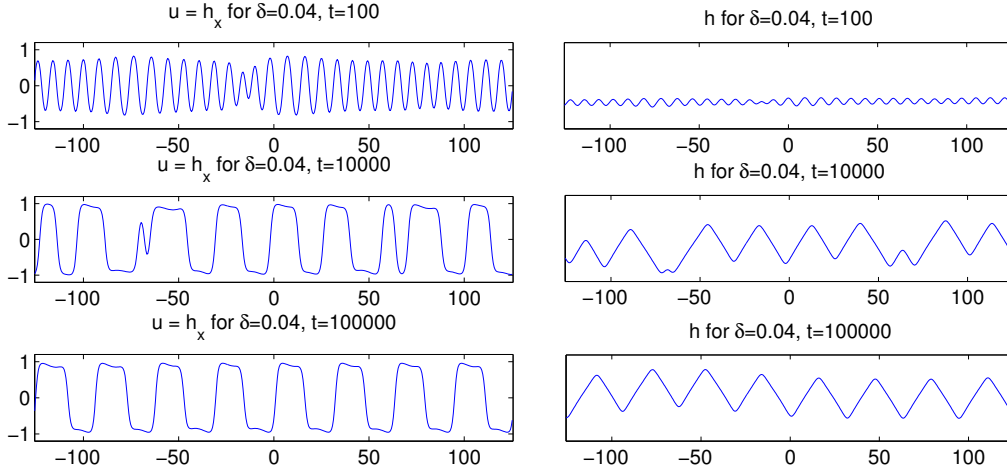


Figure 3.6: Typical evolution of the slopes $u(x,t)$ and the corresponding shapes $h(x,t)$ for the HCCH equation. Triangular structures form that coarsen by a collision mechanism. Here at $t = 10^5$ a steady state is formed that does not further change with time.

extension of the HCCH model with a wetting layer yields similar results as in heteroepitaxial systems [43]. Similarly as observed in the evolution of domain walls in phase separating systems [79], the coarsening to the HCCH equation is described by kink-antikink pairs and kink-antikink-kink triplets. Each time a pyramid vanishes, such a triplet-combination evolves to a simple kink. The remaining pattern at $t = 10^5$ appears to be stationary or traveling.

Kink pair and kink triplet interactions are mainly responsible for the ripening observed in all simulations (from now on write k for kinks and a for antikinks so that pairs become (k, a) and triplets (a, k, a) , and other orderings are possible). In Figure 3.6 one can observe that arrays of the simplest stationary kink profiles (heteroclinic connections) appear during the evolution and define corners of the pyramids. Note that during a coarsening event as in Figure 3.6, $t = 10^4$, the transition state resembles a het_1 solutions found in the discussion of stationary solutions. Although these shapes seem numerically unstable, they can be observed during evolution.

Kink pair interaction

For $\delta = 0$ — the case without deposition — it is shown in Figure 3.7 that (k, a) or (a, k) pairs form stationary profiles. In the time space plots regions with bright shades correspond to the solution where u is positive, negative values have dark shades. Since the profiles consist roughly of two values and short transitions between these states, mainly one bright and one dark shade appear in the figures. The plots on the right in the same figure show the nearly binary valued profile of u which looks perfectly symmetric. This property is broken for a nonzero deposition term. Then also kink pairs are able to form traveling waves as it is shown in Figure 3.8 for $\delta = 0.01$.

For the intermediate kink distance the pair tends to a different direction than for the other

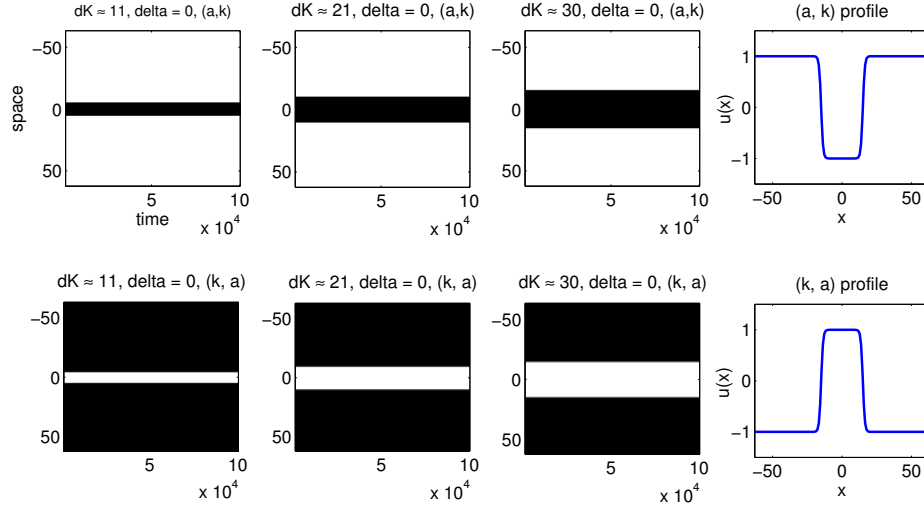


Figure 3.7: Kink pair interaction for the HCCH equation with $\delta = 0$. Upper plots correspond to an (a, k) combination and one line in the black and white space time plots belongs to a profile as on the right. The first three figures show the evolution (in time versus space plots) for three different (a, k) combinations with different kink distances. Analogously the lower plots correspond to (k, a) , inverting the black and white distribution.

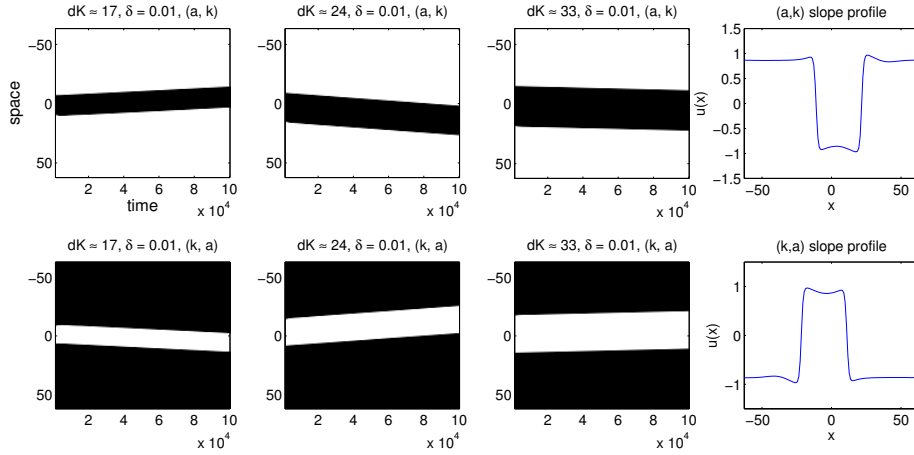


Figure 3.8: Kink pair interaction for the HCCH equation for $\delta = 0.01$. As in Figure 3.7 the upper plots belong to the kink pair (a, k) , while the lower plots correspond to the other kink pair (k, a) .

two cases. Repeated simulations with more grid points yield the same results, so the observed effects do not seem to be numerical artefacts. For the simulations simple linear combinations of tanh profiles were used as initial conditions. These evolve fast to the kink pairs sought, (a, k) and (k, a) , respectively. This way of deriving the kinks and antikinks does allow only for approximate control over the distance between the kinks. In case of triplets this approach has been used analogously, only that a third tanh function had to be considered in the initial profile.

In the plots for kink interactions the time point is set to $t = 0$ when $u(x, t)$ already evolved to a stationary or traveling wave shape.

Kink-triplets

While the single kink and kink pair simulations do not indicate coarsening since the number of domain walls stays unchanged, the triplets do so. As seen in Figure 3.9 (a), (a, k, a) triplets form stationary solutions, while qualitative changes in u appear in Figure 3.9 (b). The (k, a, k) triplet merges to one simple kink after some time. Translated to the shapes $h(x, t)$ this means that a pyramid that is surrounded by two bigger pyramids vanishes. This coarsening structure is visible throughout long-time evolution on big domains. It seems that traveling wave patterns are driven by kink pairs, while for coarsening at least three kinks have to be adjoint. This clearly reminds of the CCH equation where the same observations were made [79, 109].

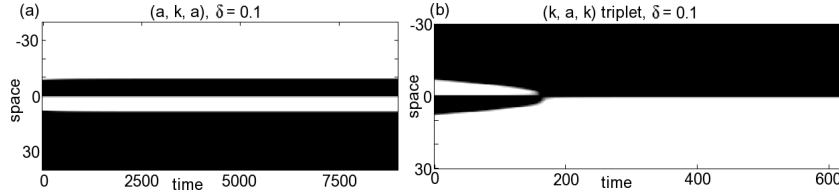


Figure 3.9: Dynamics of triplets; as before depicted in a space time plot as in Figure 3.7. In (a) an (a, k, a) triplet forms a stationary solution while in (b) an (k, a, k) triplet shows a collision that results in one kink — a typical event driving the coarsening.

Coarsening

The detailed analysis of the kink behavior is recovered in simulations on big domains with many kinks. Figure 3.10 shows the evolution in a black and white space time plot with the same brightness to height correspondences as before. Every time the surface ripens, when pyramids vanish, one sees that a black-white-black-white combination collides to a simple black-white combination, meaning that a (k, a, k) triplet evolves to one single antikink exactly in the way as in Figure 3.9 (b).

During several runs, such as for $\delta = 0.04$ in Figure 3.6, it was observed, that at late time the coarsening tends to stop. The oscillatory stationary solutions also found by Savina [89] leave open questions: (i) Are the observed solutions indeed there, or are they artefacts of the numerical methods? (ii) If they are not produced by the numerics, are they really stable? (iii) Do traveling waves exist as indicated by the kink pair simulations? (iv) Is there any regularity in the appearance (e.g. the wave length) of such shapes?

For the first three questions (i), (ii), (iii) the following answers are proposed: Yes, these stationary solutions exist, yes they are stable, yes there exist traveling wave solutions. Computations were carried out with a pseudospectral method, with a finite difference method and for different grid sizes in space and time, all of them exposing the same stationary shapes. Calculations on

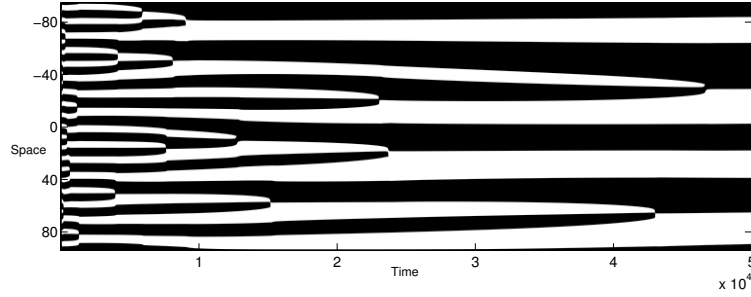


Figure 3.10: Coarsening plot for the HCCH equation on a 60π long domain. White shades correspond to values of u near $+1$ while dark shades indicate $u \approx -1$. Ternary events governing the coarsening are visible throughout the whole evolution.

larger domains reveal the same characteristic lengths of the solutions, so that the truncation of the spatial interval is not responsible for the observed phenomenon. Additionally a more detailed numerical study shows that also traveling wave multi-hump solutions are possible, yielding an answer to (iii). However, although the following numerics indicates the behavior of the solutions, analytical studies should be carried out that support — or confirm— these results. This task is left for future work and it should be noted that an ansatz like by Zaks et al. [115] might lead to the desired result. Because of the strong similarities between the CCH and the HCCH equation it can be expected that similar parameter planes for periodic solutions as in this work also exist for the higher order equation.

In Figure 3.11 the evolution on smaller domains $[-10\pi, 10\pi]$ has been visualized to investigate the long-time behavior of the solutions to the HCCH equation dependent on small deposition rates. Starting from a randomly perturbed zero state, oscillatory surfaces evolve that were stored to be able to initiate additional runs with less grid points. They yield the same results, supporting the validity of the numerical scheme. At earlier times coarsening as in Figure 3.10 takes place. However, for most values of δ it is not visible on the plots in Figure 3.11, since it happens in the very early phase of evolution. For twelve increasing values of δ corresponding space time plots show how the shapes evolve. To help understanding the grayscale distribution the shape at the latest time point is plotted below.

It can be observed that for increasing values of δ the number of stripes in the space time plots grows logarithmically slow in δ . This behavior is shown in Figure 3.12, where maxima for $u > 0$ have been considered and where the x axis is logarithmic to show the moderation of the characteristic frequency growth. For the nonequilibrium solutions the number of maxima has been counted at the latest computed time point $t = 10^5$. However, the figure does not reveal the additional information seen in Figure 3.11. Apart from stationary solutions (such as for $\delta = 0.05, 0.5$) also traveling waves with various speed rates are observed (e.g. $\delta = 0.07, 3$) and interestingly, for $\delta = 5$ and higher values chaotic behavior is observed. In no reference frame this

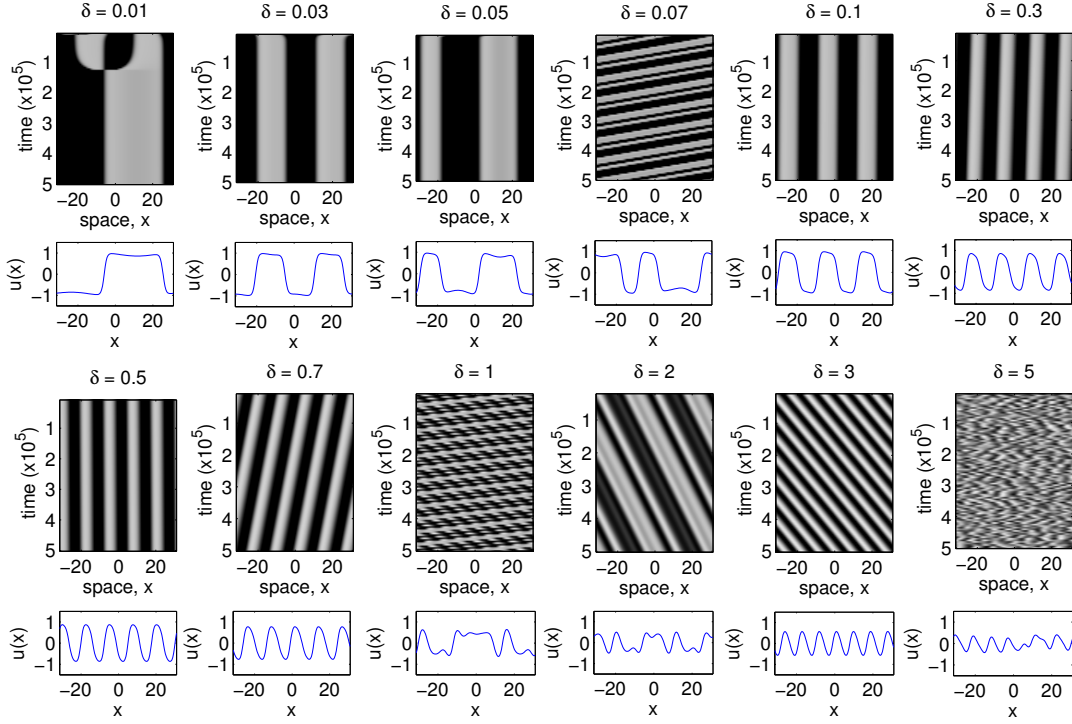


Figure 3.11: Multi-hump stationary solutions, traveling waves and transition to chaotic behavior for the HCCH equation for values of δ between 0.01 and 5.

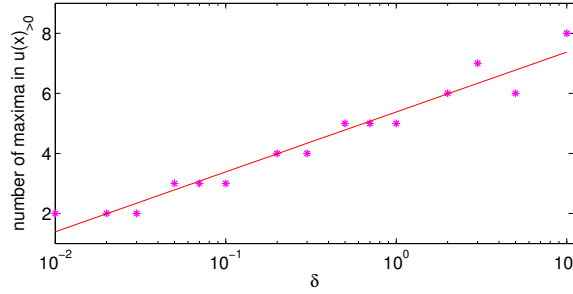


Figure 3.12: Number of local maxima for $u > 0$ in the stationary and traveling wave solutions to the HCCH equation for values of δ between 0.01 and 3. For higher values of δ the number of maxima at $t = 10^5$ has been counted. The solid curve is a nonlinear least squares data fit for a logarithmic ansatz function. The δ axis is logarithmic in the plot.

solutions is in equilibrium.

The solution space to the HCCH equation is worth to be analyzed further in future. However, here the analysis of this rich equation comes to an end. In the following chapter a realistic quantum dot self-assembly model is derived, a linear stability analysis is carried out and sim-

ulation results are presented. This PDE extends the previous model, since additionally to an anisotropic surface energy and an atomic flux also wetting interactions and an elastic subproblem are incorporated.

Chapter 4

The QDM equation: Derivation, analysis and simulation results

The greatest challenge to any thinker is stating the problem in a way that will allow a solution.

Bertrand Russell (1872 - 1970)

In the previous sections equation (2.14) has been studied extensively. It describes a surface that undergoes faceting during the growth of this one material solid. To model more complex systems, such as the self-assembly of quantum dots in a Stranski-Krastanov growth mode, more effects have to be taken into account and the model has to be extended. In this chapter a thin film growing on top of a substrate is considered. Heteroepitaxial growth as in the Ge/Si system (see Section 0.4) is described. The model incorporates a misfit between the lattices of film and substrate, which leads to stresses, one of the major reasons for the observed Stranski-Krastanov growth mode. At a certain thickness an ATG instability takes place and a transition from layer to layer growth to island coarsening is observed. The bulk energy plays an as important role as the surface energy. Furthermore intermolecular interactions at the interface are added, resulting in a wetting layer that connects the single dots (the terminology is taken from thin liquid films and is used analogously for solids). The surface energy is anisotropic and leads to preferred orientations during growth as it has been also seen in solutions to the HCCH equation. However, a Wilmore term that would allow for strong anisotropy is not treated here. The model extends the equations from the isotropic case from Tekalign and Spencer [102, 103]. It has been introduced by Korzec and Evans [56] and is kept more general in this thesis. In particular other anisotropies than for pyramidal dots can be used and deposition is included, which is essential to simulate realistic Stranski-Krastanov systems. As mentioned in the elasticity Section 1.3, only isotropic theory will be used for the bulk equations, and faceting is achieved by the orientation dependency of the surface energy.

First, in the following Section 4.1, the reduced quantum dot model (QDM) equation is derived, then in Section 4.2 a linear stability analysis is carried out which explains several of the observed effects during evolution. Bigger anisotropy coefficients turn out to destabilize flat surfaces and the critical thickness decreases with its increase. Above a certain anisotropy strength, all wave numbers become unstable and a regularizing term would be necessary for such strong anisotropies. In Section 4.3 stationary solutions are computed for the 2D and the 3D case, showing that the anisotropy formulas are well reflected in equilibrium shapes. These shapes are also observed during coarsening on large domains in Section 4.4. Above a critical height Ostwald ripening is observed and at later times the number of islands decreases like a power law. Finally, in Section 4.5, an atomic flux is added to the simulations and some runs are compared to experiments. Certain important features of Stranski-Krastanov systems such as Ge/Si are visible, in particular the island density grows for increased deposition rates. Hundreds of dots can be simulated with a pseudospectral method since the reduced model is a self-contained PDE that generically fits to Fourier based methods.

4.1 Derivation of the QDM equation

To use the general evolution equation (1.7) with a randomly perturbed flux (1.10), a realistic chemical potential reflecting the effects that appear during QD self-assembly has to be defined. Since in heteroepitaxy bulk stresses compete with the surface energy, it has the twofold form

$$\mu = \mathcal{E}_{sed} + \mathcal{E}_{surf} \quad ,$$

where \mathcal{E}_{sed} is the strain energy density evaluated at the free surface (1.25), which is governed by the linear elasticity equations that have been introduced in Section 1.3. The other term is subdivided into three terms

$$\mathcal{E}_{surf} = \mathcal{E}_{\kappa} + \mathcal{E}_{wet} + \mathcal{E}_{anis} \quad ,$$

which, as discussed in Section 1.2, is a result of a surface energy model SE^{III} , $\gamma = \gamma(h, h_x, h_y)$. The first term \mathcal{E}_{κ} appears for any possible surface energy under consideration, \mathcal{E}_{wet} is responsible for the creation of a thin layer connecting the dots. The term for the anisotropy \mathcal{E}_{anis} results from the slope-dependency which defines preferred orientations of the surface. In this model it is renounced to use a Wilmore regularization. It will be shown that even small anisotropy coefficients are sufficient to describe 'nearly faceted' islands. The terminology 'faceted' will be used repeatedly, although the preferred orientations do not appear perfectly flat in the simulations. However, the deviation from perfect, nonsmooth facets with edges is not very big, on the other side dealing with more pronounced edges may become problematic, especially when it comes to numerical implementations. A derivation with the additional smoothing term (2.2) may be carried out in a future work. Essentially a sixth order linearity would be added to the PDE and higher values for the anisotropy parameters would be chosen.

The thin-film reduction has to be applied not only to the surface energy terms as in the previous model from Chapter 2, but also to the elasticity equations. This is a rather technical work that has been presented by Tekalign and Spencer [102]. The results are reproduced in more detail than in the originating work in Appendix C. As shown there, the strain energy density evaluated at the surface can be expressed as

$$\mathcal{E}_{sed} = \mathcal{E}_{sed}^{base} \bar{\mathcal{E}}_{sed} = \mathcal{E}_{sed}^{base} (1 + \alpha \mathcal{F}^{-1}[-\tilde{e}k\mathcal{F}[H]]) + \mathcal{O}(\alpha^2) \quad , \quad (4.1)$$

when the elasticity equations from Section 1.3 are used and suitable asymptotic expansions are carried out. Here H is the nondimensional form of the surface h , the material constant \tilde{e} is introduced in formula (C.23) and $k = \sqrt{k_1^2 + k_2^2}$ is the length of the vector of two wave numbers (k_1, k_2) that appear in the two dimensional Fourier transform \mathcal{F} and its inverse \mathcal{F}^{-1} . The nondimensionalization is achieved by using the expression \mathcal{E}_{sed}^{base} that has been derived in Section 1.3.1 as solution for the base state. Expression (4.1) and the characteristic scales are used in the following to simplify a model covering the most important effects in heteroepitaxy. Additionally the reduction of the surface energy terms is carried out. As result a final, self-contained PDE describing the growth of self-assembled QDs is obtained. The analysis in Chapter 4 will show that it is indeed a suitable model for the Ge/Si system.

One big step towards the derivation of a reduced model for heteroepitaxy is made by identifying the $\mathcal{O}(\alpha)$ coefficient in the the strain energy density expansion (4.1). Next the expansion terms for the surface energy \mathcal{E}_{surf} have to be calculated. The small slope reduction is carried out similarly as in the derivation of the HCCH equation in Section 2.1.1. Here the surface energy is kept more general than in the work by Korzec and Evans [56], where a quadruple well potential is used to model the anisotropy of Ge/Si(001) QDs. Furthermore a randomly perturbed deposition flux is taken into account.

The surface energy is defined as a variation of the boundary layer formula

$$\gamma(h, h_x, h_y) = \frac{1}{2}(\gamma^f(h_x, h_y) + \gamma^s) + (\gamma^f(h_x, h_y) - \gamma^s) \frac{1}{\pi} \arctan(h/b) \quad (4.2)$$

that was discussed by Spencer as special case of a general class of boundary-layer transition models [93]. The explicit choice of the arctan function has been made before by Kutka and Freund [59]. The behavior of function (4.2) is sketched in Figure 4.1. The smooth transition of the surface energy of the substrate γ^s to the surface energy of the film γ^f is given by incorporating the arctan function that varies with height. Depending on the orientation of the film, a different value of γ^f is adopted, so preferred facets have a smaller value than those orientations not preferred (also called forbidden orientations). The transition between film and substrate takes place on a small transition length scale b . γ^f is similar to the formula in Section 1.2.2, though here without the edge regularization term

$$\gamma^f(h_x, h_y) = \gamma_0 \bar{\gamma}(h_x, h_y) = \gamma_0 (1 + \mathcal{W}(h_x, h_y)) \quad . \quad (4.3)$$

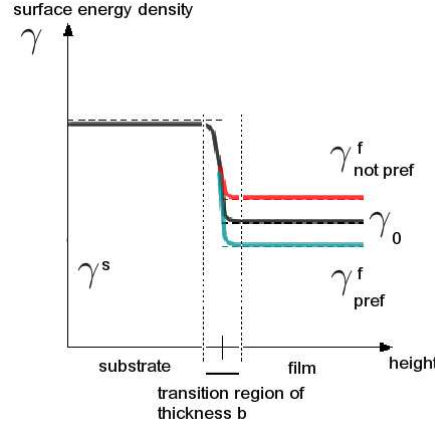


Figure 4.1: Boundary layer formula with isotropic surface energy of the substrate γ^s and different anisotropy states for the film. The $\{001\}$ orientation with surface energy γ_0 is in between a preferred energy for a facet, γ_{pref}^f , and a not preferred orientation with surface energy $\gamma_{notpref}^f$.

The nondimensionalized surface energy is $\bar{\gamma} = 1 + \mathcal{W}$ and the nondimensionalized anisotropy term can be written as

$$\mathcal{W}(h_x, h_y) = \sum_{k=2}^N \sum_{j=0}^k g_{kj} h_x^j h_y^{k-j} . \quad (4.4)$$

A slight change has been made in comparison to equation (1.24). The sum is taken to be finite, the first index starts at $k = 2$, because the constant values are collected in γ_0 , the surface energy density of a horizontally oriented film, and here $[g_{kj}] = 1$. For a quadruple well that leads to faceted pyramidal quantum dots [56], one could set

$$N = 4, g_{20} = g_{02} = -2G, g_{40} = g_{04} = \tilde{G}$$

and $g_{kj} = 0$ for all other index pairs (k, j) . Then

$$\mathcal{W}(h_x, h_y) = \tilde{G}(h_x^4 + h_y^4) - 2G(h_x^2 + h_y^2), \quad \tilde{G}, G > 0 . \quad (4.5)$$

However, the general form (4.4), which allows for various anisotropies, is used for the rest of this chapter. The expansions of the terms $\mathcal{E}_\kappa, \mathcal{E}_{wet}$ and \mathcal{E}_{anis} defined by the formulas (1.15), (1.17) and (1.18), respectively, will be determined. A restriction on the polynomial is $\gamma^f \rightarrow \infty$ for $h_x, h_y \rightarrow \pm\infty$. In this way high slopes, which are not allowed to be preferred in any case when using a small slope approximation, are punished.

The terms $\partial_{h_x}\gamma$ and $\partial_{h_y}\gamma$ appearing in the chemical potential (1.18) are given as derivatives of the anisotropy function \mathcal{W}

$$\nabla_{\nabla h}\gamma = \begin{pmatrix} \partial_{h_x} \\ \partial_{h_y} \end{pmatrix} \gamma = \gamma_0 \Psi(b, h) \nabla_{\nabla h} \mathcal{W} , \quad (4.6)$$

scaled by the transition function

$$\Psi(b, h) = \frac{1}{2} + \frac{1}{\pi} \arctan(h/b) \quad . \quad (4.7)$$

The derivative is

$$\nabla_{\nabla h} \mathcal{W} = \left(\frac{\sum_{k=2}^N \sum_{j=1}^k g_{kj} j h_x^{j-1} h_y^{k-j}}{\sum_{k=2}^N \sum_{j=0}^{k-1} g_{kj} (k-j) h_x^j h_y^{k-j-1}} \right) \quad . \quad (4.8)$$

After nondimensionalization of the evolution equation, expansions will be used to identify small terms that are then neglected. For the application of the small slope reduction the thin-film assumption has to hold. This is reasonable for several systems, however, the focus lies on the epitaxial pair Ge/Si. Drucker writes, as also described in Section 0.4, that pyramidal Ge/Si quantum dots are flat [23]. Small bumps — prepyramids — are formed in the first stage. These grow or collapse, they evolve to pyramids with $\{105\}$ facets that undergo further coarsening in an Ostwald ripening process. Further evolution to dome-like dots of bigger sizes is not considered here, so that the basis lengths of the dots remain large in comparison to their height for the time window of interest.

As for the space variables in the HCCH equation derivation, a generic scaling under the thin-film assumption is

$$\begin{aligned} h &= H_0 H = \alpha L H, \quad z = \alpha L Z, \quad (x, y) = (LX, LY), \\ t &= \tau T, \quad u_i(x, y, z) = L U_i(X, Y, Z) \quad , \end{aligned}$$

where the scaling for the displacements u_i is used in Appendix C to derive an expansion for the strain energy density. Furthermore the transition thickness is chosen orders of magnitude smaller, it is scaled by

$$b = L \alpha^3 \bar{b} \quad ,$$

so that the leading order of the wetting term \mathcal{E}_{wet} will be of the same order as the surface energy term \mathcal{E}_κ . To guarantee that the overall reduced PDE reflects the anisotropic behavior anticipated, orientation dependent variations have to be reflected in the leading order term of \mathcal{E}_{anis} . Therefore assumption (2.9) from the first model is used. In this way the slope polynomial becomes $\mathcal{W} = \alpha^2 W$ with W defined by (2.10). From the nondimensionalization of the chemical potential

$$\mu = \frac{\gamma_0}{L} \bar{\mu}, \quad \bar{\mu} = \bar{\mathcal{E}}_{sed} + \bar{\mathcal{E}}_\kappa + \bar{\mathcal{E}}_{wet} + \bar{\mathcal{E}}_{anis} \quad ,$$

and from the natural scalings

$$\sigma_{ij} = \mathcal{E}_{sed}^{base} \bar{\sigma}_{ij}, \quad \kappa = \frac{1}{L} \bar{\kappa}, \quad \gamma = \gamma_0 \bar{\gamma}, \quad \nabla_s^2 = \frac{1}{L^2} \bar{\nabla}_s^2 \quad ,$$

one can derive the characteristic length and time scales

$$L = \frac{\gamma_0}{\mathcal{E}_{sed}^{base}} \quad \text{and} \quad \tau = \frac{L^4}{\mathcal{D} \gamma_0} \quad . \quad (4.9)$$

Evolution equation (1.11) in nondimensional form becomes

$$H_T = \sqrt{1 + \alpha^2(H_X^2 + H_Y^2)} \frac{1}{\alpha} (\bar{\nabla}_s^2 (\bar{\mathcal{E}}_{sed} + \bar{\mathcal{E}}_\kappa + \bar{\mathcal{E}}_{wet} + \bar{\mathcal{E}}_{anis}) + \bar{f}) \quad ,$$

with the constituent potential terms

$$\begin{aligned} \bar{\mathcal{E}}_{sed} &= \frac{1}{2} \sum_{i,j} \bar{\sigma}_{ij} \epsilon_{ij} \quad , \\ \bar{\mathcal{E}}_\kappa &= -\bar{\gamma} \bar{\kappa} \quad , \\ \bar{\mathcal{E}}_{wet} &= \frac{(\gamma^f - \gamma^s) \alpha \bar{b}}{\gamma_0 \pi (\alpha^4 \bar{b}^2 + H^2) \sqrt{1 + \alpha^2 |\bar{\nabla} H|^2}} \quad , \end{aligned} \tag{4.10}$$

$$\begin{aligned} \bar{\mathcal{E}}_{anis} &= -2\alpha \frac{(H_X H_{XX} + H_X H_{XY}) \partial_{H_X} \mathcal{W} + (H_Y H_{YY} + H_Y H_{XY}) \partial_{H_Y} \mathcal{W}}{(1 + \alpha^2 (H_X^2 + H_Y^2))^{1/2}} \tag{4.11} \\ &\quad - \frac{1}{\alpha} (1 + \alpha^2 (H_X^2 + H_Y^2))^{1/2} (\partial_X [\Psi \partial_{H_X} \mathcal{W}] + \partial_Y [\Psi \partial_{H_Y} \mathcal{W}]) \quad , \end{aligned}$$

where in the last expression the transition function with rescaled arguments $\Psi = \Psi(L\alpha^3 \bar{b}, H_0 H)$ has been used. The flux term is

$$\bar{f} = \tilde{F} \frac{-\alpha r_1 H_X - \alpha r_2 H_Y + r_3}{|w|}$$

with the dimensionless deposition number

$$\tilde{F} = \frac{FL^3}{\mathcal{D}\gamma_0} \quad . \tag{4.12}$$

Here, the randomly disturbed vector is $w = (r_1, r_2, r_3)^T$, defined as in equation (1.10).

Now all terms are expanded with respect to the small parameter α . In particular the leading order terms of the nondimensionalized chemical potential

$$\bar{\mu} = \bar{\mu}^{(0)} + \alpha \bar{\mu}^{(1)} + \mathcal{O}(\alpha^2)$$

and for the flux

$$\bar{f} = \bar{f}^{(0)} + \alpha \bar{f}^{(1)}$$

will be determined. Derivative operators such as the nabla operator $\nabla = (\partial_X, \partial_Y)^T$ or the Laplacian ∇^2 are from now on defined in the (X, Y) variables. The surface Laplacian $\bar{\nabla}_s^2$ can be expanded as before to a standard Laplacian plus higher order perturbations (see equation (2.8)), so that to order α the evolution equation can be written as

$$H_T = \nabla^2 \left(\frac{1}{\alpha} \bar{\mu}^{(0)} + \bar{\mu}^{(1)} \right) + \frac{1}{\alpha} \bar{f}^{(0)} + \bar{f}^{(1)}. \tag{4.13}$$

In the following paragraphs the leading order terms of the chemical potential that can be inserted into the above equation (4.13) are derived.

The strain energy density terms $\bar{\mathcal{E}}_{sed}^{(0)}, \bar{\mathcal{E}}_{sed}^{(1)}$:

The expansion

$$\bar{\mathcal{E}}_{sed} = \bar{\mathcal{E}}_{sed}^{(0)} + \alpha \bar{\mathcal{E}}_{sed}^{(1)} + \mathcal{O}(\alpha^2) \quad .$$

is given with formula (4.1), it yields the coefficients

$$\bar{\mathcal{E}}_{sed}^{(0)} = 1 \quad \text{and} \quad \bar{\mathcal{E}}_{sed}^{(1)} = \mathcal{F}^{-1}[-\tilde{e}k\mathcal{F}[H]] \quad . \quad (4.14)$$

The surface energy terms $\bar{\mathcal{E}}_{\kappa}^{(0)}, \bar{\mathcal{E}}_{\kappa}^{(1)}$:

To leading order in α the mean curvature is just the Laplacian

$$\bar{\kappa} = \alpha \bar{\kappa}^{(1)} + \mathcal{O}(\alpha^3), \quad \bar{\kappa}^{(1)} = \nabla^2 H \quad . \quad (4.15)$$

The overall expansion for the surface energy term \mathcal{E}_{κ} becomes

$$\begin{aligned} \bar{\mathcal{E}}_{\kappa} &= - \left\{ \frac{1}{2} \frac{\gamma_0 + \gamma^s}{\gamma_0} + \frac{\tilde{\gamma}}{\bar{b}} \arctan \left(\frac{H}{\alpha^2 \bar{b}} \right) \right\} \bar{\kappa}^{(1)} \alpha + \mathcal{O}(\alpha^3) \\ &= -\alpha \bar{\kappa}^{(1)} + \mathcal{O}(\alpha^2) \quad , \end{aligned}$$

with $\tilde{\gamma} = \bar{b}(\gamma^s - \gamma_0)/(\gamma_0\pi)$. Usually $\tilde{\gamma} > 0$, when a film covering the substrate is favorable. The coefficients in the expansion are

$$\bar{\mathcal{E}}_{\kappa}^{(0)} = 0 \quad \text{and} \quad \bar{\mathcal{E}}_{\kappa}^{(1)} = -\nabla^2 H \quad . \quad (4.16)$$

The wetting energy terms $\bar{\mathcal{E}}_{wet}^{(0)}, \bar{\mathcal{E}}_{wet}^{(1)}$:

\mathcal{E}_{wet} from equation (4.10) is expanded to

$$\bar{\mathcal{E}}_{wet} = \alpha \frac{-\tilde{\gamma}}{H^2} \left(1 - \frac{\alpha^2 |\nabla H|^2}{2} \right) + \mathcal{O}(\alpha^4) \quad ,$$

so the the coefficients in the expansion

$$\bar{\mathcal{E}}_{wet} = \bar{\mathcal{E}}_{wet}^{(0)} + \alpha \bar{\mathcal{E}}_{wet}^{(1)} + \mathcal{O}(\alpha^2)$$

are

$$\bar{\mathcal{E}}_{wet}^{(0)} = 0 \quad \text{and} \quad \bar{\mathcal{E}}_{wet}^{(1)} = -\frac{\tilde{\gamma}}{H^2} \quad . \quad (4.17)$$

The anisotropy terms $\bar{\mathcal{E}}_{anis}^{(0)}, \bar{\mathcal{E}}_{anis}^{(1)}$:

The coefficients for the anisotropy term

$$\bar{\mathcal{E}}_{anis} = \bar{\mathcal{E}}_{anis}^{(0)} + \alpha \bar{\mathcal{E}}_{anis}^{(1)} + \mathcal{O}(\alpha^2)$$

are determined now. Therefore the fractions and the transition function in (4.11) are expanded

$$\begin{aligned} \bar{\mathcal{E}}_{anis} = & -2\alpha \left(1 - \alpha^2 \frac{H_X^2 + H_Y^2}{2} \right) \left(1 - \alpha^2 \frac{\bar{b}}{H} \right) \{ (H_X H_{XX} + H_X H_{XY}) \partial_{H_X} \mathcal{W} \\ & + (H_Y H_{YY} + H_Y H_{XY}) \partial_{H_Y} \mathcal{W} \} + \mathcal{O}(\alpha^3) \\ & - \frac{1}{\alpha} \left(1 + \alpha^2 \frac{H_X^2 + H_Y^2}{2} \right) \left(\partial_X \left[(1 - \alpha^2 \frac{\bar{b}}{H}) \partial_{H_X} \mathcal{W} \right] + \partial_Y \left[(1 - \alpha^2 \frac{\bar{b}}{H}) \partial_{H_Y} \mathcal{W} \right] \right) . \end{aligned}$$

The choice of \mathcal{W} (2.10) gives the leading order expression

$$\bar{\mathcal{E}}_{anis}^{(1)} = -\frac{1}{\alpha^2} \nabla \cdot \nabla_{\nabla H} \mathcal{W}(H_X, H_Y) = -\nabla \cdot \nabla_{\nabla H} W(H_X, H_Y) \quad . \quad (4.18)$$

The deposition terms $\bar{f}^{(0)}, \bar{f}^{(1)}$:

Finally the deposition terms can be read off from

$$\begin{aligned} \bar{f} &= \tilde{F} \frac{-\alpha r_1 H_X - \alpha r_2 H_Y + r_3}{|w|} \\ &= \frac{\tilde{F} r_3}{|w|} - \alpha \frac{\tilde{F}}{|w|} (r_1 H_X + r_2 H_Y) \quad , \end{aligned}$$

giving

$$\bar{f}^{(0)} = \frac{\tilde{F} r_3}{|w|} \quad (4.19)$$

$$\text{and } \bar{f}^{(1)} = -\frac{\tilde{F}}{|w|} (r_1 H_X + r_2 H_Y) \quad . \quad (4.20)$$

At this point it should be recalled that the flux has been chosen such that it models a perturbed beam of atoms which is oriented in the $(0, 0, -1)$ direction. Therefore the time-dependent vector $w = w(t) = (r_1, r_2, r_3)$ has been defined, where $r_1 = r(0, \sigma_1), r_2 = r(0, \sigma_1), r_3 = r(1, \sigma_2)$ and $r(\tilde{\mu}, \tilde{\sigma})$ denotes a Gaussian random number with expectation $\tilde{\mu}$ and standard deviation $\tilde{\sigma}$.

The quantum dot model (QDM) evolution equation:

Using $\nabla^2 \mu^{(0)} = 0$ the evolution equation (4.13) becomes

$$H_T = \nabla^2 (\bar{\mathcal{E}}_{sed}^{(1)} + \bar{\mathcal{E}}_{\kappa}^{(1)} + \bar{\mathcal{E}}_{wet}^{(1)} + \bar{\mathcal{E}}_{anis}^{(1)}) + \bar{f}^{(0)} / \alpha + \bar{f}^{(1)} \quad . \quad (4.21)$$

Insertion of the derived terms (4.14), (4.16), (4.17), (4.18), (4.19) and (4.20) into (4.21) results in the final evolution equation

$$H_T = \nabla^2 \left(\mathcal{F}^{-1} [-\tilde{e} k \mathcal{F}[H]] - \nabla^2 H - \frac{\tilde{\gamma}}{H^2} - \nabla \cdot \nabla_{\nabla H} W(H_X, H_Y) \right) + \frac{\tilde{F} r_3}{|w|} - \frac{\tilde{F}}{|w|} (r_1 H_X + r_2 H_Y) \quad , \quad (4.22)$$

where now

$$\tilde{F} = \frac{FL^4}{\mathcal{D}\gamma_0 H_0} \quad . \quad (4.23)$$

In the following this PDE is discussed in many details. For the case without deposition a linear stability analysis will show the destabilizing properties of the anisotropy. Stationary solutions are computed to show the actual effect of the anisotropy. Then simulation results are presented on large domains. Computations with atomic flux are compared to real Stranski-Krastanov growth.

After the derivation of a PDE it has to be proven that the model indeed reflects the anticipated effects. This is done in the following sections for the derived model for heteroepitaxial growth — the QDM equation (4.22) — by appropriate analysis and numerical simulations. In Section

4.2 a linear stability analysis for the model in absence of deposition shows how the effects of stresses due to lattice misfit, wetting interactions, surface diffusion and anisotropy influence the stability of planar surfaces. In particular it explains that stronger anisotropies make flat films less stable and that above a certain critical anisotropy number an infinite range of wave numbers is unstable.

In Section 4.3 stationary solutions are analyzed on the influence of the anisotropy strength. In 2D triangular shapes are obtained that do not further change after sufficiently long time of evolution. Additionally the same shapes are computed as numerical solutions to an ODE supporting the correctness of the numerical method. In 3D various shapes are observed — dependent on the specific definition of the anisotropy coefficients. In Section 4.4 a pseudospectral method is used to compute the evolution of the surface on large domains. As in the epitaxy results by IBM (see introduction, i.e. Figures 3 and 4), also in the simulations the typical Ostwald ripening behavior is observed. At the expense of the bigger dots that continue growing, smaller islands are absorbed. It is found that the number of islands per unit volume decreases like a power law. Finally, in Section 4.5, deposition is added to the model which is necessary to compare the results with experiments. The shapes are similar as before, but now indeed a Stranski-Krastanov growth mode can be observed. As expected by the precedent results, below a critical thickness flat films are stable to perturbations with arbitrary wave numbers. Qualitative agreement between simulations and experiments is observed. Faceting remains a feature as without the deposition term and also a wetting layer forms. For the same amount of deposited material it is shown that an increased deposition rate yields more dots with smaller base lengths and less wetted regions.

For the following three sections it is assumed that the flux is absent, $f = 0$ (so that $f_k = 0, k = 1, 2, 3$), then the evolution equation writes

$$H_T = \nabla^2 \left(\mathcal{F}^{-1}[-\tilde{e}k\mathcal{F}[H]] - \nabla^2 H - \frac{\tilde{\gamma}}{H^2} - \nabla \cdot \nabla_{\nabla H} W(H_X, H_Y) \right) . \quad (4.24)$$

In this discussion mass is conserved, which is not the case with a deposition flux. It will be added again after carrying out a stability analysis and coarsening studies in two and three dimensions.

4.2 Linear stability analysis

A linear stability analysis can yield a priori information about the behavior of the surface evolution, even if the underlying equation is nonlinear. When a flat film is perturbed by normal modes, a dispersion relation shows which wave lengths are visible during the first stage of evolution. Such a study has been carried out for equation (4.24) without the anisotropy term by Tekalign and Spencer [102], and with a particular anisotropy term which is suitable to model pyramidal shapes by Korzec and Evans [56]. Here the discussion is slightly more general since the anisotropy is kept less specific. The critical thickness of a flat film decreases as the unstable regime grows with increasing anisotropy strength. Above a critical value an infinite range of wave

numbers is unstable. This results from the following conclusion.

Proposition 22 *The dispersion relation for the QDM equation (4.24) writes*

$$\sigma = -k^4 + \tilde{e}k^3 - \frac{2\tilde{\gamma}}{\bar{H}^3}k^2 - 2k^2(G_{20}k_2^2 + G_{21}k_1k_2 + G_{22}k_1^2) \quad . \quad (4.25)$$

Proof The normal mode ansatz

$$H = \bar{H} + \delta\check{H}, \quad \check{H} = e^{\sigma t + ik_1 X + ik_2 Y} \quad , \quad (4.26)$$

with a small $\delta \ll \bar{H}$ and the wave numbers k_1, k_2 , is inserted into evolution equation (4.24). The four constituent terms are analyzed separately.

Insertion of the ansatz (4.26) into the surface term $\bar{\mathcal{E}}_\kappa^{(1)}$ gives

$$\begin{aligned} \bar{\mathcal{E}}_\kappa^{(1)} = -\nabla^2 H &= -\delta(\partial_{XX} + \partial_{YY})e^{\sigma t + ik_1 X + ik_2 Y} \\ &= \delta k^2 \check{H} \quad , \end{aligned} \quad (4.27)$$

where as before $k = \sqrt{k_1^2 + k_2^2}$. The strain energy density term gives

$$\begin{aligned} \bar{\mathcal{E}}_{sed}^{(1)} &= \mathcal{F}^{-1} [-\tilde{e}k\mathcal{F}[\bar{H} + \delta e^{\sigma t + ik_1 X + ik_2 Y}]] \\ &= \mathcal{F}^{-1} [-\tilde{e}k(\mathcal{F}[\bar{H}] + \delta e^{\sigma t} \mathcal{F}[e^{ik_1 X + ik_2 Y}])] \\ &= \mathcal{F}^{-1} [-\tilde{e}k\mathcal{F}[\bar{H}]] - \tilde{e}k\delta e^{\sigma t} \mathcal{F}^{-1} [\mathcal{F}[e^{ik_1 X + ik_2 Y}]] \\ &= -\tilde{e}k\bar{H} - \tilde{e}k\delta\check{H} \quad . \end{aligned} \quad (4.28)$$

Since the first term is constant it will vanish under differentiation and hence it can be ignored when inserted into equation (4.24).

The wetting term is expanded with respect to the small quantity δ

$$\begin{aligned} \bar{\mathcal{E}}_{wet}^{(1)} &= -\frac{\tilde{\gamma}}{(\bar{H} + \delta\check{H})^2} \\ &= -\frac{\tilde{\gamma}}{\bar{H}^2} + 2\frac{\tilde{\gamma}}{\bar{H}^3}\delta\check{H} + \mathcal{O}(\delta^2) \end{aligned} \quad (4.29)$$

and also here the first term does not play a role for the dispersion relation.

The anisotropy term is

$$\begin{aligned} \bar{\mathcal{E}}_{anis}^{(1)} &= -\nabla \cdot \nabla_{\nabla H} W(H_X, H_Y) \\ &= -\nabla \cdot \left(\frac{\sum_{k=2}^N \sum_{j=0}^k G_{kj} j H_X^{j-1} H_Y^{k-j}}{\sum_{k=2}^N \sum_{j=0}^k G_{kj} (k-j) H_X^j H_Y^{k-j-1}} \right) \\ &= -\sum_{k=2}^N \sum_{j=0}^k G_{kj} \left(j \partial_X [H_X^{j-1} H_Y^{k-j}] + (k-j) \partial_Y [H_X^j H_Y^{k-j-1}] \right) \end{aligned} \quad (4.30)$$

and by inserting the normal mode ansatz it becomes

$$\begin{aligned} \bar{\mathcal{E}}_{anis}^{(1)} &= -\sum_{k=2}^N \sum_{j=0}^k G_{kj} (j \partial_X [(ik_1 \delta\check{H})^{j-1} (ik_2 \delta\check{H})^{k-j}] + (k-j) \partial_Y [(ik_1 \delta\check{H})^j (ik_2 \delta\check{H})^{k-j-1}]) \\ &= -\delta \{ 2G_{20} \partial_Y [ik_2 \check{H}] + G_{21} (\partial_X [ik_2 \check{H}] + \partial_Y [ik_1 \check{H}]) + 2G_{22} \partial_X [ik_1 \check{H}] \} + \mathcal{O}(\delta^2) \\ &= 2(G_{20}k_2^2 + G_{21}k_1k_2 + G_{22}k_1^2)\delta\check{H} + \mathcal{O}(\delta^2) \quad . \end{aligned}$$

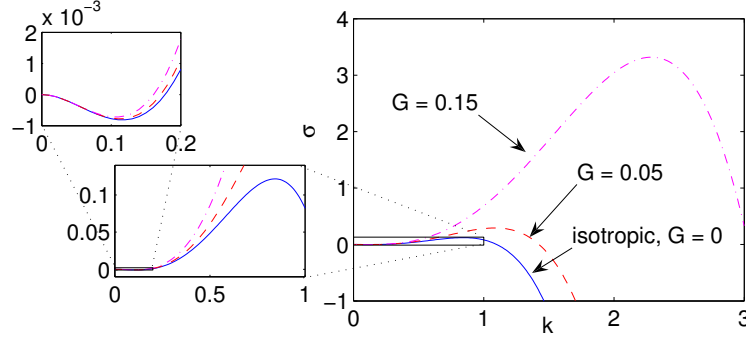


Figure 4.2: Plots for the dispersion relation (4.31) for the isotropic case and two anisotropy parameters ($G = 0, 0.05, 0.15$) with fixed flat state $\bar{H} = 0.8$. The magnifications on the left show that a local minimum is adopted for all three cases at small wave numbers.

Using (4.26) and (4.27) - (4.30) in the evolution equation (4.24) yields

$$\sigma \delta \tilde{H} = -k^2 \left(k^2 - \tilde{e}k + 2 \frac{\tilde{\gamma}}{\bar{H}^3} + 2(G_{20}k_2^2 + G_{21}k_1k_2 + G_{22}k_1^2) \right) \delta \tilde{H} \quad ,$$

and finally division by $\delta \tilde{H}$ gives (4.25). \square

Remark Assume that for materials with cubic symmetry the anisotropy constants in the X and Y directions are equal and that the crystal is aligned with those axes, $G_{20} = G_{22} = -2G$ and $G_{21} = 0$. Then

$$\sigma = (4G - 1)k^4 + \tilde{e}k^3 - \frac{2\tilde{\gamma}}{\bar{H}^3}k^2 \quad . \quad (4.31)$$

The above equation (4.31) stems from the anisotropy formula

$$W_\diamond(H_X, H_Y) = G[H_X^4 + H_Y^4 - 2(H_X^2 + H_Y^2)] \quad , \quad (4.32)$$

which has been introduced by Korzec and Evans [56] for simulations of Ge/Si(001) patterning. The following discussion relates to this quadruple well model if not stated otherwise. Figure 4.2 shows a plot of the corresponding dispersion relation (4.31). For small wave numbers the films are stable and an unstable regime for intermediate wave numbers grows as the anisotropy parameter G is increased. The maximal value is attained at a larger wave number and with higher modulus when G is growing. In fact for $G > 0.25$, the sign of the highest power of the polynomial (4.31) switches and the unstable regime becomes infinite. For the case that stronger anisotropy would be sought, an ansatz as for the model for the faceting of growing surfaces from Section 2.1 could be incorporated. A regularization term in the surface energy would prevent the unwanted and unphysical backward diffusion for $G > 0.25$.

The critical thickness below which all flat films are stable depends on G . It becomes larger, the smaller the anisotropy is. This can be read off from

$$H_c = H_c(G) = 2 \left(\frac{\tilde{\gamma}(1 - 4G)}{\tilde{e}^2} \right)^{1/3} \quad , \quad (4.33)$$

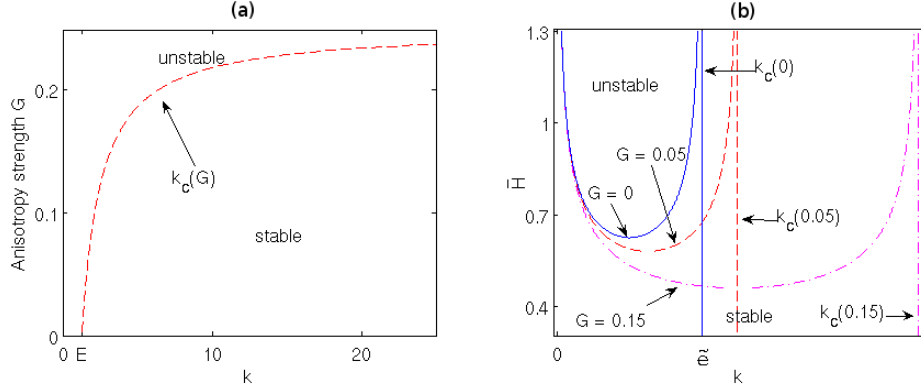


Figure 4.3: Results from the dispersion relation (4.31): (a) The critical number k_c as function of the wave number modulus k . With increasing anisotropy strength G the stable regime shrinks until at $G = 0.25$ the unstable interval becomes infinite. (b) Stability regime plot for three values of G , $G = 0, 0.05, 0.15$; it shows that for increasing anisotropy parameter the critical thickness H_c shrinks while the unstable regime grows. The critical wave numbers $k_c(G)$ for the three cases are depicted as vertical lines.

with a maximal value obtained in the isotropic case $H_c^{max} = H_c(0) = 2(\tilde{\gamma}/\tilde{e}^2)^{1/3}$.

The corresponding critical wave number modulus k_c above which all thicknesses are stable is

$$k_c = k_c(G) = \frac{\tilde{e}}{1 - 4G} \quad ,$$

which is minimal for $G = 0$, $k_c^{min} = k_c(0) = \tilde{e}$. The results are summarized visually in Figure 4.3, where (a) depicts how $k_c \rightarrow \infty$ as $G \rightarrow 0.25$, while (b) shows how the unstable regime grows and the critical thickness decreases for increasing anisotropy strength (in the figure this is just the value of \bar{H} on the vertical axis where the transition from stable wave numbers only to existing intervals of unstable wave numbers happens). Note that when G becomes bigger, higher frequencies become unstable. Starting a time dependent simulation with a planar initial profile that is above the critical thickness $H_c(G)$ and which is perturbed by small random values should show more oscillations for bigger G , since the high frequency components of the initial condition are unstable. Indeed this is exactly the behavior observed and described in following sections.

4.3 Periodic stationary solutions

Stationary solutions to a PDE involving time often yield information about the patterning during time-dependent evolution. In this section one-island steady states of equation (4.24) are computed consecutively in two and three dimensions. These equilibrium states should reflect the anisotropic surface energy — and indeed its impact is visible when comparing the shapes with the evolving patterns in the following Sections 4.4 and 4.5. For the simulations the material constants for the Ge/Si system, which will be introduced in Section 4.5, were used

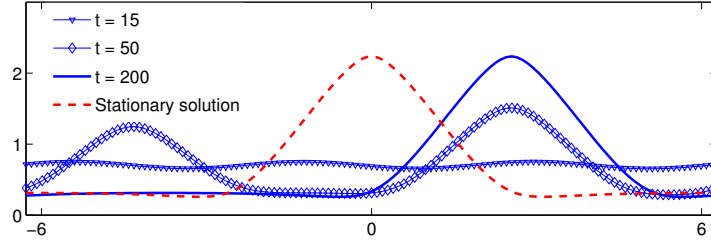


Figure 4.4: Growth of a two-dimensional solid film governed by equation (4.34) with anisotropy strength $G = 0.1$. Initially a uniform profile is perturbed by small random numbers. During the evolution, islands form, collapse, and the shifted, triangularly shaped profile approaches that given by the steady state solution obtained by solving the ODE (4.36) (dashed curve).

The two-dimensional case

Here a further simplified model is considered by ignoring one of the two lateral dimensions. By using a double-well potential for the slopes (formula (4.32) with $H_Y = 0$), the quasilinear PDE

$$H_T = \partial_{XX} \left(\mathcal{F}^{-1}[-\tilde{\epsilon}|k|\mathcal{F}[H]] + (4G - 12GH_X^2 - 1)H_{XX} - \frac{\tilde{\gamma}}{H^2} \right) \quad (4.34)$$

is obtained on the periodic domain $[0, L]$. Note that in this dimension-reduced case the absolute value of the wave numbers has to be taken for the inverse Fourier transform in the elasticity term. This is crucial for the simulations, where also wave numbers smaller than zero are allowed. In Figure 4.4 a typical evolution of the 2D film is depicted. Starting from a flat state $H(X, 0) = 0.7 + rd$, where rd is a random number with mean zero and amplitude 0.0001, on a rather small domain $[-2\pi, 2\pi]$, the perturbation evolves into small oscillations that merge to two small, more rounded humps. These finally shrink to one stationary island. By $T = 200$ the numerical method produces film profiles that are stationary in the sense that successive iterates H_k and H_{k+1} relatively differ by less than a small threshold $\bar{\epsilon}$ times the time step dT

$$\frac{|H_{k+1} - H_k|}{|H_k|} < \bar{\epsilon} dT \quad . \quad (4.35)$$

The figure shows that due to the boundary layer formula and the differences in the surface energy of film and substrate a thin layer between the dots is created, that the anisotropy results in faceting and that the slopes of the final triangular shape are $H_X \approx \pm 1$, which is of order $\mathcal{O}(\alpha)$ in the original scales. Detailed information about the underlying numerics can be found in Chapter 5, in particular in Section 5.2, where code snippets for FFT based pseudospectral methods in Matlab are explained.

The other shape visualized in Figure 4.4 as a dashed line is the solution from the steady state problem with $H_T = 0$ in equation (4.34). It leads to a constant chemical potential, hence it has to hold

$$-H_{XX} - \tilde{\epsilon}\mathcal{F}^{-1}[|k|\mathcal{F}[H]] - \frac{\tilde{\gamma}}{H^2} - \mathcal{F}^{-1}[ik\mathcal{F}[4G(H_X^3 - H_X)]] = C \quad . \quad (4.36)$$

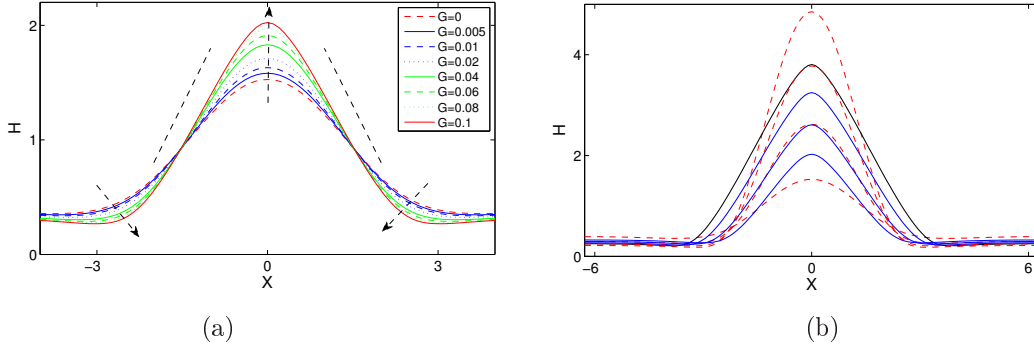


Figure 4.5: Steady profiles for periodic solutions on a 2π long interval. (a) Increasing surface energy anisotropy strength G , with fixed film volume V . (b) Increasing V from $V = 2.6\pi$ to $V = 4.8\pi$ for $G = 0.1$ leads to a family of faceted islands (solid lines). With constant surface energy, width remains approximately constant (dashed lines).

The constant C is treated as unknown in a Newton-type method that is used to satisfy (4.36) at each mesh point. As in the numerical simulations of the time-dependent system, a pseudospectral approach is chosen, so that periodic boundary conditions are the natural choice. Additionally a fixed volume V is prescribed, such that

$$\int_{-2\pi}^{2\pi} H dX = V \quad (4.37)$$

and the solution is supposed to be symmetric around $X = 0$. Both ways to compute the stationary states yield the same result, supporting the correctness and accuracy of the numerical methods. Only a phase shift relocates the two shapes by a certain amount.

The simulations for the stationary case were then used to explore the effect of the anisotropy. In Figure 4.5 (a) different solutions for various values of G are plotted. For stronger anisotropy the shapes appear more faceted and tend to have slopes ± 1 , corresponding to the minima of the anisotropy function W . In Figure 4.5 (b) a fixed value $G = 0.1$ and increasing volumes $V \in [2.6\pi, 4.8\pi]$ yield a family of triangular dots which are compared to isotropic humps with the same volumes. While the anisotropic islands increase their base width and keep their facets, for $G = 0$ this length remains constant, which is balanced by an increase of the maximal height. The shapes remain bell-shaped.

The three-dimensional case

For the three-dimensional case (4.24) stationary pyramidal structures are computed for various anisotropy formulas by running simulations with an initial profile that resembles somewhat a quantum dot, a Gaussian

$$H(X, Y, 0) = 0.5 + e^{-\left(\frac{X}{2}\right)^2 - \left(\frac{Y}{2}\right)^2} \quad (4.38)$$

As before the iterations are stopped once the relative change is smaller than a prescribed tiny threshold using (4.35). Figure 4.6 is a three-dimensional analog to Figure 4.4 for the two-

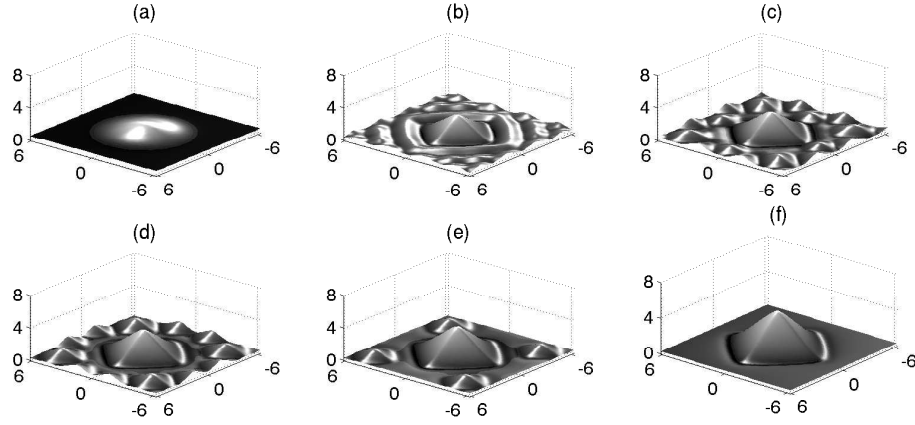


Figure 4.6: Evolution of a three-dimensional solid film governed by equation (4.24), starting with a Gaussian initial profile and with the anisotropy strength $G = 0.2$. The figures (a)-(f) correspond to the dimensionless times $T = 0, 1, 3, 5, 10, 30$.

dimensional case. The initially round, low-amplitude hump in (a) develops some oscillatory ridges around a middle island in (b). These turn into faceted pyramids and the development of a thin layer is visible in (c) and (d). The small dots, which surround the middle pyramid, shrink and are eventually absorbed by the layer (e) and (f), respectively). There remains one steady, faceted dot, which does not further change with time.

The general form of the anisotropy (2.10) also allows to model systems other than Ge/Si(001). Without much effort one can give different polynomials a trial and use a slightly adjusted numerical method to compute the dynamical behavior. To test if the theory works as expected with alternative anisotropies three other W -functions are defined

$$\begin{aligned}
 W_{\parallel}(H_X, H_Y) &= G(H_X^4 - H_Y^4 - H_X^2 + H_Y^2) \quad , \\
 W_{\diamond}(H_X, H_Y) &= G((H_X - 0.3)^4 + (H_X + 0.3)^4 + H_Y^4 - H_Y^2 - H_X^2) \quad , \\
 W_{\Delta}(H_X, H_Y) &= G(2H_X^2 H_Y^2 + H_X^4 + H_Y^4 + H_X H_Y^2 + H_X^2 H_Y - H_Y^2 - H_X^2) \quad . \quad (4.39)
 \end{aligned}$$

In Figure 4.7 the contour lines of the four introduced anisotropy formulas are visualized in H_X, H_Y plots. The outer lines correspond to bigger values of the anisotropy function and the minima are marked with small x . Beneath, four shapes of corresponding stationary solutions are visualized. They indeed reflect the positions of the minima of the anisotropy function. As initial condition the Gaussian (4.38) has been used. The computations have been carried out with a pseudospectral method that used a 64×64 grid of wave numbers and they were stopped when the convergence condition (4.35) was fulfilled. The formulas are constructions which help to verify that the reduced anisotropy term works also properly when defining other preferred orientations. However, the elasticity problem has not been adjusted for these simulations.

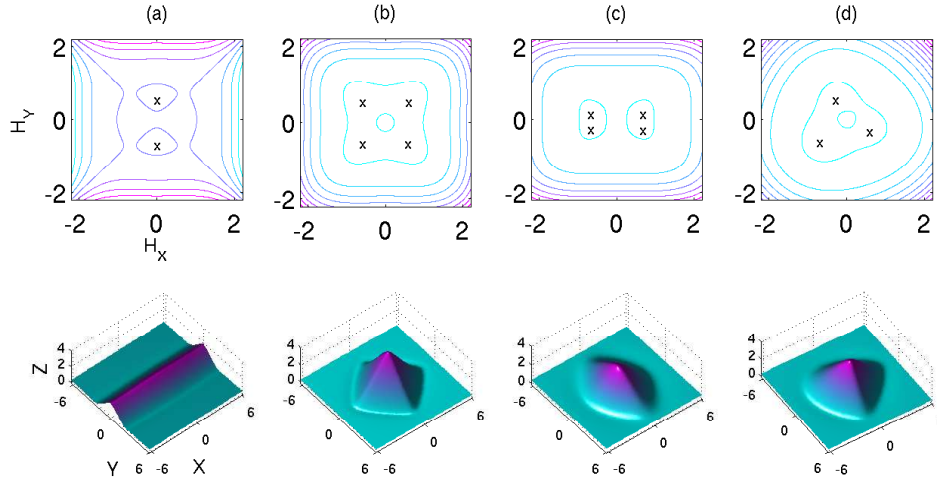


Figure 4.7: Steady profiles for periodic three-dimensional solutions. The upper row depicts the contour lines of the surface energy associated with the anisotropy functions W_{\square} , W_{\diamond} , W_{\diamond} and W_{Δ} . The lower row shows plots of corresponding three-dimensional islands. (a) Ridge; (b) Pyramid; (c) Rhombic pyramid; (d) Tetrahedron-like dot.

With all four formulas an evolution similar as in Figure 4.6 can be observed and after sufficient time a steady state is adopted. The first potential, W_{\square} , has two minima at slopes with opposite sign and results in a ridge, a quantum wire like structure, as in Figure 4.7 (a). (b) shows a Ge/Si(001) like dot based on W_{\diamond} , (c) an elongated version of (b). Here the two pairs of minima are closer together leading to a pyramid with a rhombic base. The last function W_{Δ} has three minima, one is slightly offside and deeper than the other two as shown in (d), where one can see that one side of the tetrahedron-like dot is more pronounced than the other two attributing to the difference of the minima.

The stationary shapes occur also during the time-dependent evolution. Study of the coarsening of such three-dimensional structures is investigated in the following section, just after the analysis of the long time evolution of large two-dimensional arrays. All following time-dependent simulations show that the observed stationary shapes appear scaled in size as non-steady states long before equilibrium is reached.

4.4 Evolution on big domains

The coarsening of arrays of two- and three-dimensional quantum dots is discussed in this section. First the case with one lateral dimension is considered, then the full QDM equation (4.24) is analyzed. All results are obtained with the numerical PSM which is introduced in Section 5.2. It allows to simulate very large arrays in the two-dimensional case without too high computa-

tional costs, and also for the three-dimensional case the treatable size of quantum dot arrays is astonishingly big. Computational run-time is not a major problem for the thin-film reduced model once a suitable pseudospectral scheme is set up. In related fields the problems with one lateral dimension are even further reduced. ODEs describing the evolution of the individual island positions are derived. For the CCH equation this has been done by Watson et al. [109]. The following results show that such a reduction is not necessary in 2D when reliable PSMs can be applied to simulate hundreds of dots. However, since the computational time needed in the 3D case can become large, it might be useful to set up a piecewise-affine dynamical surface (PADS) as done by Watson and Norris for a related problem [73, 108].

4.4.1 Coarsening of two-dimensional arrays

For simulations with one lateral dimension using equation (4.34) on equidistant grids with 8192 or 4096 points for domains of length 600π or 300π in dimensionless units have been used and the constant time step has been chosen to be either $dt = 0.0001$ or $dt = 0.00001$. Shapes foretold by the computed stationary solutions from the previous section are observed, differing in size. After an initial phase, where a random perturbation of a flat state above the critical thickness evolves into a surface with many humps, they evolve into triangular structures.

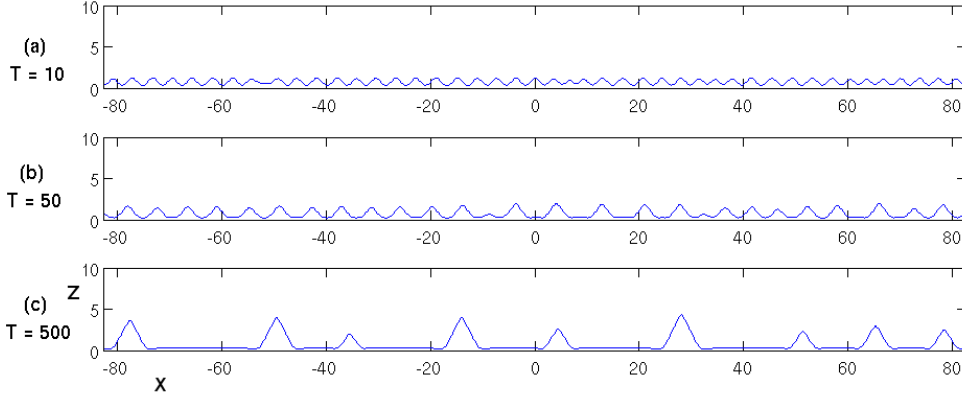


Figure 4.8: Evolution of the 2D Ge/Si(001) system at three time points on a section of an overall nearly 2000 dimensionless units long one-dimensional domain with $G = 0.15$. (a) Wrinkles appear just after starting the simulation. (b) Triangular islands and a thin layer form. (c) Further coarsening leads to separated, faceted two-dimensional dots.

A small section of the overall nearly 2000 dimensionless units long domain at three time points of one run of the simulation is plotted in Figure 4.8. The initial height of the film was chosen to be $H_0 = 0.75$ and it was randomly perturbed with deviations up to a modulus of 0.0001 and zero mean. Already in the beginning of the simulation humps start to evolve. In (a) an oscillatory surface with a wave length similar to the most critical value from the linear stability analysis

forms wrinkle patterns. In (b) the humps are already bigger and a thin layer appears. During the transition to (c), an Ostwald ripening process (survival of the fattest), where smaller dots are eaten in expense of the bigger ones, takes place. In (c) a few dots are left while the ripening process continues.

Figure 4.9 shows the same run in a space time plot on the whole domain. Brighter shades correspond to bigger film thicknesses and the vertical axis represents the time scale. The Ostwald ripening process and collapse of dots appear as white drops creeping from top down before they are absorbed by the thin layer which is black in this figure. This kind of evolution is reminiscent of coarsening in liquid films where similar plots can describe the evolution of two-dimensional droplets [39].

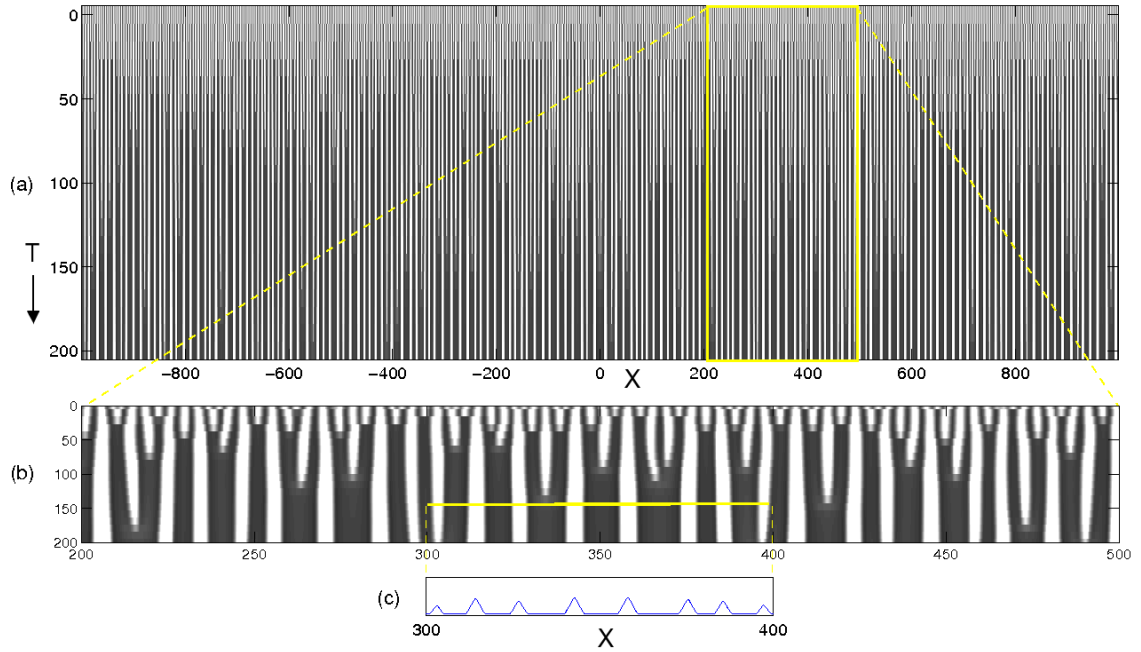


Figure 4.9: Simulation of coarsening of the 2D system. White shades correspond to thicker regions. The lower 'zebra' plot is a magnification of the marked rectangular section in the whole space time plot. Below, the shape $H(X, 500)$ at $T = 500$ is shown on a subinterval. It corresponds to one horizontal line in the above black and white plot at a certain time point.

Coarsening rates of the system can be obtained by analyzing the data in Figure 4.9 — essentially by counting islands. Therefore an island density function

$$\langle N \rangle = \langle N \rangle (t) = \frac{\text{number of islands}}{\text{domain length}} \quad (4.40)$$

is introduced. It is averaged over four independent runs for the isotropic case $G = 0$ and for the two anisotropy strengths $G = 0.05$ and $G = 0.15$ to obtain statistics for the ripening of the

surfaces. The results are shown in Figure 4.10, where the time on a logarithmic scale is plotted against the averaged characteristic density number denoted by $\langle N \rangle_a$. There appear to be two phases during the evolution, one where the island-structures form — being larger for smaller values of G — and a second where actual coarsening takes place. Surface energies that depend on orientation lead to more islands in the first stage of evolution. This is confirmed by the linear stability analysis from the last section, which has shown that for bigger values of G the most unstable wave number increases. For $G = 0.15$ the fast coarsening regime sets in quickly, while in the isotropic case this coarsening phase begins at much later times. On the other hand, once dots start to collapse, isotropic coarsening is faster than for non-zero values of G . The two-way logarithmic plot shows that at late stages the coarsening rates can be described by power laws since the graphs for $\langle N \rangle_a$ appear as straight lines.

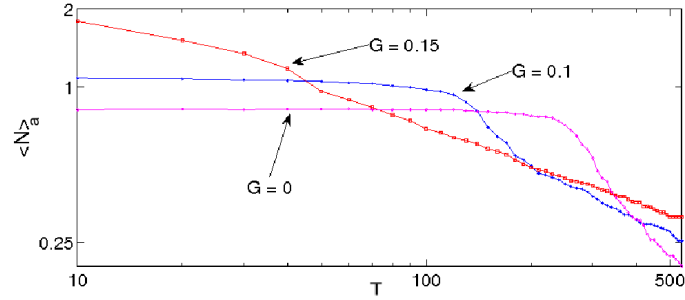


Figure 4.10: Coarsening diagram for the 2D Ge/Si system comparing dot densities for the isotropic ($G = 0$) and two anisotropic trials ($G = 0.05$ and $G = 0.15$). For each trial the island density $\langle N \rangle$ has been averaged over four runs, defining $\langle N \rangle_a$; the axes are logarithmic.

4.4.2 Three-dimensional self-assembly

Often it is difficult to set up three-dimensional simulations that are fast enough to allow for a coarsening analysis on a large time scale. Enforcedly a reduction in dimensions is applied and the simplified system is analyzed — similarly as for the QDM equation in the last section. The drawbacks of such reduced systems are that the coarsening rates are not necessarily the same when changing dimensions and especially for anisotropic problems loss of information cannot be avoided. If possible an analysis of the full equations should be accomplished. However, the 2D system can yield useful information. The derivation of a dimension reduced system is simpler and so is the numerical scheme and its implementation for simulations, which can be orders of magnitude faster than for the full model. This allows to test certain features of a new model rapidly, to tune the parameters and find optimal grid sizes that can be used similarly for the 3D system.

Now coarsening of solutions to the 3D evolution equation (4.24) is studied. The free surface depends on the lateral variables X and Y , so that $H = H(X, Y, T)$. Typical Ostwald ripening,

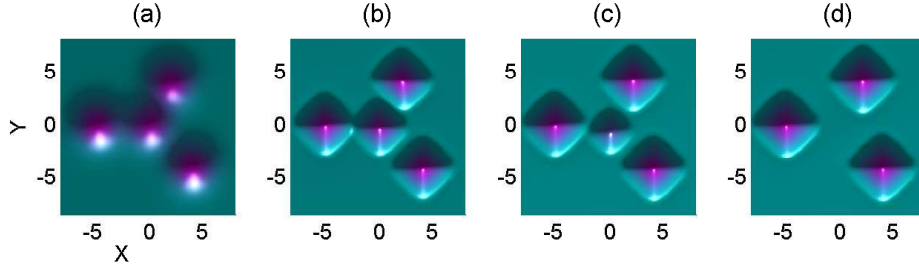


Figure 4.11: Collapse of a dot. Four islands seen from above. A darker shade (bluish) corresponds to a bigger height of the surface. The initial condition seen in (a) are four round, exponential humps. The middle island has initially a five percent smaller height than the other dots. In (b) and (c) one can see how it shrinks and finally how it is "eaten" in (d). The simulation has been carried out with $G = 0.2$. Time ($T = 0, 5, 15, 20$) and space are given here as in the other figures in dimensionless units.

coarsening of faceted nano-islands, can be simulated with an FFT-based spectral implementation using a semi-implicit Euler scheme and the discrete vectors $U \approx u$. Here an update formula for the QDM equation given in Table 5.1 in the numerics chapter has been applied. As before parameters for the Ge/Si(001) system and two different anisotropy strengths G have been used.

In Figure 4.11 a run of the PSM simulating the collapse of a dot is depicted. It reminds of the IBM experiments mentioned in the introduction, in particular Figure 4, where a similar behavior is observed. For the set-up of the simulation four initially Gaussian humps were arranged as shown in Figure 4.11 (a). The middle dot is slightly smaller than the other three islands. All of them develop facets very fast (see picture (b)). The smaller pyramid shrinks as it is absorbed by the thin layer. The shrinking and collapse is visualized on the sequence (b), (c), (d). By $T = 20$ no leftovers of the smaller dot are visible. Again this is reminiscent of Ostwald ripening and this behavior will be observed repeatedly on big domains in long-time simulations. The distances between the islands are bigger than in the pictures from the experiments. The reason for this stronger separation is the lack of a deposition flux in the simulations carried out here. The surfaces are more similar to films during annealing, where the atomic flux is already stopped. In Section 4.5 it will be shown that indeed the island density grows when a material beam is on.

Figure 4.12 shows a typical evolution at the four time points $T = 5, 50, 200, 500$ on a domain of dimensionless length 62π in each direction. The computations were carried out on 512×512 and 256×256 wave number grids, revealing the same behavior. The anisotropy strength $G = 0.2$ leads to high frequency oscillations in the first stage of the evolution as seen in the plot for $T = 5$. At $T = 50$ the faceting is pronounced and the thin layer between the dots already appears. More of the substrate is covered by a thin flat layer during the coarsening process, because the surface energy of the film is lower than that of the substrate. More and more QDs vanish as one can see comparing the surfaces at the time points $T = 50, T = 200$ and $T = 500$. The bigger islands have faceted shapes resembling the pyramids seen in experiments for the Ge/Si(001) system, or also for the GeSi films on Si [23, 32]. A section of three of the plots is depicted in Figure 4.13

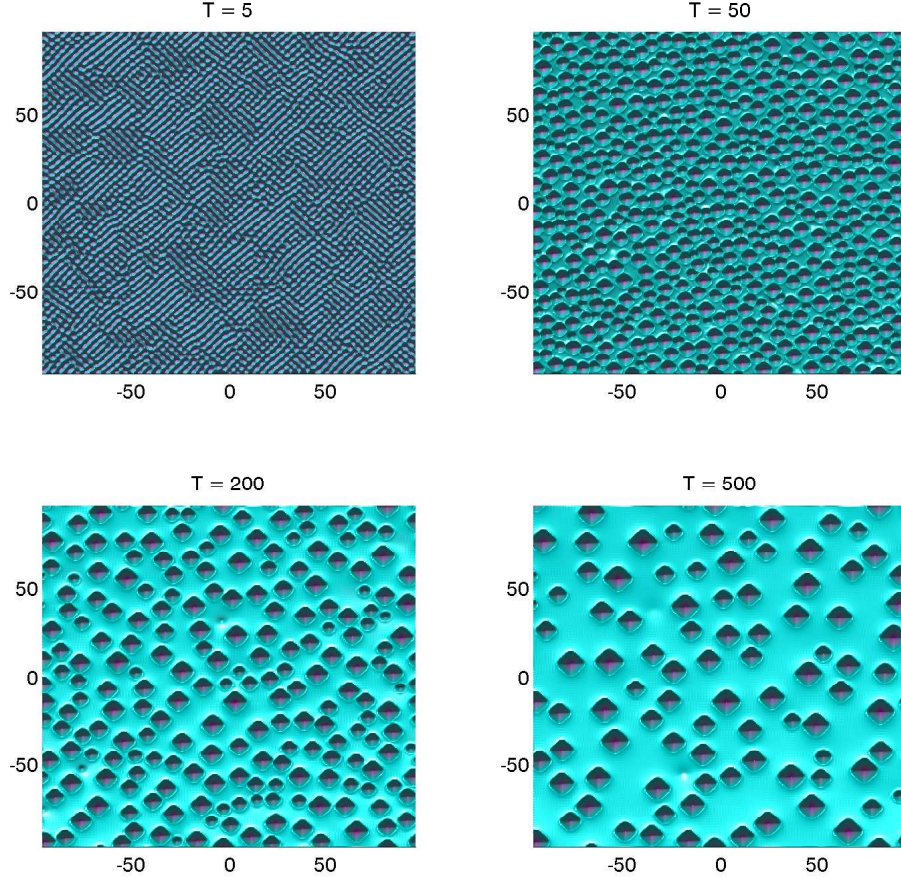


Figure 4.12: Evolution of Ge/Si(001) quantum dots without deposition seen from above. An initial small random perturbation of a flat state above the critical height evolves by self-assembly to square-based pyramids with facets. For the simulation $G = 0.2$ is used in the quadruple well formula W_{\diamond} . Note that as in the other figures in this section the X and Y variables are dimensionless units.

from a three-dimensional perspective to support better understanding of these figures.

As in the 2D case stronger anisotropy parameters lead to surfaces with oscillations of higher frequency in the first stages of the evolution and the facets are more pronounced. Figure 4.14 shows how the different anisotropy strengths influence the surfaces at later stages of the evolution. At the same point in time simulation results for $G = 0$, $G = 0.1$ and $G = 0.25$ are plotted. A few dots are enlarged for $G = 0$ and $G = 0.25$ to emphasize the effect of anisotropy. For the bigger value of G the facets are sharper and also the small islands have nearly square bases. Clearly a transition from bell-shaped structures to pyramids is visible.

To analyze coarsening rates for the same three values of G , the measure (4.40) can be used

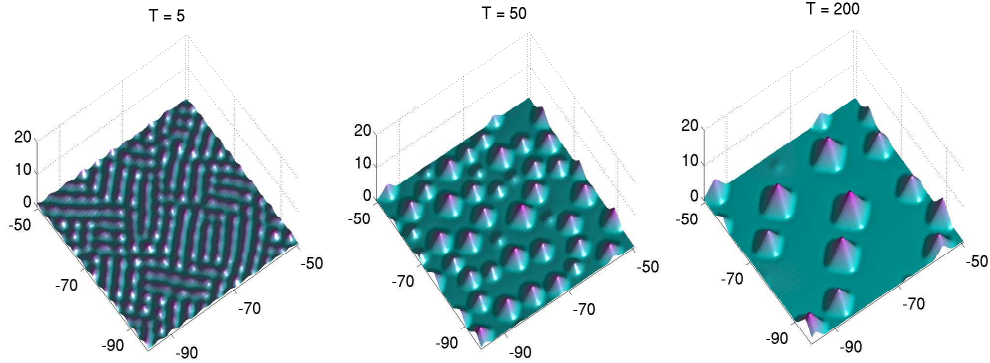


Figure 4.13: 3D sections of the the first three plots in Figure 4.12.

again, only that it has to be taken into account that the domain is two-dimensional and hence the *domain length* has to be replaced by *domain size*. Here it has 62π dimensionless units in each of the two directions.

Figure 4.15 (a) shows that the number of dots for higher values of G is bigger in early stages of evolution, confirming the prediction of the linear stability analysis. For $G = 0$, after formation of a bumpy surface, nothing relevant happens until at $T \approx 150$ coarsening sets in. It then proceeds faster than with anisotropy. It seems that the lower energy state for faceted islands slightly stabilizes the islands during ripening. For $G = 0.1$ and $G = 0.2$ similar coarsening rates are observed at later stages. The value $\langle N \rangle$ is plotted for $T \geq 250$ in a doubly logarithmic plot in (b) where the curves behave like straight lines. This indicates as in the two-dimensional case a power law behavior.

One can easily interchange the quadruple well anisotropy W_\diamond with a polynomial that more likely reflects other anisotropies. One such formula with three minima is denoted here by W_Δ . A simulation can be carried out as before with a small random perturbation of the flat state above a critical thickness as the initial state. As one can see in Figure 4.16 it leads to rather rounded oscillations which evolve to islands with three distinct orientations — where two of those are, as in the section on stationary shapes for this anisotropy formula, not that pronounced. The structures coarsen and continue to grow in a similar way as for the quadruple well potential.

This simple variation shows that it should be possible to simulate also systems like Ge/Si(111), where instead of pyramidal shapes with four facets in the same symmetry class, only three preferred directions are present in the nano-islands [68]. Since the facets here are rather curved and not symmetric, the polynomial chosen is rather academic than a realistic choice. However, it shows that the model and the numerics reflect the chosen anisotropy.

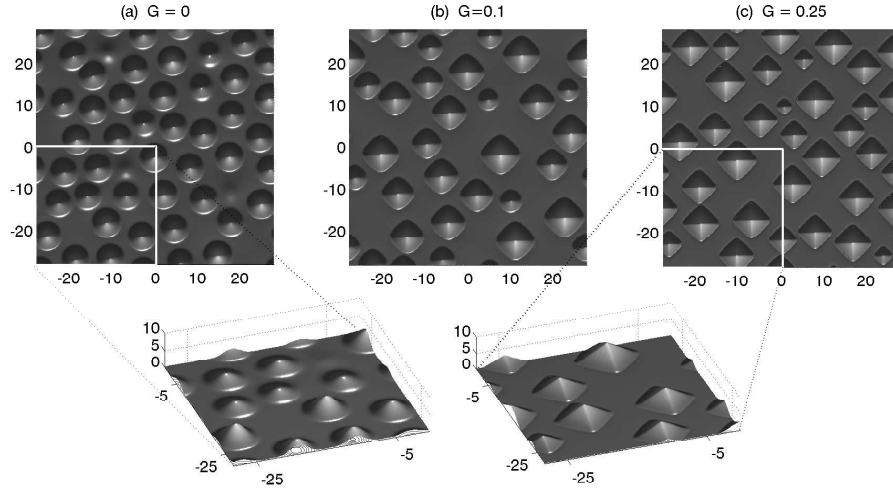


Figure 4.14: Anisotropy effect on the 3D Ge/Si(001) system. All pictures show the same time point after evolution from the same initial condition (random perturbation of a flat state above the critical thickness). The upper left is taken from a simulation with isotropic surface energy ($G = 0$) and the dots have round tips. In the other two upper pictures ($G = 0.1$ and $G = 0.25$) faceting is observed and it is stronger for the bigger anisotropy coefficient G . The two lower pictures are magnifications for $G = 0$ and $G = 0.25$, where the changed perspective shows the transition from bell shapes to pyramids when increasing G .

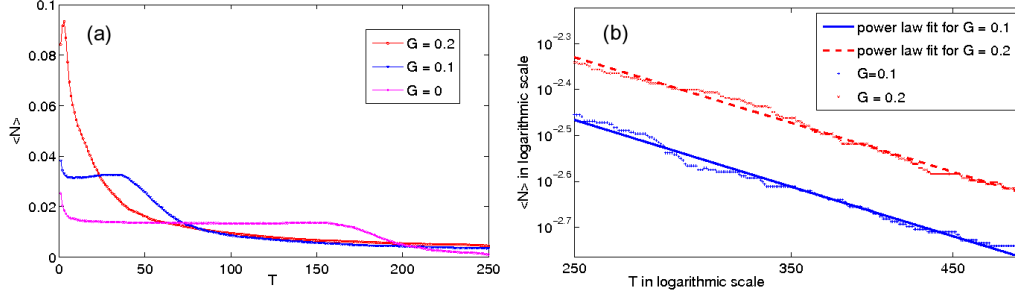


Figure 4.15: Coarsening diagram for the 3D system. The cases for no ($G = 0$), weak ($G = 0.1$) and strong ($G = 0.25$) anisotropy are plotted in (a). In (b) the data for the late stage of coarsening is replotted for the anisotropic cases in a doubly logarithmic plot.

4.5 Effect of deposition

In this section the QDM equation with nonzero flux (4.22) is considered. The numerical method used to obtain the results from the last sections has to be adapted only slightly to simulate the coarsening of QDs in presence of an atomic beam. The adjustments are explained at the end of Chapter 5. The spatial grid and time step sizes are chosen as in the previously presented simulations. Before the results are discussed, the actual parameters for the simulations are derived and the deposition strength \tilde{F} from formula (4.23) is calculated. It is not always straightforward

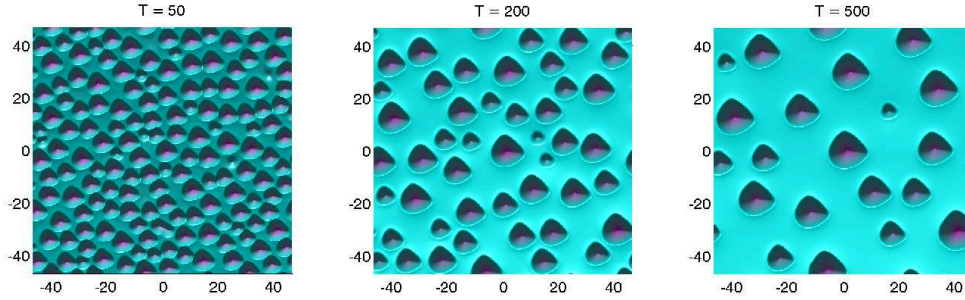


Figure 4.16: Evolution of dots based on the triple-well potential W_{Δ} . A random perturbation of a flat state evolves to self-assembling patterns. For the simulation $G = 0.2$ is used with formula (4.39).

to find exact constants that are needed for a realistic description of an experiment and sometimes variations come in by measurement errors. However, the here used quantities are adequate to show that the simulations qualitatively agree with experimental data from Ge/Si(001) self-assembled growth, which has been described in the introduction, i.e. Section 0.4. Apart from clearly specified physical quantities such as the Boltzmann constant, material specific constants that are less common are used. In the following the characteristic scales for the Ge/Si(001) system are calculated.

The characteristic length scale is several nanometers

$$L = \gamma_0 / \mathcal{E}_{sed}^{base} = \frac{\gamma_{Ge(001)}(1 - \nu_{Ge})}{2\mu_{Ge}(1 + \nu_{Ge})\epsilon^2} = 5.23 \text{ nm}.$$

Therefore the surface energy of a (001) oriented germanium crystal has been used, $\gamma^{Ge(001)} = 1.927 \times 10^{-4} \text{ J/cm}^2$. This quantity is taken from Tekalign and Spencer [102]. Here parameters are truncated after the second or third decimal place and identities hold within this accuracy. The shear modulus $\mu_{Ge} = 0.670 \times 10^7 \text{ N/cm}^2$ is taken from Wortman and Evans [113] and Poisson's ratio is $\nu^{Ge} = 0.273$ [102]. These two values could be expressed in terms of two other elasticity parameters, Young's modulus E_{Ge} and Lamé's first parameter λ_{Ge} , respectively. In Table C.1 in the appendix it is explained how these quantities can be converted into each other. Furthermore for the calculation of the length scale the lattice mismatch

$$\epsilon = \frac{a_{Ge} - a_{Si}}{a_{Si}} \approx 0.04$$

was used with the lattice spacing of germanium $a_{Ge} = 0.565 \times 10^{-7} \text{ cm}$ and of silicon, $a_{Si} = 0.543 \times 10^{-7} \text{ cm}$, respectively. For the elastic and wetting parameters $\tilde{e} = 1.28$ and $\tilde{\gamma} = 0.05$ were used [56].

For the characteristic time scale, the diffusion constant \mathcal{D} from equation (1.2) is essential. Here it is calculated as

$$\mathcal{D} = \Omega_{Ge}^2 D_s \sigma_{Ge} / (kT) = 3.49 \times 10^{-26} \text{ cm}^4 \text{ s/kg} \quad ,$$

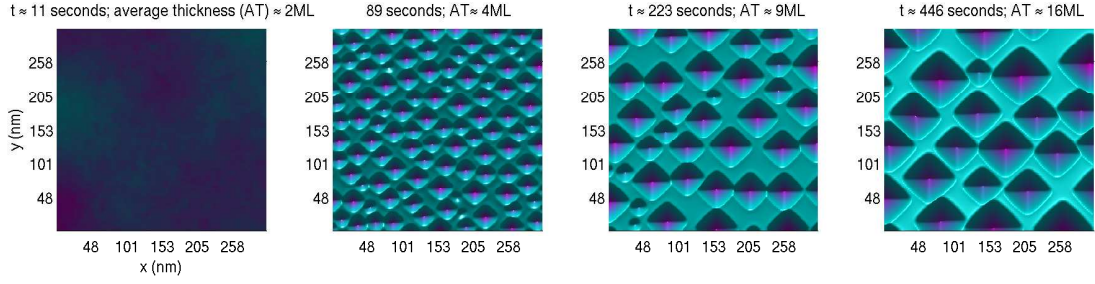


Figure 4.17: Part of the simulated domain for the deposition flux $F = 0.0053251 \text{ nm/s}$. From a flat state in the first picture, the film exceeds the critical thickness and island arrays form that coarsen in an Ostwald ripening process.

where the Boltzmann constant is $k = 1.38 \times 10^{-23} \text{ J/K}$. The temperature in the experiments under consideration is between 500 and 600°C . Here it is chosen to be $T = 873 \text{ K} (= 600^\circ \text{C})$. The diffusion constant is

$$D_s = 8.45 \times 10^{-6} e^{-0.83 \text{ eV}/(kT)} \text{ cm}^2/\text{s} = 1.37 \times 10^{-10} \text{ cm}^2/\text{s}$$

as in the work by Spencer et al. [97]. The surface density of germanium atoms is approximated by $\sigma_{Ge} = 2 \text{ atoms}/a_{Ge}^2 = 6.27 \times 10^{14}/\text{cm}^2$. The 2 was chosen since a germanium bravais lattice contains 4 atoms on a facet plus an additional face centered atom. On a (001) oriented flat surface this makes four times a quarter atom plus one in the middle in each base square. The overall time scale becomes in this way

$$\tau = L^4/(\gamma_0 \mathcal{D}) \approx 1.11 \text{ s} \quad .$$

To add deposition the dimensionless quantity \tilde{F} from equation (4.23) has to be calculated. For F the values $F_1 = 0.005 \text{ nm/s}$, $F_2 = 0.01 \text{ nm/s}$, $F_3 = 0.05 \text{ nm/s}$, corresponding to rates between 2 to 25 ML per minute, were implemented. Similar rates are used in experiments, though the third may be already too big for epitaxial growth. Then $\tilde{F}_1 = 0.0053$, $\tilde{F}_2 = 0.0107$, $\tilde{F}_3 = 0.0533$. In Figure 4.17 a typical simulation run is visualized for the deposition strength F_1 . Here and in all following simulations the anisotropy strength has been set to $G = 0.2$, resulting in a critical thickness of about 3ML, similarly as in experiments. Since the simulations start with a flat film below the critical thickness, during evolution a first phase is observed, where only the tiny fluctuations from the randomly perturbed flux influence an otherwise planarly growing film. This is depicted in the first of the four time shots. Eventually the ATG instability sets in and islands form, coarsen and undergo faceting. This is visible in plot two to four in Figure 4.17. Already in these pictures it can be noticed that the island density is bigger than without deposition. The flux tends to slow down the coarsening process. How much influence it has is shown in Figure 4.18, where simulation results are depicted for the three different deposition rates F_k , $k = 1, 2, 3$. The computational domain was in each direction about 120 dimensionless units, making more

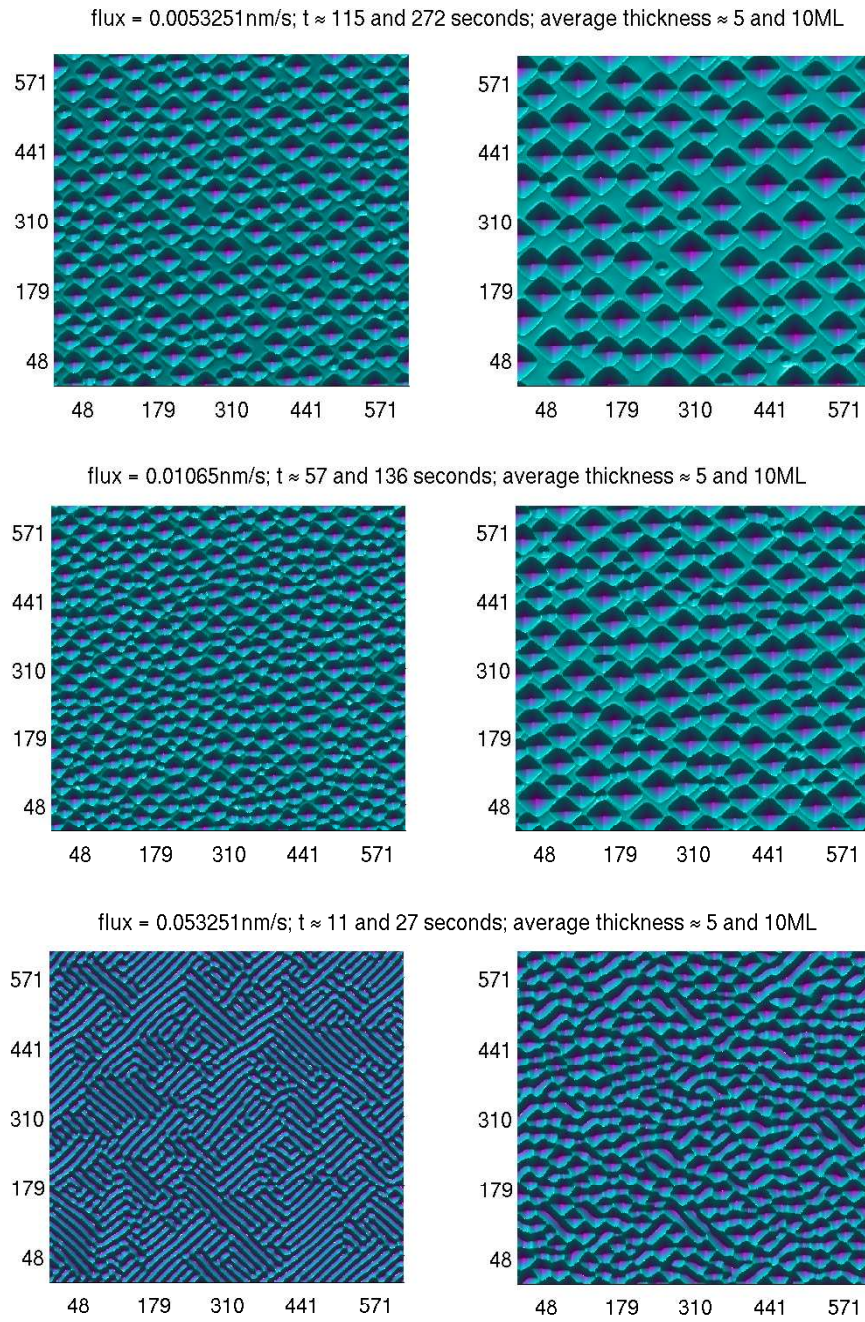


Figure 4.18: The three rows depict the surface from above for the three different deposition rates $F_i, i = 1, 2, 3$ at two time points, where in each case the same amount of material has been deposited.

than 600nm in scales with dimensions. Also in Figure 4.17 the computational domain was that big. However, to better see how the anisotropy and the flux influence the island shapes, only a

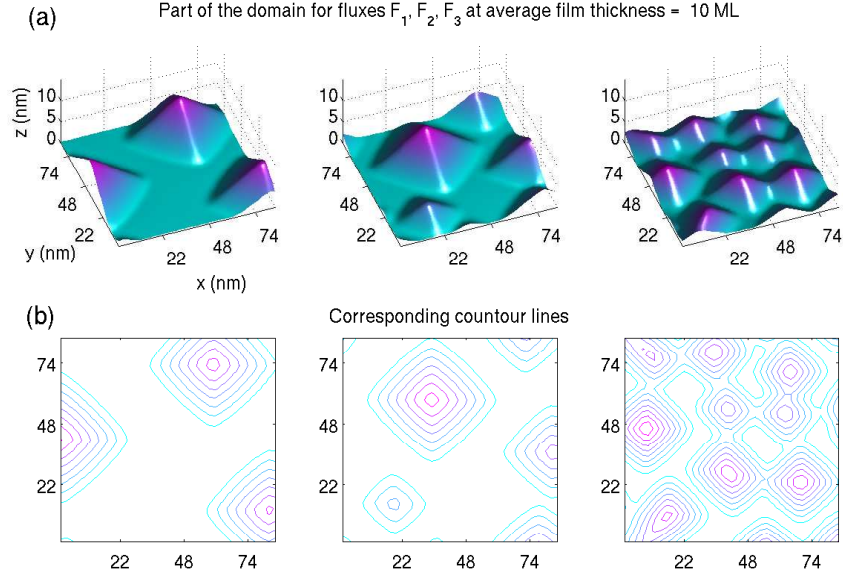


Figure 4.19: Section of the computational domain from Figure 4.18. Deposition rates $F_i, i = 1, 2, 3$ at the time points when 10ML have been deposited. x, y and z axes are in nanometers.

quarter of the domain has been plotted. In Figure 4.18 the whole domains are shown. The three rows correspond to the three different fluxes. In each of the two columns either an 5 or 10 ML film atom equivalent has been deposited. Three observations can be made directly. For small flux the evolution is more similar to the case without deposition. Ostwald ripening of square based pyramids is visible. These are clearly separated by a wetting layer. By increasing the rate one can see that more dots exist for the same amount of deposited atoms. In the average they are smaller and overall they leave less of the substrate covered by a thin layer. For the strong flux an additional effect is visible. Since the island density is further increased, islands tend to remain connected to others, resulting in elongated ridges. Only after further evolution they eventually dissolve into separate islands. In all cases the anisotropic character of the shapes of the islands is clearly pronounced. This is well visible in Figure 4.19, where in (a) a 3D view for the shapes from sections of the domains in Figure 4.18 is shown and below in (b) contour lines visualize the effect of the anisotropy. The islands are clearly oriented, even in case of strong deposition. In the simulations, out of the range of allowed parameters, a rather strong anisotropy has been used. Still, in experiments real facets have even less curvature. However, the author believes that the observed anisotropy effect is already a good approximation to perfectly flat faces with corners at the edges — especially since a smooth framework would be destroyed by using such a description. As mentioned, for the case that more planar facets are sought, the approach from the other model, where a Wilmore regularization (2.2) is used to allow for strong anisotropy, could be applied. In the reduced equations a linear sixth order term would appear similarly as

in (2.13).

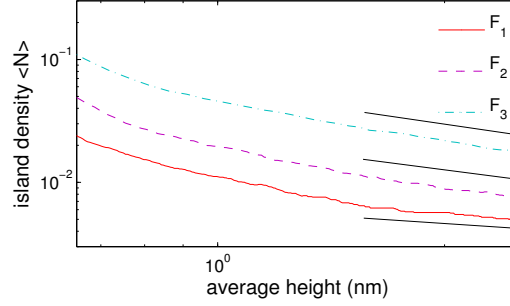


Figure 4.20: Coarsening diagram for the case with deposition. The average height is plotted against the island density in a doubly logarithmic plot. F_1, F_2, F_3 are the deposition rates introduced before.

As before for the case without deposition a coarsening diagram has been created. The island density function (4.40) has been used for 3D islands by replacing the domain length, by domain size, which is $L \cdot L$ for a square domain with equally long sides of length L . In Figure 4.20 the rates for three deposition rates are shown in a doubly logarithmic plot. It is clearly visible that a much higher island density is given for higher deposition rates. All three rates appear nearly as straight lines. A slight convexity is visible, but a power law behavior seems possible at later stages of the evolution.

Concluding, one sees that the deposition terms influence the growth similarly as in experiments, where an increasing flux rate also leads to a higher island density. For detailed comparisons it would be preferable to work with experimentalists who can supply the exact data that is needed for comparisons with simulation results. Such a cooperation might be aspired in future, until then comparisons to data from literature have to suffice.

In the following final chapter the numerical methods that were used throughout the work are introduced. Local and global interpolation is used to set up finite difference and pseudospectral methods.

Chapter 5

Numerical methods for evolution equations on periodic domains

The process of preparing programs for a digital computer is especially attractive, not only because it can be economically and scientifically rewarding, but also because it can be an esthetic experience much like composing poetry or music.

Donald E. Knuth (1938 -)

During the work on this thesis several codes had to be written to simulate high order PDEs on periodic domains. While in the beginning they were in parts cumbersome and slow, they evolved to short and fast programs over the months. Finally the working numerics is indeed rewarding and esthetic due to compactness and simplicity.

I didn't have time to write a short letter, so I wrote a long one instead. These words by Mark Twain can be transferred analogously to the letters of a computer scientist — his codes. It needs time to write qualitatively rich source texts that work properly and are easy to understand. For mathematical implementations a deep understanding of the theory helps to simplify the numerics. In this chapter it is described how to avoid laborious, slow numerics for the problems under consideration. Short, elegant solution schemes and their implementation in Matlab will be described. It is not claimed that these are optimal, most accurate or the fastest codes possible. However, they are really short, easy to understand and sufficiently fast for the considered problems.

Here, and also in many other works on phase-separating systems, partial differential equations of n th order

$$h_t = F(h, h_x, h_y, h_{xx}, h_{xy}, h_{yy}, h_{xxx}, \dots) \quad , \quad (5.1)$$

have to be solved. As in the previous chapters the space variables are $(x, y) \in \Omega$, the time is denoted by $t \in [0, T], T > 0$, $h = h(x, y, t)$ is an at least n times and $F : \mathbb{R} \rightarrow \mathbb{R}$ is an

at least one time continuously differentiable function. Often the problems are assumed to be periodic in space, this is also done throughout this chapter. The induced boundary conditions are naturally fulfilled when using pseudospectral methods (PSMs) based on periodic functions, while the stiffness matrices used in finite difference methods need to be altered for that end. But not for this reason the PSM is the favorable method for the introduced PDE problems. The benefits, such as accuracy and runtime, will become clear in this chapter, where throughout Ω is chosen to be a square domain $\Omega = [0, L]^2$ and most times for convenience $L = 1$.

The following theory could be easily extended to higher dimensional systems. This may become useful, for example the third dimension z is added in models for phase separation in bulk materials (e.g. as in the numerical study on a CH model [99]). However, here additionally to the time t only the variables x and y will be allowed, since all problems in this work depend at the most on two lateral variables. The equations for the faceting of growing surfaces, (2.14), (2.13), and also the QDM model with and without deposition, (4.22), (4.24), can be simulated by the PSMs explained in this chapter.

The problem equations contain nonlinearities and thus they are not easy or not at all solvable analytically. In this case numerical simulations have to be carried out to see how solutions evolve. Unexperienced researchers might be worried when high derivatives come into play. These are obsolete as it will be shown on the next few pages. The described line-methods, where the lateral domain is discretized first to obtain an ODE in time, are explained and applied to high order problems. As in the existence theory from Chapter 2 it will become clear that treatment of high order derivatives is no insuperable hurdle.

The discussion begins in Section 5.1 with a tool every mathematician, physicist and engineer learns during his studies: The finite difference method (FDM). Matlab works optimally with matrices, not for nothing its name stems from the first letters in *matrix laboratory*, and since the presented numerics will be supported with Matlab codes, the FDM will be introduced in terms of differentiation matrices. A simple and fast matrix vector product then yields derivative approximations based on Taylor expansions. This concept can be expanded to a wide class of interpolation methods, and also PSMs can be introduced in this way. To gain computational speed the fast Fourier transform (FFT) can be used (when talking about PSMs, here always the method based on trigonometric interpolation is meant; other PSMs are possible, but they are not further addressed). Since the differentiation matrices for these global interpolants are dense, the FFT allows to avoid dense matrix-vector operations and reduces the operations count from quadratic to $\mathcal{O}(N \log(N))$, when N is the number of grid points. This is still more than with local interpolation methods, where sparse matrices yield a reduction in operation count to $\mathcal{O}(N)$. However, the PSM offers huge benefits in accuracy and allows to use much coarser grids when the underlying problem is sufficiently smooth. Here, both methods are motivated as interpolation methods, then spectral differentiation is compared to finite differences and finally the method is applied to the problems from the previous chapters.

The introduction to finite differences is less interesting to readers familiar with this topic, however the way it is presented should clarify the relation and difference to the PSM and it shows how simply both methods can be implemented. The short codes might support the reader in the opinion that the main work for solving a partial differential equation are multiplications with matrices or wave-vectors. This is of course not true in general. When problems are differently structured than those discussed in this work, trouble may start. When it comes to complex domains and sharp transition regions in the solutions, the standard FDM and PSM might not be useful. Then finite element or finite volume methods remain the tools of choice, since these allow to deal with geometrically complex domains and adaptive grids. Then a lot of work has to be invested to define and refine proper meshes and handle index sets, which are used to define correct stiffness matrices that play the role of differentiation matrices. This can be circumvented for periodic problems on square domains. The following FDM and PSM are great tools which can be implemented astonishingly easily.

5.1 Finite difference methods (FDMs)

Consider first one of the simplest PDE problems, a diffusion equation in two spatial dimensions. The initial value problem on a periodic domain and time interval $[0, T]$ is a paradigm for a parabolic equation and it is discussed in any numerics lecture on PDEs. A function $u : [0, T] \times [0, 1] \times [0, 1] \rightarrow \mathbb{R}$ that fulfills

$$\begin{aligned} u_t &= u_{xx} + u_{yy}, & u(0, x, y) &= u_0(x, y), & (x, y) \in \Omega = [0, 1]^2, \\ u(t, x, y) &= u(t, x + 1, y) = u(t, x, y + 1), & (x, y) \in \Omega, \end{aligned} \quad (5.2)$$

is sought. The right hand side, the Laplacian of a function, appears in many PDEs. It is probably the most common differential operator. Before starting to discretize, it will be explained how this operator works. By looking onto the one-dimensional diffusion equation it is easier to show how the terms in the diffusion equation influence the shape u . The PDE writes in this case

$$u_t = u_{xx} \quad , \quad (5.3)$$

rate of change *'curvature'* .

The annotations below the equation describe the effect of the derivatives on both sides of the equality sign. To leading order the second derivative describes the curvature, so that convex regions pull the function down with time, while concave parts push the function up (here convex means $u_{xx} < 0$). Since the diffusion equation is also known as heat equation, it can be interpreted in context of heat transfer. As example in Figure 5.1 one can imagine a periodic wire (by making a circle out of the curves in the figure and connecting the ends), which is heated in one central area, giving the heat profile as in Figure 5.1 (a). With time the heat is smoothly distributed over the whole wire as shown in the following two pictures (b) and (c) — it diffuses. The same

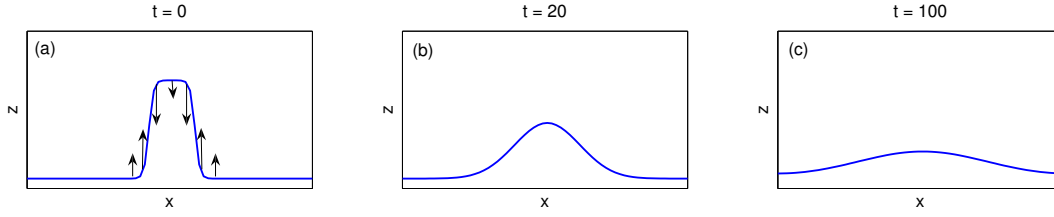


Figure 5.1: Simulation of diffusion equation (5.3) with initial condition $h(0, x) = \tanh(x + 5)/2 - \tanh(x - 5)/2$ on a 20π long domain. Convex parts of the shape are pulled down, while concavity indicates the opposite effect, as denoted by the arrows in (a).

property of the Laplacian applied to a function can be observed in two dimensions,

$$\nabla^2 u = u_{xx} + u_{yy} \quad \text{on} \quad [0, 1] \times [0, 1] \quad .$$

The formula describes the mean curvature in two lateral dimensions to leading order. During simulations the convex surface regions are pulled down while the others are pushed up. Assuming u to be sufficiently smooth, the Laplace operator differentiates this function twice in each of the two directions when it is applied to this function. To compute the derivatives approximately, an equidistant discretization, $0 = x_1 < x_2 < \dots < x_n = 1$, $dx = x_{i+1} - x_i$, in both directions can be used. On each grid point the values $U_{i,j} = u(x_i, x_j)$, $i, j = 1, \dots, n$ are computed. Taylor expansions in $\pm x$ and $\pm y$ directions lead to the finite difference approximation of the Laplacian of u at one point

$$\nabla^2 u|_{(x_i, x_j)} = \frac{U_{i,j-1} - 2U_{i,j} + U_{i,j+1}}{dx^2} + \frac{U_{i-1,j} - 2U_{i,j} + U_{i+1,j}}{dy^2} + \mathcal{O}(dx^2) \quad . \quad (5.4)$$

Naturally all function values would be stored in a matrix

$$\begin{array}{c|c|c|c|c} & & \vdots & & \\ \hline & U_{i-1,j-1} & U_{i-1,j} & U_{i-1,j+1} & \\ \hline \cdots & U_{i,j-1} & U_{i,j} & U_{i,j+1} & \cdots \\ \hline & U_{i+1,j-1} & U_{i+1,j} & U_{i+1,j+1} & \\ \hline & & \vdots & & \end{array} \quad ,$$

however since differentiation matrices will work on all n^2 data points, these are collected from now on in one $N = n^2$ vector

$$U = (U_{1,1}, U_{2,1}, \dots, U_{n,1}, U_{1,2}, U_{2,2}, \dots, U_{n,2}, U_{1,3}, \dots)^T \quad . \quad (5.5)$$

A matrix $D_2 \in \mathbb{R}^{N \times N}$ based on the differentiation scheme (5.4) can be defined such that it approximates the Laplace operator

$$\nabla^2 u \approx D_2 U \quad .$$

By staring long enough at the finite difference (5.4) and the ordering of the vector (5.5), one can read off one typical row of this matrix

$$\frac{1}{dx^2}(0, \dots, 0, 1, 0, \dots, 0, 1, -4, 1, 0, \dots, 0, 1, 0, \dots, 0) \quad ,$$

where the far left and far right 1 are n entries away from the -4 that is positioned on the main diagonal of D_2 . Periodicity is not yet included. For incorporation of boundary conditions to the rather simple matrix, every time in the finite difference star (5.4) an index is bigger N or less than 1, the periodicity has to be applied

$$U_{i,j} = U_{i+n,j} \quad \text{or} \quad U_{i,j} = U_{i,j+n} \quad . \quad (5.6)$$

The resulting sparsity structure of the differentiation matrix D_2 is shown in Figure 5.2. Additional super- and subdiagonals are added in the upper-right and lower-left corner because of the periodicity. The round dots resemble ones, except on the main diagonal which contains the -4 entries. The number of nonzeros $p = 5N$ grows only linearly in N , while the overall number of

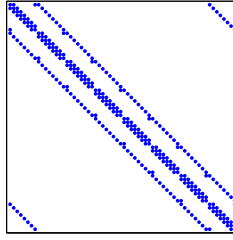


Figure 5.2: Sparsity pattern for the Laplace operator with a central difference scheme for both directions. Here with $N = 64$.

matrix entries grows quadratically. Hence $p/N^2 \xrightarrow{N \rightarrow \infty} 0$ like $1/N$. For an $n \times n$ domain this means the relation decreases like $1/n^2$. With $n = 128$, the matrix has already 268435456 entries, while only 81920 are nonzero. This shows the importance of using sparse structures. Matlab offers the possibility to define a sparse matrix D by using the command `sparse(D)` or `spdiags` which needs all the nonzero (sub-, super-) diagonals and their positions as input.

A solution for equation (5.2) can be approximated with help of the derived differentiation matrix D_2 . Discretized the PDE approximation writes

$$U_t = D_2 U \quad ,$$

which is one of the simplest ODEs imaginable. Once the stiffness matrix D_2 is defined (as sparse structure), the problem can be solved on the time interval $[0, T]$ with a standard Matlab ODE solver, as in the following code snippet (here u_0 is the initial profile given as N -vector as input data and subscripts are lifted in all codes).

```
[t,y]=ode45(@ (t,y)laplacian(t,y,D2),[0, T],u0);
```

```
function dy = laplacian(t,y,D)
dy = D*y;
```

The function handle `@(t,y)laplacian(t,y,D2)` points to the function underneath the `ode45` call, which is an adaptive, explicit Runge-Kutta based solver — a standard Matlab routine. The first bracket $()_1$ contains the argument for the solver, while the second bracket $()_2$ additionally allows for parameters (or as here the differentiation matrix) that have to be available to evaluate the system function. Any other ODE method, such as an implicit Euler implemented by hand, can be chosen as solution scheme. Therefore the time domain is decomposed equidistantly with time step dt , which does not need to fulfill a CFL condition. This gives with the $n \times n$ identity matrix I_n

$$\frac{U^+ - U}{dt} = D_2 U^+ \Leftrightarrow (I_n - dt D_2) U^+ = U \quad .$$

The implicitity makes it necessary to solve a linear system in each iteration. With Matlab's easy-to-handle sparsity commands, the implementation is nearly trivial and fast, as shown in the next few lines.

```
M = sparse(sparse(eye(N)) - dt*D2);

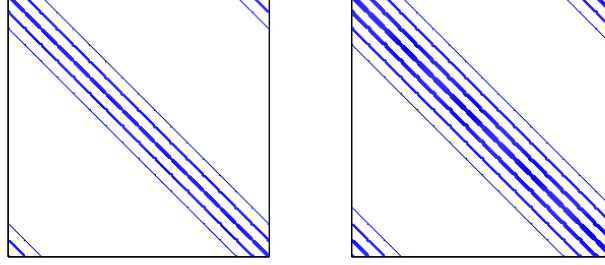
for t = 0:dt:T
    u = M\u;
end
```

Here `eye(N)` defines a $N \times N$ identity matrix. Once the differentiation matrix is assembled and the system function is coded, the diffusion equation can be solved with a one line command in the time loop (' $u = M \backslash u$ ' solves the system $MU^+ = U$).

As long as PDEs are linear one can set up analogous procedures to compute approximate solutions. Consider for example the bi-Laplacian $\nabla^4 u = u_{xxxx} + 2u_{xxyy} + u_{yyyy}$, or maybe directly the even more complicated tri-Laplacian $\nabla^6 u = u_{xxxxx} + 3u_{xxxxy} + 3u_{xyyyy} + u_{yyyyy}$. Discretizing and writing down a scheme based on Taylor's expansions can yield the first term

$$(u_{xxxxx})|_{(x_i, y_i)} \approx \frac{U_{i,j+3} - 6U_{i,j+2} + 15U_{i,j+1} - 20U_{i,j} + 15U_{i,j-1} - 6U_{i,j-2} + U_{i,j-3}}{(dx)^6} \quad .$$

The other derivative approximations yield similar expressions. It then is necessary to collect the coefficients of equal terms and as before periodic boundary conditions are imposed. Although this is possible and Pascal's triangle can help to find the coefficients, nobody can want to do that by hand. Once lower order differentiation matrices are defined, higher derivative operators can be approximated by taking powers of the already given matrices. For the bi-Laplacian the

Figure 5.3: Sparsity patterns for the bi-Laplacian and the tri-Laplacian with $N = 256$.

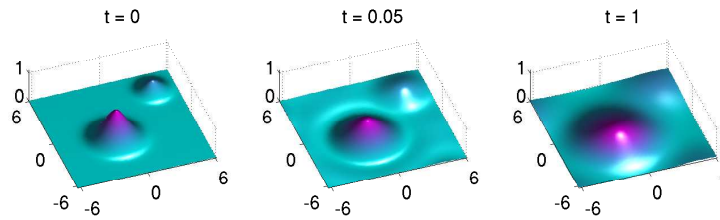
differentiation matrix can be defined as $D_4 = D_2^2$ and for the tri-Laplacian it can be set to $D_6 = D_2^3$, giving the sparsity patterns shown in Figure 5.3. These matrices correspond to the definition of the higher order operators as powers of the Laplacian, $\nabla^4 u = (\nabla^2)^2 u$, $\nabla^6 u = (\nabla^2)^3 u$. The matrix-matrix multiplications have to be carried out with care to avoid a cubic operation count. The "tri-Laplace-equation"

$$u_t = \nabla^6 u \quad (5.7)$$

can now be solved approximately by defining the system matrix

$$M = I_n - \Delta_t D_6$$

and applying the implicit Euler scheme exactly as before, or by using any favorite, often more accurate, ODE solver. The evolution of initially two overlapping Gaussians is shown in Figure 5.4. As in the usual diffusion equation the humps gradually decrease, while the flatter areas grow. However, although the pictures of the evolution appear very similar as in standard diffusion problems, the time-scale is way faster.

Figure 5.4: Evolution of the tri-Laplace equation (5.7) on a 64×64 grid. The initial condition on the $[-2\pi, 2\pi] \times [-2\pi, 2\pi]$ domain is $u(0, x, y) = \exp(-(x+1)^2/2 - (y+1)^2/2) + \exp(-(x-4)^2 - (y-4)^2)/3$.

This was easy. As easy that you might be tempted to solve the discussed equations analytically. This is of course not the point. The overall aim is to solve equations that incorporate nonlinearities — where analytical solutions are hard to find.

Now, again in one lateral dimension, a more complicated problem is considered, the HCCH equation (2.14), which describes the faceting of a growing surface in 2D. It is a semilinear PDE, with two nonlinearities, one from the deposition flux and the other from the anisotropy of the surface energy. To approximate a first derivative one can use a simple central difference

$$(u_x)_{|x_i} = \frac{U_{i+1} - U_{i-1}}{2dx} + \mathcal{O}(dx^2)$$

that defines the differentiation matrix (periodicity included)

$$D = \frac{1}{2dx} \begin{pmatrix} 0 & 1 & 0 & 0 & \dots & 0 & -1 \\ -1 & 0 & 1 & 0 & 0 & \dots & 0 \\ 0 & -1 & 0 & 1 & 0 & \dots & \vdots \\ \vdots & \ddots & \ddots & \ddots & \ddots & \ddots & \vdots \\ 0 & \dots & \dots & 0 & -1 & 0 & 1 \\ 1 & 0 & \dots & 0 & 0 & 1 & 0 \end{pmatrix}. \quad (5.8)$$

Second derivatives could also be approximated with a central difference

$$(u_{xx})_{|x_i} = \frac{U_{i+1} - 2U_i + U_{i-1}}{dx} + \mathcal{O}(dx^2)$$

yielding

$$D_2 = \frac{1}{dx} \begin{pmatrix} -2 & 1 & 0 & 0 & \dots & 0 & 1 \\ 1 & -2 & 1 & 0 & 0 & \dots & 0 \\ 0 & 1 & -2 & 1 & 0 & \dots & \vdots \\ \vdots & \ddots & \ddots & \ddots & \ddots & \ddots & \vdots \\ 0 & \dots & \dots & 0 & 1 & -2 & 1 \\ 1 & 0 & \dots & 0 & 0 & 1 & -2 \end{pmatrix}. \quad (5.9)$$

When defining fourth and sixth derivative matrices via $D_4 = D_2^2$, $D_6 = D_2^3$, the spatial terms on the right hand side of the HCCH equation can be approximated by

$$\frac{\delta}{2} D[U^2] + D_2^3 U + D_2^2 [U - U^3] \quad .$$

Based on this expression one can set up an explicit method. It would be easy to implement, however, due to the sixth order derivatives, by the rule of thumb a CFL condition gives a hard to adhere restriction $dt \leq Cdx^6$, which makes stable computations on large time domains impossible due to the too strict step size restriction. Instead one can implement an implicit Euler scheme

$$\frac{U^+ - U}{dt} = \frac{\delta}{2} D[(U^+)^2] + D_2^3 U^+ + D_2^2 [U^+ - (U^+)^3] \quad . \quad (5.10)$$

Therefore in each iteration a nonlinear system of equations

$$F(U^+) = 0$$

has to be solved for each time step, where

$$F(U^+) = U^+ - U - dt\left(\frac{\delta}{2}D[(U^+)^2] + D_2^3U^+ + D_2^2[U^+ - (U^+)^3]\right) \quad .$$

A possible implementation is shown in Code 5.5. Input data is the maximal time T , the time

```
function u = hcch_implicit_fd(T, dt, n, L, delta)
xgrid = linspace(-L/2, L/2, n);
dx = xgrid(2) - xgrid(1);

D = sparse(zeros(n,n));
D2 = sparse(zeros(n,n));
for k=1:n-1
    D(k,k+1) = 1/(2*dx); D(k+1,k) = -1/(2*dx);
    D2(k,k)=-2/dx; D2(k,k+1) = 1/dx; D2(k+1,k) = 1/dx;
end

% periodicity
D(1,n) = -1/(2*dx); D(n,1) = 1/(2*dx);
D2(1,n) = 1/dx; D2(n,1) = 1/dx;

% bi-Laplacian and tri-Laplacian
D4 = D2^2;
D6 = D2^3;

%initial shape
u = h_init(xgrid)';

%time loop
for t = 0:dt:T
    uplus = fsolve(@(uplus)myfun(uplus, u, dt, delta, D, D4, D6), u);
    u = uplus;
end

% system function called by Newton solver
function Y = myfun(Up, U, dt, delta, D, D4, D6)
Y = Up - U + dt*(-delta/2*D*(Up.^2) - D6*Up - D4*(Up - Up.^3));
```

Code 5.5: Program code for the simulation of the HCCH equation with an implicit Euler scheme based on finite differences.

step size dt , the number of grid points n , the domain length L and the deposition parameter δ . Also a function h_{init} is needed to define an initial shape as n -vector. The assembly of the

matrices could be established with the `spdiags` command, however, the presented way is more suitable to show that the matrices indeed are of the form (5.8) and (5.9). By defining them as sparse objects only the nonzero entries and their positions are stored in the Matlab structure. Since the scheme is implicit, the time step may be chosen quite big. However, it must not be forgotten, that this quantity stems from a Taylor expansion where it is used as small parameter. The error of the overall scheme grows, when it is increased.

Generally implicit codes are slow when systems of nonlinear equations have to be solved in each iteration. If one is interested in many runs for parameter studies, long-time evolution or extensions to higher dimensions, an improved implementation might be necessary. Since explicit methods can imply hard restrictions on the time step size, something in between explicit and implicit might be preferable. Above, the linear bi- and tri-Laplacian have a major influence on the stability regions. A common trick is to treat these high derivatives implicitly and only the nonlinearity explicitly. This relaxes the step size restrictions and gives benefits in run-time (more comments on such a semi-implicit method will be given in the PSM Section 5.2). For the HCCH equation the scheme writes

$$\frac{U^+ - U}{dt} = \frac{\delta}{2} D U^2 + D_2^3 U^+ + D_2^2 (U^+ - U^3) \quad (5.11)$$

and it yields the linear system for U^+

$$(I_n - dt(D_2^3 + D_2^2))U^+ = U + dt\left(\frac{\delta}{2} D[U^2] - D_2^2[U^3]\right) \quad , \quad (5.12)$$

which has to be solved in each iteration. Note that this is a major simplification in relation to the fully implicit scheme. Treating the nonlinearity explicitly makes the system of equations that has to be solved linear. No Newton-like methods need to be applied. The matrix $(I_n - dt(D_2^3 + D_2^2))$ can be stored as sparse system matrix. D and D_2^2 should also be saved in separate arrays, so that they do not need to be recomputed in each time step. The few lines in Code 5.6 show how the HCCH equation can be simulated in the above framework with Matlab. The input parameter are as before in Code 5.5.

Finite difference methods are easy to derive in one dimension. Also in two lateral directions they are frequently used, but it may be nasty to assemble the system matrices. Considering three or more lateral dimensions leads to an exhaustive fight with indices and other methods or the use of programs that help to assemble the stiffness matrices might be advantageous.

The accuracy of the FDM is not as good as it can be achieved with a PSM for a certain problem class. So-called spectral accuracy yields large benefits for sufficiently smooth problems and in the next section it is presented how this can be achieved. However, changing boundary conditions in FDMs for one lateral dimension is simple, while this can be already a major obstacle for PSMs.

```

function u = hcch_solve_fd(T, dt, n, L, delta)

...

% bi-Laplacian and system matrix
D4 = D2^2;
M = sparse(eye(n,n)) - dt*(D2^3+D4);

%initial shape
u = h_init(xgrid)';

%time loop
for t = 0:dt:T
    u = M\u + dt*(delta/2*D*(u.^2)) - D4*(u.^3);
end

```

Code 5.6: Program code for the simulation of the HCCH equation with a semi-implicit finite difference scheme. The first lines denoted by the three dots are as in Code 5.5.

5.2 Pseudospectral methods (PSMs)

Differentiation matrices have been discussed in Trefethen's modern introduction [105] in conjunction with PSMs. Fornberg has written a guide on these topics some time earlier [33] and in general PSMs are used since the 1970s. However, the basis for the most popular PSM is the Fourier transform, which is known since about 200 years. PDEs have been solved with help of spectral differentiation throughout the last decades (generally in the field of fluids [13]; an example for a specific problem is the simulation of seismic waves [100]). Anyhow for many people the PSM seems to be non-existent, even if their problems are very PSM friendly (very smooth solutions, simple domains and preferably periodic boundary conditions). This is quite astonishing, once one has understood how easy a PSM can be implemented and how accurate it works.

Here the introduction to the method begins in one space dimension, where the PSM can be derived from trigonometric, hence global, interpolation. This closes the circle to the local interpolation method, the FDM from the foregoing section. The computations are then accelerated by using the FFT [21]. Thereafter an extension to two space dimensions is presented and finally the results are used to solve PDEs numerically.

5.2.1 Spectral differentiation and accuracy

In this section differentiation in one lateral variable x is considered and an equidistant grid as before is used. For the set-up of finite-difference schemes Taylor expansions have been used

to define reasonable differentiation matrices in the last section. A derivative obtained by a forward-backward Taylor expansion (central difference scheme) is equivalent to the derivative of the unique second order polynomial crossing three neighboring function values on the grid evaluated in the middle point. Hence the FDM can be interpreted as interpolation method and this viewpoint shows that it can be generalized easily. Using higher order polynomials that rely on more neighboring function values leads to higher order finite difference schemes. The higher the order, the more entries appear in the differentiation matrices. To obtain an approximate derivative of a smooth function u , which is sampled on an equidistant grid $\{x_j : j = 1, \dots, N\}$ such that $u_j = u(x_j)$, $j = 1, \dots, N$, an interpolation procedure for a central difference derivative might be written as (ignoring the boundaries)

- Find unique $p_j \in \mathcal{P}_2$ with $p_j(x_j) = u_j$ and $p_j(x_{j\pm 1}) = u_{j\pm 1}$,
- Set $v_j = p'_j(x_j)$.

Here \mathcal{P}_2 denotes the set of all polynomials of degree two and v_j are the derivative approximations. The set \mathcal{P}_2 may be replaced by either higher order polynomials, or by completely different sets. Accordingly the number of points where the interpolant is supposed to match the function has to be adjusted. In case of PSM global interpolation in all points x_j , $j = 1, \dots, N$ is carried out with a set of trigonometric functions \mathcal{F} . The procedure changes to

- Find $p \in \mathcal{F}$ with $p(x_j) = u_j, \forall_j$,
- Set $v_j = p'(x_j), \forall_j$.

This is already the basis for a PSM, it is spectral differentiation based on global trigonometric instead of finite difference approximations based on local polynomial interpolation. Note that for the second procedure the question of uniqueness is more complicated. Figure 5.7 shows that sums of cosines and sines as interpolants have to be used with care. In (a) the underlying periodic function is plotted together with the discrete points used for the interpolations. While in Figure 5.7 (b) the second order polynomials are uniquely defined and give a unique approximation for the derivative, there are infinitely many possible interpolants when applying trigonometric interpolation. Figures 5.7 (c) and (d) show the qualitative difference that can be achieved with truncated Fourier series that use different sets of wave lengths. While in (c) the "bad" coefficients lead to totally wrong derivative approximations in the sample points, the accuracy in (d) is in some sense perfect, because of the chosen trigonometric form of u .

For a trigonometric PSM the function space \mathcal{F} contains the complex exponentials, $\mathcal{F} = \{e^{ikx}, k \in \mathcal{K}\}$. The set of wave numbers $\mathcal{K} = \{k_1, \dots, k_N\}$ is finite, but since there exists an infinite number of wave numbers k that can be chosen, the so-called aliasing effect can occur. Picking the wrong wave lengths can lead to unwanted oscillations. This becomes more clear by

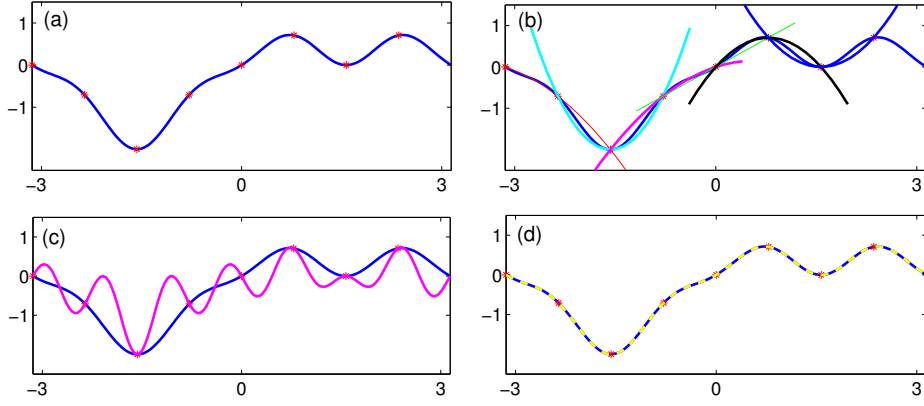


Figure 5.7: (a) Periodic function $u(x) = \sin(x) + \cos(2x)\sin(x)^2$ on $[-\pi, \pi]$, sampled over 8-points. (b) Local interpolation with second order polynomials. (c) "Bad" trigonometric interpolation. (d) Trigonometric interpolation with minimal mean square slope (the dashed line of the interpolant lays just on top of the function curve).

looking on the definition of the trigonometric interpolant

$$I_N(x) = \mathcal{F}^{-1}[\hat{u}](x) = \frac{1}{N} \sum_{j=1}^N \hat{u}_j \exp(ik_j x) \quad , \quad (5.13)$$

where $\hat{u} = (\hat{u}_j)_j = \mathcal{F}[u]$ is the discrete Fourier transform (DFT) of u and \mathcal{F}^{-1} is its inverse. It can be used with different sets \mathcal{K} and this formula still yields an interpolant of the sampled function. However, picking highly pitched sines and cosines in the expansions leads to the aliasing effect. As it is visible in Figure 5.7, the derivative values do not match at all, although the function values are correct.

The derivative of the interpolant can be calculated easily. It is

$$I'_N(x) = \frac{1}{N} \sum_{j=1}^N (ik_j \hat{u}_j) \exp(ik_j x) \quad ,$$

which shows that the vector of the approximate derivative values in the sample points is

$$(v_j)_j = \mathcal{F}^{-1}[(ik_j u_j)_j] \quad .$$

The main idea of differentiation via trigonometric interpolation is already explained. It can be achieved with the inverse of the Fourier transform that is previously multiplied by the imaginary number and suitably chosen wave numbers. If these are picked such that the interpolant has minimal mean square slope, spectral accuracy of the derivative approximation can be observed — for analytic functions this means that asymptotically it is more accurate than any finite difference approximation.

As in the FDM Section 5.1, differentiation matrices can be set up. They yield derivative approximations through simple matrix vector products. Later differentiation will be carried out in terms of the FFT, because it offers benefits in runtime. However, using differentiation matrices might become necessary when other than periodic boundary conditions have to be handled (for examples see Trefethen's book [105]). Also the relation, similarities and differences, between FDMs and PSMs becomes more clear. Trefethen shows that the *band-limited interpolant* — the DFT interpolant (5.13) with minimal mean square slope — can be written in terms of periodic sinc functions S_N ,

$$I_N(x) = \sum_{j=1}^N u_j S_N(x - x_j), \quad \text{with} \quad S_N(x) = \frac{dx \sin(\pi x/dx)}{2\pi \tan(x/2)}.$$

Now differentiation expressions such as u_{xx} can be approximated by $I_N''(x) = \sum_{j=1}^N u_j S_N''(x - x_j)$, or evaluated in the grid points

$$u_{xx} \approx D_S(u_j)_j, \quad (5.14)$$

with the differentiation matrix $(D_S)_{k,l} = S_N''(x_k - x_l)$. With this approach the theory from the foregoing sections can be applied equivalently to solve PDEs. Bigger sets of various differentiation matrices are already available and need not to be implemented from scratch (see Weidemann and Reddy [112]).

Using differentiation matrices can enable to apply more complicated boundary conditions than periodicity. However, since this is not necessary for the problems in this work, the derivative approximations will be obtained with help of existing FFT codes which are generically optimal for smooth periodic functions. Instead of the $\mathcal{O}(N^2)$ operations needed to evaluate (5.14), the costs are reduced to $\mathcal{O}(N \log(N))$ — which is a significant improvement. As mentioned, the correct order of the wave numbers is essential to obtain derivatives with spectral accuracy. The user has to be careful, since it varies with the packages that can be used. As before in this document, the theory will refer to Matlab's FFT and all codes will be written in Matlab script. Since the routines are based on Fortran's FFTW — fastest Fourier transform in the west [36] — the algorithm in Matlab is similarly efficient.

Differentiation with the Matlab FFT

A differentiable, periodic function $f(x)$, given by the user as discretization on a sampled domain $[0, 2\pi]$, can be differentiated with the few lines presented in Matlab Code 5.8. The only critical point is given with the definition of the wave numbers which needs to correspond to the ordering of the wave vector Matlab uses for its FFT routine. It is

$$\mathcal{K} = [0, 1, \dots, N/2 - 1, N/2, -N/2 + 1, -N/2 + 2, \dots, -1] \quad (5.15)$$

Computing derivatives in this way is not only easy, as long as the underlying functions are very

```

% N number of grid points, dx equidistant spacing of grid xgrid
N=100; dx = 2*pi/N;
xgrid = 0:dx:2*pi-dx;
%coefficients for the differentiation in spectral space
coeff = i*[[0:N/2] [-N/2+1:-1]];

% f user-defined function; 2 pi - periodic, smooth
u = f(xgrid)

% transform into Fourier space, multiply with coefficients, transform back
a = fft(u);
ax = coeff.*a;
ux = real(ifft(ax));

```

Code 5.8: Spectral differentiation with the FFT.

smooth, it is also more accurate than any approximation with local polynomial interpolation on sufficiently fine grids. While polynomials can only achieve a consistency order of $\mathcal{O}(dx^p)$ for some $p \in \mathbb{N}$, the trigonometric interpolation based derivatives for analytic functions have the order $\mathcal{O}(c^N)$, for some $c < 1$. This result is specified soon in more detail, but first the HCCH equation (2.14) will be solved with help of trigonometric interpolation. The solution approximation is denoted as earlier by $U = (U_j)_{j=1,\dots,N}$. The equation is transformed into discrete Fourier space ($\hat{U} = \mathcal{F}(U)$, $U = (U_j)_{j=1,\dots,N}$), giving

$$\hat{U}_t = \frac{\delta}{2} ik \mathcal{F}[U^2] + (k^4 - k^6) \hat{U} - k^4 \mathcal{F}[U^3], \quad k \in \mathcal{K}. \quad (5.16)$$

This formula is a scalar equation in \mathbb{C} . When writing \hat{U} , the Fourier transform at a particular wave number $\hat{U}(k)$ is meant. An expression like $ik \mathcal{F}[U^2]$ has to be read as follows. U is squared pointwise in discrete real space. The transformation $V = (V_j)_j = \mathcal{F}[U^2]$ gives an N -vector in Fourier space. Then for $k_j \in \mathcal{K}$ one calculates the N values $ik_j V_j$.

Applying a semi-implicit scheme as for the FDM method (5.11) gives

$$\frac{\hat{U}^+ - \hat{U}}{dt} = \frac{\delta}{2} ik \mathcal{F}[U^2] + (k^4 - k^6) \hat{U}^+ - k^4 \mathcal{F}[U^3], \quad k \in \mathcal{K}. \quad (5.17)$$

While for the presented FDM the system of equations (5.12) has to be solved in each time step, this is not necessary for the PSM. Although the high order derivatives are treated implicitly, the update formula for the new vector in Fourier space is explicit,

$$\hat{U}^+ = \frac{\hat{U} + dt\{\frac{\delta}{2} ik \mathcal{F}[U^2] - k^4 \mathcal{F}[U^3]\}}{1 + dt(k^6 - k^4)}, \quad k \in \mathcal{K}. \quad (5.18)$$

An efficient implementation in Matlab is shown in Code 5.9. First the k -vectors and S , the vector of denominator values for the system function in (5.18), which is constant when using an

equidistant time discretization, are defined. Then initial values are set up and as one can see the final time loop is very short. Note that the input parameters are as in the FDM Codes 5.5 or 5.6, only that the domain length L is replaced by a positive integer M defining the $2\pi M$ long domain.

```
function u = hcch_solve_psm(T, dt, n, M, delta)
xgrid = linspace(-M*pi, M*pi, n);

% wave vector, differentiation vectors and constant denominator
k = [[0:n/2] [-n/2+1: -1]]./M;
ik = i*k;
k4 = k.^4;
S = [1 + dt*(k.^6-k4)];

% initial shape and its Fourier transform
U = h_init_random(xgrid);
u = fft(U);

% time loop
for t = 0:dt:T
U = real(ifft(u));
    u = (u + dt*(delta/2*ik.*fft(U.^2) - k4.*fft(U.^3)))./S;
end
```

Code 5.9: Program for the simulation of the HCCH equation with a simple PSM.

Comparison of derivative approximations

Two different methods (5.6) and (5.9) have been presented that are both capable of approximating solutions to the HCCH equation. Now the accuracy of the used derivative approximations is discussed, since these determine the accuracy of the whole methods.

As mentioned, all finite difference derivative approximations have a truncation error of order $\mathcal{O}(dx^p)$, where p is some integer dependent on the order of the polynomial that is used for the interpolation. No matter how good the FDM is, the error is always bounded by a power of the grid spacing dx . This is not the case for spectral derivatives when the underlying problem is analytic, since then the error decreases faster than any power of dx . To be more precise, two theorems taken from Trefethen [105] are cited. The first gives a statement about the accuracy of C^k functions and the second yields the result for analytical functions.

Theorem 23 (Spectral accuracy) *Let $u \in C^p(\mathbb{R})$, $p \geq 1$ with $\partial^l u \in L^2(\mathbb{R})$, $l \in \{0, 1, \dots, p\}$ with $\partial^p u$ of bounded variation. Furthermore let u_l be the l th spectral derivative, that is the*

approximation of $\partial^l u$ on a grid $dx\mathbb{Z}$, $l < p$, and let $\partial^l u$ be of bounded variation, then

$$|u_l - \partial^l u| = \mathcal{O}(dx^{(p-l)})$$

in the small limit $dx \rightarrow 0$. □

This is a result finite differences that are adapted for the underlying problem could theoretically also achieve. However, the smoother the function, the better does spectral differentiation work. Best results are obtained for analytical functions as the next Theorem says.

Theorem 24 (Spectral accuracy for analytic functions) *Let $u \in C^\infty(\mathbb{R})$ with $\partial^p u \in L^2(\mathbb{R})$, $p \in \mathbb{N}$ and of bounded variation. Additionally let u_p be the p th spectral derivative, then*

$$\forall_{m \in \mathbb{N}} |u_p - \partial^p u| = \mathcal{O}(dx^m)$$

in the small limit $dx \rightarrow 0$. □

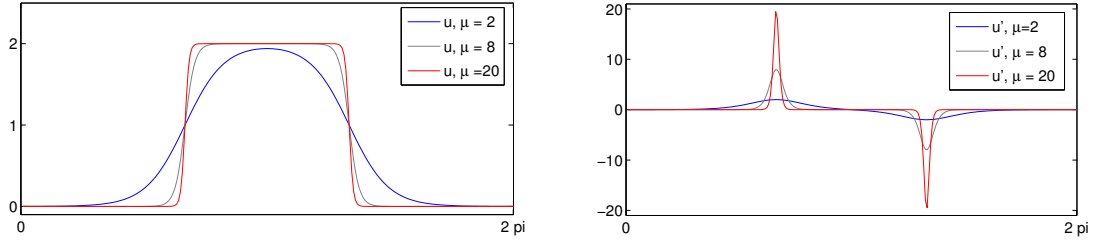
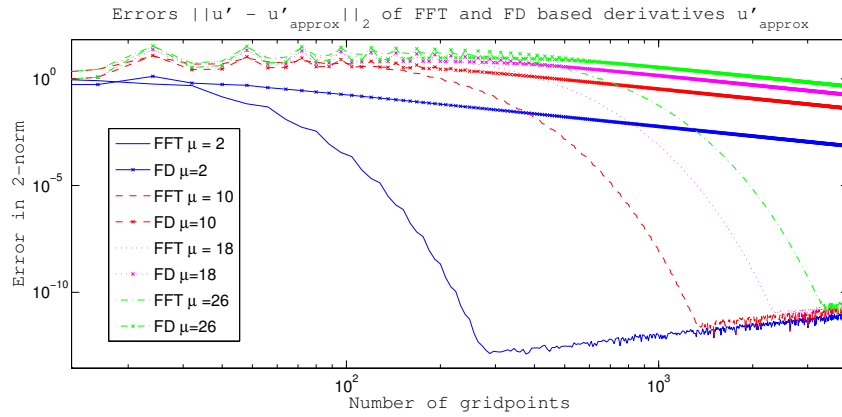
Although these results are stated for functions on whole \mathbb{R} , they apply analogously to periodic functions on bounded domains. This will be visible in the following examples.

It is a quite common opinion that FFT based methods bring along problems when discontinuities or sharp transitions come into play. Although this is true, it should be noted that this effect is not necessarily worse than when using finite differences. These also rely on the smoothness of the underlying function. The following example is more or less contrary to the expectation of better working finite differences. A '2-phase function' is defined as

$$u(x) = \tanh(\mu(x - \frac{3}{4}\pi)) - \tanh(\mu(x + \frac{3}{4}\pi)), \quad x \in [0, 2\pi] \quad .$$

It can be interpreted as a transition between two states, which become steeper the bigger the parameter μ becomes, as shown in Figure 5.10. Because of the huge slope it may appear like a discontinuity on a discrete grid with coarse spacings. Although it is a constructed, academic function, it relates to phase-separating systems like the CH equation, where the simplest stationary solutions describing the transition between two states are just tanh functions. Such functions also appeared in leading order during the discussion of stationary solutions to the HCCH equation in Chapter 3.

Figure 5.11 shows that the error between a central finite differences approximation and the derivative of the example function decreases with increasing number of grid points like a straight line with finite slope in a log-log-plot — as expected by the power of dx in the consistency residual — while the spectral derivatives accelerate the decrease of the error slope. It would be steeper than any straight line after sufficient increase of grid points if this effect would not be stopped by round-off, which comes in shortly above machine precision and accumulates with bigger grid-sizes. These observations have been made for all tested values of μ .

Figure 5.10: '2-phase functions' (left) and its derivatives (right) with different values of μ .Figure 5.11: Doubly logarithmic error plot for the '2-phase-function' for different values of μ . The different curves without markers correspond to FFT based differentiation, while the nearly straight lines marked with crosses show the error of a central finite difference.

5.2.2 PSMs for 3D problems

For the three-dimensional problems, two directions in space and one in time, the FFT gives a linear relation between the spatial variables (x, y) and the wave numbers (k_1, k_2) in Fourier space. This bond will be denoted by $(x, y) \leftrightarrow (k_1, k_2)$ and the set of wave numbers \mathcal{K} becomes now a set of wave number pairs $(k_1, k_2) \in \mathcal{K}$. The discretized Laplacian then obeys the rule

$$u_{xx} + u_{yy} \leftrightarrow (ik_1)^2 \hat{U} + (ik_2)^2 \hat{U} = -k^2 \hat{U} \quad ,$$

with $k = \sqrt{k_1^2 + k_2^2}$. As before for one-dimensional derivatives, the accuracy of the Laplacian approximation with spectral differentiation in two dimensions is astonishing as the error plot for an exemplary Gaussian function in Figure 5.11 shows. In this log-log plot the error of the second order FD approximation to the exact Laplacian of a given C^∞ function appears as straight line for growing numbers of grid points. Interestingly the differentiated function is not periodic, but anyhow its spectral derivative gives the desired result of spectral accuracy. Since the tails of the exponential decay rapidly, they are essentially zero at the boundaries and define an artificial periodicity. This can be used for other problems, too. One well-known example where this is done

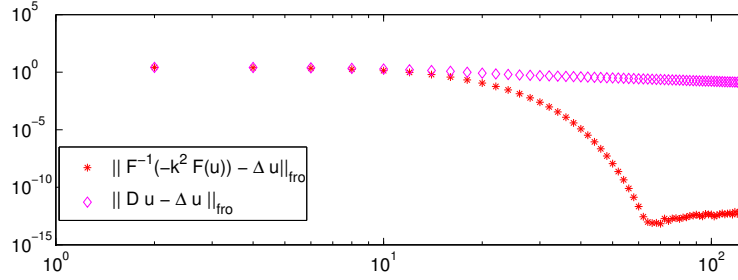


Figure 5.12: Difference of the finite difference and the pseudospectral derivative to the exact Laplacian of $u(x, y) = 1/3 \exp(-2x^2 - 2y^2)$ computed on a $[-2\pi, 2\pi] \times [-2\pi, 2\pi]$ domain. The errors are calculated in the Frobenius norm. Here D is a differentiation matrix that stems from a second order difference scheme.

is the Korteweg de Vries (KdV) equation modeling the evolution of solitary waves. Trefethen gives examples how PSMs can be applied to this equation [105].

To solve PDEs one can proceed as before. Consider as simple example the diffusion problem (5.2) with periodic boundary conditions. Discretized and transformed into Fourier space one has for each wave vector (k_1, k_2)

$$\hat{U}_t = -k^2 \hat{U} \quad , (k_1, k_2) \in \mathcal{K} \quad ,$$

which is an ODE in Fourier space. An explicit Euler scheme writes

$$\frac{\hat{U}^+ - \hat{U}}{dt} = -k^2 \hat{U} \quad \Leftrightarrow \quad \boxed{\hat{U}^+ = (1 - dt k^2) \hat{U} \quad , (k_1, k_2) \in \mathcal{K}}$$

and leads to the usual problem that a CFL condition has to be fulfilled and only tiny time steps are feasible. However, here the stable implicit Euler scheme for linear equations has the nice benefit that it results in an explicit update formula and hence it is not computationally more expensive than the unfavored explicit method.

$$\frac{\hat{U}^+ - \hat{U}}{dt} = -k^2 \hat{U}^+ \quad \Leftrightarrow \quad \boxed{\hat{U}^+ = \hat{U} / (1 + dt k^2) \quad , (k_1, k_2) \in \mathcal{K} \quad .}$$

Generally any ODE solver is applicable. With the Matlab ode45 solver a short routine can be implemented as in Code 5.13. These few commands not only solve the problem, but also plot the solution. It seems more work to convert the two-dimensional array to a one-dimensional array and back with the Matlab command `reshape`, than actually to solve the problem. Any linear PDE with periodic boundary conditions and a square domain can be simulated in a similarly simple way. It becomes more interesting when nonlinearities come into play.

Evolution equations with nonlinearities

As before all problems have a square domain and the PDEs are supported with periodic boundary conditions. As first example consider a binary phase-separating system, a special reaction-diffusion equation, the Allen-Cahn equation as in Section 2.2. With a usual scaling (ϵ is a


```

k2 = reshape(k2,n^2, 1);
[t,y]=ode45(@(t,y)laplacian(t,y,k2),[t_min t_max], U);
for k=1:length(t)
    mesh(X,Y, real(ifft2(reshape(y(k,:),n,n)')));
    axis([-L, L, -L, L, 0, 2]);
end

function dy = laplacian(t,y,k2)
dy = -k2.*y;

```

Code 5.13: Program code for the computation of a numerical solution for the diffusion equation with a PSM.

small number, if it is chosen too small, the presented method may fail) it can be written for two-dimensional square domains as

$$u_t = \epsilon \nabla^2 u + \frac{1}{\epsilon}(u - u^3) \quad \text{on} \quad [-L, L] \times [-L, L].$$

The system function is a Laplacian applied on the order parameter and an additional nonlinear term in u , the reaction term. Discretized and transformed into Fourier space, $\hat{U} = \mathcal{F}(u)$, it becomes

$$\hat{U}_t = -\epsilon k^2 \hat{U} + \frac{1}{\epsilon}(\hat{U} - \mathcal{F}(U^3)) \quad , (k_1, k_2) \in \mathcal{K} \quad .$$

The nonlinearity prevents an implicit Euler to define an explicit update formula as this is the case for linear PDEs. For this system it writes

$$\hat{U}^+ - \hat{U} = -\epsilon dt k^2 \hat{U}^+ + dt \frac{1}{\epsilon}(\hat{U}^+ - \mathcal{F}((U^+)^3)) \quad , (k_1, k_2) \in \mathcal{K} \quad .$$

A nonlinear, complex system would have to be solved in each iteration. This would be very costly, because Newton-like methods would have to be incorporated. As before this is avoided by using semi-implicit methods. For a semilinear PDE it is of big advantage to treat the high (and luckily linear) derivatives implicitly and leave the nonlinearities explicit. For the Allen-Cahn equation this gives

$$\begin{aligned} \frac{\hat{U}^+ - \hat{U}}{dt} &= -k^2 \epsilon \hat{U}^+ + \frac{1}{\epsilon}(\hat{U}^+ - \mathcal{F}(U^3)) \\ \Leftrightarrow \boxed{\hat{U}^+ &= (\hat{U} - dt \frac{1}{\epsilon} \mathcal{F}(U^3))/S} \quad (k_1, k_2) \in \mathcal{K} \quad . \end{aligned}$$

Here

$$S = S(k_1, k_2) = (1 + dt(k^2 \epsilon - \frac{1}{\epsilon}))$$

is a constant $N \times N$ matrix and this explicit updating scheme makes an implementation straightforward. Once S is defined, the main iteration in a Matlab environment can be written as

```

for t = 0:dt:T
    u = (u - dt*(fft2(real(ifft2(u)).^3)./epsilon))./S;
end

```

Note that when $L = 2\pi M$ for some $M \in \mathbb{N}$, the Matlab wave vector \mathcal{K} in (5.15) has to be scaled by dividing by M . As for linear PDEs, now no system of equations has to be solved. However, as often when computational speed and simplicity is gained there exists a drawback. Since the nonlinearity is treated explicitly, the scheme is not stable for big time steps and a CFL like restriction on its size has to be considered to prevent blow-up. However, for problems that involve nonlinearities it is difficult to derive analytical bounds on the step size and sometimes only trial and error gives sufficient experience to determine how big it can be chosen. Nevertheless it is a huge benefit in comparison to a purely explicit formula, since the high derivatives would make the restriction not or at least very difficult to manage. This is less probable for purely nonlinear problems.

Analogously a scheme can be obtained to simulate the Cahn-Hilliard equation in two lateral dimensions

$$u_t = \nabla^2[u^3 - u - \nabla^2 u] \quad \text{on} \quad [-L, L] \times [-L, L].$$

The additional two derivatives appear as multiplication by $-k^2$, so that the update formula writes

$$\boxed{\hat{U}^+ = (\hat{U} - dt(k^2 \mathcal{F}(U^3)))/S}, (k_1, k_2) \in \mathcal{K},$$

with the slightly altered expression

$$S = 1 + dt(k^4 - k^2). \quad (5.19)$$

For the equation describing the faceting of a growing surface, (2.13), one can proceed in the same way. The tri-Laplacian

$$\nabla^6 u = u_{xxxxx} + 3(u_{xxxxy} + u_{xyyyy}) + u_{yyyyy}$$

discretized and in Fourier space becomes

$$\widehat{\nabla^6 U}_{|(k_1, k_2)} = -(k_1^6 + 3k_1^4 k_2^2 + 3k_1^2 k_2^4 + k_2^6) \hat{U} = -k^6 \hat{U}, (k_1, k_2) \in \mathcal{K},$$

so that the expression (5.19) can be used accordingly. A semi-implicit Euler PSM then writes

$$\begin{aligned} \frac{\hat{U}^+ - \hat{U}}{dt} &= \mathcal{L} \hat{U}^+ + \mathcal{N}, \\ \Leftrightarrow \boxed{\hat{U}^+ = \frac{\hat{U} + dt \mathcal{N}}{1 - dt \mathcal{L}}}, (k_1, k_2) \in \mathcal{K}, \end{aligned} \quad (5.20)$$

with the linear operator

$$\mathcal{L} = k^4 - k^6$$

and the nonlinear, explicit term

$$\mathcal{N} = \frac{\delta}{2} \mathcal{F}[H_X^2 + H_Y^2] + k^2 \mathcal{F}[b(H_X^2 H_{YY} + H_Y^2 H_{XX} + 4H_X H_Y H_{XY}) + 3H_X^2 H_{XX} + 3H_Y^2 H_{YY}] \quad .$$

For the evaluation of the nonlinearity, the derivatives can be obtained with spectral differentiation. For example $H_X H_Y H_{XY}$ can be evaluated as $\mathcal{F}[\mathcal{F}^{-1}[ik_1 \hat{U}] \mathcal{F}^{-1}[ik_2 \hat{U}] \mathcal{F}^{-1}[-k_1 k_2 \hat{U}]]$.

For neither of the CH type equations it is difficult to establish a PSM that works as long as not too small parameters are involved. Corresponding ODE schemes are summarized in Table 5.1. It remains to introduce the scheme that has been used for the other main equation of this work, the QDM equation (4.24). It can be solved with scheme (5.20), with new linear and nonlinear terms

$$\mathcal{L} = \tilde{e}k^3 - k^4 \quad , \quad (5.21)$$

$$\mathcal{N} = k^2 (ik_1 \mathcal{F}[\partial_{H_X} W] + ik_2 \mathcal{F}[\partial_{H_Y} W] + \tilde{\gamma} \mathcal{F}[\frac{1}{H^2}]) \quad .$$

For the case with deposition, equation (4.22), the update formula is slightly adjusted, it becomes

$$\boxed{\hat{U}^+ = \frac{\hat{U} + dt(\mathcal{N} + r)}{1 - dt\mathcal{L}} \quad , (k_1, k_2) \in \mathcal{K}} \quad (5.22)$$

where $r = \tilde{F}r_3/|w|$ and the linearity is adjusted to

$$\mathcal{L} = \tilde{e}k^3 - k^4 - i\tilde{F}(k_1 r_1 + k_2 r_2)/|w| \quad . \quad (5.23)$$

Finally, before this last regular Chapter is finished and a short discussion and the outlook for future work completes this document, a last remark on the difference between PSM and spectral methods (SM) is given. Generally PSMs are a subclass of SMs. One can derive either FDMs, FEMs, SMs or PSMs as methods of weighted residuals. Therefore the sought solution is expanded and a residual based on this expansion is defined. It then is inserted into a scalar product with suitable test functions as dual pairing and minimization of this product gives an approximate solution. Dependent on the test and basis functions, this approach results in the different numerical methods known for solving PDEs. In case of SMs and PSMs one chooses global functions such as trigonometric functions or Chebyshev polynomials as basis elements. In case of the PSM the test functions are special, delta functions are chosen for that end. As a result integrals are evaluated only in certain points — the collocation points — while for other SMs the integrals have to be evaluated completely. This explains why PSMs are also called collocation methods.

PDE in real space $h_t = f(h, h_x, \dots)$	Scheme in Fourier space $\hat{U}_t = \mathcal{L}\hat{U} + \mathcal{N}$
$f = \nabla^2 h$	$\mathcal{L} = -k^2$
$f = -\nabla^4 h$	$\mathcal{L} = -k^4 = -(k_1^4 + 2k_1^2 k_2^2 + k_2^4)$
$f = \nabla^6 h$	$\mathcal{L} = -k^6 = -(k_1^6 + 3k_1^4 k_2^2 + 3k_1^2 k_2^4 + k_2^6)$
$f = \nabla^2 h - h^3 + h$	$\mathcal{L} = -k^2 + 1, \mathcal{N}(H) = -\mathcal{F}[H^3]$
$f = \nabla^2(-\nabla^2 h + h^3 - h)$	$\mathcal{L} = -k^4 + k^2, \mathcal{N}(H) = -k^2 \mathcal{F}[H^3]$
$f = \nabla^4(\nabla^2 h - h^3 + h)$	$\mathcal{L} = -k^6 + k^4, \mathcal{N}(H) = -k^4 \mathcal{F}[H^3]$
$f = \nabla^4 H + \nabla^6 H - \nabla^2[b(H_X^2 H_{YY} + H_Y^2 H_{XX} + 4H_X H_Y H_{XY}) + 3H_X^2 H_{XX} + 3H_Y^2 H_{YY}]$	$\mathcal{L} = -k^6 + k^4$ $\mathcal{N} = k^2[b\mathcal{F}[H_X^2 H_{YY} + H_Y^2 H_{XX} + 4H_X H_Y H_{XY}] + 3\mathcal{F}[H_X^2 H_{XX} + H_Y^2 H_{YY}]]$
$f = \nabla^2[\mathcal{F}^{-1}[-\tilde{e}k\mathcal{F}[H]] - \nabla^2 H - \frac{\tilde{\gamma}}{H^2} - \nabla \cdot \nabla_{\nabla H} W(H_X, H_Y)]$	$\mathcal{L} = \tilde{e}k^3 - k^4$ $\mathcal{N} = ik_1 \mathcal{F}[\partial_{H_X} W] + ik_2 \mathcal{F}[\partial_{H_Y} W] + \tilde{\gamma} \mathcal{F}[\frac{1}{H^2}]$
$f = \nabla^2[\mathcal{F}^{-1}[-\tilde{e}k\mathcal{F}[H]] - \nabla^2 H - \frac{\tilde{\gamma}}{H^2} - \nabla \cdot \nabla_{\nabla H} W(H_X, H_Y)] + \frac{\tilde{F}r_3}{ w } - \frac{\tilde{F}}{ w }(r_1 H_X + r_2 H_Y)$	$\mathcal{L} = \tilde{e}k^3 - k^4 - i\tilde{F}/ w (r_1 k_1 + r_2 k_2)$ $\mathcal{N} = ik_1 \mathcal{F}[\partial_{H_X} W] + ik_2 \mathcal{F}[\partial_{H_Y} W] + \tilde{\gamma} \mathcal{F}[\frac{1}{H^2}]$ $r = \tilde{F}r_3/ w $

Table 5.1: Summarizing table: System functions for the evolution equations in 3D for the different PDEs considered in this work and corresponding schemes in Fourier space.

Chapter 6

Summary and discussion

From the end spring new beginnings.

Pliny the Elder (23 AD - 79 AD)

In this work many important topics concerning the self-assembly of thin crystalline films have been addressed, several questions were answered, others were posed. From the set-up of continuum models, to reduction via small slope approximations, existence of solutions, their long-time behavior, analysis of stationary solutions and numerical simulations, many new results have been presented. To work with the high order equations of Cahn-Hilliard type new theory has been established. The thesis is summarized on these last pages and at the end possibilities for future research are outlined.

It has been described how to model an epitaxy process in terms of a continuum theory based on Mullins' surface diffusion formula. Various equations introduced in publications from the last two or three decades can be derived with help of the presented modeling approach. Self-contained evolution equations of fourth and sixth order are obtained by applying a consistent model reduction. Therefore characteristic scales of the underlying problem are incorporated to define asymptotic expansions, which can be used to identify less important terms that can be neglected. How to define a reasonable chemical potential, which at the end of the day has the main influence on the evolution, is still under discussion although the models improved a lot during the last decades. Over the years more and more of the important effects one wishes to model have been captured. Two fundamentally different potentials for two phenomena have been addressed in this work. They result in two evolution equations called here the HCCH equation [89] and the new QDM equation [56], which were simulated and analyzed on many aspects.

The first model relies on a strongly anisotropic surface energy that is regularized by a Wilmore term and additionally a normal atom flux impinges onto the surface. For the resulting PDE existence of weak solutions has been proved. A Galerkin approach has been applied to establish the result. To obtain lower order bounds in the first stage, a suitable inverse operator of the

bi-Laplacian has been applied to the equation which then has been tested with suitable functions. One can proceed with the standard form of the equation to derive higher order bounds. Passing to the limit of the Galerkin approximation yields the desired result. A pseudospectral method was used to actually compute approximate solutions. With help of this numerical method it has been found that the characteristic wave lengths of the traveling wave or stationary solutions decrease, until a chaotic regime is reached. In a next step possible stationary solutions have been derived and certain features were described analytically. Heteroclinic connections in a fifth order phase space have been found. These can be tracked in a parameter plane by application of a suitable continuation approach. For solutions on one of the branches a method of matched asymptotics has been introduced. It is special in that it retains exponentially small terms in a matching procedure to derive expressions for the far-field parameter for the new spatially nonmonotonous solutions in the limit of small driving strength. It extends a method that has been introduced by Lange [62]. Furthermore a characteristic hump spacing has been related to the Lambert W function, which closes the analysis to the HCCH equation within this work. Although many results have been established, more work is on the way. For the original equation for the faceting of a growing surface in three dimensions (2.13) an existence proof for weak solutions is prepared. Uniqueness is still an open question up to now.

The QDM equation is the first consistent small slope reduced equation for quantum dot growth which includes the effects of stresses, wetting interactions, anisotropic surface energy and a deposition flux at once. An elastic problem has to be considered, because of the coherent interface a destabilizing coherency stress is created in the growing crystal. It competes with the surface energy, whose variable anisotropy allows for different preferred facets. A height-dependency of the surface energy results in a connection of the islands by a very thin film. Simulations have shown that the QDM equation is capable to describe the assembly of Ge/Si(001) pyramids and their Ostwald ripening. A pseudospectral method enables large-scale simulations that show triangular solutions in two dimensions and faceted islands in three dimensions whose shapes depend on the incorporated anisotropy formula. The linear stability analysis describes analytically what can be observed in early stages of simulations. The anisotropy acts destabilizing and the critical thickness of flat films decreases when the anisotropy parameter is increased. The most unstable wave lengths then become smaller. A randomly perturbed deposition flux has been added into the model and indeed the Stranski-Krastanov growth mode is observed during simulations. As in experiments the island density increases for stronger atomic fluxes. Ostwald ripening of quantum dots as in experiments by IBM qualitatively validate the model. The ripening takes place with a rate that obeys a power law for the late time of evolution.

A chapter about the numerical schemes used for the simulations in this thesis has completed the work. Motivated as interpolation methods, finite difference and pseudospectral methods were introduced that are applicable to solve the high order PDEs describing the self-assembly of thin crystalline surfaces. Due to the smoothness of the solutions, the PSM works especially well when

periodicity of the solutions is assumed, as this is also the case in the existence proof. Matlab codes were enclosed to show how short the implementations of such effective methods may be.

The field of modeling, analysis and numerical simulation of self-assembled solid structures allows for further research. A possible task is the extension of the QDM equation to anisotropic elasticity. Similarly as done by Pang and Huang [78], Hooke's law might be adjusted to bulk anisotropy. However, the authors treated a half-space problem, while a real extension of the QDM equation would need the possibility to allow for different elastic constants in the film and in the substrate. Of particular interest in modeling are the interface conditions which are crucial in heteroepitaxial systems. Since it becomes popular to use *stacked* quantum dots [15, 90] — atoms are deposited epitaxially on a substrate that contains 'built-in' strain due to underlying inclusions — the derived QDM equation might be extended to a model for the growth of such many-layer systems in a similar way as for fluids, where several layers of liquid material are covering each other [80]. A study of the interfaces and conditions at these boundaries would be necessary. Furthermore the numerics might be another challenge due to growing complexity for both, the evolution equation and the coupled elasticity problem. From the theoretical side existence of solutions may be analyzed further, be it for the QDM equation, for stationary solutions or a possible new model for stacked nanoislands.

Bibliography

- [1] K. L. Adams, J. R. King, and R. H. Tew. Beyond-all-orders effects in multiple-scales asymptotics: travelling-wave solutions to the Kuramoto-Sivashinsky equation. *J. Engr. Math.*, 45:197–226, 2003.
- [2] S. M. Allen and J. W. Cahn. A microscopic theory for antiphase boundary motion and its application to antiphase domain coarsening. *Acta Metall.*, 27(6):1085–1095, 1979.
- [3] J.-N. Aqa, T. Frisch, and A. Verga. Nonlinear evolution of a morphological instability in a strained epitaxial film. *Phys. Rev. B*, 76:165319, 2007.
- [4] R. J. Asaro and W. A. Tiller. Interface morphology development during stress corrosion cracking. II. Via volume diffusion. *Acta Metall.*, 23:341–344, 1975.
- [5] R. W. Atherton and G. M. Homsy. On the derivation of evolution equations for interfacial waves. *Chem. Eng. Com.*, 2:57–77, 1976.
- [6] W.-J. Beyn. The Numerical Computation of Connecting Orbits in Dynamical Systems. *IMA J. Num. Anal.*, 9:379–405, 1990.
- [7] A. Bodzenta, M. D. Korzec, P. Nayar, and P. Rybka. Global weak solutions to a sixth order Cahn-Hilliard type equation. *Work in preparation*.
- [8] H. P. Bonzel and E. Preuss. Morphology of periodic surface profiles below the roughening temperature: aspects of continuum theory. *Surf. Sci.*, 336(1-2):209–224, 1995.
- [9] A. J. Bray. Theory of phase-ordering kinetics. *Adv. Phys.*, 43(3):357–459, 1994.
- [10] T. M. Burbaev, T. N. Zavaritskaya, V. A. Kurbatov, N. N. Melânik, V. A. Tsvetkov, K. S. Zhuravlev, V. A. Markov, and A. I. Nikiforov. Optical Properties of Germanium Monolayers on Silicon. *Semiconductors*, 35(8):941–946, 2001.
- [11] M. Burger, F. Haußer, C. Stöcker, and A. Voigt. A level set approach to anisotropic flows with curvature regularization. *J. Comput. Phys.*, 225(1):183–205, 2007.

-
- [12] O. Caha, V. Holý, and K. E. Bassler. Nonlinear Evolution of Surface Morphology in InAs/AlAs Superlattices via Surface Diffusion. *Phys. Rev. Lett.*, 96(13):136102, 2006.
- [13] C. G. Canuto, M. Y. Hussaini, A. Quarteroni, and T. A. Zang. *Spectral Methods: Evolution to Complex Geometries and Applications to Fluid Dynamics*. Springer, 2007.
- [14] T. Chen, H. Levine, and P. Sacks. Analysis of a convective reaction-diffusion equation. *Nonl. Anal.*, 12:1349–1370, 1988.
- [15] W.-Y. Chen, W.-H. Chang, A. T. Chou, T. M. Hsu, P. S. Chen, Z. Pei, and L. S. Lai. Optical properties of stacked Ge/Si quantum dots with different spacer thickness grown by chemical vapor deposition. *Appl. Surf. Sci.*, 224(148), 2004.
- [16] C.-h. Chiu. The self-assembly of uniform heteroepitaxial islands. *Appl. Phys. Lett.*, 75(22):3473–3475, 1999.
- [17] C.-h. Chiu. Stable and uniform arrays of self-assembled nanocrystalline islands. *Phys. Rev. B*, 69:165413, 2004.
- [18] C.-H. Chiu and Z. Huang. Common features of nanostructure formation induced by the surface undulation on the Stranski-Krastanow systems. *Appl. Phys. Lett.*, 89:171904, 2006.
- [19] C.-H. Chiu and Z. Huang. Numerical simulation for the formation of nanostructures on the Stranski-Krastanow systems by surface undulation. *J. Appl. Phys.*, 101:113540, 2007.
- [20] G. Conibeer, M. Green, E.-C. Cho, D. König, Y.-H. Cho, T. Fangsuwannarak, G. Scardera, E. Pink, Y. Huang, T. Puzzer, S. Huang, D. Song, C. Flynn, S. Park, X. Hao, and D. Mansfield. Silicon quantum dot nanostructures for tandem photovoltaic cells. *Thin Solid Films*, 516:6748–6756, 2008.
- [21] J. W. Cooley and J. W. Tukey. An algorithm for the machine calculation of complex Fourier series. *Math. Comp.*, 19:297–301, 1965.
- [22] A. Danescu. The Asaro-Tiller-Grinfeld instability revisited. *Int. J. Solids Struct.*, 38:4671–4684, 2000.
- [23] J. Drucker. Self-Assembling Ge(Si)/Si(001) Quantum Dots. *IEEE J. Quantum Electronics*, 38(8):975–987, 2002.
- [24] A. Eden and V. K. Kalantarov. The convective Cahn-Hilliard equation. *App. Math. Lett.*, 20(4):455–461, 2007.
- [25] H. R. Eisenberg and D. Kandel. Wetting Layer Thickness and Early Evolution of Epitaxially Strained Thin Films. *Phys. Rev. Lett.*, 85(6):1286–1289, 2000.

-
- [26] H. R. Eisenberg and D. Kandel. Origin and properties of the wetting layer and early evolution of epitaxially strained thin films. *Phys. Rev. B*, 66:155429, 2002.
- [27] H. R. Eisenberg and D. Kandel. Formation, ripening, and stability of epitaxially strained island arrays. *Phys. Rev. B*, 71:115423, 2005.
- [28] C. M. Elliott and Z. Songmu. On the Cahn-Hilliard equation. *Arch. Rat. Mech. Anal.*, 96:339–357, 1986.
- [29] C. L. Emmott and A. J. Bray. Coarsening Dynamics of a One-Dimensional Driven Cahn-Hilliard System. *Phys. Rev. E*, 54(5):4568–4575, 1996.
- [30] J. D. Evans, V. A. Galaktionov, and J. R. King. Unstable sixth-order thin film equation: I. Blow-up similarity solutions . *Nonlinearity*, 20:1799–1841, 2007.
- [31] L. C. Evans. *Partial Differential Equations*. AMS, 1998.
- [32] J. A. Floro, E. Chason, R. D. Twisten, R. Q. Hwang, and L. B. Freund. SiGe Coherent Islanding and Stress Relaxation in the High Mobility Regime. *Phys. Rev. Lett.*, 79(20):3946–3949, 1997.
- [33] B. Fornberg. *A Practical Guide to Pseudospectral Methods*. Cambridge Monographs Appl. Comp. Math., 1998.
- [34] L. B. Freund and S. Suresh. *Thin Film Materials*. Cambridge Univ. Press, 2003.
- [35] M. J. Friedman and E. J. Doedel. Numerical Computation and Continuation of Invariant Manifolds Connecting Fixed Points. *SIAM J. Numer. Anal.*, 28(3):789–808, 1991.
- [36] M. Frigo and S. G. Johnson. The Design and Implementation of FFTW3. *Proc IEEE*, 93(2):216–231, 2005.
- [37] H. Garcke. On Cahn-Hilliard Systems with Elasticity. *Proc. Roy. Soc. Edinburgh*, 133 A, 307, 2003.
- [38] K. Glasner, F. Otto, T. Rump, and D. Slepcev. Ostwald ripening of droplets: The role of migration. *Euro. Jour. of Appl. Math.*, 20:1–67, 2009.
- [39] K. B. Glasner and T. P. Witelski. Coarsening dynamics of dewetting films. *Phys. Rev. E*, 67(1):016302, 2003.
- [40] A. A. Golovin, S. H. Davis, and A. A. Nepomnyashchy. A convective Cahn-Hilliard model for the formation of facets and corners in crystal growth. *Phys. D*, 122(1-4):202–230, 1998.
- [41] A. A. Golovin, S. H. Davis, and A. A. Nepomnyashchy. Model for faceting in a kinetically controlled crystal growth. *Phys. Rev. E*, 59(1):803–825, 1999.

- [42] A. A. Golovin, S. H. Davis, and P. W. Voorhees. Self-organization of quantum dots in epitaxially strained solid films. *Phys. Rev. E*, 68:056203, 2003.
- [43] A. A. Golovin, M. S. Levine, T. V. Savina, and S. H. Davis. Faceting instability in the presence of wetting interactions: A mechanism for the formation of quantum dots. *Phys. Rev. B*, 70:235342, 2004.
- [44] A. A. Golovin, A. A. Nepomnyashchy, S. H. Davis, and M. A. Zaks. Convective Cahn-Hilliard Models: From Coarsening to Roughening. *Phys. Rev. Lett.*, 86(8):1550, 2001.
- [45] M. B. Gratton and T.P. Witelski. Coarsening of dewetting thin films subject to gravity. *Phys. Rev. E*, 77(016301):1–11, 2008.
- [46] J. Guckenheimer and P. Holmes. *Nonlinear Oscillations, Dynamical Systems, and Bifurcations of Vector Fields*. Springer, 1983.
- [47] J. K. Hale and H. Kocak. *Dynamics and Bifurcations*. Springer-Verlag, New York, 1991.
- [48] E. J. Hinch. *Perturbation Methods*. Cambridge University Press, 1991.
- [49] Q. Hu and N. M. Ghoniem. The Early Stages of Quantum Dot Self-Assembly: A Kinetic Monte Carlo Simulation. *J. Comp. Theor. Nanosci.*, 3(5):696–701(6), 2006.
- [50] H. Jeong, A. M. Chang, and M. R. Melloch. The Kondo Effect in an Artificial Quantum Dot Molecule. *Sci.*, 293(5538):2221 – 2223, 2001.
- [51] K. Kawasaki and T. Ohta. Kink dynamics in one-dimensional nonlinear systems. *Physica*, 116, 1982.
- [52] J. Kevorkian and J. D. Cole. *Multiple Scale and Singular Perturbation Methods*. Springer, 1996.
- [53] J. Kierzenka and L. Shampine. A BVP Solver Based on Residual Control and the MATLAB PSE. *ACM Transactions on Mathematical Software*, 27(3):299–316, 2001.
- [54] G. Kitavtsev and B. Wagner. Coarsening dynamics of slipping droplets. *J. Eng. Math.*, 66(1-3):271–292, 2010.
- [55] R. Kornhuber and R. Krause. Robust multigrid methods for vector-valued Allen-Cahn equations with logarithmic free energy. *Comp. Visual. Sci.*, 9(2):103–116, 2006.
- [56] M. D. Korzec and P. L. Evans. From bell shapes to pyramids: A reduced continuum model for self-assembled quantum dot growth. *Phys. D*, 239:465–474, 2010.
- [57] M. D. Korzec, P. L. Evans, A. Münch, and B. Wagner. Stationary solutions of driven fourth- and sixth-order Cahn-Hilliard type equations. *SIAM J. Appl. Math.*, 69:348–374, 2008.

-
- [58] M. D. Korzec and P. Rybka. On a higher order convective Cahn-Hilliard equation. *WIAS preprint, in preparation*.
- [59] R. V. Kutka and L. B. Freund. Minimum energy configuration of epitaxial material clusters on a lattice-mismatched substrate. *J. Mech. Phys. Solids*, 45, 1997.
- [60] O. A. Ladyzenskaja, V. A. Solonnikov, and N.N. Uralceva. *Linear and quasilinear equations of parabolic type*. Amer. Math. Soc., 1968.
- [61] L. D. Landau and E. M. Lifshitz. *Theory of Elasticity, 3rd Edition*. Pergamon Press, 1986.
- [62] C. G. Lange. On spurious solutions of singular perturbation problems. *Studies in Applied Mathematics*, 68:227–257, 1983.
- [63] F. C. Larché and J. W. Cahn. The effect of self-stress on diffusion in solids. *Acta Metall.*, 30:1835–1845, 1982.
- [64] M. S. Levine, A. A. Golovin, S. H. Davis, and P. W. Voorhees. Self-assembly of quantum dots in a thin epitaxial film wetting an elastic substrate. *Phys. Rev. B*, 75:205312, 2007.
- [65] B. Li, J. Lowengrub, A. Rätz, and A. Voigt. Geometric Evolution Laws for Thin Crystalline Films: Modeling and Numerics. *Com. Comp. Phys.*, 6(3):433–482, 2009.
- [66] D. Loss and D. P. DiVincenzo. Quantum computation with quantum dots. *Phys. Rev. A*, 57(1):120–126, 1998.
- [67] G. B. McFadden, S. R. Coriell, and R. F. Sekerka. Effect of surface tension anisotropy on cellular morphologies. *J. Crystal Growth*, 91(1-2):180–198, 1988.
- [68] N. Motta. Self-assembling and ordering of Ge/Si(111) quantum dots: scanning microscopy probe studies. *J. Phys.: Condens. Matter*, 14:8353–8378, 2002.
- [69] W. W. Mullins. Theory of Thermal Grooving. *J. Appl. Phys.*, 28(3):333–339, 1957.
- [70] A. Münch, B. Wagner, and T. P. Witelski. Lubrication models with small to large slip lengths. *J. of Eng. Math.*, 53:359–383, 2005.
- [71] S. Nakamura, G. Fasol, and S.J. Pearton. *The Blue Laser Diode: The Complete Story*. Springer, 2000.
- [72] C. Neto and K. Jacobs. Dynamics of hole growth in dewetting in polystyrene films. *Phys. A*, 339:66–71, 2004.
- [73] S.A. Norris and S.J. Watson. Geometric simulation and surface statistics of coarsening faceted surfaces. *Acta Mat.*, 55:6444–6452, 2007.

- [74] A. Novick-Cohen. On Cahn-Hilliard Type Equations. *Nonlin. Anal., Theory, Meth. and Appl.*, 15(9):797–814, 1990.
- [75] A. Novick-Cohen and L. A. Peletier. Steady states of the one-dimensional Cahn-Hilliard equation. *Proc. Roy. Soc. Edinburgh*, 123(6):1071–1098, 1993.
- [76] R. E. O’Malley, Jr. Phase-plane solutions to some singular perturbation problems. *J. Math. Anal. Appl.*, 54(2):449–466, 1976.
- [77] Y. Pang and R. Huang. Nonlinear effect of stress and wetting on surface evolution of epitaxial thin films. *Phys. Rev. B*, 74:075413, 2006.
- [78] Y. Pang and R. Huang. Effect of elastic anisotropy on surface pattern evolution of epitaxial thin films. *Int. J. Sol. Struct.*, 46(14-15):2822–2833, 2009.
- [79] A. Podolny, M. A. Zaks, B. Y. Rubinstein, A. A. Golovin, and A. A. Nepomnyashchy. Dynamics of domain walls governed by the convective Cahn-Hilliard equation. *Phys. D*, 201:291–305, 2005.
- [80] A. Pototsky, M. Bestehorn, D. Merkt, and U. Thiele. Evolution of interface patterns of three-dimensional two-layer liquid films. *Europhys. Lett.*, 74(4):665–671, 2006.
- [81] L. G. Reyna and M. J. Ward. Metastable internal layer dynamics for the viscous Cahn-Hilliard equation. *Meth. App. Anal.*, 2:285–306, 1995.
- [82] J. Robinson. *Infinite-Dimensional Dynamical Systems - From Basic Concepts to Actual Calculations*. Cambridge University Press, 2001.
- [83] T. M. Rogers, K. R. Elder, and R. C. Desai. Numerical studies of the late stages of spinodal decomposition. *Phys. Rev. B*, 37(16), 1988.
- [84] S. Rosenblat and R. Szeto. Multiple solutions of nonlinear boundary-value problems. *Stud. Appl. Math.*, 63:99–117, 1980.
- [85] F. M. Ross, J. Tersoff, M. Reuter, F. K. Legoues, and R. M. Tromp. In situ transmission electron microscopy observations of the formation of self-assembled Ge islands on Si. *Microscopy Res. Tech.*, 42(4):281–294, 1998.
- [86] F. M. Ross, J. Tersoff, and R. M. Tromp. Coarsening of Self-Assembled Ge Quantum Dots on Si(001). *Phys. Rev. Lett.*, 80(5):984–987, 1998.
- [87] M. H. Sadd. *Elasticity : theory, applications, and numerics*. Academic Press, 2009.
- [88] K. Sanderson. Quantum dots go large. *Nature*, 459:760–761, 2009.

-
- [89] T. V. Savina, A. A. Golovin, S. H. Davis, A. A. Nepomnyashchy, and P. W. Voorhees. Faceting of a growing crystal surface by surface diffusion. *Phys. Rev. E*, 67:021606, 2003.
- [90] O. G. Schmidt, N. Y. Jin-Phillipp, C. Lange, U. Denker, K. Eberl, R. Schreiner, H. Grabeldinger, and H. Schweizer. Long-range ordered lines of self-assembled Ge islands on a flat Si(001) surface. *App. Phys. Lett.*, 77:4139–4141, 2000.
- [91] D. J. Seol, S. Y. Hu, Z. K. Liu, and L. Q. Chen. Phase-field modeling of stress-induced surface instabilities in heteroepitaxial thin films. *J. Appl. Phys.*, 98:044910, 2005.
- [92] L. F. Shampine, P. H. Muir, and H. Xu. A User-Friendly Fortran BVP-solver. *J. Num. Anal., Ind. Appl. Math.*, 1(2):201–217, 2006.
- [93] B. J. Spencer. Asymptotic derivation of the glued-wetting-layer model and contact-angle condition for Stranski-Krastanow islands. *Phys. Rev. B*, 59(3):2011–2017, 1999.
- [94] B. J. Spencer. Asymptotic solutions for the equilibrium crystal shape with small corner energy regularization. *Phys. Rev. E*, 69:011603, 2004.
- [95] B. J. Spencer, S. H. Davis, and P. W. Voorhees. Morphological instability in epitaxially strained dislocation-free solid films: Nonlinear evolution. *Phys. Rev. B*, 47(15):9760–9777, 1993.
- [96] B. J. Spencer and J. Tersoff. Stresses and first-order dislocation energetics in equilibrium Stranski-Krastanow islands. *Phys. Rev. B*, 63(20):205424, 2001.
- [97] B. J. Spencer, P. W. Voorhees, and S. H. Davis. Morphological instability in epitaxially strained dislocation-free solid films. *Phys. Rev. Lett.*, 67(26):3696–3699, 1991.
- [98] B. J. Spencer, P. W. Voorhees, and S. H. Davis. Morphological instability in epitaxially strained dislocation-free solid films: Linear stability theory. *J. Appl. Phys.*, 73(10):4955–4970, 1993.
- [99] R. H. Stogner, G. F. Carey, and B. T. Murray. Approximation of Cahn-Hilliard diffuse interface models using parallel adaptive mesh refinement and coarsening with C^1 elements. *Int. J. Num. Meth. Eng.*, 64:1–19, 2006.
- [100] H. Takenaka, Y. Wang, and T. Furumura. An efficient approach of the pseudospectral method for modelling of geometrically symmetric seismic wavefield. *Earth Planets Space*, 51:73–79, 1999.
- [101] C. Teichert, J. C. Bean, and M. C. Lagally. Self-organized nanostructures in $\text{Si}_{1-x}\text{Ge}_x$ films on Si(001). *Appl. Phys. A*, 67:675–685, 1998.

-
- [102] W. T. Tekalign and B. J. Spencer. Evolution equation for a thin epitaxial film on a deformable substrate. *J. Appl. Phys.*, 96(10):5505–5512, 2004.
- [103] W. T. Tekalign and B. J. Spencer. Thin-film evolution equation for a strained solid film on a deformable substrate: Numerical steady states. *J. Appl. Phys.*, 102:073503, 2007.
- [104] K. Thornton, J. Ågren, and P. W. Voorhees. Modelling the evolution of phase boundaries in solids at the meso- and nano-scales. *Acta Mater.*, 51(19):5675–5710, 2003.
- [105] L. N. Trefethen. *Spectral methods in MATLAB*. SIAM, 2000.
- [106] A. Voigt, editor. *Multiscale Modeling in Epitaxial Growth*. Birkhauser, 2005.
- [107] M. J. Ward. Eliminating indeterminacy in singularly perturbed boundary value problems with transition invariant potentials. *Stud. Appl. Math.*, 87:95–134, 1992.
- [108] S. J. Watson and S.A. Norris. Scaling Theory and Morphometrics for a Coarsening Multi-scale Surface, via a Principle of Maximal Dissipation . *Phys. Rev. Lett.*, 96:176103, 2006.
- [109] S. J. Watson, F. Otto, B. Rubinstein, and S. H. Davis. Coarsening dynamics of the convective Cahn-Hilliard equation. *Phys. D*, 178:127–148, 2003.
- [110] J. Wei and M. Winter. On the Stationary Cahn-Hilliard Equation: Interior Spike Solutions. *J. Diff. Eq.*, 148:231–267, 1998.
- [111] J. Wei and M. Winter. Stationary solutions for the Cahn-Hilliard equation. *Annales de l’I.H.P., section C*, 4:459–492, 1998.
- [112] J. A. Weideman and S. C. Reddy. A MATLAB differentiation matrix suite. *ACM Trans. Math. Soft. (TOMS)*, 26:465–519, 2000.
- [113] J. J. Wortman and R. A. Evans. Young’s Modulus, Shear Modulus, and Poisson’s Ratio in Silicon and Germanium. *J. Appl. Phys.*, 36(1), 1965.
- [114] Y. Xiang and W. E. Nonlinear evolution equation for the stress-driven morphological instability. *J. Appl. Phys.*, 91(11):9414–9422, 2002.
- [115] M. A. Zaks, A. Podolny, A. A. Nepomnyashchy, and Alexander A. Golovin. Periodic Stationary Patterns Governed by a Convective Cahn-Hilliard Equation. *SIAM J. Appl. Math.*, 66(2):700–720, 2006.
- [116] Y. W. Zhang. Self-organization, shape transition, and stability of epitaxially strained islands. *Phys. Rev. B*, 61(15):10388–10392, 2000.
- [117] Y. W. Zhang, A. F. Bower, and P. Liu. Morphological evolution driven by strain induced surface diffusion. *Thin Solid Films*, 424(1):9–14, 2003.

- [118] Y. W. Zhang, A. F. Bower, L. Xia, and C. F. Shih. Three dimensional finite element analysis of the evolution of voids and thin films by strain and electromigration induced surface diffusion. *J. Mech. Phys. Solids*, 47(1):173–199, 1999.
- [119] Y. W. Zhang and D. J. Srolovitz. Surface instability and evolution of nonlinear elastic heteroepitaxial thin-film structures. *Phys. Rev. B*, 70:041402, 2004.

Appendix A

Mathematical basics: Surface modeling

The following mathematical basics are presented without detailed assumptions that can be imposed. All function are assumed to be sufficiently smooth, so that the expressions stated make sense.

Consider a function $h : \Omega \rightarrow \mathbb{R}$ that smoothly parameterizes a surface

$$S = \{(x, y, z) \in \mathbb{R}^3 | \exists_{(x,y) \in \Omega} : h(x, y) = z\} \quad ,$$

where $\Omega \subset \mathbb{R}^2$ is bounded with Lipschitz boundary and connected. Then one can define tangential and normal vectors, the mean curvature and the surface Laplacian.

Two *tangent vectors*, t_1 and t_2 , are defined by differentiating the graph function $(x, y) \rightarrow (x, y, h(x, y))$ with respect to the domain variables x and y :

$$t_1 = (1, 0, h_x)^T, \quad t_2 = (0, 1, h_y)^T \quad .$$

The unit normal n is orthogonal to both of these vectors and it has unit length. The orthogonality is by construction given as cross product and normalization yields the desired unit length.

$$n = \frac{t_1 \times t_2}{\|t_1 \times t_2\|} = \frac{1}{\sqrt{1 + |\nabla h|^2}} \begin{pmatrix} -h_x \\ -h_y \\ 1 \end{pmatrix} \quad . \quad (\text{A.1})$$

The *mean curvature* is defined as

$$\kappa = \frac{h_{xx}(1 + h_y^2) + h_{yy}(1 + h_x^2) - 2h_x h_y h_{xy}}{(1 + |\nabla h|^2)^{\frac{3}{2}}} \quad . \quad (\text{A.2})$$

There are different definitions in other works, in particular crucial sign changes may be found. Here a parabola bounded below has a mean curvature bigger zero. The *surface Laplacian*, applied

for surface diffusion problems, is given as

$$\nabla_s^2 = \frac{1}{1 + |\nabla h|^2} \left((1 + h_y^2) \partial_{xx} + (1 + h_x^2) \partial_{yy} - 2h_x h_y \partial_{xy} - \kappa \sqrt{1 + |\nabla h|^2} (h_x \partial_x + h_y \partial_y) \right). \quad (\text{A.3})$$

However, use of this longsome expression is mostly avoided by application of a long wave approximation. To leading order, for surfaces with small slopes, it simply becomes the standard Laplacian.

Often surface integrals are used in the modeling of surface energies. There it is useful to define an infinitesimal surface element. It is given as

$$dS = \sqrt{1 + |\nabla h|^2} dx dy \quad .$$

It can be derived in one dimension with help of Taylors expansion and Pythagoras

$$\begin{aligned} \Delta s &= \sqrt{\Delta x^2 + \Delta z^2} = \sqrt{\Delta x^2 + [h(x + \Delta x) - h(x)]^2} \\ &\doteq \sqrt{\Delta x^2 + [h(x) + h_x \Delta x - h(x)]^2} = \Delta x \sqrt{1 + h_x^2} \quad . \end{aligned}$$

In mathematical modeling the Euler-Lagrange equation appears frequently when instead of direct solving of a PDE a minimizer of a functional is sought. Let

$$\int_{\Omega} F(h, \nabla h) dV$$

be a functional with a sufficiently smooth kernel $F : \Omega \rightarrow \mathbb{R}, F \mapsto F(h, \nabla h)$. To find a minimizer, any *direction* $(\bar{h}, \nabla \bar{h})$ (here: a function in a suitable space, e.g. $\nabla \bar{h} \cdot n = 0$ on $\partial\Omega$ or periodic, so that partial integration can be applied such that boundary terms are zero) the directional derivative has to vanish

$$\begin{aligned} 0 &= \frac{d}{d\epsilon} \int_{\Omega} F(h + \epsilon \bar{h}, \nabla h + \epsilon \nabla \bar{h}) dx \\ &= \int_{\Omega} \frac{d}{d\epsilon} F(h, \nabla h) + F_h(h, \nabla h) \epsilon \bar{h} + F_{\nabla h}(h, \nabla h) \epsilon \nabla \bar{h} + \mathcal{O}(\epsilon^2) dx \\ &= \int_{\Omega} F_h(h, \nabla h) \bar{h} + F_{\nabla h}(h, \nabla h) \nabla \bar{h} + \mathcal{O}(\epsilon) dx \\ &= \int_{\Omega} [F_h(h, \nabla h) - \nabla F_{\nabla h}(h, \nabla h)] \bar{h} + \mathcal{O}(\epsilon) dx \quad . \end{aligned}$$

The fundamental lemma of calculus of variation says that F has to fulfill the so-called *Euler-Lagrange-equation* as necessary condition for an extremum h in the leading order

$$\frac{\partial}{\partial h} F(h, \nabla h) - \nabla \cdot \nabla_{\nabla h} F(h, \nabla h) = 0 \quad .$$

For higher order gradient dependency of the energy functional the results can be extended. In general one refers to the terms on the left as the functional or variational derivative $\delta E/\delta h$. For more spatial dimensions the general form writes

$$\frac{\delta}{\delta h} \int_{\Omega} F(h, \nabla h, \nabla^2 h, \dots) dV = \frac{\partial F}{\partial h} - \nabla \cdot \frac{\partial F}{\partial(\nabla h)} + \nabla^2 \cdot \frac{\partial F}{\partial(\nabla^2 h)} - \dots \quad . \quad (\text{A.4})$$

Appendix B

Mathematical basics: Dynamical systems

Following this book by Guckenheimer and Holmes [46], here the most important terminology from the field of dynamical systems is briefly introduced. The following definitions are needed when heteroclinic solutions, connections between two saddle points, are sought. Starting with an autonomous, explicit ODE

$$\partial^n u = f(u, \partial u, \dots, \partial^{n-1} u) \quad ,$$

one obtains by setting $U_1 = u, U_2 = \partial u, \dots, U_n = \partial^{n-1} u$ a first order system

$$U' = F(U) \in \mathbb{R}^n \quad .$$

It defines an n dimensional phase space — the topological space where solutions live. Precisely one defines:

A *dynamical system* is a tuple (X, ϕ) , where X is the *phase space* (say $X = \mathbb{R}^n$) and ϕ is an *evolution operator*

$$\phi : X \times \mathbb{R} \rightarrow X, \quad \phi = \phi(U, t) \quad ,$$

which fulfills (with $U \in X, t_i \in \mathbb{R}, i = 1, 2$)

1. $\phi(U, 0) = U$
2. $\phi(U, t_1 + t_2) = \phi(\phi(U, t_1), t_2) \quad .$

These conditions come into play naturally, since typically t is the time so that the first condition states that the position of a point under a flow is unchanged in the beginning of observation and that stepping successively forward two times t_1 and t_2 is the same as if one would directly make one big step $t_3 = t_1 + t_2$.

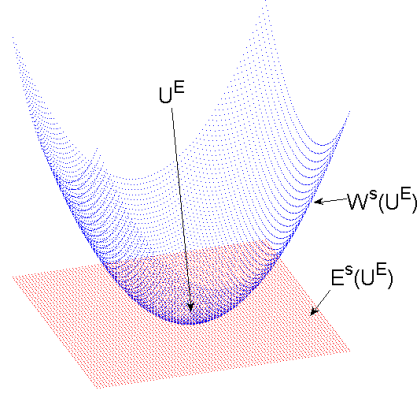


Figure B.1: Stable manifold W^S of an equilibrium point U^E and its linear approximation E^S .

A *flow* is a dynamical system (X, ϕ) which fulfills

$$\frac{d}{dt}\phi(U, t) = F(\phi(U, t)) \quad .$$

For example solutions to ODEs define flows. These are sets of trajectories in the phase space. An *orbit* or a *trajectory* (for $U \in X$) is the set

$$\{\phi(U, t) \mid t \in \mathbb{R}\} \quad .$$

A point $U^E \in X$ is called *fixed/equilibrium/stationary point* or *steady state* if $\phi(U^E, t) = U^E$ for all time. The *stable and unstable manifolds* are defined as the set of trajectories tending to or away from such an equilibrium point U^E

$$\begin{aligned} W^s(U^E) &= \{U \in X \mid \lim_{t \rightarrow \infty} \phi(U, t) = U^E\} \quad , \\ W^u(U^E) &= \{U \in X \mid \lim_{t \rightarrow -\infty} \phi(U, t) = U^E\} \quad . \end{aligned} \quad (\text{B.1})$$

A *heteroclinic connection* is an orbit between two hyperbolic equilibrium points U_+^E and U_-^E

$$\phi(U, t) \quad \text{with} \quad \lim_{t \rightarrow \pm\infty} \phi(U, t) = U_{\pm}^E \quad (\text{or } U_{\mp}^E) \quad .$$

Usually tangent linearizations $E^{s/u}(U^E) \approx W^{s/u}(U^E)$ near equilibrium points are used to compute approximately the whole manifolds with a computer. A very simple example is depicted in Figure B.1. A linearized manifold yields a local description of the nonlinear manifold near the stationary point. Taylor's expansion

$$F(U^E + \delta U) \doteq F(U^E) + \delta F'(U^E)U$$

and

$$F(U^E) = 0 \Rightarrow F(U^E + \delta U) = (U^E)' + \delta U' = \delta U'$$

yield the ODE

$$U' = F'(U^E)U = AU \quad .$$

The eigenvectors of the system matrix A span the solution space. The sign of the eigenvalues determines exponential growth or decay for the fundamental solutions, hence one classifies different subspaces spanned by the eigenvectors of A :

1. The stable subspace $E_s = \text{span}\{v_1, \dots, v_{n_s}\}$
2. The unstable subspace $E_u = \text{span}\{u_1, \dots, u_{n_u}\}$
3. The centered subspace $E_c = \text{span}\{w_1, \dots, w_{n_c}\}$

The vectors v_i are the (generalized) Eigenvectors corresponding to solutions with exponential decay, hence to Eigenvalues with $\Re(\lambda_i) < 0$, u_i to those with $\Re(\lambda_i) > 0$ and w_i correspond to Eigenvalues with zero real part, hence indicate oscillations with constant amplitude or constants (for $\lambda = 0$). Obviously $n = n_s + n_u + n_c$. In this work the case $n_c = 0$ and hence $n = n_s + n_u$ is considered for calculations of steady states of the HCCH equation.

So-called *infinite-dimensional semi-dynamical systems* are frequently used in connection with evolution equations. The solution to a time-dependent PDE $u_t = F(u, u_x, u_y, u_{xx}, \dots)$ at one particular time point t is typically an element of a Banach space X . The PDE defines trajectories in an infinite semi-dynamical phase space via

$$u : [0, T] \rightarrow X, t \mapsto u(t) \in X \quad .$$

Since $t \geq 0$ (the other direction of integration typically leads to blow-up), such equations form semi-dynamical systems.

Appendix C

Elasticity

In this appendix the long wave approximation for the elasticity problem, which has not been addressed in detail in the body of the document, is presented. Characteristic scales are used to define expansions of the displacements in film and substrate. This yields different problems to different orders. With suitable matching one can derive an expansion for the strain energy density \mathcal{E}_{sed} . The following calculations have been carried out by Tekalign and Spencer [102], here they are repeated with more details.

Reduced expressions for the strain energy density

To evaluate the strain energy density at the surface (1.25), it is necessary to obtain expressions for the displacements. In Section 1.3.1 these have been derived for a simple configuration — the base state. In general it is not easy to determine analytical expressions for the strain energy density and either laborious numerical approximations are sought or analytical simplifications are made. Here a thin-film reduction first introduced by Tekalign and Spencer [102] is carried out. To use the small-slope approximation requires to scale the Navier-Cauchy equations, the boundary conditions and the strain and stress with the characteristic lengths. The characteristic horizontal length scale on the wafer in systems like Ge/Si is large in comparison to the vertical scale. The facets have small slopes which can be used to identify small terms that may be neglected. The characteristic thickness is H_0 and the horizontal length scale in x and y directions is L . Then $\alpha = H_0/L \ll 1$ is a small parameter used for the overall scaling

$$\begin{aligned}(x, y) &= (LX, LY), \quad z = H_0Z = \alpha LZ \quad , \\ h &= H_0H = \alpha LH, \quad u_i(x, y, z) = LU_i(X, Y, Z) \quad .\end{aligned}\tag{C.1}$$

Insertion into the Navier-Cauchy equations (1.31), the strain tensor (1.29), the stress tensor (1.28) and boundary conditions at $Z = H$, (1.32) results in the scaled elasticity equations

$$\begin{aligned} (1 - 2\nu)(\partial_X^2 + \partial_Y^2 + \frac{1}{\alpha^2}\partial_Z^2)U_1 + \partial_X^2 U_1 + \partial_X \partial_Y U_2 + \frac{1}{\alpha} \partial_X \partial_Z U_3 &= 0, \\ (1 - 2\nu)(\partial_X^2 + \partial_Y^2 + \frac{1}{\alpha^2}\partial_Z^2)U_2 + \partial_Y^2 U_2 + \partial_X \partial_Y U_1 + \frac{1}{\alpha} \partial_Y \partial_Z U_3 &= 0, \\ (1 - 2\nu)(\partial_X^2 + \partial_Y^2 + \frac{1}{\alpha^2}\partial_Z^2)U_3 + \frac{1}{\alpha^2} \partial_Z^2 U_3 + \frac{1}{\alpha} \partial_Y \partial_Z U_2 + \frac{1}{\alpha} \partial_X \partial_Z U_1 &= 0. \end{aligned} \quad (\text{C.2})$$

The symmetric strain tensor becomes

$$(\epsilon_{ij})_{i,j} = \begin{pmatrix} \partial_X U_1 & \frac{1}{2}(\partial_X U_2 + \partial_Y U_1) & \frac{1}{2}(\partial_X U_3 + \frac{1}{\alpha} \partial_Z U_1) \\ \frac{1}{2}(\partial_X U_2 + \partial_Y U_1) & \partial_Y U_2 & \frac{1}{2}(\partial_Y U_3 + \frac{1}{\alpha} \partial_Z U_2) \\ \frac{1}{2}(\partial_X U_3 + \frac{1}{\alpha} \partial_Z U_1) & \frac{1}{2}(\partial_Y U_3 + \frac{1}{\alpha} \partial_Z U_2) & \frac{1}{\alpha} \partial_Z U_3 \end{pmatrix}, \quad (\text{C.3})$$

while the symmetric stress tensor $(\sigma_{ij})_{i,j}$ can be written component-by-component as

$$\begin{aligned} \sigma_{11} &= \lambda^f (\partial_X U_1 + \partial_Y U_2 + \frac{1}{\alpha} \partial_Z U_3) + 2\mu^f \partial_X U_1, \\ \sigma_{22} &= \lambda^f (\partial_X U_1 + \partial_Y U_2 + \frac{1}{\alpha} \partial_Z U_3) + 2\mu^f \partial_Y U_2, \\ \sigma_{33} &= \lambda^f (\partial_X U_1 + \partial_Y U_2 + \frac{1}{\alpha} \partial_Z U_3) + \frac{2}{\alpha} \mu^f \partial_Z U_3, \\ \sigma_{12} &= \sigma_{21} = \mu^f (\partial_X U_2 + \partial_Y U_1), \\ \sigma_{13} &= \sigma_{31} = \mu^f (\partial_X U_3 + \frac{1}{\alpha} \partial_Z U_1), \\ \sigma_{23} &= \sigma_{32} = \mu^f (\partial_Y U_3 + \frac{1}{\alpha} \partial_Z U_2). \end{aligned} \quad (\text{C.4})$$

λ^f and μ^f are the two Lamé parameters, see also Table C.1 for elasticity parameter conversion.

The boundary conditions on the film $\sigma_{ij} n_j = 0 \Leftrightarrow \sigma_{ij} n_j N = 0$ become

$$\begin{aligned} 0 &= \frac{\mu^f}{\alpha} \partial_Z U_1 + (\mu^f \partial_X U_3 - \lambda^f H_X \partial_Z U_3) \\ &\quad - \alpha ((\lambda^f (\partial_X U_1 + \partial_Y U_2) + 2\mu^f \partial_X U_1) H_X + \mu^f (\partial_X U_2 + \partial_Y U_1) H_Y), \\ 0 &= \frac{\mu^f}{\alpha} \partial_Z U_2 + (\mu^f \partial_Y U_3 - \lambda^f H_Y \partial_Z U_3) \\ &\quad - \alpha (\mu^f (\partial_X U_2 + \partial_Y U_1) H_X + (\lambda^f (\partial_X U_1 + \partial_Y U_2) + 2\mu^f \partial_Y U_2) H_Y), \\ 0 &= \frac{1}{\alpha} (2\mu^f + \lambda^f) \partial_Z U_3 + (\lambda^f (\partial_X U_1 + \partial_Y U_2) - \mu^f (H_X \partial_Z U_1 + H_Y \partial_Z U_2)) \\ &\quad - \alpha (\mu^f (H_X \partial_X U_3 + H_Y \partial_Y U_3)). \end{aligned} \quad (\text{C.5})$$

The displacements in the film (here without superscripts) are expanded in terms of the slope parameter

$$U_i = U_i^{(0)} + \alpha U_i^{(1)} + \alpha^2 U_i^{(2)} + \mathcal{O}(\alpha^3), \quad i = 1, 2, 3. \quad (\text{C.6})$$

These are inserted into the rescaled Navier-Cauchy equations (C.2) and the boundary conditions (C.5) which results in different problems at different orders. These are

$\mathcal{O}(1)$:

To the leading order the Navier-Cauchy equations write

$$\partial_Z^2 U_1^{(0)} = 0, \quad \partial_Z^2 U_2^{(0)} = 0, \quad \partial_Z^2 U_3^{(0)} = 0$$

and the boundary conditions at $Z = H$ become

$$\partial_Z U_1^{(0)} = 0, \quad \partial_Z U_2^{(0)} = 0, \quad \partial_Z U_3^{(0)} = 0 \quad .$$

$\mathcal{O}(\alpha)$:

The film equations for the next order problem write

$$0 = \check{\nabla} \cdot (U_i^{(1)}, U_3^{(0)}) + \delta_{3i} (\partial_Z^2 U_3^{(1)} + \partial_X \partial_Z U_1^{(0)}), \quad i = 1, 2, 3, \quad Z \in (0, H), \quad (\text{C.7})$$

in the film and on the upper boundary

$$\begin{aligned} 0 &= \frac{2\nu}{1-2\nu} \partial_Z U_3^{(0)} H_X - \partial_Z U_1^{(1)} - \partial_X U_3^{(0)}, \\ 0 &= \frac{2\nu}{1-2\nu} \partial_Z U_3^{(0)} H_Y - \partial_Z U_2^{(1)} - \partial_Y U_3^{(0)}, \\ 0 &= \frac{2(\nu-1)}{1-2\nu} \partial_Z U_3^{(1)} - \frac{2\nu}{1-2\nu} (\partial_X U_1^{(0)} + \partial_Y U_2^{(0)}) + \partial_Z U_1^{(0)} H_X + \partial_Z U_2^{(0)} H_Y, \quad \text{at } Z = H, \end{aligned} \quad (\text{C.8})$$

where for the Navier-Cauchy equations the second order differential operator

$$\check{\nabla} = \begin{pmatrix} (1-2\nu)\partial_Z^2 \\ \partial_X \partial_Z \end{pmatrix}$$

was used.

$\mathcal{O}(\alpha^2)$:

One order up it can be proceed analogously with the Navier-Cauchy equations, while the upper boundary conditions write

$$\begin{aligned} \partial_Z U_1^{(2)} &= -\partial_X U_3^{(1)} + \frac{2\nu}{1-2\nu} \left(\partial_X U_1^{(0)} + \partial_Y U_2^{(0)} + \partial_Z U_3^{(1)} \right) H_X \\ &\quad + 2H_X \partial_X U_1^{(0)} + (\partial_X U_2^{(0)} + \partial_Y U_1^{(0)}) H_Y, \\ \partial_Z U_2^{(2)} &= -\partial_Y U_3^{(1)} + \frac{2\nu}{1-2\nu} \left(\partial_X U_1^{(0)} + \partial_Y U_2^{(0)} + \partial_Z U_3^{(1)} \right) H_Y \\ &\quad + 2H_Y \partial_Y U_2^{(0)} + (\partial_X U_2^{(0)} + \partial_Y U_1^{(0)}) H_X, \\ \partial_Z U_3^{(2)} &= \frac{\nu}{2(1-\nu)} (\partial_Z U_1^{(1)} H_X + \partial_Z U_2^{(1)} H_Y) + \frac{\nu}{\nu-1} (\partial_X U_1^{(1)} + \partial_Y U_2^{(1)}) \\ &\quad + \frac{\nu}{2(1-\nu)} (\partial_X U_3^{(0)} H_X + \partial_Y U_3^{(0)} H_Y) \quad . \end{aligned} \quad (\text{C.9})$$

Now the derived PDEs have to be solved. This is done also one order after another, so that the just derived expressions for lower orders can be inserted into the actual calculations.

$\mathcal{O}(1)$:

The general solutions for the film equations are

$$U_1^{(0)} = A_1(X, Y)Z + B_1(X, Y), \quad U_2^{(0)} = A_2(X, Y)Z + B_2(X, Y), \quad U_3^{(0)} = A_3(X, Y)Z + B_3(X, Y)$$

with integration factors $A_i(X, Y)$ and $B_i(X, Y)$. The boundary conditions imply that the coefficients of the linear terms are zero, so that the leading order solutions simplify to

$$U_1^{(0)} = B_1(X, Y), \quad U_2^{(0)} = B_2(X, Y), \quad U_3^{(0)} = B_3(X, Y) \quad .$$

The leading order solution for the film displacements should correspond to the solution to the base state (1.37), which is in the new scales

$$u = \begin{pmatrix} \epsilon LX \\ \epsilon LY \\ -\frac{2\nu}{1-\nu}\epsilon\alpha LZ \end{pmatrix} \equiv L \begin{pmatrix} U_1 \\ U_2 \\ U_3 \end{pmatrix} = L \begin{pmatrix} \epsilon X \\ \epsilon Y \\ 0 \end{pmatrix} + L\alpha \begin{pmatrix} 0 \\ 0 \\ \frac{2\nu}{\nu-1}\epsilon Z \end{pmatrix} \quad .$$

This leads to expressions for the B_i terms, so that the leading order solution is the linear function

$$U_1^{(0)} = \epsilon X, \quad U_2^{(0)} = \epsilon Y, \quad U_3^{(0)} = 0 \quad . \quad (\text{C.10})$$

$\mathcal{O}(\alpha)$:

Equations (C.7) and (C.8) give the $\mathcal{O}(\alpha)$ displacements

$$U_i^{(1)} = A_i^{(1)}(X, Y), \quad i = 1, 2, \quad U_3^{(1)} = \frac{2\nu}{\nu-1}\epsilon Z + A_3^{(1)}(X, Y) \quad . \quad (\text{C.11})$$

Here $A_i^{(1)}$ are functions that will have to be specified through expressions of the substrate displacements and the boundary conditions at the interface. To derive the $\mathcal{O}(\alpha)$ strain tensor the procedure has to be repeated once more for the next order.

$\mathcal{O}(\alpha^2)$:

The general solutions is as in the preceding orders

$$U_i^{(2)} = B_i^{(2)}(X, Y)Z + A_i^{(2)}(X, Y) \quad . \quad (\text{C.12})$$

The boundary conditions to the same order, (C.9), simplify after inserting the lower order solutions to

$$\begin{aligned} \partial_Z U_1^{(2)} &= -\partial_X A_3^{(1)}(X, Y) - 2\frac{\nu+1}{\nu-1}\epsilon H_X \quad , \\ \partial_Z U_2^{(2)} &= -\partial_Y A_3^{(1)}(X, Y) - 2\frac{\nu+1}{\nu-1}\epsilon H_Y \quad , \\ \partial_Z U_3^{(2)} &= \frac{\nu}{\nu-1}(\partial_X A_1^{(1)}(X, Y) + \partial_Y A_2^{(1)}(X, Y)) \quad . \end{aligned}$$

These expressions are just the B_i functions in (C.12), so that the second order terms become

$$\begin{aligned} U_1^{(2)} &= \left(-\frac{2(\nu+1)}{\nu-1}\epsilon H_X - \partial_X A_3^{(1)}(X, Y) \right) Z + A_1^{(2)}(X, Y) \quad , \\ U_2^{(2)} &= \left(-\frac{2(\nu+1)}{\nu-1}\epsilon H_Y - \partial_Y A_3^{(1)}(X, Y) \right) Z + A_2^{(2)}(X, Y) \quad , \\ U_3^{(2)} &= \frac{\nu}{\nu-1} \left(\partial_X A_1^{(1)}(X, Y) + \partial_Y A_2^{(1)}(X, Y) \right) Z + A_3^{(2)}(X, Y) \quad . \end{aligned}$$

Insertion of the expressions for the displacements into the strain and the stress tensor ((C.3) and (C.4)), respectively, give the leading order strain energy density

$$\mathcal{E}_{sed}^{(0)} = \frac{1}{2} \sigma_{ij}^{(0)} \epsilon_{ij}^{(0)} = \frac{E}{1-\nu} \epsilon^2 = \mathcal{E}_{sed}^{base}$$

and the next order correction

$$\begin{aligned} \mathcal{E}_{sed}^{(1)} &= \frac{1}{2} \left(\sigma_{ij}^{(1)} \epsilon_{ij}^{(0)} + \sigma_{ij}^{(0)} \epsilon_{ij}^{(1)} \right) \\ &= \frac{\epsilon}{2} \left(\frac{E}{1-\nu} (\partial_X A_1^{(1)} + \partial_Y A_2^{(1)}) \right. \\ &\quad \left. + \frac{E}{1-\nu^2} \partial_X A_1^{(1)} + \frac{E\nu}{1-\nu^2} \partial_Y A_2^{(1)} + \frac{E}{1-\nu^2} \partial_Y A_2^{(1)} + \frac{E\nu}{1-\nu^2} \partial_X A_1^{(1)} \right) \\ &= \frac{\epsilon E}{1-\nu} (\partial_X A_1^{(1)} + \partial_Y A_2^{(1)}) \quad . \end{aligned} \quad (C.13)$$

The leading order term is just the strain energy density of the base state (1.36). To sufficiently describe epitaxial growth, this order has to be incorporated into the evolution equation and hence the integration factors $A_i^{(j)}$ have to be determined. This will be done by calculating the elastic response of the substrate. Here, the scaling is chosen slightly differently. Unlike the film, the vertical and the horizontal scales are similar and the displacements are scaled with the same length

$$(x, y, z) = L(X, Y, \bar{Z}), \quad u_i^s = L U_i^s \quad .$$

\bar{Z} is different than the Z from before, however, for convenience the bar will be dropped. The problem is transformed into Fourier space for the two horizontal, infinite dimensions. With the wave numbers k_1 and k_2 , 2D transforms for the film height and the substrate displacements write

$$\begin{aligned} \hat{H}(k_1, k_2, t) &= \int_{\mathbb{R}^2} H(X, Y, t) e^{-ik_1 X - ik_2 Y} dX dY, \\ \hat{U}_i^s(k_1, k_2, Z, t) &= \int_{\mathbb{R}^2} U_i^s(X, Y, Z, t) e^{-ik_1 X - ik_2 Y} dX dY \quad , i = 1, 2, 3 \quad . \end{aligned}$$

The corresponding inverse transformations are

$$\begin{aligned} H(X, Y, t) &= \frac{1}{(2\pi)^2} \int_{\mathbb{R}^2} \hat{H}(k_1, k_2, t) e^{ik_1 X + ik_2 Y} dk_1 dk_2, \\ U_i^s(X, Y, Z, t) &= \frac{1}{(2\pi)^2} \int_{\mathbb{R}^2} \hat{U}_i^s(k_1, k_2, Z, t) e^{ik_1 X + ik_2 Y} dk_1 dk_2 \quad , i = 1, 2, 3 \quad . \end{aligned}$$

Navier-Cauchy equations (1.31) in Fourier-space write (with $\hat{U}_i^s = \hat{U}_i^s(k_1, k_2, Z, t)$)

$$\begin{aligned} 0 &= \int_{\mathbb{R}^2} \left((1-2\nu)(-k^2 + \partial_{ZZ}) \hat{U}_1^s - k_1^2 \hat{U}_1^s - k_1 k_2 \hat{U}_2^s + i k_1 \partial_Z \hat{U}_3^s \right) e^{ik_1 X + ik_2 Y} dk_1 dk_2, \\ 0 &= \int_{\mathbb{R}^2} \left((1-2\nu)(-k^2 + \partial_{ZZ}) \hat{U}_2^s - k_1 k_2 \hat{U}_1^s - k_2^2 \hat{U}_2^s + i k_2 \partial_Z \hat{U}_3^s \right) e^{ik_1 X + ik_2 Y} dk_1 dk_2, \\ 0 &= \int_{\mathbb{R}^2} \left((1-2\nu)(-k^2 + \partial_{ZZ}) \hat{U}_3^s + i k_1 \partial_Z \hat{U}_1^s + i k_2 \partial_Z \hat{U}_2^s + \partial_{ZZ} \hat{U}_3^s \right) e^{ik_1 X + ik_2 Y} dk_1 dk_2, \end{aligned}$$

where $k = \sqrt{k_1^2 + k_2^2}$ is the length of the wave vector. These equations are fulfilled if the kernels of the integrals are identically zero

$$\begin{aligned} 0 &= (1 - 2\nu)(-k^2 + \partial_{ZZ})\hat{U}_1^s - k_1^2\hat{U}_1^s - k_1k_2\hat{U}_2^s + ik_1\partial_Z\hat{U}_3^s, \\ 0 &= (1 - 2\nu)(-k^2 + \partial_{ZZ})\hat{U}_2^s - k_1k_2\hat{U}_1^s - k_2^2\hat{U}_2^s + ik_2\partial_Z\hat{U}_3^s, \\ 0 &= (1 - 2\nu)(-k^2 + \partial_{ZZ})\hat{U}_3^s + ik_1\partial_Z\hat{U}_1^s + ik_2\partial_Z\hat{U}_2^s + \partial_{ZZ}\hat{U}_3^s, \end{aligned} \quad (\text{C.14})$$

in the infinite half-space below the solid-solid interface, hence for $Z < 0$. At minus infinity the condition

$$U_i \xrightarrow{Z \rightarrow -\infty} 0$$

has to hold. Expanding the displacements

$$U_i^s = U_{i0}^s + \alpha U_{i1}^s + \alpha^2 U_{i2}^s + \mathcal{O}(\alpha^3) \quad (\text{C.15})$$

and its transform analogously gives the interface condition (1.34) at $Z = 0$,

$$\begin{aligned} U_1^{(0)} + \sum_{j=1}^{\infty} \alpha_j U_1^{(j)} &= (U_{10}^s + \epsilon X) + \sum_{j=1}^{\infty} \alpha_j U_{1j}^s, \\ U_2^{(0)} + \sum_{j=1}^{\infty} \alpha_j U_2^{(j)} &= (U_{20}^s + \epsilon Y) + \sum_{j=1}^{\infty} \alpha_j U_{2j}^s, \\ \sum_{j=0}^{\infty} \alpha_j U_3^{(j)} &= \sum_{j=0}^{\infty} \alpha_j U_{3j}^s. \end{aligned} \quad (\text{C.16})$$

For the corresponding orders this leads to the conditions

$$U_{i0}^s = 0, \quad U_{ij}^s = U_{ij}^f, \quad i = 1, 2, 3, j \in \{1, 2, \dots\} \quad \text{at} \quad Z = 0. \quad (\text{C.17})$$

Because of the linear character, equations (C.14) are fulfilled if the $\mathcal{O}(\alpha^j)$ problems

$$\begin{aligned} 0 &= (1 - 2\nu)(-k^2 + \partial_{ZZ})\hat{U}_{1j}^s - k_1^2\hat{U}_{1j}^s - k_1k_2\hat{U}_{2j}^s + ik_1\partial_Z\hat{U}_{3j}^s, \\ 0 &= (1 - 2\nu)(-k^2 + \partial_{ZZ})\hat{U}_{2j}^s - k_1k_2\hat{U}_{1j}^s - k_2^2\hat{U}_{2j}^s + ik_2\partial_Z\hat{U}_{3j}^s, \\ 0 &= (1 - 2\nu)(-k^2 + \partial_{ZZ})\hat{U}_{3j}^s + ik_1\partial_Z\hat{U}_{1j}^s + ik_2\partial_Z\hat{U}_{2j}^s + \partial_{ZZ}\hat{U}_{3j}^s, \end{aligned} \quad (\text{C.18})$$

hold true. The solutions are

$$\hat{U}_{ij}^s = C_{ij}e^{kZ} + Ze^{kZ} \frac{k_i}{k(3 - 4\nu^s)} \sum_{l=1}^3 k_l C_{lj}. \quad (\text{C.19})$$

Here $k_3 = ik$ for notational convenience and not a third wave number as one might think. The unknown functions C_{ij} are determined by the boundary conditions (C.17). For orders α and α^2 these give

$$C_{ij} = (\hat{U}_i^{(j)})|_{Z=0} = \hat{A}_i^{(j)}, \quad i = 1, 2, 3, j = 1, 2. \quad (\text{C.20})$$

Furthermore the continuity condition on the normal stresses (1.35) to these orders is

$$(\sigma_{i3}^{(l)})^f|_{z=0} = (\sigma_{i3}^{(l)})^s|_{z=0}, \quad l = 1, 2 \quad . \quad (\text{C.21})$$

As described later this gives

$$\begin{aligned} C_{11} &= i\tilde{e}\epsilon \frac{k_1}{k} \hat{H}, \\ C_{21} &= i\tilde{e}\epsilon \frac{k_2}{k} \hat{H}, \\ C_{31} &= -\tilde{e}\epsilon \frac{1-2\nu^s}{1-\nu^s} \hat{H} \quad , \end{aligned} \quad (\text{C.22})$$

with

$$\tilde{e} = \frac{2\mu^f(1+\nu^f)(1-\nu^s)}{(1-\nu^f)\mu^s} \quad . \quad (\text{C.23})$$

Using equation (C.20) in the strain energy term of order α (C.13) gives in Fourier space

$$\hat{\mathcal{E}}_{sed}^{(1)} = \frac{\epsilon E^f}{1-\nu^f} \left(ik_1 i\tilde{e}\epsilon \frac{k_1}{k} \hat{H} + ik_2 i\tilde{e}\epsilon \frac{k_2}{k} \hat{H} \right) = -\frac{E^f}{1-\nu^f} \epsilon^2 (\tilde{e}k\hat{H}) \quad ,$$

so that overall the strain energy density correction is

$$\mathcal{E}_{sed}^{(1)} = \mathcal{F}^{-1}[-\mathcal{E}_{sed}^{base} \tilde{e}k\hat{H}] \quad . \quad (\text{C.24})$$

As last step, the expressions in (C.22) are derived. Using the expansions (C.15) in Hooke's law (1.28), which relates the stress and the strain tensor, gives

$$\begin{aligned} (\sigma_{11}^{(l)})^s &= \lambda^s (\partial_X U_{1l}^s + \partial_Y U_{2l}^s + \partial_Z U_{3l}^s) + 2\mu^s \partial_X U_{1l}^s \quad , \\ (\sigma_{22}^{(l)})^s &= \lambda^s (\partial_X U_{1l}^s + \partial_Y U_{2l}^s + \partial_Z U_{3l}^s) + 2\mu^s \partial_Y U_{2l}^s \quad , \\ (\sigma_{33}^{(l)})^s &= \lambda^s (\partial_X U_{1l}^s + \partial_Y U_{2l}^s + \partial_Z U_{3l}^s) + 2\mu^s \partial_Z U_{3l}^s \quad , \\ (\sigma_{12}^{(l)})^s &= \mu^s (\partial_X U_{2l}^s + \partial_Y U_{1l}^s) \quad , \\ (\sigma_{13}^{(l)})^s &= \mu^s (\partial_X U_{3l}^s + \partial_Z U_{1l}^s) \quad , \\ (\sigma_{23}^{(l)})^s &= \mu^s (\partial_Y U_{3l}^s + \partial_Z U_{2l}^s) \quad . \end{aligned} \quad (\text{C.25})$$

These formulas are inserted together with the expressions (C.4) for the film stress into the interface normal continuity condition (C.21). To order α^{-1} no conditions are obtained. To order $\mathcal{O}(1)$ also no restrictions can be found as follows from the next calculation.

$\mathcal{O}(1)$:

$$\begin{aligned} \lambda^f (\partial_X U_1^{(0)} + \partial_Y U_2^{(0)} + \partial_Z U_3^{(1)}) + 2\mu^f \partial_Z U_3^{(1)} &= \lambda^s (\partial_X U_{10}^s + \partial_Y U_{20}^s + \partial_Z U_{30}^s) + 2\mu^s \partial_Z U_{30}^s, \\ \mu^f (\partial_X U_2^{(0)} + \partial_Y U_1^{(0)}) &= \mu^s (\partial_X U_{20}^s + \partial_Y U_{10}^s), \\ \mu^f (\partial_X U_3^{(0)} + \partial_Z U_1^{(1)}) &= \mu^s (\partial_X U_{30}^s + \partial_Z U_{10}^s). \end{aligned}$$

Inserting the solutions (C.11) and (C.10) and using (C.17) shows that these equations do not define any new restrictions. Only in the first equation there are nonzero terms on the left hand side, these are

$$\lambda^f(2\epsilon + \frac{2\nu}{\nu-1}\epsilon) + 2\mu^f \frac{2\nu}{\nu-1}\epsilon = 0$$

and thus also do not contribute anything. The next order is important.

$\mathcal{O}(\alpha)$:

$$\begin{aligned} \lambda^f(\partial_X U_1^{(1)} + \partial_Y U_2^{(1)} + \partial_Z U_3^{(2)}) + 2\mu^s \partial_Z U_3^{(2)} &= \lambda^s(\partial_X U_{11}^s + \partial_Y U_{21}^s + \partial_Z U_{31}^s) + 2\mu^s \partial_Z U_{31}^s, \\ \mu^f(\partial_X U_3^{(1)} + \partial_Z U_1^{(2)}) &= \mu^s(\partial_X U_{31}^s + \partial_Z U_{11}^s), \\ \mu^f(\partial_Y U_3^{(1)} + \partial_Z U_2^{(2)}) &= \mu^s(\partial_Y U_{31}^s + \partial_Z U_{21}^s) \quad . \end{aligned}$$

Inserting the expressions for the solutions and changing to Fourier space gives

$$\begin{aligned} 0 &= \lambda^s \left(ik_1 C_{11} + ik_2 C_{21} + k C_{31} + \frac{k_3}{k(3-4\nu^s)} \sum_{l=1}^3 k_l C_{l1} \right) + 2\mu^s \left(k C_{31} + \frac{k_3}{k(3-4\nu^s)} \sum_{l=1}^3 k_l C_{l1} \right), \\ -\mu^f \frac{2(\nu^f+1)}{\nu^f-1} \epsilon i k_1 \hat{H} &= \mu^s \left(ik_1 C_{31} + k C_{11} + \frac{k_1}{k(3-4\nu^s)} \sum_{l=1}^3 k_l C_{l1} \right), \\ -\mu^f \frac{2(\nu^f+1)}{\nu^f-1} \epsilon i k_2 \hat{H} &= \mu^s \left(ik_2 C_{31} + k C_{21} + \frac{k_2}{k(3-4\nu^s)} \sum_{l=1}^3 k_l C_{l1} \right) \quad . \end{aligned}$$

This is a 3x3 linear system for the C_{k1} functions, giving exactly the expressions in (C.22).

Conversion of elasticity parameters

For homogeneous isotropic media generally two elastic moduli are sufficient for the description of Hooke's law. However, there are different such parameters and these can be transformed into each other. Table C.1 shows the most important transformations, which are especially useful when other publications are studied. There frequently other parameters are used in the elasticity expressions.

	(ν, E)	(μ, E)	(μ, ν)	(ν, λ)	(μ, λ)
E	id	id	$2\mu(1 + \nu)$	$\lambda \frac{(1-2\nu)(1+\nu)}{\nu}$	$\mu \frac{3\lambda+2\mu}{\lambda+\mu}$
λ	$\frac{E\nu}{(1+\nu)(1-2\nu)}$	$\mu \frac{E-2\mu}{3\mu-E}$	$\frac{2\mu\nu}{1-2\nu}$	id	id
μ	$\frac{E}{2(1+\nu)}$	id	id	$\lambda \frac{1-2\nu}{2\nu}$	id
ν	id	$\frac{E}{2\mu} - 1$	id	id	$\frac{\lambda}{2(\lambda+\mu)}$

Table C.1: E Young's modulus (or elastic modulus), λ Lamé's first parameter, μ Lamé's second parameter (shear modulus), ν Poisson's ratio. The table shows some transformation between the elasticity parameters (source Wikipedia or any good book on elasticity).

Constants for HCCH matching

Here the constants abbreviated for use in Chapter 3 are given:

$$\begin{aligned}
 d_1 &= -\frac{2^{1/3}}{12}c_1 + \frac{1}{3}(A_1c_2 + A_2c_1) - \frac{59}{216}c_1A_1^2 \quad , \\
 d_2 &= \left(\frac{\sqrt{2}}{12}c_1 - \frac{2^{1/6}}{3}(A_1c_2 + A_2c_1) + \frac{17}{72}2^{1/6}A_1^2c_1 \right) \quad , \\
 d_3 &= \frac{2^{1/3}}{18}A_1^2c_1 \quad , \\
 d_4 &= -\frac{23}{7}c_1c_2 + \frac{7}{12}A_1c_1^2 \quad , \\
 \check{e}_1 &= -\frac{1}{8}A_1^2 + \frac{1}{3}c_1A_1 + c_2 - \frac{23}{14}c_1^2 + \frac{1}{2}A_2 \quad , \\
 \check{e}_2 &= -\left(\frac{1}{4}A_1 + \frac{1}{3}c_1\right)A_2 + \left(\frac{7}{12}c_1^2 + \frac{1}{3}c_2\right)A_1 + \frac{1}{2}A_3 - \frac{59}{216}c_1A_1^2 - \frac{1}{12}2^{1/3}c_1 \\
 &\quad + d_1 - \frac{23}{7}c_1c_2 + \frac{1}{16}A_1^3 + \frac{127}{28}c_1^3 \quad .
 \end{aligned} \tag{C.26}$$

Spaces, scalar products and norms

Let $\Omega \subset \mathbb{R}^n$ bounded with Lipschitz boundary and $f : \Omega \rightarrow \mathbb{R}$. Then the spaces, corresponding scalar products and induced norms can be defined as follows.

- Standard Euclidean norm for vectors $v \in \mathbb{R}^n$: $|v| = (\sum_{j=1}^n v_j^2)^{1/2}$
- $C^k(\Omega, \mathbb{R}) = \{f : \Omega \rightarrow \mathbb{R} : f \text{ is } k \text{ times continuously differentiable}\}$
- $C^\infty(\Omega, \mathbb{R}) = \{f : \Omega \rightarrow \mathbb{R} : f \text{ is } \infty \text{ times continuously differentiable}\}$
- L^p -norm: $\|f\|_{L^p(\Omega)} = (\int_\Omega |f|^p dV)^{1/p}$
- Notation for L^2 : $\|f\| = \|f\|_{L^2(\Omega)}$
- $\|f\|_{L^\infty} = \lim_{p \rightarrow \infty} \|f\|_{L^p(\Omega)} = \text{ess sup}_{x \in \Omega} |f(x)| = \inf_{c \geq 0} \{|f(x)| \leq c, a.e.\}$
- Lebesgue spaces: $L^p(\Omega) = \{f : \Omega \rightarrow \mathbb{R} \text{ measurable; } \|f\|_{L^p(\Omega)} < \infty\}, p \in (0, \infty]$
- The scalar products inducing the p -norm are for $f, g : \Omega \rightarrow \mathbb{R}$: $(f, g)_{L^p} = \int_\Omega (fg)^{p/2} dV$
- Sobolev spaces with time:
 $L^p(0, T; X) = \{f : [0, T] \rightarrow X : f \text{ measurable, } \|\|f(t)\|_X\|_{L^p([0, T])} < \infty\}$
- $L^\infty(0, T; X) = \{f : [0, T] \rightarrow X : f \text{ measurable, } \text{ess sup}_{t \in [0, T]} \|u(t)\|_X < \infty\}$
- Locally integrable functions:
 $L^1_{loc}(\Omega) = \{f : [0, T] \rightarrow X : f \text{ measurable, } \forall X \subset \Omega \text{ compact } \int_X |f| dx < \infty\}$
- Norm for Sobolev space: $\|f\|_{k,p} = (\sum_{j=0}^k \|f^{(j)}\|_p^p)^{1/p}$
- Sobolev spaces: $W^{k,p}(\Omega) = \{f : \Omega \rightarrow \mathbb{R} : \|f\|_{k,p} < \infty\}$
 Functions that have weak derivatives up to order k which belong to L^p
- The most common Sobolev spaces: $H^k(\Omega) = W^{k,2}(\Omega)$ (i.e. $H^0 = L^2$)
- Inner product in H^k : $(f, g)_{H^k} = \sum_{j=0}^k (f^{(j)}, g^{(j)})_{L^2}$
- $\dot{H}^k(\Omega) = \dot{W}^{k,2}(\Omega) = \{f \in H^k(\Omega) : \int_\Omega f dV = 0\}$

- From here on: $\Omega = [0, L]^m$, then:

$$C_{per}^\infty(\Omega) = \{f \in C^\infty(\Omega) : f(x + e_j L) = f(x), j = 1, \dots, m\}$$
- $H_{per}^k(\Omega)$ is the completion of $C_{per}^\infty(\Omega)$ in the H^k -norm
- $\dot{H}_{per}^k(\Omega) = H_{per}^k(\Omega) \cap \dot{H}^k(\Omega)$
- Norm for periodic Sobolev spaces with zero mean: $\|f\|_{\dot{H}_{per}^k} = \sum_{|\alpha|=k} |D^\alpha f|^2$
- $H^{-k}(\Omega)$ is the dual space to $H_{per}^k(\Omega)$: $H^{-k}(\Omega) = (H_{per}^k(\Omega))^*$
- For a Hilbert space H and dual H^* it is $\|f\|_{H^*} = \sup\{(f, u)_H : u \in H \text{ with } \|u\|_H \leq 1\}$

List of Abbreviations

a.e.	-	almost everywhere
AC	-	Allen-Cahn
ATG	-	Asaro-Tiller-Grinfeld
CAC	-	convective Allen-Cahn
CCH	-	convective Cahn-Hilliard
CFL	-	Courant-Friedrichs-Levy
CH	-	Cahn-Hilliard
CVD	-	chemical vapor deposition
DE	-	differential equation
FDM	-	finite difference method
FEM	-	- finite element method
HCCH	-	higher order convective Cahn-Hilliard
MEG	-	multiple exciton generation
MBE	-	molecular beam epitaxy
ML	-	monolayer
ODE	-	ordinary differential equation
PDE	-	partial differential equation
PSM	-	pseudospectral method
PVD	-	physical vapor deposition
QD	-	quantum dot
QDM	-	quantum dot model
SM	-	spectral method
STM	-	scanning tunneling microscopy
TEM	-	transmission electron microscopy

Acknowledgements

You can't help someone get up a hill without getting closer to the top yourself.

H. Norman Schwarzkopf (1934 -)

This work was made possible by Barbara Wagner who was not deterred from my nonstandard application for the PhD position and gave me unlimited support and motivation to get things done, by Peter Evans who always took the time to discuss all aspects of applied analysis, mathematical modeling or physics with me and by Andreas Münch who in the first weeks gave me a kick-off for many of the new topics. These colleagues introduced me into the world of PDEs, i.e. into thin films, dynamical systems, matched asymptotics, stability analysis among many others. The fundamental difference of these mathematical areas to numerical optimization and numerical linear algebra, which were my prior main research fields during my work on my diploma thesis, were a major obstacle which I had to master. The help of the group was essential to gain enough insights to write this document in a reasonable time window. I also thank Volker Mehrmann, the chair of the Matheon research center, for his support, and the center itself together with the Weierstraß institute (WIAS) for the financial support.

For the theoretical part of this work, which is related to the existence of solutions for a sixth order semilinear PDE, I have to thank Lutz Recke from the Humboldt University who helped me to understand the fundamental theory for the related CCH equation. Special thanks go to Piotr Rybka from the University of Warsaw. When he invited me to Poland we were able to make substantial progress in the existence theory.

I want to thank the young research colleagues Christoph, Clemens, Daniel, Dirk, Ernst, Georgy, Lars, Margarita, Robert, Sven-Joachim and Thomas (in alphabetical order) for all the lunches, slacklining, coffees, math and cakes. Furthermore, thanks to anyone met on conferences, summer schools, research weekends or seminars for inspiration and motivation.

Finally I thank everyone outside the research world that filled my life during the last four years with other things than mathematics. To mention a few: my parents Teresa and Darek, my brother Tomasz, my girlfriend Johanna, my friends Heiko, Jan, Thomas, Werner, Jochen, Tim, Mathis, Hugo, Julio, Claudia, Dominik, Holger, May, Moritz, Martin, all the handball boys and girls, the Sunday's soccer team, team Zissou and those forgotten.